Advancing Fundamentals and Applications of X-ray Birefringence Imaging

by

YATING ZHOU

Thesis Submitted for

DOCTOR OF PHILOSOPHY

SCHOOL OF CHEMISTRY

CARDIFF UNIVERSITY

June 2018

DECLARATION

This work has not been submitted in substance for any other degree or award at this or any other university or place of learning, nor is being submitted concurrently in candidature for any degree or other award.

Signed …..... (candidate) Date …….....

STATEMENT 1

This work is being submitted in partial fulfillment of the requirements for the degree of …… (insert MCh, MD, MPhil, PhD etc, as appropriate)

Signed …..... (candidate) Date …….....

STATEMENT 2

This work is the result of my own independent work/investigation, except where otherwise stated, and the thesis has not been edited by a third party beyond what is permitted by Cardiff University's Policy on the Use of Third Party Editors by Research Degree Students. Other sources are acknowledged by explicit references. The views expressed are my own.

Signed …..... (candidate) Date …….....

STATEMENT 3

I hereby give consent for my thesis, if accepted, to be available online in the University's Open Access repository and for inter-library loan, and for the title and summary to be made available to outside organisations.

Signed …..... (candidate) Date …….....

STATEMENT 4: PREVIOUSLY APPROVED BAR ON ACCESS

I hereby give consent for my thesis, if accepted, to be available online in the University's Open Access repository and for inter-library loan **after expiry of a bar on access previously approved by the Academic Standards & Quality Committee.**

Signed …..... (candidate) Date …….....

Abstract

This thesis is mainly focused on the new technique of X-ray Birefringence Imaging (XBI). It reports applications of XBI in different research areas and also presents some developments of the fundamental theory of XBI analysis. At the end of the thesis, work on crystal structure determination directly from powder X-ray diffraction data is also included.

Chapter 1 and Chapter 2 provide the theoretical background of XBI and introduce the other techniques used in this thesis. As XBI is analogous to Polarizing Optical Microscopy (POM), the introduction begins with a discussion of general optics, which is then expanded to specific case of polarized X-rays. The methodology for structure determination directly from powder X-ray diffraction data is also described.

Chapter 3 demonstrates the application of XBI to study liquid crystalline materials, representing the first investigation of liquid-state samples by XBI. The experimental results show that the XBI technique is successful to elucidate the molecular orientational ordering in different liquid crystalline phases, demonstrating that characterization of molecular orientations by XBI is not limited to the solid-state.

Chapter 4 explores a novel type of material – bending crystals. As an effective technique to investigate molecular orientations, XBI is shown to provide clear information on the crystal curvature. Both plastic and elastic types of bending crystal are analysed in both static and dynamic experiments. A theoretical analysis of XBI behaviour of a material containing multiple molecular orientations is also established.

In Chapter 5, XBI is used to study composite organic materials. The experimental results vindicate the ability of XBI to characterize spatial distribution of molecules in composite samples.

Chapter 6 reports XBI behaviour for the novel case in which two different crystals with independent orientations are present in the X-ray beam. The development of an experimental set-up for recording XBI data using a transmission-based polarization analyzer is also reported for the first time.

Chapter 7 is focused on structure determination directly from powder X-ray diffraction. Three crystal structures are determined – two different urea co-crystals and one poly-aromatic compound.

Chapter 8 summarises the work in this thesis, gives an appraisal of the strengths and limitations of the XBI technique, and proposes some potential research directions for the future.

Acknowledgements

Firstly, I would like to express my thanks to my supervisor, Professor Kenneth Harris, for his constant guidance and help during my PhD study. I am thankful to him for providing me with so many interesting research opportunities, and it is a pleasant experience to do something I like as my PhD project. His patience, encouragement and immense knowledge ensured my PhD study has gone smoothly and efficiently.

I would also like to thank the Diamond Light Source for providing beam time and facilities to conduct all the synchrotron experiments. In particular, I would like to acknowledge Professor Stephen Collins, Dr. Igor Dolbnya, Dr. Ian Pape and Andrew Malandain for their professional advice and skillful operations to realize many different types of experimental design.

Furthermore, I am thankful to Dr. Benson Kariuki for discussing and solving crystal structures from single-crystal X-ray diffraction. I am also thankful to Dr. Andrew Williams and Dr. Colan Hughes for teaching me the procedures of crystal structure determination from powder X-ray diffraction, and helping me in many different research aspects. It has been enjoyable working within the group and I would like to thank all the members, especially Dr. Benjamin Palmer, Dr. Gregory Edwards-Gau, Rhian Patterson and Okba Al Rahal.

Finally, I would like to thank my family and friends for their encouragement and company. A special thanks to my parents, this thesis would not have been possible without their support and love.

An old Chinese saying goes: “It is better to travel ten thousand miles than to read ten thousand books.” Knowledge comes from books and from experience of the world. I am thankful to life for bringing me the experience to live and study in another country, and this will be an unforgettable part in my life journey.

Table of Contents

Chapter 1

Introduction

1.1 Birefringence and Polarizing Optical Microscopy

1.1.1 Birefringence

When a ray of light passes from one medium to another medium, the direction of the ray will change from its original direction. This phenomenon is called "refraction",[1] and it happens universally in our daily life, from observing fish in a river to looking out through home windows. Snell's law[2] (Eq.1.1) explains the relationship between the angles of incidence (θ_1) and refraction (θ_2): the ratio of the sines of the two angles is equivalent to the inverse of the ratio of the refractive indices (n_1 and n_2). Each kind of medium has its own refractive index (n), which is the ratio of the speed of light (c) in vacuum and the velocity of light (v) in the medium (Fig. 1.1).

$$\frac{Sin\theta_1}{Sin\theta_2} = \frac{n_2}{n_1} \qquad (1.1)$$

As the medium is different, the velocity of light (v) changes when it enters another medium, and the velocity of light depends on the molecular structure of the medium, e.g., light travels faster in air (~ 80% N_2 and 20% O_2) than in water (H_2O). Because both incident ray and refracted ray come from the same source, the two light waves have the same frequency (f). Thus, we can connect together the angle, velocity, wavelength and refractive index (Eq.1.2 – Eq.1.4). It is obvious that the molecular-level components of the medium have a real impact on how light travels.

$$v_1 = f\lambda_1 \qquad (1.2)$$

$$v_2 = f\lambda_2 \qquad (1.3)$$

$$\frac{Sin\theta_1}{Sin\theta_2} = \frac{v_1}{v_2} = \frac{\lambda_1}{\lambda_2} = \frac{n_2}{n_1} \qquad (1.4)$$

Snell's law is quite helpful for understanding a lot of phenomena, i.e., a pencil looks broken in a glass of water (Fig. 1.2.a). However, sometimes we come across some "double refraction" situations. Figure 1.2.b is an image of a calcite crystal above a line

drawn on paper, in which it looks like there are two lines behind. This is because the incident ray disperses into two different rays in the calcite crystal. Then, when the two rays reach the detector (human eyes or a camera), it forms two images.

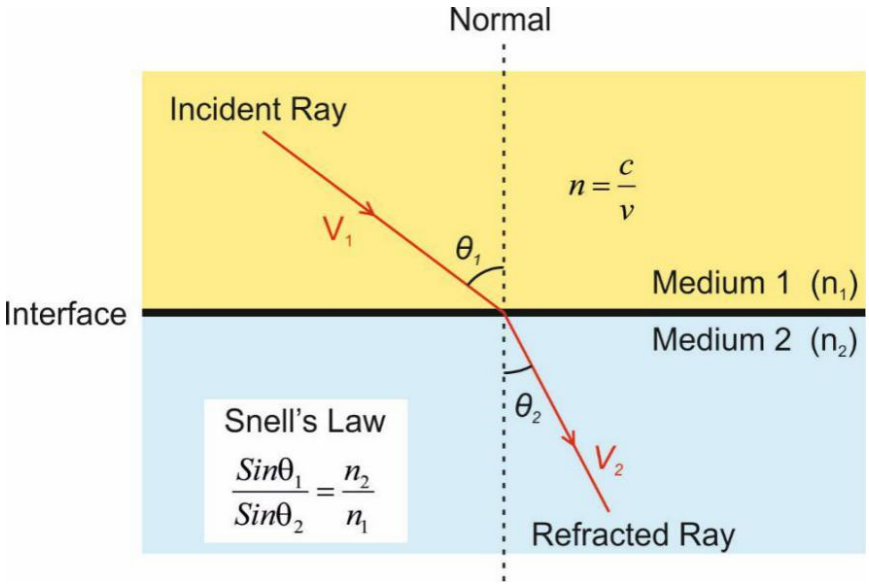

Figure 1.1 *Refraction: when an incident ray travels from medium 1 to medium 2, the direction of the propagation of the ray is altered (forming a refracted ray). The normal line is perpendicular to the interface of medium 1 and medium 2. The angle between the incident ray and the normal line is the incident angle (θ_1); the angle between the refracted ray and the normal line is the refracted angle (θ_2). Medium 1 and medium 2 are composed of different materials, thus the light speed is different (v_1 and v_2), and hence each medium has its unique refractive index (n_1 and n_2).*

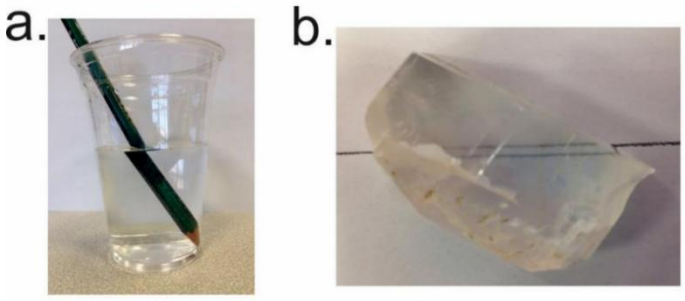

Figure 1.2 *(a) Refraction: a pencil looks broken at the boundary of water and air. (b) Double Refraction: a single line gives rise to an image of double lines when viewed through a calcite crystal.*

As discussed above, the molecular-level components are important in these phenomena. So, why does the calcite case have "double refraction"? While the water does

not? The reason is that in water, air, and even glass, the molecules in the medium are packed randomly, without any long range order, which is called "isotropic". Thus, the light travels at the same speed in any direction. However, the calcite crystal is an anisotropic material, and so the light can find two possible ways to go at a different speed: one is the ordinary ray and obeys the Snell's law; the other is the extraordinary ray and has a different refractive index (Fig. 1.3). The difference between the two refractive indices is defined as "birefringence (Δn)" (Eq. 1.5).[3] If the refractive index of the extraordinary ray (n_e) is greater than the refractive index of the ordinary ray (n_o), $n_e > n_o$, it is positive birefringence, which also means that the speed of the ordinary ray is faster than the extraordinary ray; and *vice versa*, if $n_e < n_o$, it is negative birefringence. We can conclude that only anisotropic materials can have birefringent behaviour.

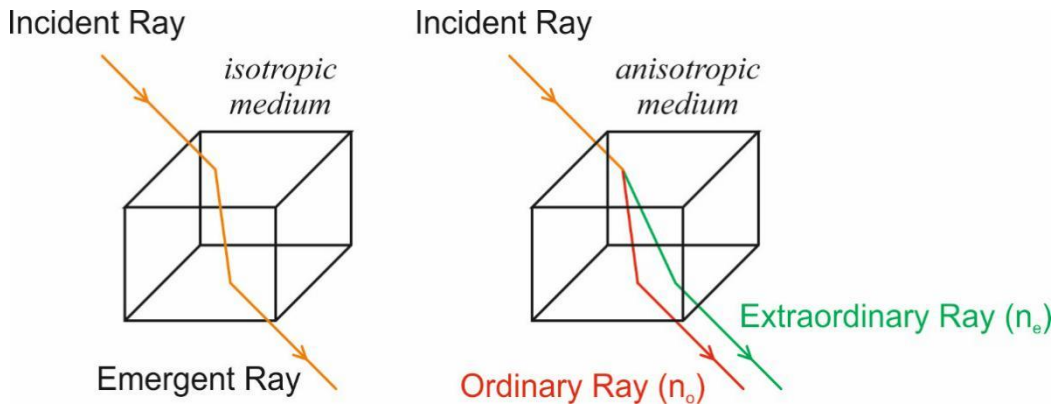

Figure 1.3 *When an incident ray passes through an isotropic medium, it will obey the Snell's law and the emergent ray remains as one ray; while, in an anisotropic medium, one incident ray is split into two rays – the ordinary ray and the extraordinary ray.*

$$\Delta n = n_e - n_o \qquad (1.5)$$

Crystals can be classified into seven systems according to the symmetry of the structure: triclinic, monoclinic, orthorhombic, tetragonal, trigonal, hexagonal and cubic.[4] Among these seven systems, six of them are birefringent – except cubic, all the other six can show double refraction. These six systems can be further divided into two types depending on how many optical axes it has: uniaxial (only one optical axis) and biaxial (having two optical axes).[5] As we discussed before, birefringence gives rise to a split incident ray; however, there is still a special direction in which the incident ray is not split into two. This direction is called the "optical axis". Tetragonal, hexagonal and trigonal

crystal systems are uniaxial; while, triclinic, monoclinic and orthorhombic crystal systems are biaxial (Fig. 1.4).

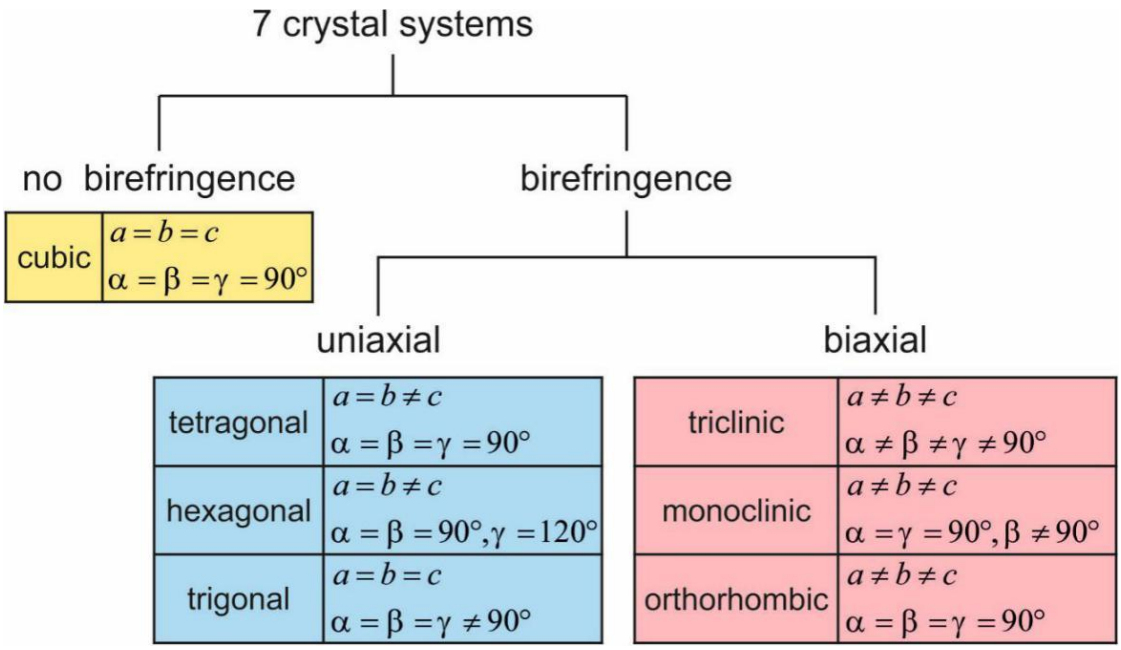

Figure 1.4 *Classification of seven crystal systems, according to birefringence and the number of optical axes.*

1.1.2 Polarized Light and Plane Waves

Light is a form of electromagnetic radiation with a certain wavelength.[3] Visible light is in a range of wavelengths that human eyes can detect, which is from 400 nm to 700 nm (Fig. 1.5). If the light waves vibrate in only one plane, the light is linearly polarized; however, if the light waves vibrates in all planes, it is unpolarized light. Most light sources or illuminators emit unpolarized light, e.g., the sun, a light bulb and a fire. Polarized light can be achieved with the help of a suitable optical filter, called a polarizer, which only allows polarized light parallel to its transmitted direction to pass through, and absorbs or blocks all other polarization directions. Light transmitted through a polarizer is in the form of a plane wave (Fig. 1.6, Page 6).

A plane wave of light moves at a constant rate in a uniform medium and can be described mathematically as a sine wave: $y = A\sin x$ (Fig. 1.7, Page 6).[6] As the rate of the propagation is constant, we can also use a model of a point (P') moving around a circle with a constant velocity (ω). The radius of the circle is equal to the amplitude of the sine

function (A), and φ is the angle between the real axis and the vector from the circle centre to the moving point ($\overrightarrow{OP'}$). If we put this circle in the complex plane and let the circle centre be at (0, i0), the position of the moving point (P') should be ($A\cos\varphi$, $iA\sin\varphi$). When the point (P') moves anti-clockwise, the imaginary part describes the sine wave. With Euler's formula (Eq. 1.6), the plane wave can be described in a complex exponential form (Eq. 1.7).

If one optical filter allows plane waves of a certain polarization direction to pass through, what would happen if we put a second filter behind the first one? According to Malus's law,[3] the emerging light depends on the angle between the two filters. Usually, the second filter is called an "analyzer". As the incident and the transmitted beams come from the same light source, the frequency remains the same, but the amplitude is changed. With the intensity of light proportional to the square of the amplitude, the intensity (I) of a beam of plane polarized light transmitted by the analyzer is equal to the original intensity multiplied by the square of the cosine of the angle between the transmitted direction of the polarizer and the analyzer (Fig. 1.8, Page 7).

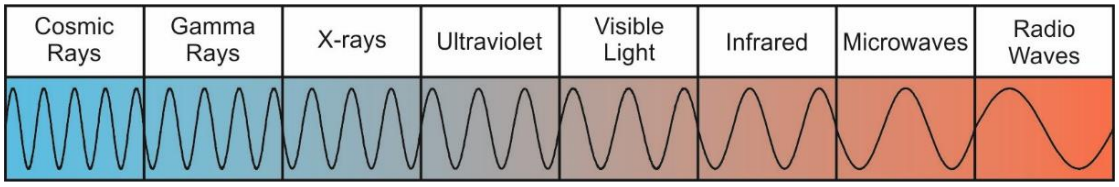

Figure 1.5 *A diagram of the electromagnetic spectrum, ranging from cosmic rays to radio waves with increase of wavelength. Violet is the colour of the shortest wavelength of visible light. Electromagnetic radiation with shorter wavelengths (i.e., less than 400 nm) is ultraviolet (UV). If the wavelengths are bigger than the red edge of the visible spectrum (700 nm), the radiation is infrared (IR).*

$$e^{i\delta} = \cos\delta + i\sin\delta \tag{1.6}$$

$$f(t) = Ae^{i\omega t} \tag{1.7}$$

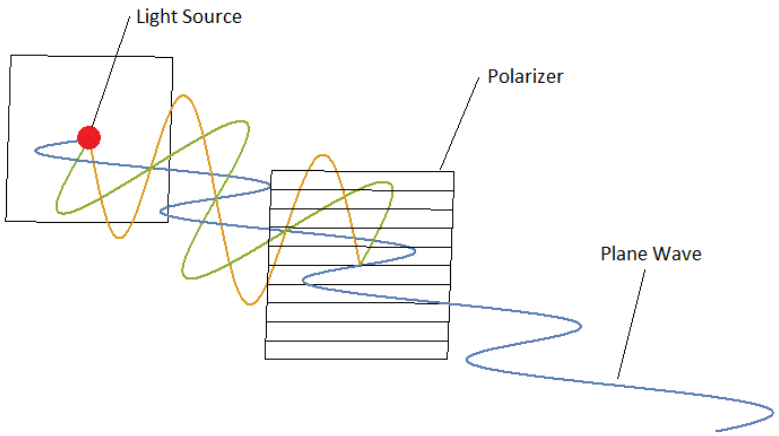

Figure 1.6 *The light source emits unpolarized light, which has several planes of electromagnetic waves (blue line, yellow line, and green line; in reality, the wave planes will have all possible orientations, here only three are drawn for clarity). The polarizer allows only waves vibrating horizontally to pass through. So, the wave after the polarizer is a plane wave (blue line), which is parallel to the polarization direction of the polarizer.*

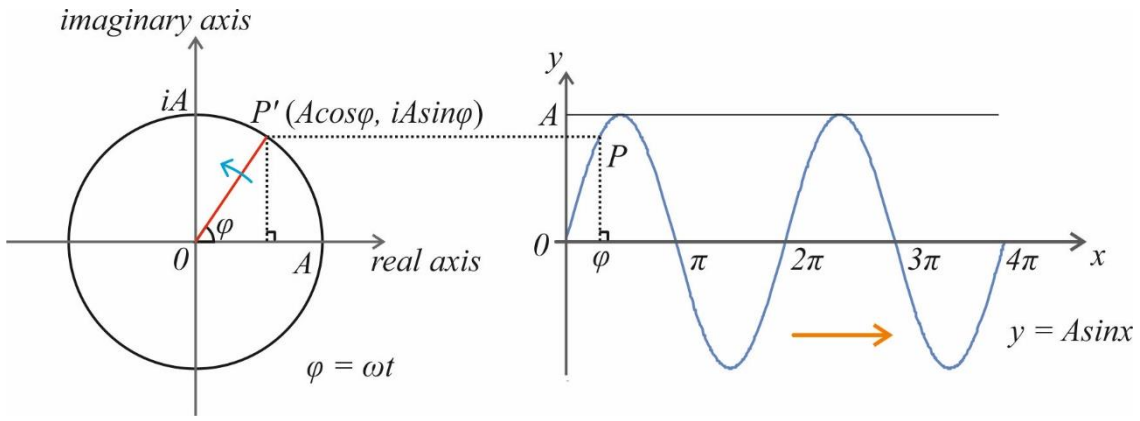

Figure 1.7 *Representation of a plane wave in two forms. The left part is a circle in the complex plane, and its radius is equal to the amplitude A. Point (P') is moving anti-clockwise around the circle (blue arrow) at a constant angular speed (ω). After time t, its position would be (Acosφ, iAsinφ). The right part is a sine wave (y = Asinx), which moves to the right (orange arrow). If we put P on the sine wave, it has the same height as P', then the position of P would be (φ, Asinφ).*

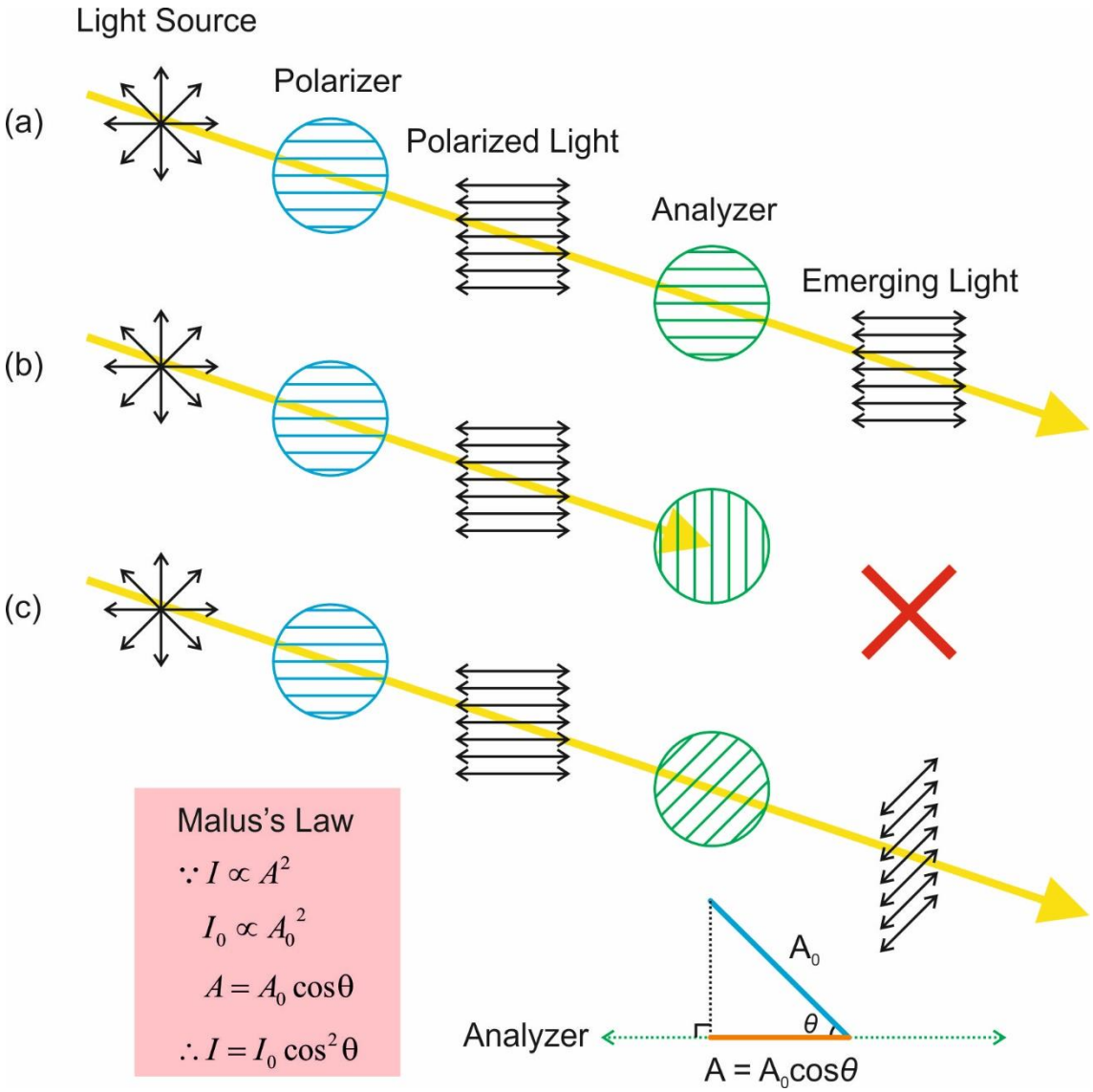

Figure 1.8 *Illustration of transmitted light for different relative orientations of polarizer and analyzer. (a) Parallel, all light can transmit without any loss before and after the analyzer; (b) vertical, no light can pass through; (c) between parallel and vertical, only a component of the polarized light can transmit. The angle between the directions of transmission of the polarizer and the analyzer is θ. Before the analyzer, the amplitude of the plane wave is A_0. After the analyzer, the amplitude is changed to $A_0 \cos\theta$, i.e., the component of A_0 in the analyzer direction. Because intensity is proportional to the square of its amplitude, the intensity relationship between the light before and after the analyzer depends on $\cos^2\theta$. The yellow arrow is the direction of light propagation.*

1.1.3 Polarizing Optical Microscopy

According to Malus's law, when the analyzer is perpendicular to the polarizer, no beam can pass through (Fig. 1.8.b). However, if we place something between the polarizer and analyzer that can change the polarization direction of the original polarized light, there will be some components that can pass through the analyzer (Fig. 1.9). Thus, we can get information on the optical properties of a sample by putting it between a polarizer and analyzer that are perpendicular to each other (called "crossed" polarizer configuration). This is the principle of Polarizing Optical Microscopy (POM); optical properties can be evaluated by analysing the intensity measured on the detector, and in particular by studying the changes in intensity as the orientation of the sample is changed.[7]

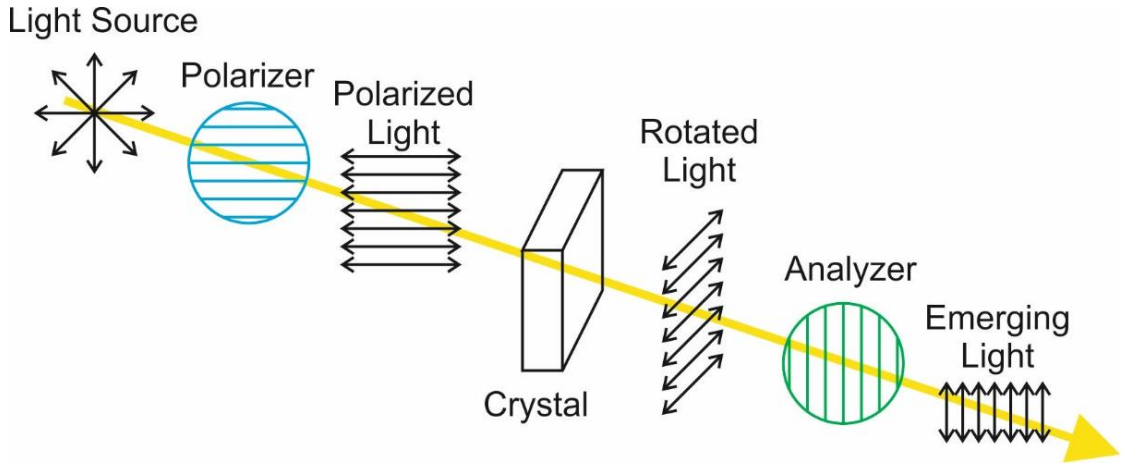

Figure 1.9 *Diagrammatic representation of Polarizing Optical Microscopy (POM). The sample (crystal) is placed between crossed polarizer and analyzer. If the sample object rotates the polarized light from the polarizer, there will be some components of light that can pass through the analyzer, i.e., the detector can receive some photons. The yellow arrow is the direction of light propagation.*

In 1.1.1 we mentioned that birefringence happens based on the split rays, because the incident ray can have two possible directions to travel at the same time. Photons will travel at different rates, because the molecular environment in each of these directions is different. Apart from the nomenclature of the ordinary ray and extraordinary ray, we can also call these two rays the "slow ray" and "fast ray" according to which ray travels faster in the medium, and each ray has its unique refractive index (n_s and n_f). In positive birefringence, the ordinary ray is the fast ray; while, in negative birefringence, the extraordinary ray is the fast ray.

When a plane wave enters a birefringent medium, this plane wave will split into two plane waves, and these two planes are perpendicular to each other. Thus, we can describe this situation in a Cartesian coordinate system, in which the propagation direction of the incident ray is the *z-axis*, and the slow wave plane and the fast wave plane are in the *yz-plane* and *xz-plane* respectively (Fig. 1.10).

Because of the different speeds of the slow ray and the fast ray, when the slow ray reaches the end of the birefringent medium, there is a lag behind the fast ray, which is called the "retardation (Δ)".[7] We denote d as the thickness of the crystal; v_s, v_f, and v as the velocities of the slow ray, the fast ray and the light in the air, respectively. The retardation can be represented by the distance and the three velocities (Eq. 1.8 – Eq. 1.10): when the slow ray travels within the birefringent crystal, the fast ray has already transmitted out of the crystal and gone a little further in the air. If we assume that the velocity in the air is close to the light speed in vacuum, thus, the refractive index of each ray can be represented by the ratio of the light velocities in the air and in the medium (Eq. 1.11 and Eq. 1.12). Then, we can get the representation of the retardation, which is only dependent on the thickness of the birefringent medium and the refractive indices of the two rays (Eq. 1.13).

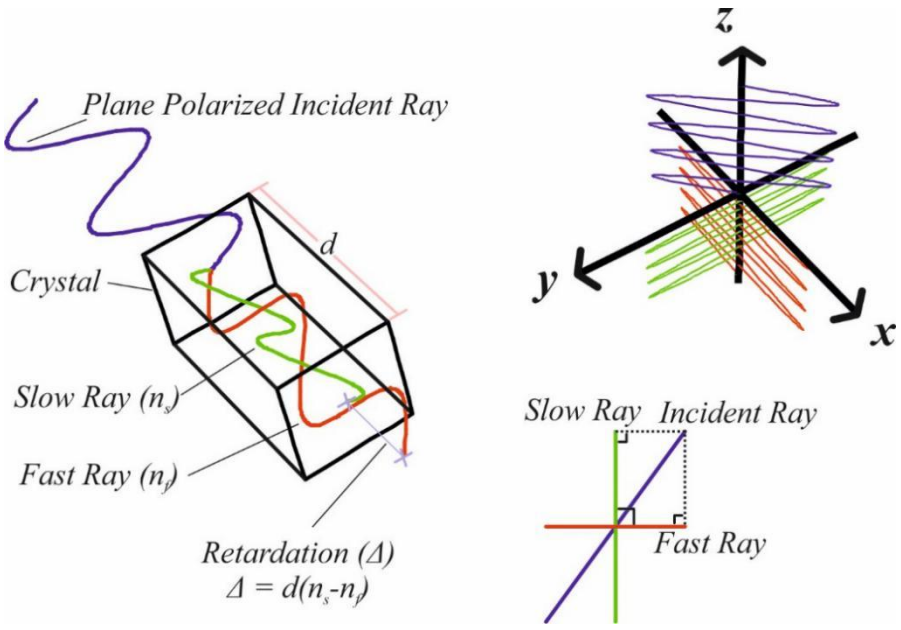

Figure 1.10 *A plane polarized incident ray (blue) is split into two mutually perpendicular plane waves (green and red) with different velocities when it enters into a birefringent crystal. Retardation is the distance due to lagging of the slow ray, and is proportional to the thickness of the crystal.*

$$\frac{d}{v_s} = \frac{d}{v_f} + \frac{\Delta}{v} \tag{1.8}$$

$$\frac{\Delta}{v} = \frac{d}{v_s} - \frac{d}{v_f} \tag{1.9}$$

$$\Delta = d\left(\frac{v}{v_s} - \frac{v}{v_f}\right) \tag{1.10}$$

$$n_s = \frac{v}{v_s} \tag{1.11}$$

$$n_f = \frac{v}{v_f} \tag{1.12}$$

$$\Delta = d\left(n_s - n_f\right) \tag{1.13}$$

Now we put this crystal (with retardation, Δ) between a crossed polarizer and analyzer (Fig. 1.11). The incident ray $\overrightarrow{QP}$ (Eq. 1.14) will be split into the fast ray $\overrightarrow{QF}$ and the slow ray $\overrightarrow{QS}$, which depends on the crystal structure. The angle between the polarization direction of the fast ray and the incident ray is θ. Since $\overrightarrow{QF}$ and $\overrightarrow{QS}$ are perpendicular to each other, both can be generated by the equation for $\overrightarrow{QP}$ giving Eq. 1.15 and Eq. 1.16 respectively. The components of $\overrightarrow{QF}$ and $\overrightarrow{QS}$ along the analyzer can also be represented in trigonometric form (Eq. 1.17 and Eq. 1.18). Because the intensity of light after the analyzer is proportional to the square of its amplitude, the final intensity is calculated in Eq. 1.21. When δ is constant for a given crystal (the thickness d is fixed), the intensity is only dependent on $\sin^2(2\theta)$ (Eq. 1.22).[8]

Figure 1.12 (Page 12) shows a theoretical POM image of a sample with orientations that vary continuously through 360°. Here the bright and dark regions appear sequentially and the interval between the brightest and darkest is 45°, forming a Maltese cross pattern.

$$\overrightarrow{QP} = Ae^{i\omega t} \tag{1.14}$$

$$\overrightarrow{QS} = A\sin\theta \cdot e^{i\omega t} \tag{1.15}$$

$$\overrightarrow{QF} = A\cos\theta \cdot e^{i(\omega t+\delta)}, \delta = \frac{2\pi d\left(n_s - n_f\right)}{\lambda} \tag{1.16}$$

$$\overrightarrow{QN} = A\sin\theta\cos\theta \cdot e^{i\omega t} \tag{1.17}$$

$$\overrightarrow{QM} = A\cos\theta\sin\theta \cdot e^{i(\omega t+\delta)} \tag{1.18}$$

$$\begin{aligned}
\overrightarrow{QM} - \overrightarrow{QN} &= A\sin\theta\cos\theta \cdot e^{i\omega t}\left(e^{i\delta} - 1\right) \\
&= A\frac{\sin(2\theta)}{2}e^{i\omega t}\left(\cos\delta + i\sin\delta - 1\right) \\
&= A\frac{\sin(2\theta)}{2}e^{i\omega t}\left(\cos^2\frac{\delta}{2} - \sin^2\frac{\delta}{2} + 2i\sin\frac{\delta}{2}\cos\frac{\delta}{2} - \sin^2\frac{\delta}{2} - \cos^2\frac{\delta}{2}\right) \\
&= A\sin(2\theta)\cdot e^{i\omega t}\sin\frac{\delta}{2}\left(i\cos\frac{\delta}{2} - \sin\frac{\delta}{2}\right) \\
&= -\frac{1}{i}A\sin(2\theta)\cdot e^{i\omega t}\sin\frac{\delta}{2}\left(\cos\frac{\delta}{2} + i\sin\frac{\delta}{2}\right) \\
&= -\frac{1}{i}A\sin(2\theta)\cdot e^{i\omega t}\sin\frac{\delta}{2}\cdot e^{i\frac{\delta}{2}} \\
&= iA\sin(2\theta)\sin\frac{\delta}{2}e^{i\left(\omega t+\frac{\delta}{2}\right)}
\end{aligned} \tag{1.19}$$

$$I \propto \left|\overrightarrow{QM} - \overrightarrow{QN}\right|^2 \tag{1.20}$$

$$I \propto A^2\sin^2(2\theta)\sin^2\frac{\delta}{2} \tag{1.21}$$

$$I \propto \sin^2(2\theta) \tag{1.22}$$

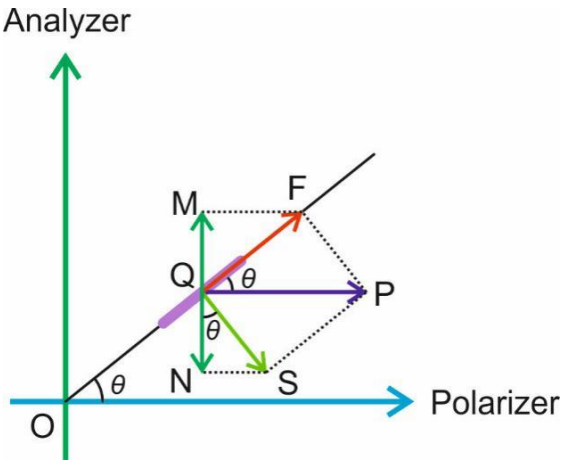

Figure 1.11 *Illustration of crossed polarizer and analyzer with birefringent sample (purple). The transmitted direction of the polarizer is horizontal; the analyzer is vertical.* $\overrightarrow{QP}$ *is the incident polarized wave, and* θ *is the angle between the plane of the fast ray (red) and the incident polarized ray (blue).* $\overrightarrow{QM}$ *and* $\overrightarrow{QN}$ *are the component vectors of the fast ray and the slow ray along the transmitted direction of the analyzer.*

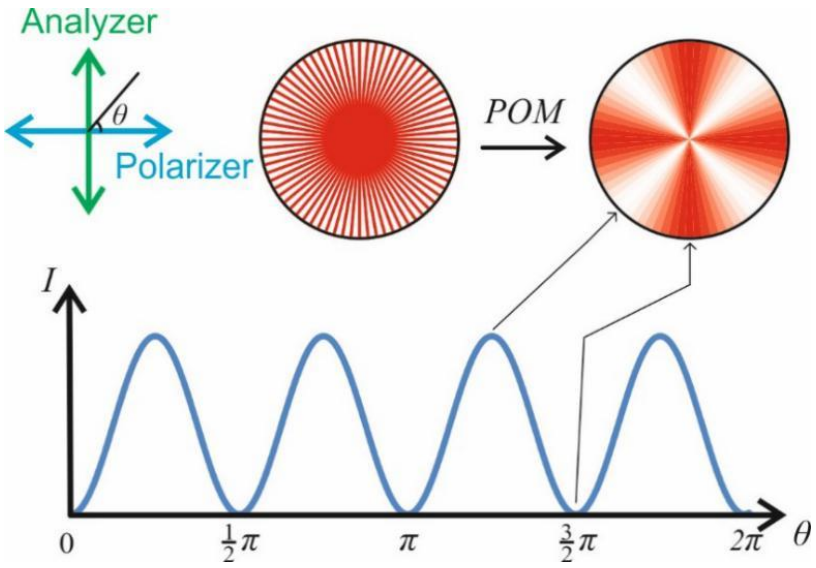

Figure 1.12 *Theoretical diagrams of intensity changing with the optical axis in a crossed polarizer and analyzer system. If we combine a lot of needle-shaped single crystals as a round pan with the needles spreading uniformly around 360°, the image under POM should be a pan with bright and dark showing up sequentially and its intensity is a function of* $\sin^2(2\theta)$*. Here we assume that birefringence happens along the long-axis of the crystal, and* θ *is the angle between the long-axis of the crystal and the transmitted direction of the polarizer.*

1.2 Interaction of Polarized X-rays with Materials

1.2.1 Brewster Angle and Polarized X-rays

Apart from refraction, reflection is also a common phenomenon when incident radiation reaches the interface of two media. According to the law of reflection, the incident angle (angle between the incident ray and the normal line) is equal to the reflected angle (angle between the reflected ray and the normal line). With Snell's law, the angles can be determined once we know the incident angle and the refractive indices of the media. As the refracted ray and the reflected ray both originate from the incident ray (the incident ray may be regarded to be split into a refracted ray and a reflected ray) and, according to the first law of thermodynamics, the combination of the intensity of the refracted ray and the reflected ray is equal to the intensity of the incident ray. As the frequency of the incident, refracted and reflected rays are the same, only the amplitude is

changed. If the incident ray is unpolarized, the reflected ray and the refracted ray are partially polarized, and their polarization and intensity depend on the incident angle.[7]

The Brewster angle[7] is a special angle of incidence at which the reflected ray is perfectly polarized, i.e., the electric vector of the reflected ray is perpendicular to the plane containing the incident ray and the reflected ray. Under the conditions of the Brewster angle, the angle between the reflected ray and the refracted ray is always 90° (Eq. 1.23). In a known system (for which the refractive indices n_1 and n_2 are known), the Brewster angle and the angles of the reflected and refracted rays are fixed (Fig. 1.13). The Brewster angle is denoted θ_b, and it can be calculated by Brewster's law (Eq. 1.24). The reflected angle (θ_{rfl}) and the refracted angle (θ_{rfr}) can be further calculated by the law of reflection (Eq. 1.25) and Snell's law (Eq. 1.26) respectively.

$$\theta_{rfl} + \theta_{rfr} = 90° \tag{1.23}$$

$$\theta_b = \arctan\left(\frac{n_2}{n_1}\right) \tag{1.24}$$

$$\theta_b = \theta_{rfl} \tag{1.25}$$

$$\frac{\sin\theta_b}{\sin\theta_{rfr}} = \frac{n_2}{n_1} \tag{1.26}$$

We now consider the situation in the specific case of incident X-rays. Because X-rays are high energy light, the frequency of the light is high, it travels in straight line and is difficult to be optically focused as no significant refraction occurs in most common materials.[9] As a consequence, the incident angle is approximately equal to the refracted angle (Eq. 1.27). Adding Eq. 1.23 and Eq. 1.25, we reach the conclusion that the Brewster angle for X-ray is approximately 45° (Eq. 1.28 and Fig. 1.14, Page 15). Thus, the polarized X-rays can be achieved when the incident angle is close to 45°.

$$\theta_b \approx \theta_{rfr} \tag{1.27}$$

$$\theta_b = \theta_{rfl} \approx \theta_{rfr} \approx 45° \tag{1.28}$$

Strictly speaking, in the same way that X-ray refraction does not actually exist (or is difficult to be observed), X-ray reflection also does not actually exist – in most cases, X-rays just pass straight through objects. The way "X-ray reflection" can be manifested is based on Bragg Diffraction,[10, 11] which arises from interference of scattered X-ray

waves from different crystal planes (Fig. 1.15). In particular, diffracted X-rays are observed only when the Bragg diffraction condition (Fig. 1.15) is satisfied.

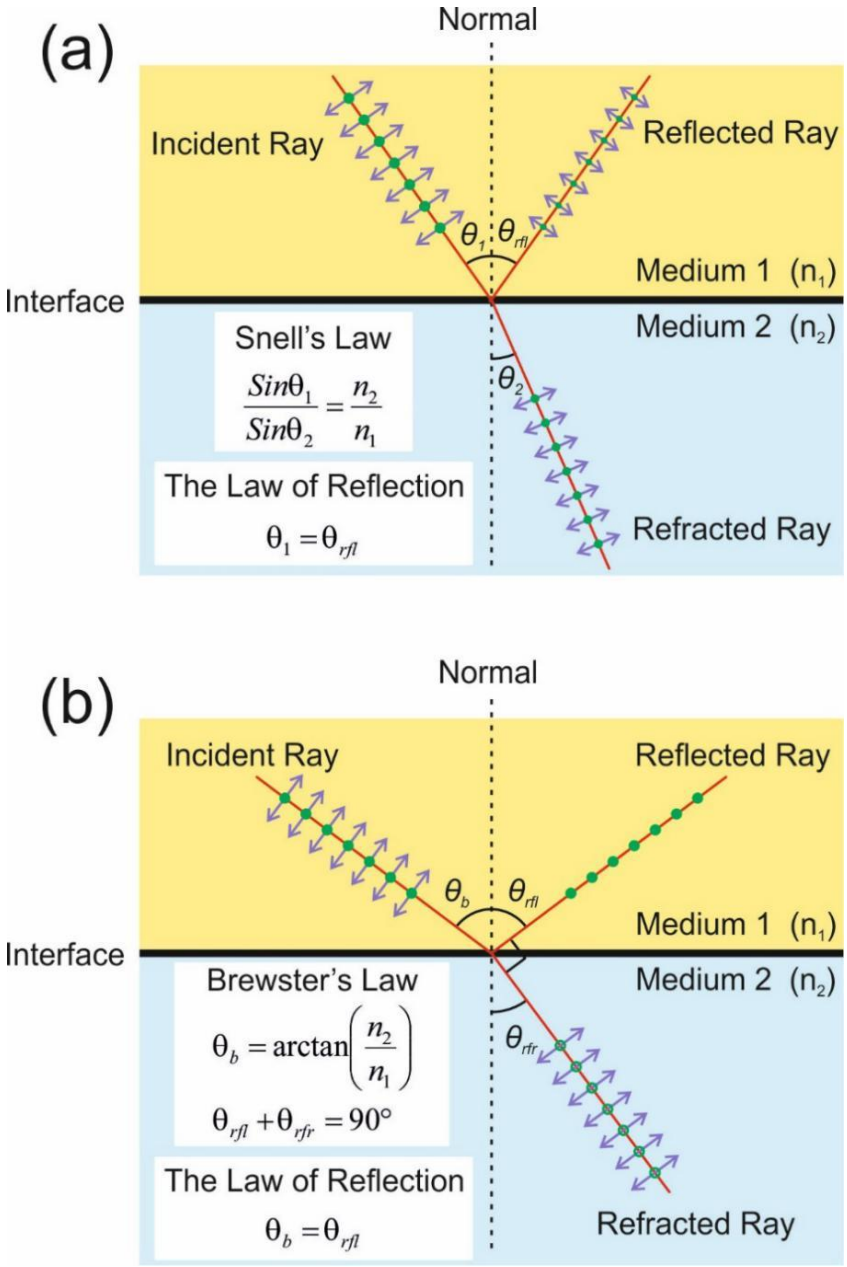

Figure 1.13 *Refraction and Reflection. (a) The incident ray, refracted ray and reflected ray are in the same plane. Refraction obeys Snell's law, and reflection obeys the law of reflection. If the incident ray is unpolarized, the reflected ray and the refracted are partially polarized. (b) If the incident angle is equal to the Brewster angle, the reflected ray is totally polarized – the electric vector is perpendicular to the plane containing the incident, reflected and refracted rays. The law of reflection and Snell's law still hold. The propagation direction of the reflected ray and the propagation direction of the refracted ray are perpendicular to each other.*

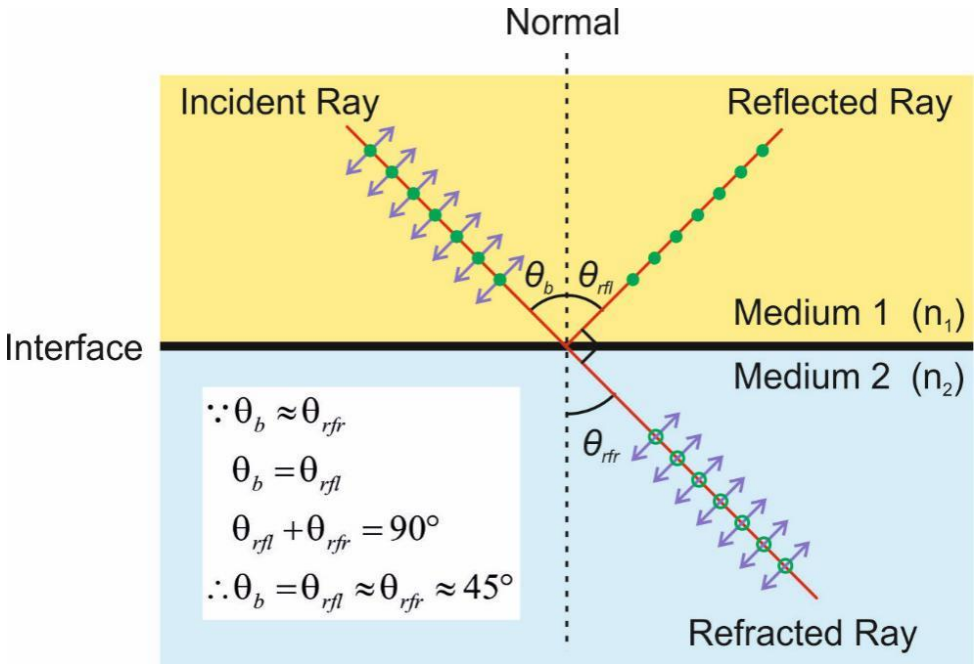

Figure 1.14 *In the case of X-rays, the incident ray is essentially parallel to the refracted ray, and the Brewster angle is 45°. According to the Snell's law, if the incident angle is equal to the refracted angle, the refractive indices are equal (n_1=n_2), which means they are the same medium and there's no refraction. In the case of X-rays, refraction may still happen, but the refractive index is essentially constant in different materials, so we can treat the refracted rays as parallel to the incident ray.*

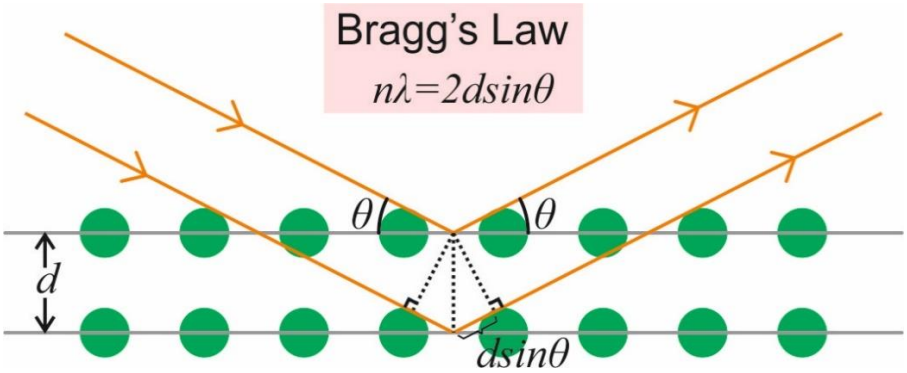

Figure 1.15 *Bragg Diffraction: when X-rays are scattered by adjacent crystal planes with the same set of Miller indices (hkl), the phase difference is 2dsinθ. According to the principle of superposition of waves, constructive interference occurs only when the phase difference is equal to an integer multiple (n) of the wavelength (λ). The perpendicular distance between the lattice planes is denoted d.*

In the theory of X-ray diffraction from crystalline materials, a polarization factor (p)[12] (Eq. 1.29) is introduced within the description of the intensity of the scattered X-

rays observed at the detector. This factor arises from regarding the unpolarized incident beam as two equivalent components: one with the electric vector perpendicular to the scattering plane (the plane of the incident ray and the diffracted ray), and the other with the electric vector parallel to the scattering plane. According to the theory of Thomson scattering,[13] the amplitude of the scattered ray is proportional to the sine of the angle (γ) between the electric vector and the propagation direction of the scattered ray. Once the amplitude is known, we can determine the intensity, because the intensity is proportional to the square of the amplitude.

$$p = \frac{1+\cos^2(2\theta)}{2} \qquad (1.29)$$

For the first component (green arrows in Fig. 1.16, Page 18) with the electric vector perpendicular to the scattering plane, γ is always 90°; for the second component (violet arrows in Fig. 1.16, Page 18) with the electric vector parallel to the scattering plane, γ depends on the incident angle (θ_i) or the Bragg angle (θ), with $\gamma = 90° - 2\theta$. As the amplitude of each component is proportional to $\sin(\gamma)$, and as the intensity of each component is therefore proportional to $\sin^2(\gamma)$, the average intensity of the two components is given by Eq. 1.30, which corresponds to the polarization factor (p). Thus, the intensity of the scattered ray is proportional to this factor.

$$\frac{\sin^2 90° + \sin^2(90° - 2\theta)}{2} = \frac{1+\cos^2(2\theta)}{2} \qquad (1.30)$$

The above hypothesis is based on the assumption that the incident ray is unpolarized. If the incident ray is polarized, the situation becomes more complicated. We assume that the incident ray is polarized with its electric vector neither parallel nor perpendicular to the scattering plane, as indicated by the blue arrows in top part of Fig. 1.16 (Page 18). This situation is now analysed in a Cartesian coordinate system (defined in the bottom part of Fig. 1.16, Page 18): the electric vector is in the *yz–plane* and the diffracted ray is in the *xy–plane*; the angle between the diffracted ray and the *y-axis* is α; the angle between the electric vector and the *y-axis* is β; and the angle between the electric vector and the diffracted ray is γ (which relates to the intensity of the diffracted ray as discussed above).

The position *N* represents a point on the wave crest of the incident polarized ray with amplitude of *A* and has coordinates (0, $A\cos\beta$, $A\sin\beta$). We also draw another point

M, making sure that the distance to the origin is also *A*; thus, the position of point *M* is (*A*sinβ, *A*cosβ, 0). We can use vectors to describe these two points (Eq. 1.31 and Eq. 1.32), and the angle between the electric vector and the diffracted ray is the angle between these two vectors. Thus, we can get the value of this angle through trigonometry (Eq. 1.33). As the intensity is proportional to the square of the amplitude, and the amplitude is proportional to the sine of the angle (γ) between the incident electric vector and the propagation direction of the diffracted ray, the final intensity of a polarized incident ray after diffraction can be expressed in terms of the angles α and β (Eq. 1.34).

We return now to consider the Brewster angle, which is equal to 45° in the case of X-rays, as discussed above. In Bragg diffraction, if the incident angle is 45°, the Bragg angle is also 45°, which means that α is zero in Fig 1.16. Under these circumstances, the geometry is illustrated in Fig. 1.17 (Page 19). Now, the diffracted ray is along the *y-axis*, and its intensity is only determined by the square of the sine of the angle (β) between the incident electric vector and the scattering plane. If we define δ as the angle between the electric vector and the *z-axis*, the intensity is proportional to $\cos^2(\delta)$ (Eq. 1.35, Page 19), which resembles Malus's law introduced previously (Fig. 1.8, Page 7). In this way, we have effectively described a polarization analyzer for X-rays, which only detects the component of the incident electric vector in the vertical direction.[10, 11, 14-19]

$$\overrightarrow{ON} = (0, A\cos\beta, A\sin\beta) \tag{1.31}$$

$$\overrightarrow{OM} = (A\sin\alpha, A\cos\alpha, 0) \tag{1.32}$$

$$\begin{aligned}\cos\gamma &= \frac{\overrightarrow{ON}\cdot\overrightarrow{OM}}{\left|\overrightarrow{ON}\right|\cdot\left|\overrightarrow{OM}\right|} \\ &= \frac{0\cdot A\sin\alpha + A\cos\beta\cdot A\cos\alpha + A\sin\beta\cdot 0}{\sqrt{0+A^2\cos^2\beta+A^2\sin^2\beta}\cdot\sqrt{A^2\sin^2\alpha+A^2\cos^2\alpha+0}} \\ &= \cos\alpha\cdot\cos\beta\end{aligned} \tag{1.33}$$

$$\begin{aligned}I &\propto \sin^2\gamma \\ I &\propto 1-\cos^2\gamma \\ I &\propto 1-\cos^2\alpha\cdot\cos^2\beta\end{aligned} \tag{1.34}$$

Volobuev and Tolstonogov discussed Malus's law for X-ray radiation based on quantum principles,[20] taking into account Compton scattering (not only Thomson scattering as we discussed above). The formula for Malus's law in the case of X-rays is

given in Eq. 1.36. Here, I is the intensity after scattering, I_0 is the intensity of the incident rays, Θ is the rotation angle of the polarization plane of the photon after interaction with the electron, $\hbar$ is the reduced Planck constant, ω is the cyclic frequency of the final photon, ω_0 is the cyclic frequency of the initial photon and E_0 ($E_0 = m_0 c^2$) is the energy of the motionless electron in the initial state. This equation looks complicated in the case of X-rays; however, the assumption that the intensity of the diffracted ray is proportional to the square of the cosine of the angle between the electric vector of the incident ray and the normal vector of the scattering plane is still reasonable. So, the conclusion about the polarization analyzer of X-rays is still valid. Based on this principle, X-ray polarization analyzers are utilized at synchrotron facilities to obtain polarized X-rays.

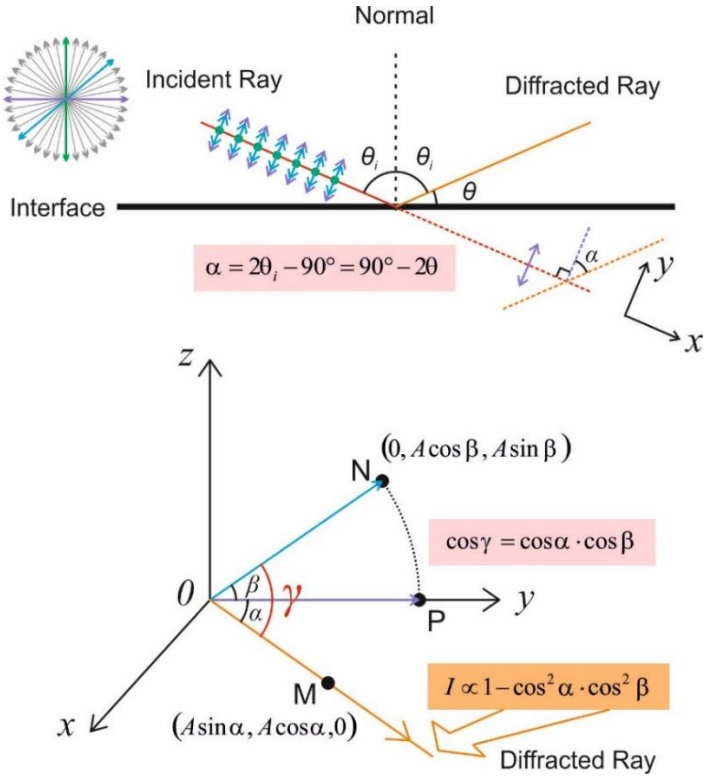

Figure 1.16 *Schematic illustration of the diffracted ray (orange) from a polarized incident X-ray (blue). The Bragg angle is denoted θ; the incident angle is denoted θ_i; the blue arrow is the electric vector of the polarized incident X-ray; the angle between the projection of the electric vector on the scattering plane and the propagation direction of the diffracted ray is denoted α; the angle between the electric vector and the scattering plane is denoted β; the angle between the electric vector and the propagation direction of the diffracted ray is denoted γ. Points M, N and P represent three positions on the diffracted ray, incident X-ray and the y-axis respectively. The intensity of the scattered ray is dependent on the angles α and β.*

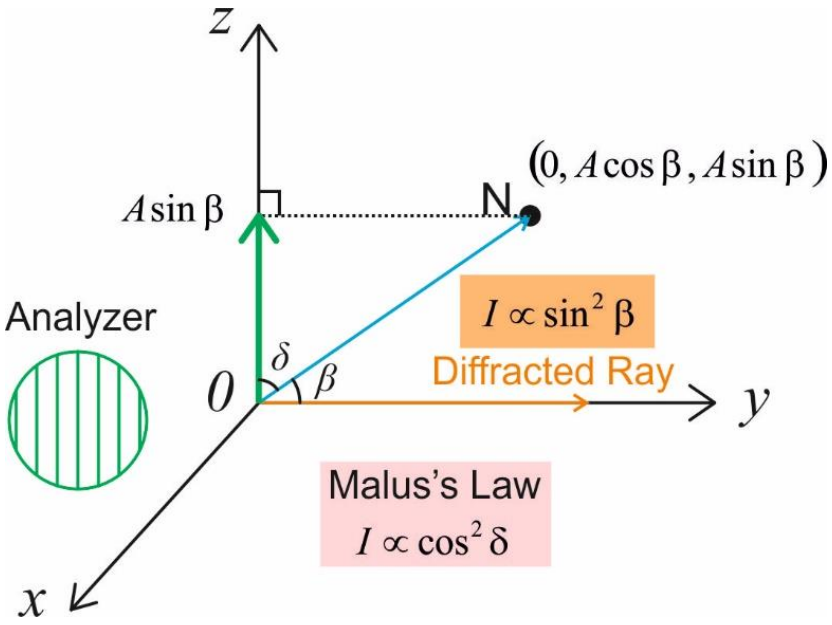

Figure 1.17 *Schematic illustration of a polarization analyzer for X-rays. If the Bragg angle is 45°, the intensity of the diffracted ray depends only on the angle between the incident electric vector and the normal vector to the scattering plane. Effectively, this situation represents a polarization analyzer for which the transmitted direction is parallel to the normal vector to the scattering plane.*

$$\begin{aligned} &\because I \propto \sin^2\beta \,(when\ \alpha = 0°) \\ &\beta + \delta = 90° \\ &\therefore I \propto \cos^2\delta \end{aligned} \tag{1.35}$$

$$I = I_0\left[1 + \frac{\hbar(\omega_0 - \omega)}{2E_0}\right]\frac{\omega}{\omega_0}\cos^2\Theta \tag{1.36}$$

As we have thus found a suitable polarization analyzer for X-rays, if we have a source of polarized incident X-rays, we can construct an experimental set-up analogous to POM but instead using X-rays. This set-up will thus allow birefringence image to be recorded using X-rays – this technique (first reported in 2014) is called "X-ray Birefringence Imaging (XBI)".[21] In this technique, the variation of intensity in the X-ray birefringence images will exhibit similar behaviour to POM, i.e., the intensity is proportional to $\sin^2(2\theta)$, where θ is the angle between the birefringence direction (optic axis) and the direction of polarization of the incident ray. In XBI, the linearly polarized incident X-ray radiation is from a synchrotron source, for which the electric vector of the incident X-ray is horizontal and the transmitted direction of the analyzer is vertical (Fig. 1.18).

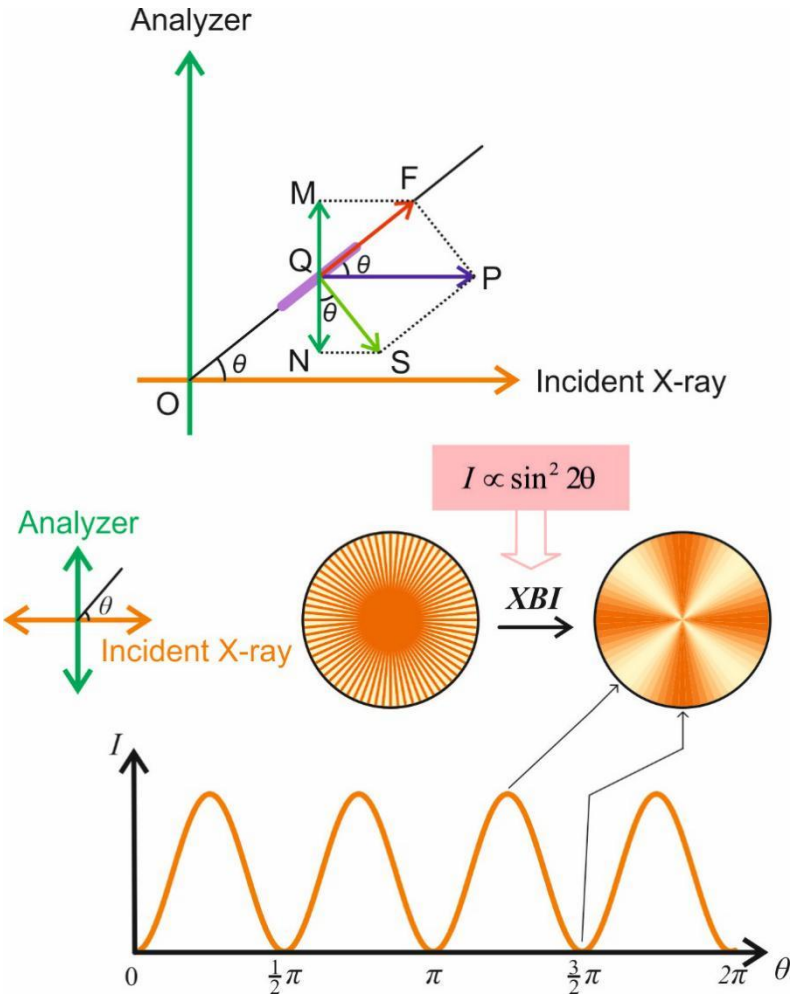

Figure 1.18 *In the experimental configuration for X-ray birefringence imaging, the incident polarized X-rays are horizontal, and the transmission direction of the analyzer is vertical. Under appropriate circumstances (see 1.2.2), birefringent materials will show a similar intensity variation to that observed in POM (Fig. 1.12, Page 12).*

1.2.2 X-ray Birefringence and X-ray Birefringence Imaging

As we discussed in 1.2.1, if the incident ray is a linearly polarized X-ray, with an analyzer crystal set at the correct orientation to give Bragg diffraction at a Bragg angle of *ca.* 45°, we effectively have an experimental configuration that represents the X-ray analogue of POM (Fig. 1.19). Studies using this kind of X-ray birefringence set-up have verified this hypothesis.[21-25] In the first experiment, single crystals of the 1-bromoadamantane/thiourea inclusion compound (1-BA/thiourea) were tested under polarized X-rays (the electric vector is horizontal) with energy corresponding to the Br K-edge, so that the interaction of the polarized X-rays with the material is sensitive to the

electron environment around the bromine atoms. In the crystal structure of 1-BA/thiourea, all the C–Br bonds are parallel to the long-axis of the single needle-shaped crystals (Fig. 1.20). The crystal was mounted on the goniometer with the long-axis perpendicular to the propagation direction of the incident X-ray beam. Here, χ is defined as the angle between the long-axis of the crystal and the horizontal plane and φ is the rotation angle of the crystal around its long-axis. The polarization analyzer was set up to transmit the vertical polarized component.

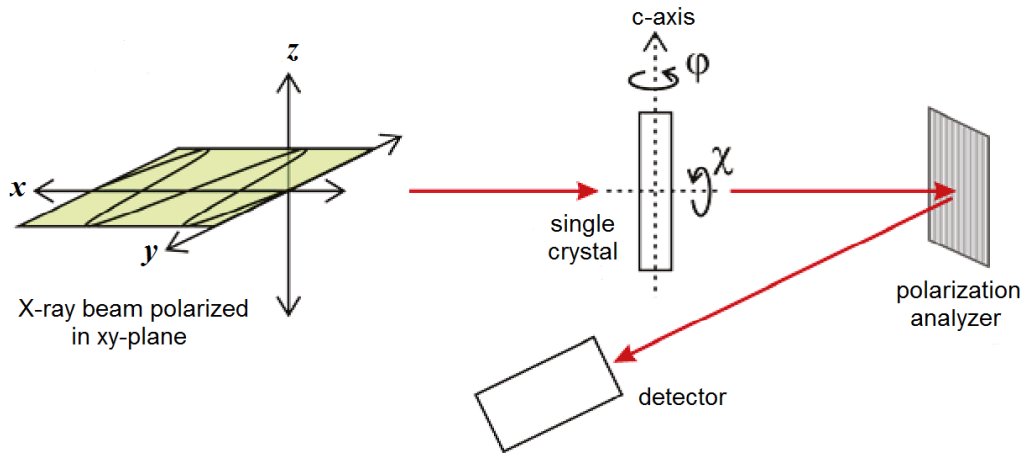

Figure 1.19 *Schematic of the experimental set-up for X-ray birefringence imaging. The propagation direction of the incident X-rays is along the x-axis, with polarization in the xy-plane. The crystal orientation angles χ and φ are defined. Modified and reprinted with permission from Palmer, B. A.; Morte-Ródenas, A.; Kariuki, B. M.; Harris, K. D. M.; Collins, S. P., X-ray Birefringence from a Model Anisotropic Crystal. J. Phys. Chem. Lett.* ***2011****, 2, 2346-2351. Copyright 2011 American Chemical Society.*

The intensity after the polarization analyzer was measured as a function of variation of χ and φ (Fig. 1.21, Page 23). During the χ scan, the intensity shows a perfect sinusoidal curve in good agreement with the intensity predicted theoretically in 1.2.1, and the effective X-ray "optic axis" is parallel to the C–Br bond. In the φ scan, which simply involves rotating the single crystal around its long-axis, the C–Br bond direction does not change, and the intensity remains essentially constant. The slight fluctuation of intensity in the experimental data may be caused by variation in the thickness of the crystal and defects or impurity inside the sample.

When the area of the incident polarized beam is made as large as possible and using an area detector, it becomes possible to record a spatially resolved two-dimensional map of the X-ray birefringence of the materials, and hence to obtain good quality "X-ray

birefringence images" of samples. Figure 1.22 (Page 24) shows the images recorded for a needle-shaped single crystal of the bromocyclohexane/thiourea inclusion compound at 20 K using this set-up. A classic bright and dark change is observed during the χ scan. However, in this case, the C–Br bond is not parallel to the long-axis of the single crystal, so the brightest and darkest images arise when the C–Br bond is oriented appropriately. When the crystal is oriented at χ = 82° the C–Br bonds form an angle of 45.5° (close to 45°) relative to the direction of polarization of the incident X-rays, hence giving higher transmitted X-ray intensity.

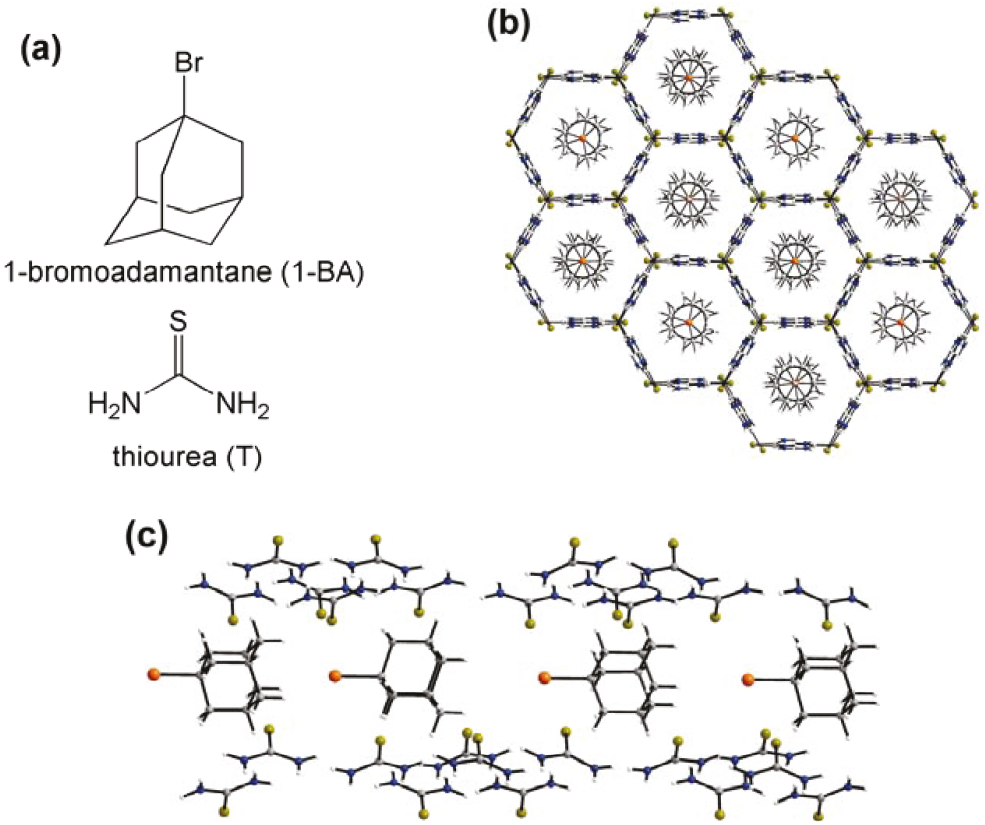

Figure 1.20 *Crystal structure of the 1-bromoadmantane/thiourea inclusion compound (1-BA/thiourea). (a) Molecular structures of 1-bromoadamantane and thiourea; (b) crystal structure of 1-BA/thiourea viewed along the thiourea host tunnel (the long-axis of the needle-shaped single crystal); (c) crystal structure of 1-BA/thiourea viewed perpendicular to the thiourea host tunnel. Thiourea molecules form the outside hexagonal tunnels as host molecules; 1-bromoadmantane molecules are packed inside the tunnels as guest molecules. Reprinted with permission from Palmer, B. A.; Morte-Ródenas, A.; Kariuki, B. M.; Harris, K. D. M.; Collins, S. P., X-ray Birefringence from a Model Anisotropic Crystal. J. Phys. Chem. Lett.* ***2011****, 2, 2346-2351. Copyright 2011 American Chemical Society.*

Figure 1.23 (Page 25) shows a comparison of XBI and POM of single crystals containing isotropically disordered bromocyclohexane guest molecules. In this situation, because the thiourea host molecules still have a well-defined host crystal structure, the crystal still shows birefringence under POM; however, no X-ray birefringence is observed, as this phenomenon only depends on the orientational distribution of the C–Br bonds, which in this case is isotropic.

Clearly the above examples demonstrate that XBI can provide information on the orientational distribution of the local bonding environment of atoms of a selected element in the materials (in this case Br), rather than depending on the overall crystal symmetry as in POM.

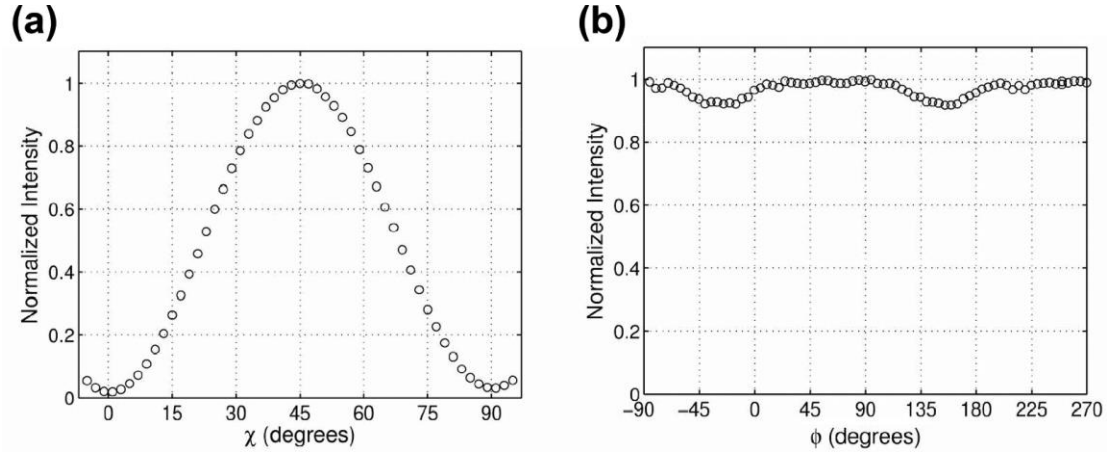

Figure 1.21 *X-ray intensity recorded in X-ray birefringence studies of a single crystal of the 1-bromoadamantane/thiourea inclusion compound (1-BA/thiourea). (a) χ scan, the brightest position is at 45° and the darkest appears at 0° and 90°; (b) φ scan, the intensity is essentially constant. Reprinted with permission from Palmer, B. A.; Morte-Ródenas, A.; Kariuki, B. M.; Harris, K. D. M.; Collins, S. P., X-ray Birefringence from a Model Anisotropic Crystal. J. Phys. Chem. Lett.* ***2011****, 2, 2346-2351. Copyright 2011 American Chemical Society.*

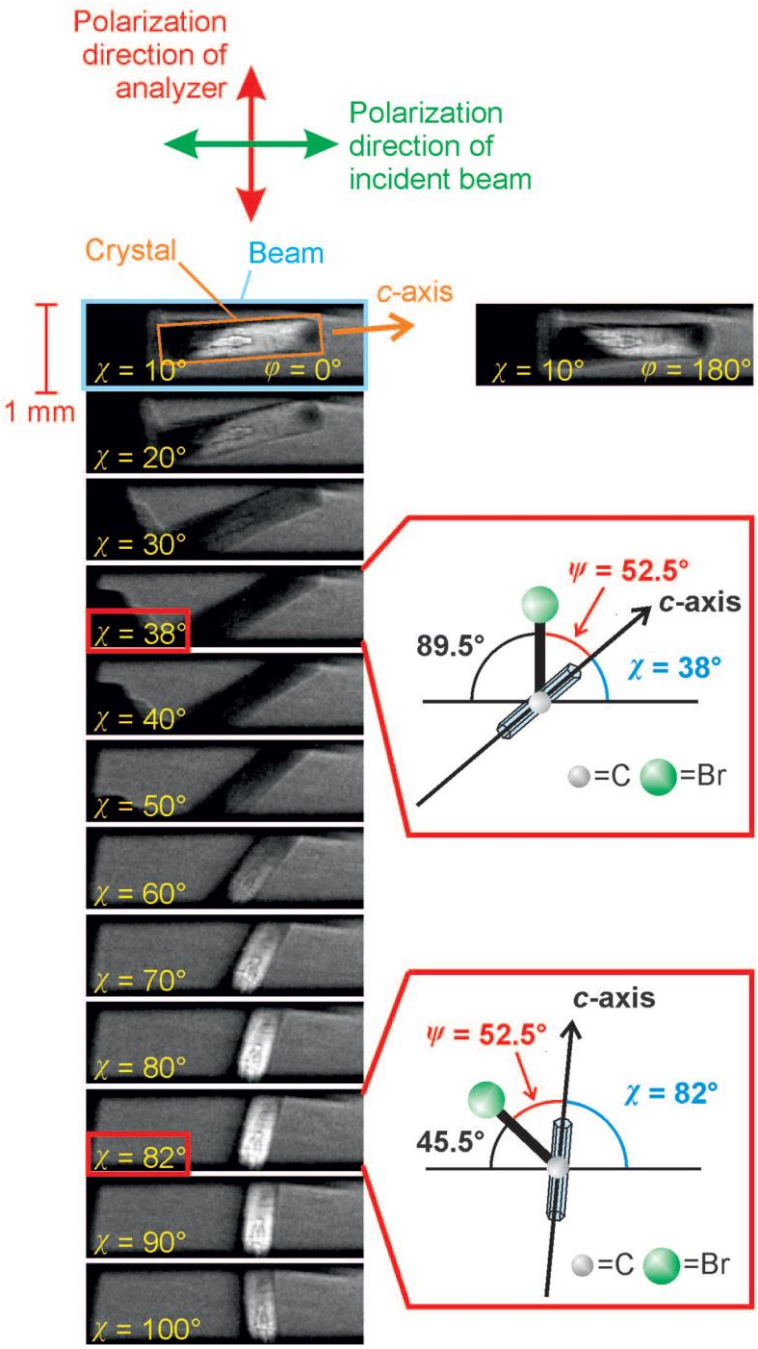

Figure 1.22 *XBI data recorded at 20 K for the bromocyclohexane/thiourea inclusion compound needle-shaped single crystal. The angle between the C–Br bond and the long-axis of the single crystal is 52.5°. The intensity of the XBI depends on the orientation of the C–Br bonds. When χ is 38°, the image is dark as the C–Br bond is close to 90° to the direction of polarization of the incident X-rays (horizontal); when χ is 82°, the image is bright as the C–Br bond is close to 45°. Reprinted with permission from Palmer, B. A.; Edwards-Gau, G. R.; Kariuki, B. M.; Harris, K. D. M.; Dolbnya, I. P.; Collins, S. P., X-ray Birefringence Imaging. Science* ***2014****, 344, 1013-1016. Copyright 2014 American Association for the Advancement of Science.*

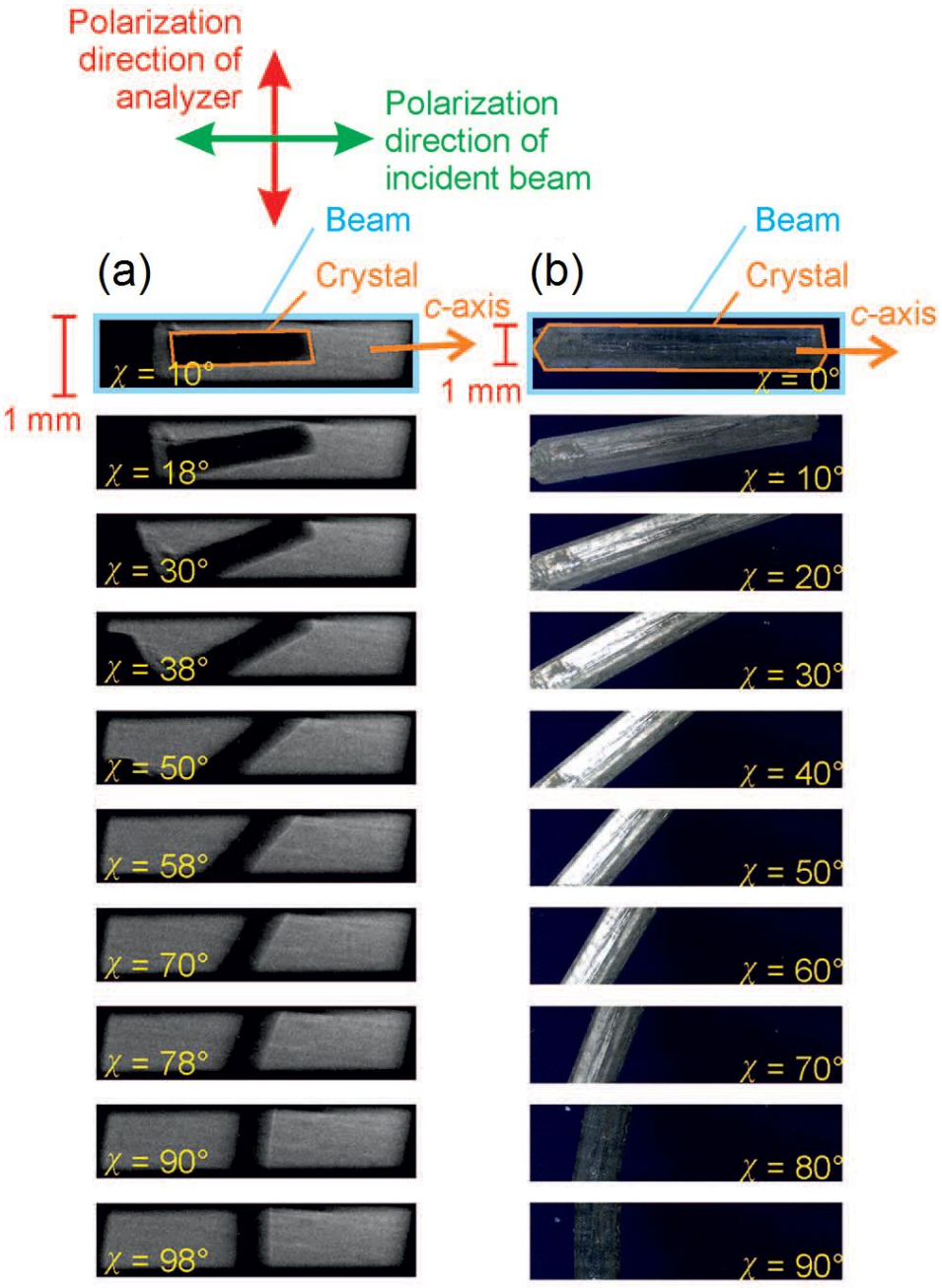

Figure 1.23 *Comparison of (a) XBI and (b) POM data for a single crystal of the bromocyclohexane/thiourea inclusion compound at ambient temperature. In this high-temperature phase, the guest molecules (bromocyclohexane) undergo isotropic reorientation, but the host tunnels structure (thiourea) maintains a well-defined crystal structure. Reprinted with permission from Palmer, B. A.; Edwards-Gau, G. R.; Kariuki, B. M.; Harris, K. D. M.; Dolbnya, I. P.; Collins, S. P., X-ray Birefringence Imaging. Science* ***2014****, 344, 1013-1016. Copyright 2014 American Association for the Advancement of Science.*

1.3 Crystal Structure Determination from Powder X-ray Diffraction Data

X-ray diffraction (XRD) has had a significant influence on the field of crystallography and crystal structure determination from the single-crystal XRD data has already become a mature technique and is now used widely.[26] However, sometimes it is unfeasible to prepare large enough single crystals for structure determination using single-crystal XRD; thus, an alternative method is to use a powder sample (many small crystals) and to record powder XRD data.[27, 28] Because the signal from the powder XRD provides only Bragg angle (2θ) and peak intensity, rather than the three-dimensional information provided by single-crystal XRD, it is much more challenging to solve a crystal structure from powder XRD data. Figure 1.24 shows the process to determine crystal structures from powder XRD data.

For crystal structure determination from powder XRD data, the precondition is to record high quality experimental data, which requires a pure phase (or, if impurity phases are present, it is essential that they are known materials of known structure), high crystallinity and no preferred orientations of the crystallites within the powder. Once the data has been recorded, several programs can be used in the "indexing" step. In this stage, the cell parameters (a, b, c, α, β, γ) and space group can be found. Further profile fitting is applied to refine the approximate cell parameters obtained at the indexing stage, and to determine the profile shape of peaks. The next step is the most important and the most challenging step, "structure solution", the aim of which is to derive an approximately correct description of the structure (starting from zero knowledge of the arrangement of the atoms/molecules within the unit cell). If the "indexing" process is likened to just defining the "box", the "structure solution" process aims to put the atoms into this "box" in the correct positions. In this thesis, the structure solution method used in this work is based on the direct-space Genetic Algorithm (GA) technique,[29-31] which is explained in detail in 2.4. Once we have found a promising structure, the structure refinement procedures are carried out in order to derive an accurate final crystal structure.

During each stage of the process, the R-factor is used to evaluate the goodness of fit of the calculated data to the experimental data.[28] A smaller value of R-factor represents a better fit. The profile R-factor (R_p) and the weighted profile R-factor (R_{wp}) are both used in this thesis, and are represented by the following equations:

$$R_p = \frac{\sum |y_{io} - y_{ic}|}{\sum y_{io}} \qquad (1.37)$$

$$R_{wp} = \sqrt{\frac{\sum w_i (y_{io} - y_{ic})^2}{\sum w_i y_{io}^2}} \qquad (1.38)$$

where, y_{io} is the intensity of the *i*th data point in the experimental data, y_{ic} is the intensity of the *i*th data point in the calculated data and w_i is the weighting factor for the *i*th data point.

After the refinement, the crystal structure is subjected to energy minimization using periodic density functional theory (DFT) calculation[32] (with fixed unit cell) to get the geometry optimized structure and to validate that the final structure obtained in the refinement is robust and energetically stable. Thus, if this DFT structure does not change too much from the refined structure, it means the final structure represents an energetic minimum and gives further evidence of correctness.

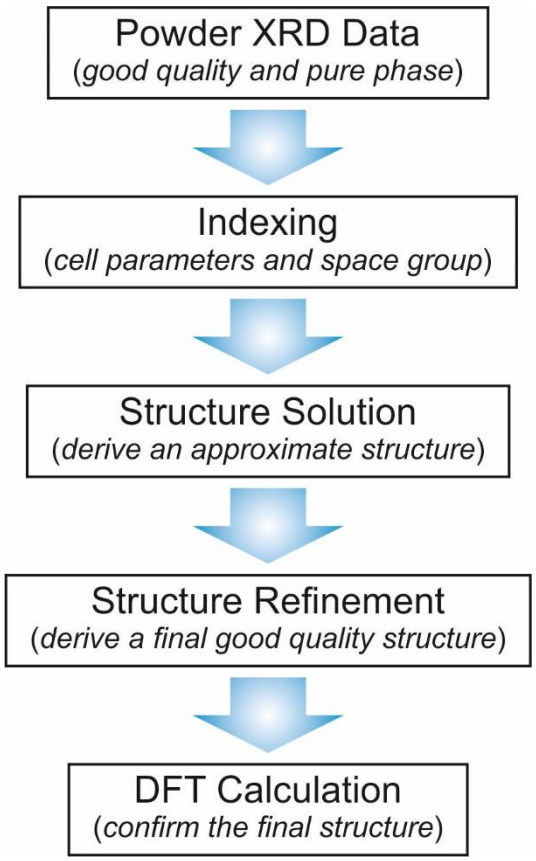

Figure 1.24 *Flow chart of the process of structure determination from powder XRD.*

Chapter 2

Experimental Methods

2.1 X-ray Birefringence Imaging

In 1.2.1, it is mentioned that a Bragg angle (defined here as θ) of 45° is important in order for a material to be a suitable analyzer for polarized X-rays. The experimental results referenced in 1.2.2 were based on the experimental XBI set-up shown in Fig. 2.1. For ease of explanation, an orthogonal coordinate system is introduced. The propagation direction of the polarized X-rays is anti-parallel to the *x-axis*. The electric vector of the polarized X-rays is along the *y-axis*. The diffracted beam after the analyzer is parallel to the *y-axis* (assuming that the Bragg angle is exactly 45°). The analyzer is mounted on a conveyor belt and can be moved into or out of the beam under remote control. Along the *x-axis*, there is another area detector (area detector 2), and when the analyzer is out of the beam, this detector will receive X-rays directly and is used to adjust the position of the sample before XBI measurements. The sample is mounted on a Huber diffractometer and can rotate in the *yz-plane* (rotation angle χ) or spin around the goniometer axis (rotation angle φ). Once the sample is at the right position for the measurement, the analyzer is moved back into the beam and will diffract the X-rays transmitted through the sample by *ca.* 90°. Another area detector (area detector 1) is down-stream of the analyzer for taking the XBI images.

In order to have good performance, the analyzer usually is chosen as a perfect crystal. According to the Bragg diffraction equation[4] (Eq. 2.1), only if the wavelength (λ) matches the inter-planar spacing (d) multiplied by $2\sin\theta$ can diffraction happen. As we also need the diffraction angle to be $\theta = 45°$ to operate as a polarization analyzer, so, for an XBI experiment with a specific wavelength, it is crucial to find a suitable analyzer crystal with a matched d value. In our experiments, we focused on bromine containing materials, so the X-ray energy was tuned to Br K-edge absorption (~ 13.4737 keV). The wavelength of the incident X-ray can be calculated by equation of Planck's equation[33] (Eq. 2.2) to be $\lambda = 0.9203$ Å. For Si (5 5 5) and Ge (5 5 5), the inter-planar spacing (d) can be calculated through Eq. 2.3, where a is the lattice parameter of the cubic crystal.[34] Thus, the Bragg angle (θ) can be calculated ($n = 1$) as $\theta = 47.193°$ and $\theta = 44.768°$ for Si

(5 5 5) and Ge (5 5 5) respectively, both of which are acceptably close to 45°. However, because the angle is not exactly 45°, this will bring some minor systematic errors.

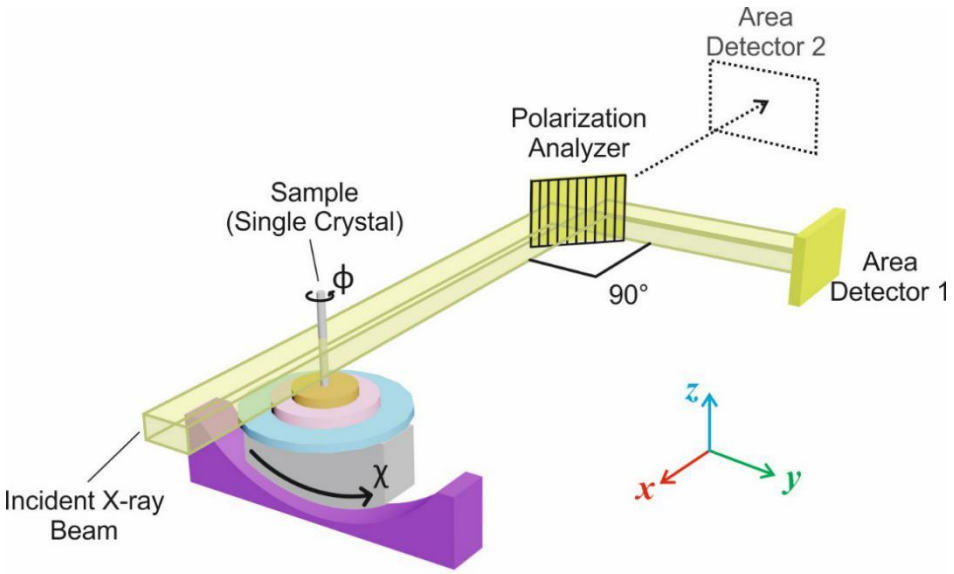

Figure 2.1 *Experimental set-up for X-ray Birefringence Imaging (XBI). The incident X-rays propagate along the x-axis, while the diffracted ray from the analyzer is approximately along the y-axis. The analyzer is a perfect crystal, and the face of the diffraction plane is vertical (i.e., parallel with the z-axis). The electric vector of the polarized incident X-rays is along the y-axis. The analyzer is set for detecting polarized X-rays with electric vector along the z-axis.*

$$n\lambda = 2d\sin\theta \tag{2.1}$$

$$E = \frac{hc}{\lambda} \tag{2.2}$$

$$d_{hkl} = \frac{a}{\sqrt{h^2 + k^2 + l^2}} \tag{2.3}$$

Another thing we should pay attention to at this stage is that the image taken after the analyzer crystal is a stripe-shaped image tilted from the horizontal direction,[35] which is a consequence of the diffraction that occurs at both the monochromator and the analyzer (Fig. 2.2). The angle of tilt and the size of the beam area are determined by the Bragg angles of the monochromator and the analyzer. As the monochromator is fixed to produce the stable polarized incident X-rays, the tilt angle is different depending on the specific analyzer used. For Si (5 5 5) and Ge (5 5 5), the tilt angle is 7.82° and 8.51° respectively, and the area of the beam region area is 5.0 × 0.871 mm^2 and 4.1 × 0.846 mm^2 respectively.

As seen in Fig. 2.2, the detected area of XBI is quite small. In order to place the sample in the middle of the observed strip, before the measurements of the XBI data, we need to adjust the position of the sample, and this adjustment is processed by the help of area detector 2 (see Fig. 2.1) with no analyzer. As shown in Fig. 2.3, area detector 2 (used for sample alignment) receives the beam directly, while area detector 1 (used to record the XBI images) receives the beam after diffraction. So, the images of the sample from the two detectors are effectively mirror images of each other, i.e., if we want to move the sample left in the XBI image, we need give a command to move it right. Only left and right are swapped, up and down are still the same. However, it is important to emphasize that it is only the image recorded on area detector 1 that provides information on the birefringence of the sample.

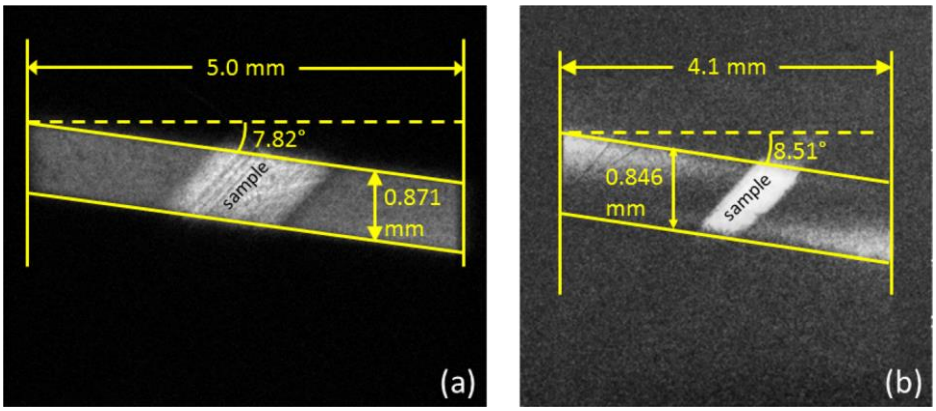

Figure 2.2 *Images on area detector 1 after the diffraction from the two different crystal analyzers: (a) Si (5 5 5) and (b) Ge (5 5 5). The middle bright part is the birefringent sample: (a) a single crystal of the 1-bromoadmantane/thiourea inclusion compound and (b) a single crystal of the 1,8–dibromooctane/urea inclusion compound. Reprinted with permission from Sutter, J. P.; Dolbnya, I. P.; Collins, S. P.; Harris, K. D. M.; Edwards-Gau, G. R.; Palmer, B. A., Theoretical Analysis of the Background Intensity Distribution in X-ray Birefringence Imaging Using Synchrotron Bending-Magnet Radiation. J. Appl. Phys.* ***2015****, 117, 164902. Copyright 2015 American Institute of Physics.*

Because the sample rotation angle φ is also introduced in XBI, the movement of the sample is a little more complicated in XBI (three dimensional, i.e., 3D) than in POM (two dimensional, i.e., 2D). As we discussed in 1.2.1, the intensity of the diffracted rays should be proportional to $\sin^2(2\theta)$ (see Eq. 2.4, Page 32, where K is a constant and I_0 is the incident ray intensity), which is under the hypothetical condition of $\varphi = 0°$ (Fig. 2.4.a). However, if $\varphi \neq 0°$ (Fig. 2.4.b), the projection of the sample on the *zy-plane* should be

considered (Fig. 2.5). The intensity of 3D should be equal to the 2D intensity multiplied by the ratio of the projection length to the actual length of the sample (Eq. 2.5).

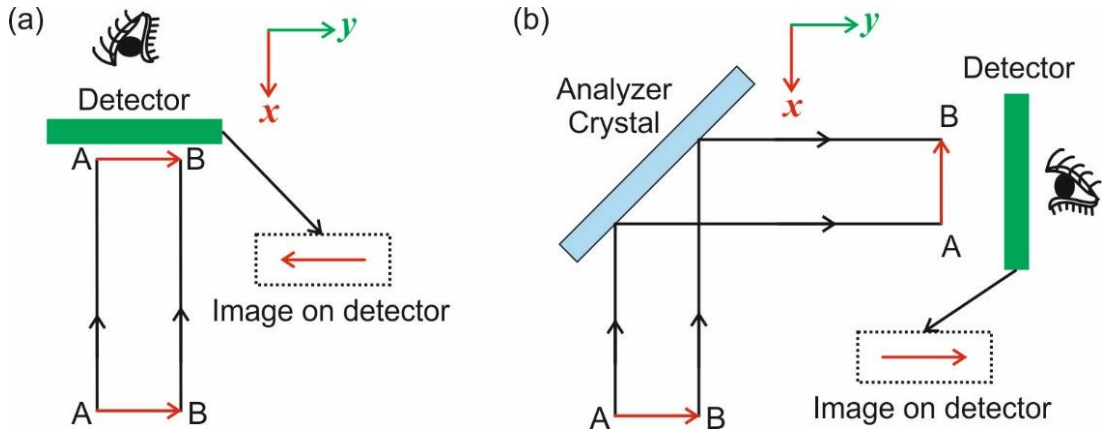

Figure 2.3 *Illustration of the two area detectors. For the same sample (the red arrow), area detector 2 (without the analyzer) just takes an image as normal, as shown in (a). However, the XBI detector (area detector 1) receives the rays diffracted from the analyzer, and therefore represents a mirror image of the sample, as shown in (b).*

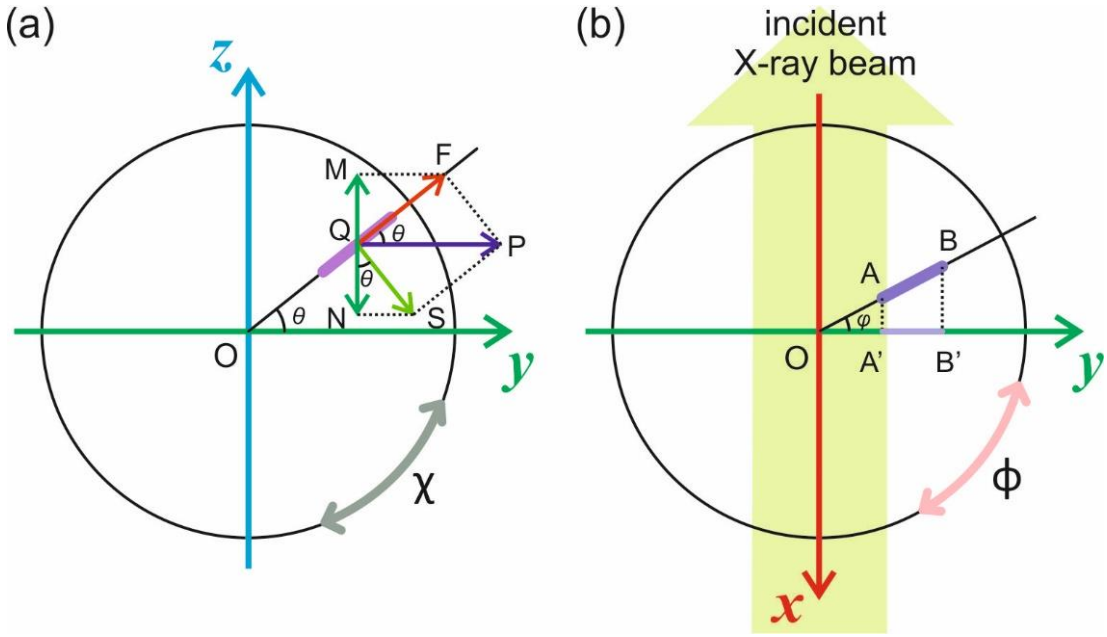

Figure 2.4 *Theoretical analysis of the XBI intensity. (a) When φ = 0°, the intensity is proportional to $\sin^2(2\theta)$ (the detailed analysis is in previous 1.1). (b) When φ ≠ 0°, the intensity is also influenced by φ. The birefringent sample is shown in purple and the X-ray optical axis is parallel to the long-axis of the sample.*

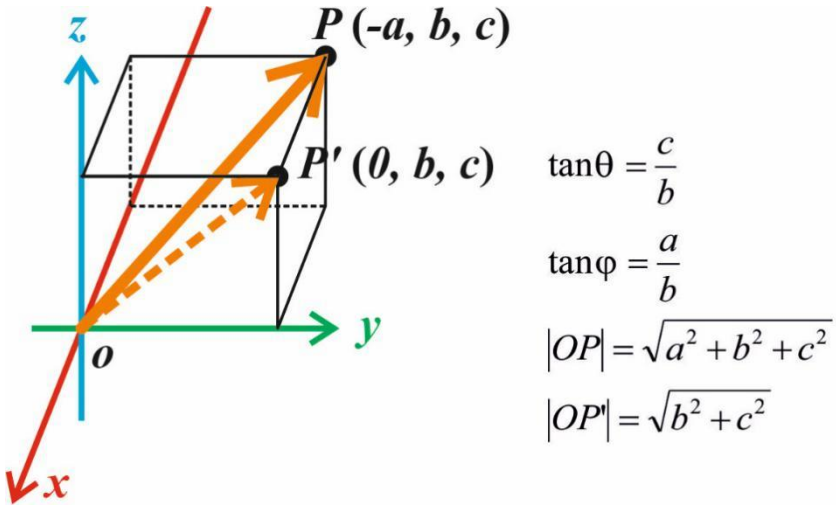

Figure 2.5 *Illustration of the projection of the sample on to the yz-plane when φ ≠ 0°. Assume the X-ray optic axis of the sample is along OP, and the projection of OP on the yz-plane is OP'. In the same coordinate system of XBI (Fig. 2.1, Page 29, and Fig. 2.4), assume P is at the position (-a, b, c). The magnitude and orientation of the projection of the X-ray optic axis can be represented by a, b and c.*

$$I_{2D} = I_0 \cdot K \cdot \sin^2(2\theta) \tag{2.4}$$

$$I_{3D} = I_{2D} \frac{|OP'|}{|OP|} \tag{2.5}$$

The above equation can be further simplified in terms of only θ and φ (Eq. 2.6). This means we can predict the intensity once we know the orientation of the sample in space. The final mathematical representation of the intensity in XBI is Eq. 2.7. Figure 2.6 is a plot of the theoretical intensity in the range of 0° to 360° on both θ and φ axes.

$$\begin{aligned} I_{3D} &= I_{2D} \frac{|OP'|}{|OP|} \\ &= I_{2D} \cdot \frac{\sqrt{b^2 + c^2}}{\sqrt{a^2 + b^2 + c^2}} \\ &= I_{2D} \cdot \frac{\sqrt{b^2 + b^2 \tan^2\theta}}{\sqrt{b^2 \tan^2\varphi + b^2 + b^2 \tan^2\theta}} \\ &= I_{2D} \cdot \frac{\sqrt{1 + \tan^2\theta}}{\sqrt{\tan^2\varphi + 1 + \tan^2\theta}} \end{aligned} \tag{2.6}$$

$$I_{3D} = I_0 \cdot K \cdot \sin^2(2\theta) \cdot \sqrt{\frac{1 + \tan^2\theta}{1 + \tan^2\theta + \tan^2\varphi}} \tag{2.7}$$

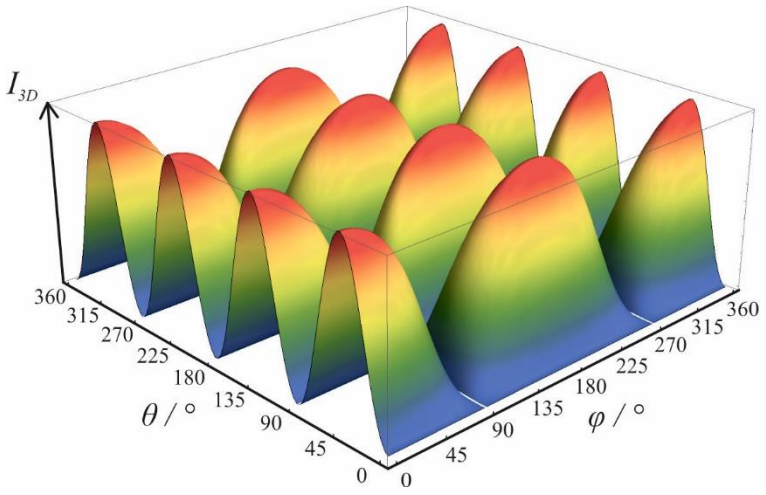

Figure 2.6 *Theoretical XBI intensity as a function of orientation of the sample defined by θ in the range of 0° – 360° and φ in the range of 0° – 360°.*

2.2 Powder X-ray Diffraction

The intensity (I_{hkl}) of Bragg diffracted X-rays from a crystalline material can be represented by Eq. 2.8;[26] here, I_0 is the intensity of the incident X-rays; F_{hkl} is the structure factor; and K is a constant value for a specific experiment. F_{hkl} represents the amplitude and phase of the diffracted X-rays on the plane with Miller indices (*hkl*), and it is determined by the position (x_n, y_n, z_n) and scattering factor (f_n) of each atom in the unit cell (Eq. 2.9). Thus, for each plane (*hkl*), there is a corresponding diffraction maximum with a certain intensity on the detector. Crystal structure determination from single-crystal XRD is undertaken by analysing the intensity and geometric relationships of the diffraction maxima recorded on the detector.

$$I_{hkl} = I_0 \cdot K \cdot \left|F_{hkl}\right|^2 \qquad (2.8)$$

$$F_{hkl} = \sum f_n \exp\left[2\pi i\left(hx_n + ky_n + lz_n\right)\right] \qquad (2.9)$$

If the sample is just one perfect single crystal, the detector will show one diffraction pattern, in which each diffraction maximum represents each corresponding plane with Miller indices (*hkl*) (Fig. 2.7.a).[4] If we have two single crystals, the detector will show two sets of the previous pattern (Fig. 2.7.b) and the disparity between the two diffraction patterns originates from the relative orientations of the two single crystals. If the sample contains four single crystals, there will be four diffraction patterns (Fig. 2.7.c),

and so on. For powder XRD, the sample actually contains a very large number of small single crystals. Because these crystals are small, it looks like a powder on the macro-level, so it is called "powder XRD". As the number of single crystals in powder XRD is very large, a very large number of individual diffraction patterns are recorded on the detector. For a good isotropic powder XRD sample (i.e., with a random distribution of crystal orientations), the detector will show several rings (with continuous intensity around each ring) instead of discrete spots (Fig. 2.7.d). By producing rings of diffraction instead of separate spots, the three dimensional diffraction data are effectively compressed into one dimension. Peaks from planes with different Miller indices but similar *d*-spacings will be overlapped; preventing accurate determination of peak intensities.

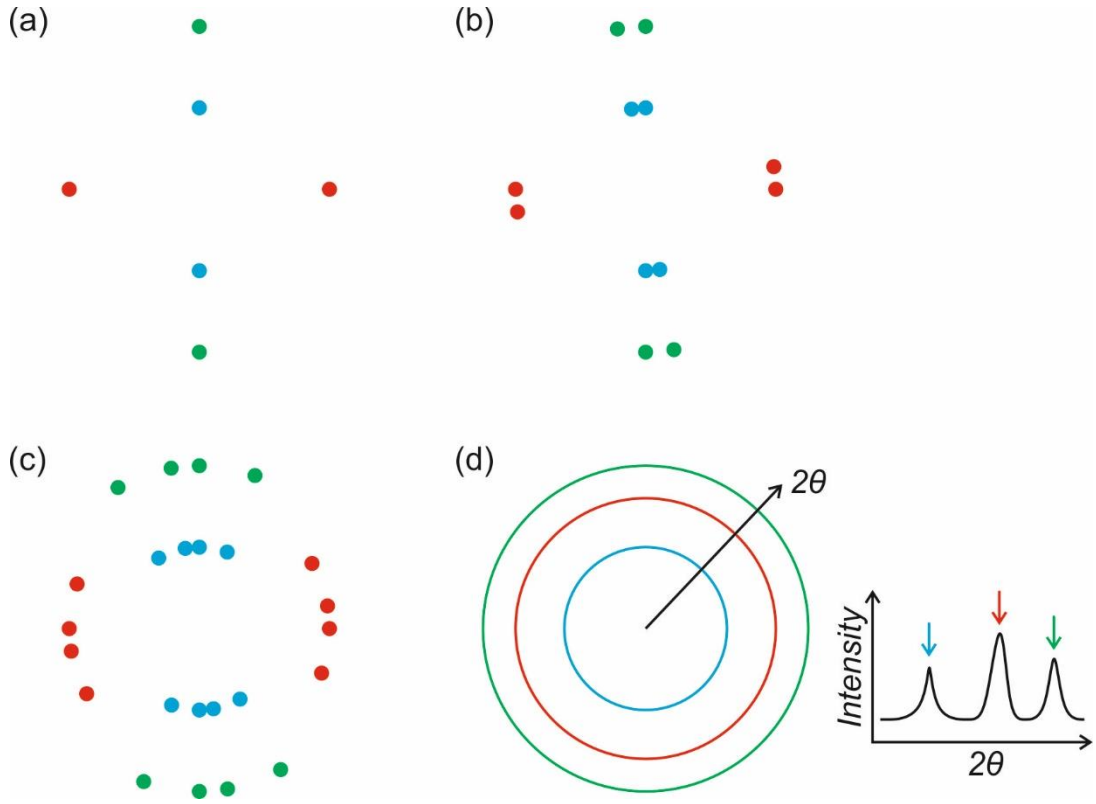

Figure 2.7 *Sketch of X-ray diffraction patterns from single-crystal XRD to powder XRD. (a) One single crystal (single-crystal XRD); (b) two single crystals; (c) four single crystals; (d) a very large number of randomly oriented single crystals and its powder XRD recorded pattern.*

We already know that XRD can be classified into powder XRD and single-crystal XRD. Powder XRD can be further divided into two modes of data collection: reflection and transmission (Fig. 2.8).[36] For reflection mode powder XRD, the defocusing effect

cannot be ignored when the incident angle is small, which needs correction when we analyse the intensity. However, in transmission mode powder XRD, the incident beam is perpendicular to the surface plane of the sample, and the defocusing effect will be decreased. So, for structure determination from powder XRD, it is advantageous to use transmission mode powder XRD. In order to get good quality data, the powder crystals are sealed into a capillary to decrease the likelihood that the sample will exhibit preferred orientation of the crystallites.

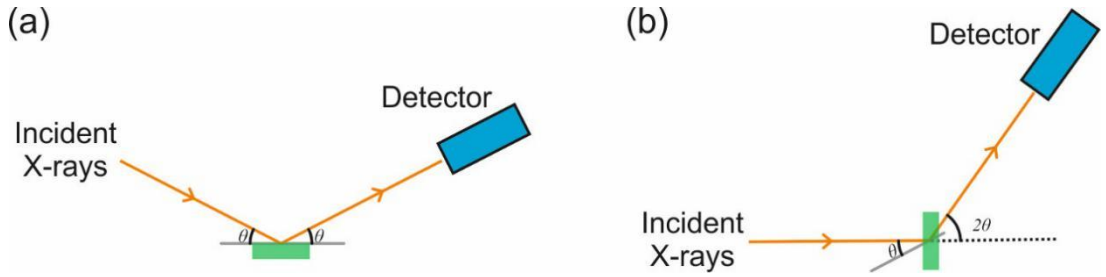

Figure 2.8 *Illustration of powder XRD measurement in: (a) reflection mode and (b) transmission mode. The powder sample is represented by the green rectangle.*

2.3 Differential Scanning Calorimetry

Differential Scanning Calorimetry (DSC) is a widely used technique to investigate the thermal properties of solid or liquid samples.[36-44] The basic principle of DSC is to measure the heat flow while the heating or cooling process is carried out at a constant rate. DSC uses two pans – one is for sample, another is for reference (Fig. 2.9). These two pans are like two plates of a pallet balance, but in DSC the balance distinguishes temperature instead of weight. The reference pan is made of a stable metal or alloy, ensuring that the pan has a constant heat capacity during the experimental process. Thus, the heat change of the reference pan can be calculated and predicted. The reference pan can also be an empty pan of the same type that is used to hold the sample. When the sample undergoes a thermal event (e.g., a phase transition), the sample absorbs heat (endothermic) or releases heat (exothermic). If the sample pan and the reference pan are to be kept at the same temperature, extra heat flow is needed into or out of the sample pan. This extra heat flow can be detected by the computer program; thus, the thermal behaviour of the sample can be investigated.

DSC can detect a lot of physical properties, such as crystallization, melting, glass transitions, phase transitions and so on.[40-43] As long as the sample releases or absorbs heat, it can be recorded in DSC curves. Usually, a DSC experiment is set to monitor the heat flow change with a constant heating or cooling rate.

DSC data are analysed in a two-dimensional graph with temperature as the horizontal axis and heat flow as the vertical axis. If the heat flow between the two pans changes, there will be a peak shown on the curve, meaning a phenomenon involving thermal change happens within the sample. Exothermic peaks and endothermic peaks occur in opposite directions.

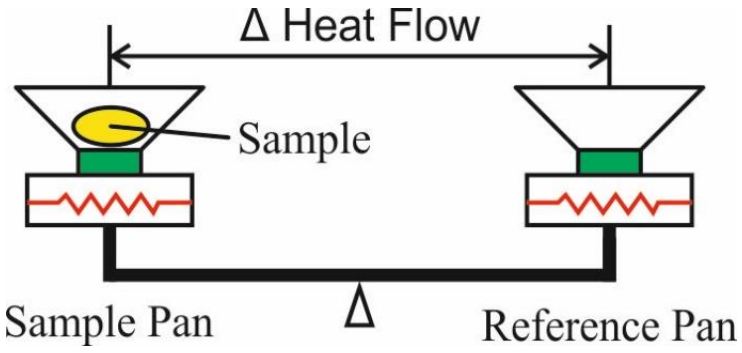

Figure 2.9 *Illustration of DSC set-up. The sample pan and the reference pan are on a "temperature balance". When a thermal change happens in the sample, some compensated heat flow will occur in order to maintain the previous balance. The heat flow is recorded by computer programs. If the sample has no thermal change, the heat flow to the two pans should be constant, which is shown as a flat line in the DSC data.*

Figure 2.10.a shows two typical DSC results corresponding to crystallization and melting. In the heating process, when the temperature reaches the melting point of the sample, the sample absorbs heat to melt, and the peak is in the negative direction. On the contrary, in the cooling process, when the temperature reaches the freezing point, the sample releases some heat and turns into crystals, with a peak in the positive direction. To identify a peak as endothermic or exothermic, it should be referred to the labelled direction ("Exo Up", "Exo Down", "Endo Up" or "Endo Down") of the DSC equipment, and this label is usually shown in the final graph.

Figure 2.10.b shows a phenomenon called "cold crystallization".[37-39] Here, crystallization happens during the heating process and the sample releases heat even though the sample pan is being heated. This phenomenon usually happens in long-chain

molecular crystallization. Because of the long-chains, in the normal cooling process, before the molecules are frozen, there is not enough time for molecules to move into the crystal lattice to pack orderly to become crystals; however, when the environment warms again, the molecules have sufficient flexibility to continue the previous crystallization process, thus an exothermic peak appears in the heating curve. As it is still a crystalline solid, when the temperature reaches the melting point, the sample will melt as normal, giving an endothermic peak in the DSC data.

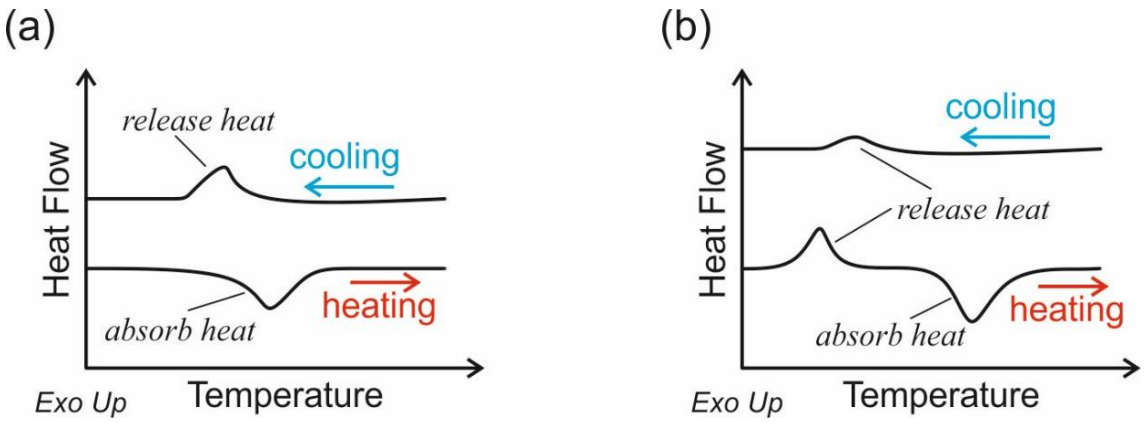

Figure 2.10 *A diagrammatic sketch of typical DSC data: (a) normal crystallization and melting; (b) cold crystallization involving an additional exothermic peak in the heating process.*

As mentioned above, DSC curves usually show the heat flow as a function of temperature with a fixed heating or cooling rate. If a different heating or cooling rate is used, the peak area is different even using the same sample.[44] Heat flow is the representation of amount of heat in unit time, with the formula given in Eq. 2.10. Heating rate is the temperature change in unit time (Eq. 2.11). Thus, heat flow can be represented in terms of heating rate in Eq. 2.12. For a given sample, the amount of heat exchange for a physical thermal change is fixed. In a given range of temperature, the heat flow is proportional to the heating rate. Thus, using a faster heating rate generates a bigger heat flow, resulting in a bigger peak in the DSC data (Fig. 2.11). A fast DSC scan gives significantly higher sensitivity, which can help us to observe transitions involving only a small heat exchange. However, the faster rate is at the expense of temperature resolution and accuracy. Traditionally, the scan rate is set as 10 °C/min or 15 °C/min. In this thesis, the heating rates used range from 1 °C/min to 10 °C/min.

$$Heat\ \ Flow = \frac{Heat}{Time} \tag{2.10}$$

$$Heating\ \ Rate = \frac{\Delta T}{Time} \tag{2.11}$$

$$Heat\ \ Flow = \frac{Heat}{\Delta T} \times Heating\ \ Rate \tag{2.12}$$

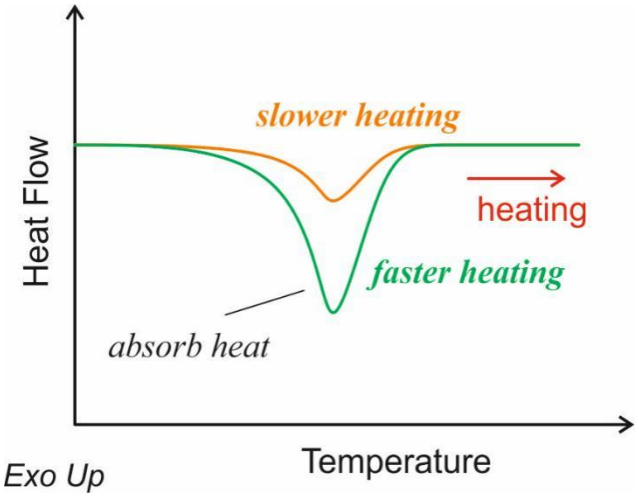

Figure 2.11 *A diagrammatic sketch of DSC data recorded at two different heating rates. The fast one shows a bigger peak, because of the higher heat flow.*

2.4 Direct-Space Structure Solution Using a Genetic Algorithm

A Genetic Algorithm (GA) is a metaheuristic in computer science to find solutions to optimization problems, which is inspired by some phenomena in evolutionary biology, like heredity, hybrid, mutation, natural selection and so on.[45] In a GA calculation, the quality of solutions is improved from generation to generation; thus, after sufficient evolution has taken place, the final generation will be the optimal solution to the original problem.

As mentioned before, crystal structure determination from powder XRD data is much more difficult than from single-crystal XRD data. Traditionally, it is necessary to analyse the intensity of each peak in the diffraction patterns. But, because most peaks are overlapped in a typical powder XRD pattern, in practice it is hard to distinguish each peak clearly especially in crowded areas containing severe peak overlap. A reverse method is to use the direct-space strategy. After unit cell determination and the profile fitting

process, the direct-space strategy places a certain amount of target molecules arbitrarily (the number of molecules is determined by density estimation) within the unit cell. The GA calculation produces new trial structures by moving the molecules from generation to generation until the simulated powder XRD pattern for the trial structures is as close to the experimental data as possible.[27, 28]

Figure 2.12 shows the detailed process on how each generation is produced from the previous one. Each generation has N_p trial structures. Each structure is defined by several variables from the following three aspects – three variables define the position of the molecule in the unit cell $\{x, y, z\}$; three variables define the orientation of the molecule relative to the unit cell axes $\{\alpha, \beta, \gamma\}$; and a number of variables define the unknown torsion angles within the molecule $\{\tau_1, \tau_2, \tau_3, \ldots, \tau_n\}$. In each generation, N_m pairs of structures are selected randomly from the above trial structures and undergo the mating process, producing $2N_m$ offspring structures. These $2N_m$ new structures and the initial trial structures combine to form an intermediate trial structure population with $(2N_m + N_p)$ numbers that undergoes natural selection and the generation of mutations. Thus, N_x structures are selected randomly from the intermediate trial structures to undergo the mutation process, and the $(N_p - N_x)$ best trial structures from the intermediate population are selected to enter the next generation by "natural selection". The way to evaluate the quality of each trial structure is based on the R-factor (R_{wp} and R_p) introduced in 1.3. Thus, after mutation and natural selection, the number of structures passing into the next generation is still N_p. Because only the best structures survive into the next generation via "natural selection", each generation is better than the previous one. So, after a sufficient number of generations (P_j), the population should contain a trial structure that is very similar to the true crystal structure.

The parameters N_p, N_m, N_x and P_j can be set manually according to the requirement of the calculation. Usually, within 100 generations, a good structure can be achieved. If not, one possible way to improve the situation is to enlarge the number of generations. As this procedure requires a large amount of calculations, in this thesis, the supercomputer "RAVEN" is applied to run the direct-space GA calculation incorporated in the program EAGER (Evolutionary Algorithm Generalised for Energy and R-factor).

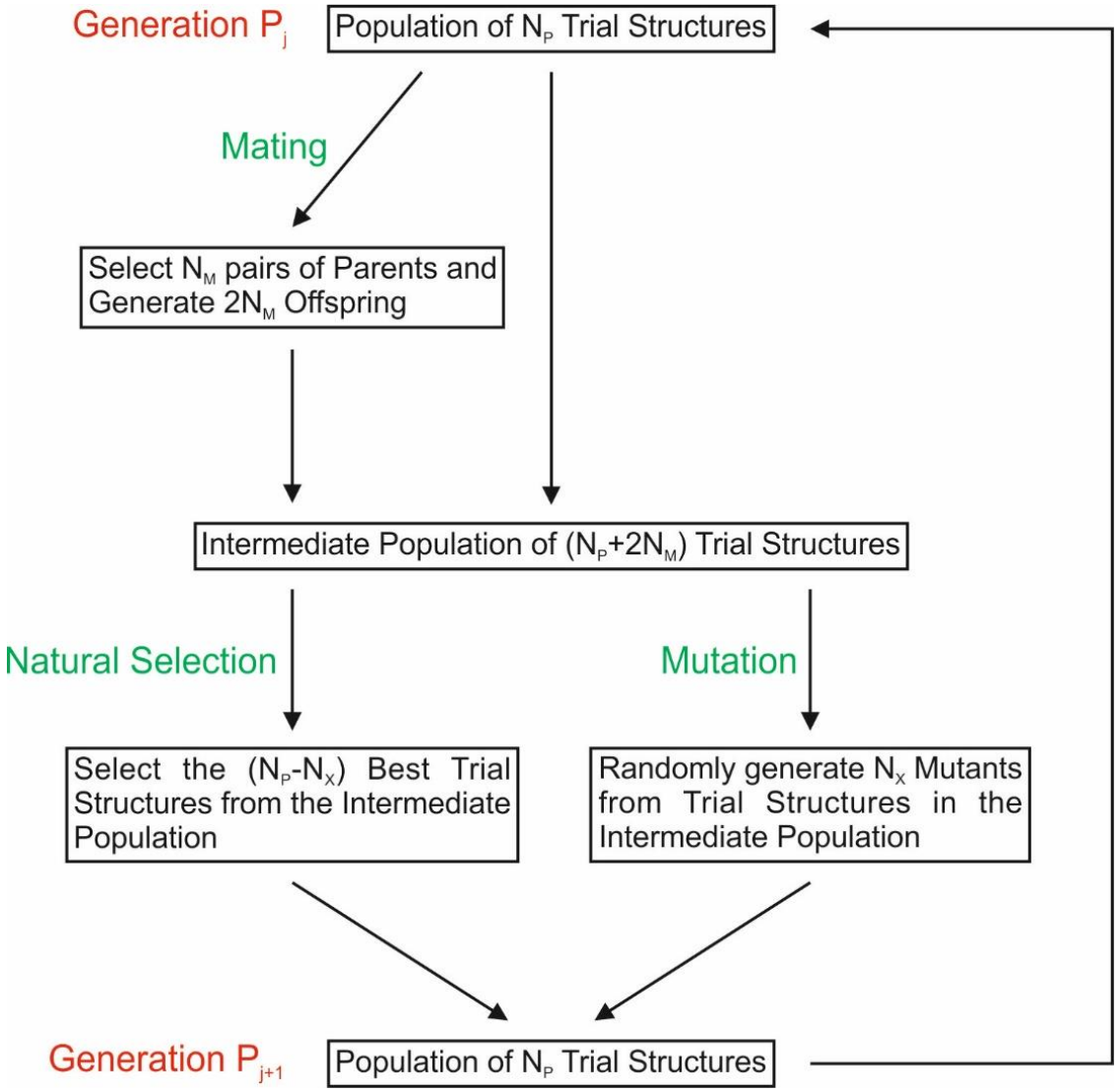

Figure 2.12 *Flow chart of the GA procedure incorporated in the program EAGER, showing the evolutionary processes involved in progressing from one generation (P_j) to the next generation (P_{j+1}) in crystal structure determination from powder XRD. Each generation has N_p trial structures.*

Chapter 3

X-ray Birefringence Imaging on Liquid Crystals

3.1 Introduction

Liquid crystals are a state of matter between crystalline solids and isotropic liquids, in which the molecules have some liquid-like mobility but still keep some crystal-like orientational properties.[46] Figure 3.1 shows how a material may change phase from solid to liquid crystal to liquid with increase of temperature. At lower temperature, the molecules have a lower degree of mobility and are fixed in the crystalline state. At higher temperature, the molecules have a high degree of mobility and undergo translational and reorientational motions, resulting in an isotropic liquid phase. Between these two states, a liquid crystal state may exist, in which the molecules are more fluid than a crystalline solid but less fluid than an isotropic liquid, and the molecules are oriented loosely along one direction.

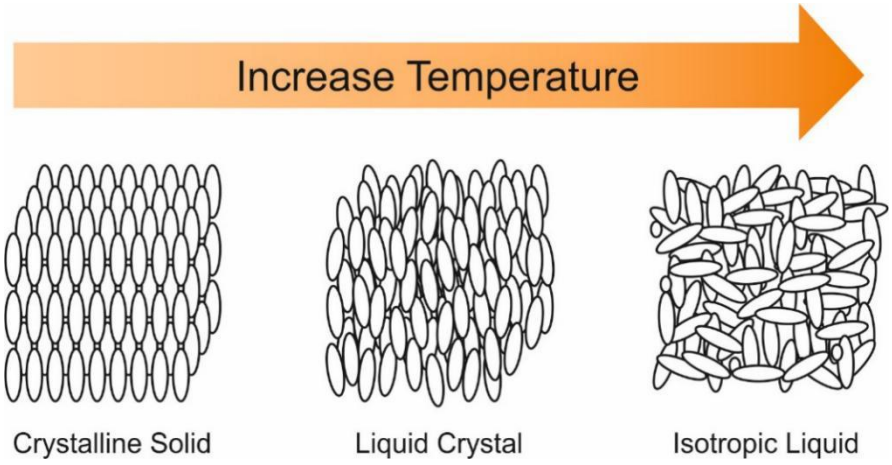

Figure 3.1 *Schematic representation of phase transitions of a liquid crystal material with increase of temperature. In the liquid crystal state, the molecules exhibit characteristic properties of both liquid (mobility) and solid (orientation) phases.*

In a magnetic field, molecules in a liquid crystal are aligned preferentially along one direction,[47] but this alignment is not strictly perfect (unlike the situation expected for molecular orientations in a crystalline solid). Within the magnetic field, the assembly of molecules adopts one preferred direction, but not all the molecules are aligned parallel to

the preferred direction. In most cases, there is a small angular deviation between the long-axis of the molecule and the preferred direction, but the average direction of the assembly of molecules is always along the preferred direction. An order parameter (S)[48-51] is used to describe this orientational distribution quantitatively (Eq. 3.1):

$$S = \frac{1}{2}\left\langle 3\cos^2\theta - 1\right\rangle = \frac{3\left\langle \cos^2\theta\right\rangle - 1}{2},\ \left(0° \le \theta \le 90°\right) \qquad (3.1)$$

where the angular brackets indicate a statistical average and θ is the angle between the long-axis of the liquid crystal molecule and the preferred direction (Fig. 3.2). For a sample with perfect orientational order (i.e., $\theta = 0°$ for all molecules in the assembly), $S = 1$. For a sample with an isotropic orientational distribution (i.e., with all orientations equally populated and with θ ranging from 0° to 90°), $S = 0$.

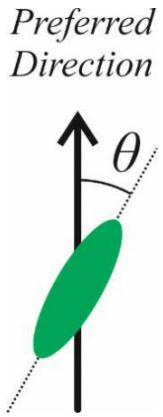

Figure 3.2 *Schematic representation of order parameter of a liquid crystal material. The black arrow is the preferred orientation direction. One molecule in the liquid crystal is shown in green. The angle between the long-axis of the molecule and the preferred direction is denoted θ.*

In order to carry out experiments on liquid crystals using X-ray Birefringence Imaging (XBI), some modifications are applied to the basic experimental set-up in Fig. 2.1 (Page 29). The new set-up developed here to study liquid crystals is shown in Fig. 3.3, comprising an added magnetic field and a sample cell for liquid crystals. The liquid crystal sample is packed into a capillary and this capillary is inserted into a graphite tube as the sample cell. Because the sample cell is made of graphite, temperature control can be achieved by passing an electric current within the graphite tube. The North and South Poles of the magnetic field are set on opposite sides of the graphite tube, positioning the graphite tube at the centre of the magnetic field. The direction of the magnetic field is

perpendicular to the propagation direction of the incident X-ray beam. The molecules of the liquid crystal are aligned preferentially along the direction of the magnetic field.

Another advantage of choosing graphite as the sample cell is that as graphite is relatively "transparent" to X-rays,[52] experimental images of the sample within the graphite tube can be seen directly in XBI. Figure 3.4 shows images of the sample on area detector 2 (i.e., with no analyzer; Fig. 3.4.b) and on area detector 1 (i.e., XBI image recorded with the analyzer; Fig. 3.4.c). After melting, air bubbles appear due to beading of the liquid sample by the capillary effect.[53] In order to avoid the air bubbles, we may need move the sample slightly, to ensure that there is no air bubble in the region of the sample probed by the X-ray beam. The image recorded on area detector 2 has a bigger field of view than the XBI image recorded on area detector 1, giving convenience to adjust the position of the sample.

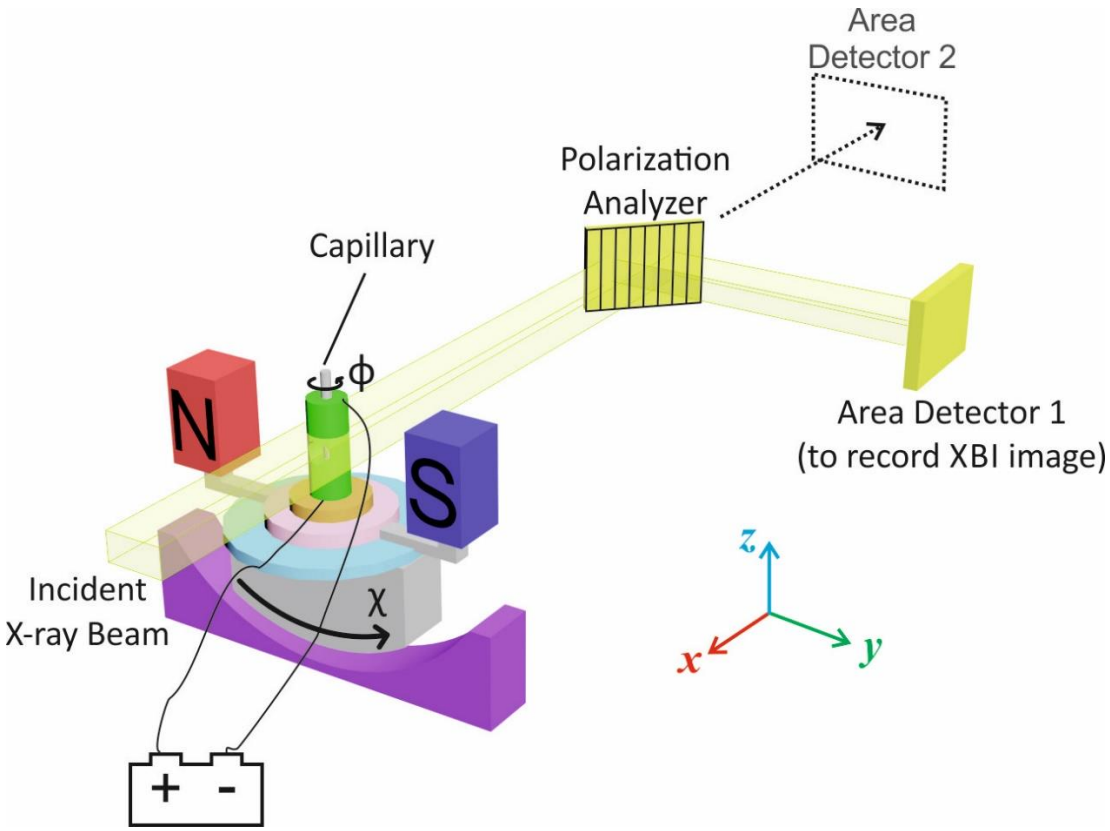

Figure 3.3 *Experimental XBI set-up for study of liquid crystals. A new liquid crystal cell with a capillary is used instead of the basic sample holder. The North Pole and South Pole of the magnetic field create a nearly parallel and uniform magnetic field within the sample space. The preferred direction of molecular orientation is along the direction of the magnetic field.*

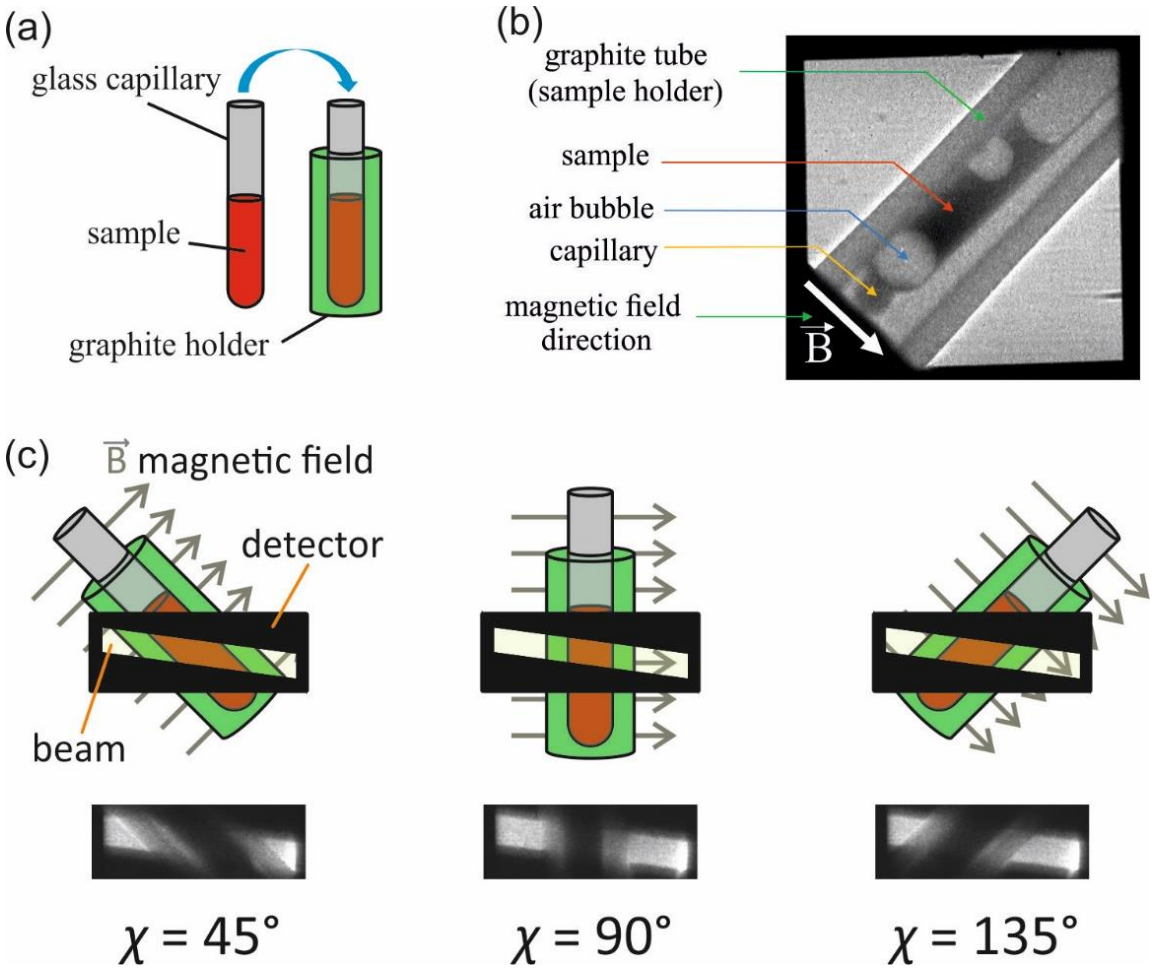

Figure 3.4 *(a) Illustration of the liquid crystal cell for XBI studies: the sample is put into a glass capillary, and this capillary is put into the graphite tube. (b) The normal X-ray image recorded using area detector 2 (with no analyzer). (c) Images recorded using area detector 1 with the analyzer crystal present (XBI images), with the sample cell oriented at χ = 45°, 90° and 135°. Here, the temperature is high, and the sample is in the isotropic liquid phase.*

3.2 Phases of Liquid Crystal

Many materials exhibit several different liquid crystalline phases between the crystalline phase and the isotropic liquid, with increase of temperature.[54] In order to study the phase transitions within liquid crystals by XBI, in this section a material (LC_1) with three liquid crystal phases between the crystalline solid and isotropic liquid is used, and its molecular structure is shown in Fig. 3.5. The temperatures of the phase transitions are 151 °C, 154 °C, 215 °C and 216 °C respectively, which correspond to the following phase

transitions: crystalline (Cr) to smectic B (SmB), SmB to smectic A (SmA), SmA to nematic (N), and N to isotropic (Iso).

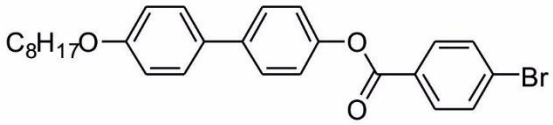

$$LC_1 : Cr \bullet 151 \bullet SmB \bullet 154 \bullet SmA \bullet 215 \bullet N \bullet 216 \bullet Iso$$

Figure 3.5 *Molecular structure of LC_1 which has the typical banana-shape of liquid crystals. Its transition temperatures are labeled below, the unit is °C.*

The definitions of the smectic and nematic phases are based on the positional and orientational ordering of the molecules.[54-57] If the preferred direction is along the *z-axis*, in the nematic phase, the rod-like molecules are aligned close to the *z-axis*, but with disordered projection on the *xy-plane* (Fig. 3.6). The nematic phase is the first phase formed after the isotropic liquid on reducing the temperature. The molecules in this phase can still flow like the molecules in liquid phases, but this mobility is restricted as the molecules prefer to be aligned along the *z-axis*.

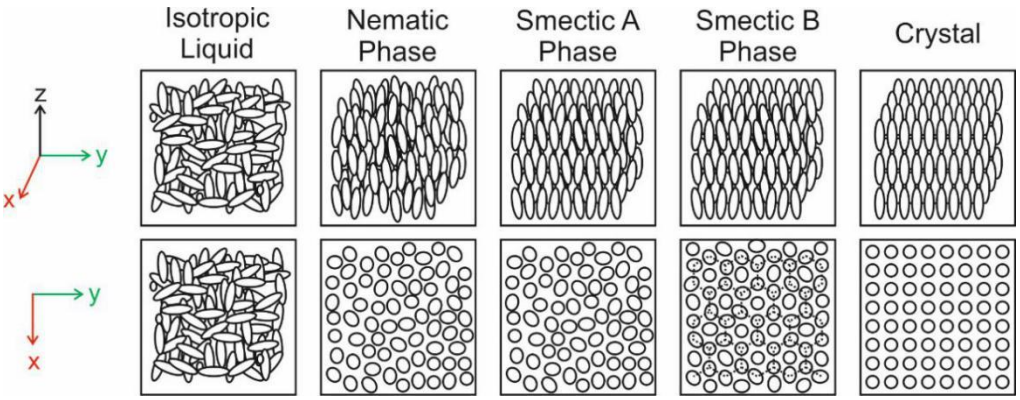

Figure 3.6 *Illustration of phases of liquid crystals. The order increases from the isotropic liquid to the crystal, passing through nematic, smectic A and smectic B phases. The preferred orientation direction is the z-axis. For each phase, the projection on the xy-plane is shown at the bottom.*

On further cooling, the nematic phase transforms to a smectic phase. The distinctive feature of a smectic phase is the layered arrangement of the molecules. Because, at this moment, the temperature is lower than in the nematic phase, the molecular mobility is further decreased – the material is less fluid, molecules are confined in each layer, and there is no molecular exchange between adjacent layers. The smectic

phase can be further classified according to the positional ordering of the molecules within the layers. In smectic A, compared with the nematic phase, the order of the molecules is increased only through layered arrangement, but the projection on the *xy-plane* is still disordered. On further decreasing the temperature, the molecules tend to form a hexagonal arrangement within each layer, and the order is increased furthermore, representing a smectic B phase.

With further cooling, the molecules become "frozen" finally, losing all mobility and becoming packed into a three-dimensionally ordered crystal lattice to form a crystalline solid with the greatest degree of positional and orientational order.

As the occurrence of phase transitions depends on changes of temperature, it is convenient to use DSC to study phase transition phenomena. Figure 3.7 shows the DSC data for LC_1, cooling from high temperature to low temperature at two different rates, 1 °C/min and 10 °C/min, which is consistent with the cooling rate of the XBI experiments discussed below.

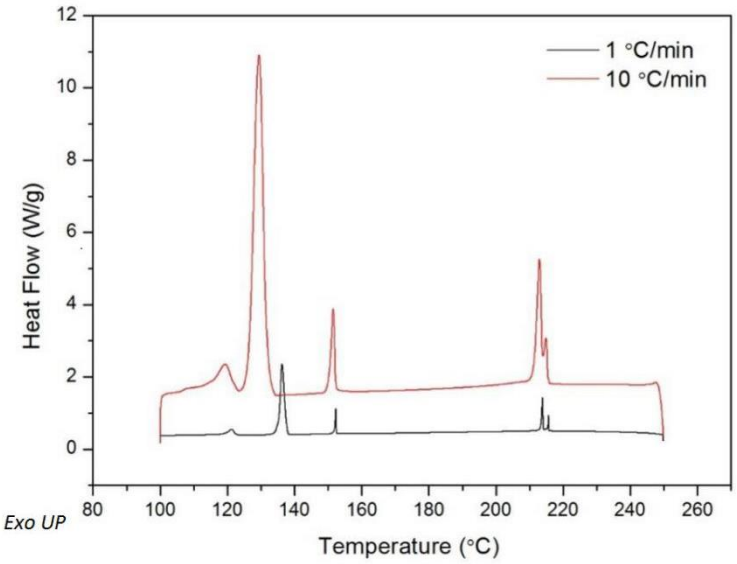

Figure 3.7 *DSC data recorded for LC_1 cooling from 250 °C to 100 °C at two different cooling rates: 1 °C/min (black) and 10 °C/min (red). The higher cooling rate results in higher heat flow.*

As mentioned in 2.3, use of a higher cooling rate results in higher sensitivity, and the peaks in the data recorded at 10 °C/min are bigger than at 1 °C/min. When cooling from 250 °C, two exothermic peaks are observed around 215 °C. The first small peak is the phase transition from the isotropic liquid to the nematic phase, and the larger peak is

the phase transition from the nematic phase to the smectic A phase. The two peaks are overlapped in the data recorded at 10 °C/min because of lower accuracy and lower resolution at the higher rate of cooling.[44]

Another exothermic peak at *ca.* 155 °C arises from the phase transition from the smectic A phase to the smectic B phase. Here, the molecules move within each layer to form a hexagonal patterns arrangement. The next peak on cooling is the biggest exothermic peak in each set of data, representing crystallization, and corresponding to release of the greatest amount of heat. It is worth noting that, from this point, the peak positions of the two curves become different, i.e., for the transition between liquid crystal phases, the transition temperatures are nearly independent of cooling rate. However, significant differences are observed for the solid state. Both sets of data show a small broad peak after the crystallization, indicating a solid-solid phase transition phenomenon.

X-ray Birefringence Imaging (XBI) has been proven to be an effective technique to investigate the anisotropy of the local bonding environment of selected elements.[21-23] At the energy of the Br K-edge, birefringence occurs, with the X-ray optic axis parallel to the C–Br bond. In the present work, LC_1 was designed specially to have a C–Br bond at the end of the molecule, with this C–Br single bond oriented parallel to the long-axis of the liquid crystal molecule (Fig. 3.5, Page 45). The orientation of the C–Br bond, therefore, gives a reliable representation of the orientation of the whole molecule.

XBI images recorded at three different temperatures and for a range of sample orientations (χ) are shown in Fig. 3.8. At 220 °C, the XBI images are dark at all measured values of χ, because at this high temperature, the material is in the isotropic liquid phase. The molecules are moving randomly and there is no preferred orientation of the C–Br bonds and hence no birefringence is observed. The corresponding surface plots show a uniform orange colour of the sample, which is in a good agreement with the expected properties of the isotropic liquid phase.

At 214 °C, the XBI images of the nematic phase are not easy to capture, as the temperatures of the phase transitions from Iso to N and from N to SmA are very close, differing by just 1 °C. The way to capture the images of the nematic phase is by cooling from the isotropic liquid phase with the sample oriented at $\chi = 45°$; once a bright part is visible in the image (signifying the presence of the nematic phase), the sample was held at this temperature and the χ scan was carried out. The boundary between the bright and

the dark regions is clearly seen, in which the dark region is the Iso phase and the bright region is the N phase. The brightness arises because the molecules align with the preferred direction in the N phase. All the C–Br bonds tend to be parallel to the direction of the magnetic field, which is perpendicular to the propagation direction of the incident beam. According to the principles of XBI in 2.1, the brightest image arises at χ = 45° and χ = 135°, and the brightness is minimized at χ = 90° (referring to Eq. 2.7, Page 32). So, the boundary of Iso and N is not easily distinguished around χ = 90°. Here, the temperature 214 °C is just the set-up temperature of the XBI experiment, and the true internal temperature of the sample is not necessarily the same temperature, with evidence of temperature gradients (which results in the co-existence of the Iso and N phases in the XBI images at 214 °C). It is, therefore, unsurprising that the temperature differs by a few °C from the phase transition temperature recorded by DSC.

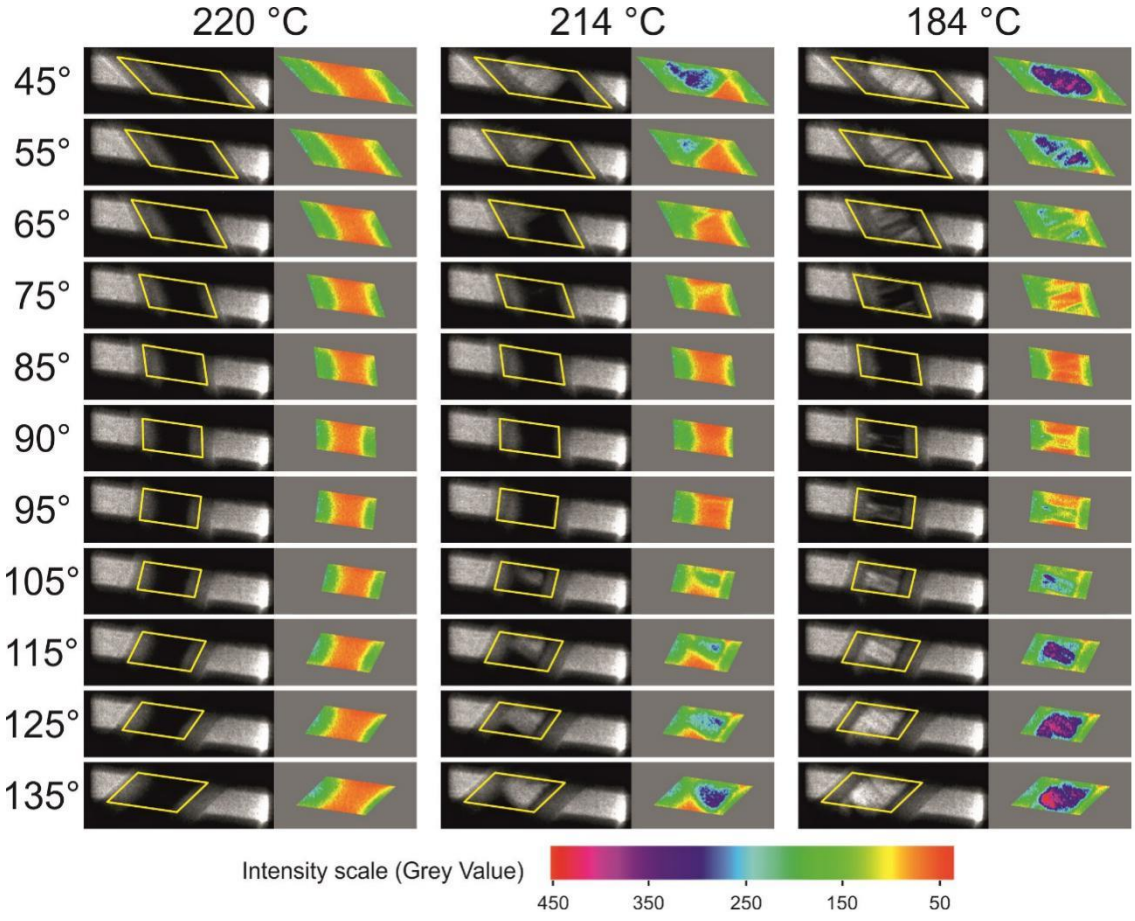

Figure 3.8 *XBI images (black and white images) and the corresponding intensity contour plots (color images) for χ scans of LC_1 at 220 °C, 214 °C and 184 °C. The χ value is varied from 45° to 135° with an increment of 5°. The yellow frames identify the area of the sample.*

As the temperature range of the SmA phase is quite wide, in the cooling process, after the phase transition from N to SmA around 215 °C, the next transition (from SmA to SmB) occurs at 154 °C. It is safe to set the temperature at 184 °C to ensure that the entire sample is in the SmA phase. XBI images at this temperature are brighter than those for the N phase at 214 °C, and also have the typical birefringence property with maximal brightness at χ = 45° and χ = 135°. This observation proves that the molecules in SmA exhibit greater orientational ordering than the N phase. However, on closer inspection of the XBI images, several bands can be seen within the sample, and further investigation is required to explain this "black-band" phenomenon. The reason may be the variation in the strength of the magnetic field, the curvature variations of the surface of the capillary or the layer-structure of the SmA itself.

The intensity of each image in Fig. 3.8 has been analysed using the program "Fiji-ImageJ". Figure 3.9 shows the intensity measured from the XBI images in Fig. 3.8. The images at 220 °C, 214 °C and 184 °C represent the Iso, N and SmA phases, respectively. In the Iso phase, the intensity is very low (close to 0) and does not change during the χ scan, because of the isotropic nature of the material. In the N and SmA phases, the intensity plot of each phase shows the familiar sinusoidal behaviour as discussed before (Fig. 1.18, Page 20), meaning that the C–Br bonds prefer to be aligned along the magnetic field direction, giving rise to birefringence. The intensity can be represented as a function of χ, and it is proportional to $\sin^2(2\chi)$. SmA has a higher intensity than N, because of increased orientational order. Unfortunately, it was not possible to record a χ scan of SmB, because it is not as easy to identify as the N phase, which can be distinguished quickly by visual inspection (for synchrotron experiments, beam time is limited and efficiency is a crucial factor). Furthermore, as the SmB phase exists only over a temperature interval of 3 °C, the discrepancy between the XBI set-up temperature and the real temperature inside the sample also causes less reliability, thus, we cannot rely on the set target temperature to identify the phase as SmB. For the final crystalline phase, carrying out the intensity analysis in depth is not meaningful, as the whole sample does not crystallize as one single crystal, but instead, several crystalline domains are generated and each domain has its own orientation. Thus, the observed XBI behaviour of the Cr phase fluctuates between experiments and between different regions of the sample in a given experiment.

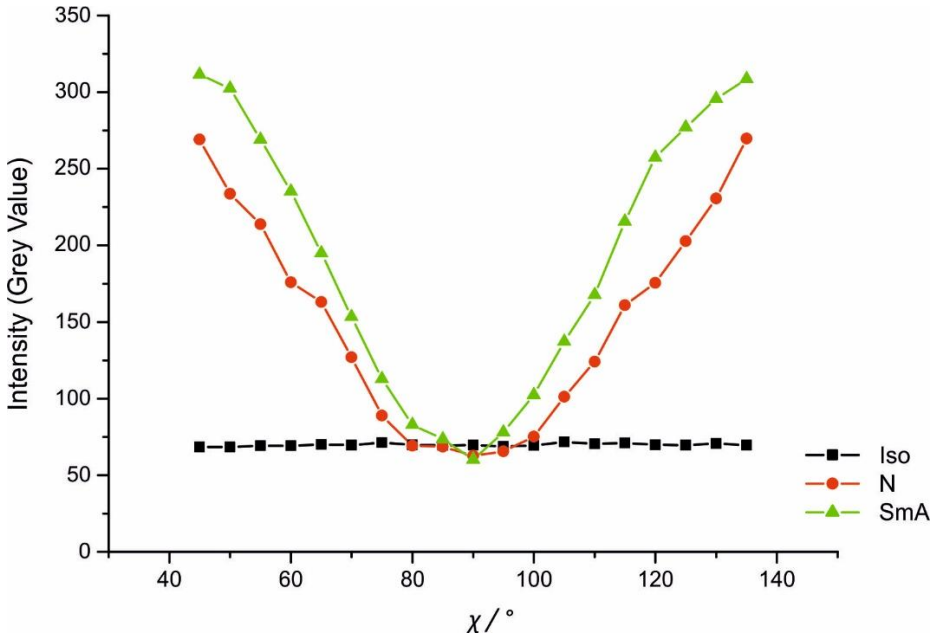

Figure 3.9 *Intensity of XBI images for the Iso, N and SmA phases as a function of χ, which is varied from 45° to 135° with an increment of 5°.*

At $\chi = 90°$, in both the theoretical predictions and experimental data, the intensities of birefringence images are always very low. It is, therefore, hard to distinguish different phases for this sample orientation. An alternative way to investigate XBI images is to fix the sample orientation at $\chi = 45°$ and to carry out a temperature scan, as the biggest contrast in intensity between the different phases arise at $\chi = 45°$.

Figure 3.10 shows the experiment of cooling from the Iso phase to the Cr phase at two different rates with sample orientation fixed at $\chi = 45°$. At the highest temperature, the intensity is very low, corresponding to the orientationally disordered molecules moving randomly inside the capillary in the Iso phase. With decreasing temperature, the Iso phase transforms to the N phase. The temperature range of the N phase is very small, from 215 °C to 216 °C. As the transformation is from a disordered phase to a more orientationally ordered phase, the intensity changes substantially and is reflected as a steep rise in the plot of intensity versus temperature (the left part of each plot). As in DSC (see 2.3), a slower cooling process can give better temperature resolution and accuracy in this type of temperature-scanning XBI experiments. Under the cooling condition of 1 °C/min, there is a small shoulder around the middle of the initial steep slope (Fig. 3.10.a), which represents the N phase. The lifetime of this feature representing the N phase is short, and the change in the plot is small, so this phenomenon is not resolved at the cooling rate of 10 °C/min.

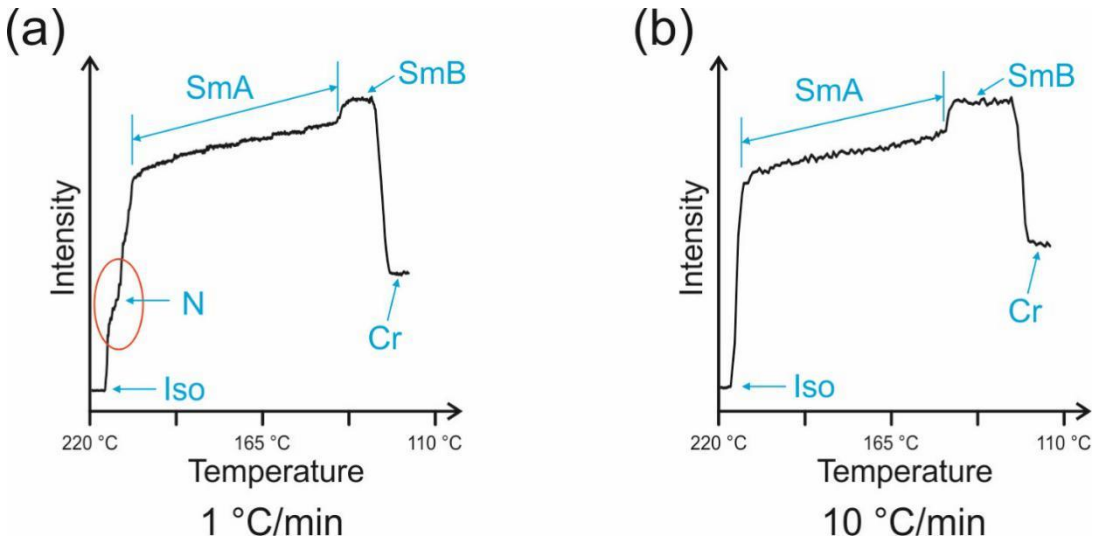

Figure 3.10 *Intensity of XBI images, recorded during the cooling process from the Iso phase to the Cr phase: (a) slow cooling rate at 1 °C/min and (b) fast cooling rate at 10 °C/min. The red circle in (a) highlights the N phase.*

After the steep slope at high temperature, the plot reaches a long plateau of SmA and the intensity gradually increases (caused by the increased orientational order of molecules) as temperature decreases, until reaching another small slope (the short slope before the highest plateau of each plot) representing the phase transition from SmA to SmB, which corresponds to highest intensity. The temperature range of SmB at 1 °C/min is shorter than at 10 °C/min, fully consistent with the DSC data in Fig. 3.7 (Page 46). After the SmB phase, the intensity drops significantly due to the formation of the Cr phase, which exists in multiple orientational domains.

Figure 3.11 shows selected images from Fig. 3.10.a. No.1 is the image of the Iso phase, with a uniform dark sample region representing isotropic orientational disorder. No.2 shows co-existence of both Iso phase (dark) and N phase (bright), meaning that the molecules began to align along the direction of the magnetic field in part of the sample (The co-existence of the Iso and N phases reflects the temperature gradient across the sample). No.3 – No.5 display the intermediate stage from the N phase to the SmA phase, with an increase of intensity. No.6 – No.8 are the images on the plateau of SmA, and the intensity increases gradually as temperature decreases, identifying that the molecules progress continually into a greater degree of orientational ordering. No.9 and No.10 are the SmB phase, which have the highest intensity. No.11 shows the irregular domains

appearing, which corresponds to crystalline phase generation. No.12 is the image of crystalline solid.

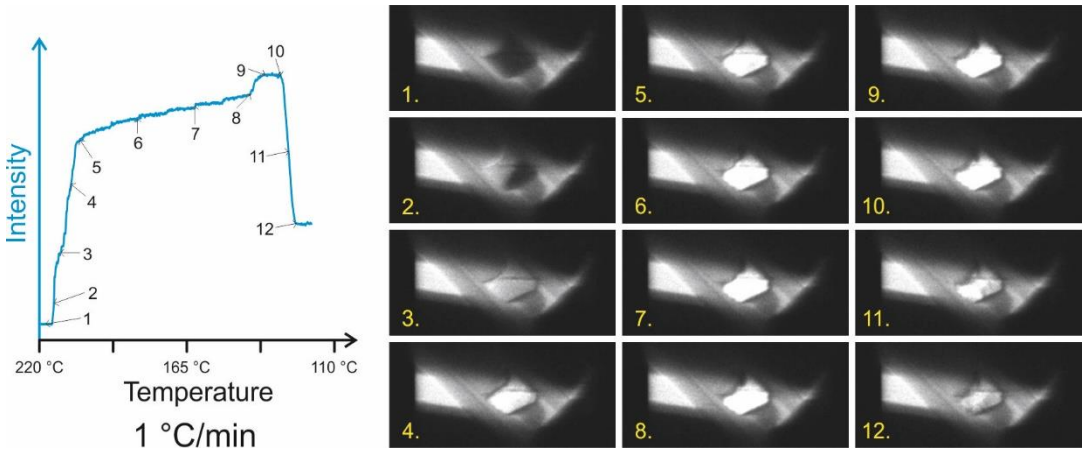

Figure 3.11 *Selected XBI images of LC_1 in the cooling process in Fig. 3.10.a. The 12 images (right) are selected from different stages in the cooling process, and their corresponding positions in the temperature-intensity plot are labelled (left).*

The above experiments show that XBI can provide information of the degree of molecular orientational order in different phases of liquid crystals. Especially with slow rates of temperature change, each phase transition can be observed clearly.

3.3 Order Parameter of Liquid Crystal

Two more liquid crystals are being investigated using XBI and they are labelled as LC_2 and LC_3. The molecular structures and the temperatures of phase transitions are shown in Fig. 3.12 and Fig. 3.13. Compared to LC_1, the molecular structure of LC_2 is quite similar with reversal of the ester group. This indicates that the molecular length of LC_1 and LC_2 are nearly the same. LC_3 is shorter than LC_1 and LC_2. In all cases, the bromine substituent has been selected such that the C–Br bond direction effectively "reports" on the molecular orientation in the orientationally ordered phases.

In 3.2, it has been proved that monitoring the intensity of the XBI images with the sample fixed at $\chi = 45°$ is an effective way to analyse the orientational order of molecules. LC_2 and LC_3 have been tested in the same way: fixing $\chi = 45°$ and decreasing temperature from the Iso phase to the Cr phase. The results of intensity as a function of temperature are shown in Fig. 3.14. At the highest temperature, all molecules are in the isotropic phase

and there is isotropic orientational disorder, resulting in low intensity. With decrease of temperature, orientational order is increased, which is represented by the increase of intensity. The highest intensity arises for the SmB phase.

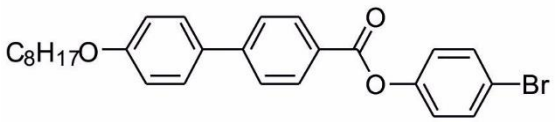

$$LC_2 : Cr \bullet 132 \bullet SmB \bullet 133 \bullet SmA \bullet 231 \bullet Iso$$

Figure 3.12 *Molecular structure of LC_2 which has the typical banana-shape of liquid crystal forming molecules. The transition temperatures are labeled below in units of °C. LC_2 has a similar structure to LC_1.*

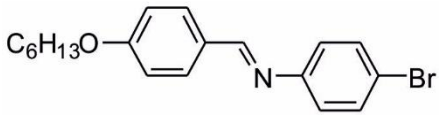

$$LC_3 : Cr \bullet 72 \bullet SmB \bullet 100 \bullet SmA \bullet 103 \bullet Iso$$

Figure 3.13 *Molecular structure of LC_3 which has the typical banana-shape of liquid crystal forming molecules. The transition temperatures are labeled below in units of °C.*

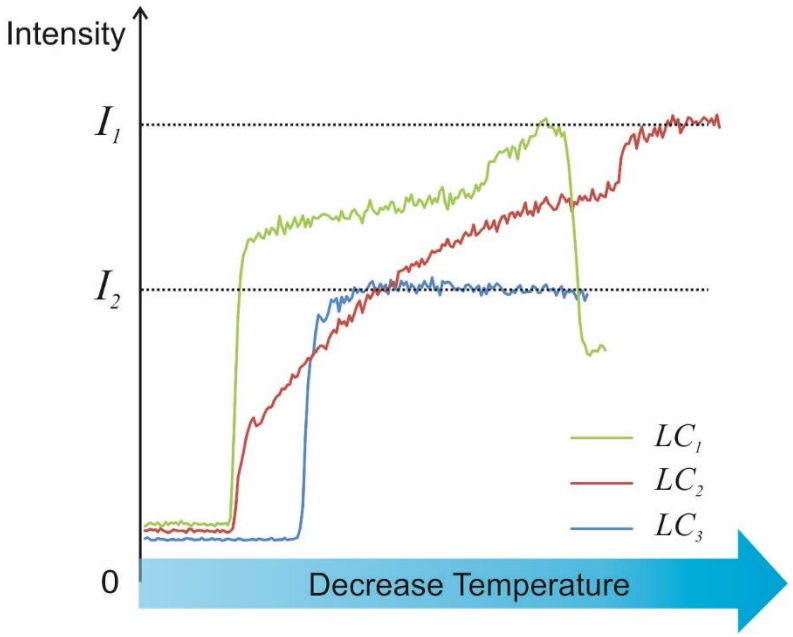

Figure 3.14 *Intensity of XBI images for LC_1 (green), LC_2 (red) and LC_3 (blue) as a function of temperature in the cooling process from the Iso phase to the Cr phase.*

Focusing on the highest value of intensity, LC_1 and LC_2 have a similar level, while the highest intensity for LC_3 is lower than for LC_1 and LC_2. This phenomenon shows that even though all liquid crystals are in the same phase (SmB), the degree of orientational order of the molecules depends on the molecular length and molecular structure.

In a magnetic field, the preferred orientation of a liquid crystal is always along the direction of the magnetic field. It is like there are lots of imaginary "tunnels" in the magnetic field and all the molecules are confined in these tunnels. The width of the imaginary tunnels should depend on the strength of the magnetic field, with a stronger field giving rise to narrower tunnels. It is reasonable to expect that longer molecules have less orientational freedom when packed into a tunnel of a given width. For the same magnetic field (in this thesis, the magnetic field is fixed), the width of the imaginary tunnels has a fixed value (d). The molecules of LC_1 and LC_2 have a similar length (denoted l_1), and the molecular length of LC_3 is denoted l_2. Figure 3.15 shows how the molecules are packed in a tunnel. The distribution of molecular orientations may be simplified by regarding the molecules in the liquid crystal to be confined within a range of θ values from $-\theta_{max}$ to $+\theta_{max}$, and thus all the molecular orientations are located within a cone-shaped object with semi-angle equal to θ_{max}. As l_1 is bigger than l_2, the shorter LC_3 molecules are expected to have more orientational variability, which is manifested as a wider range of angles between the long-axis of the molecule and the preferred direction, i.e., $\theta_{max1} < \theta_{max2}$.

For order parameter (S) of the liquid crystal, the statistical average of $\cos^2\theta$ is represented as Eq.3.2 (Page 56), which can be calculated through a sphere model in Fig. 3.16 (Page 56). Then, the order parameter (S) can be expressed as a function of θ_{max} (Eq. 3.3, Page 56). From Eq. 3.3 (Page 56), we can conclude that, in the range of $\theta_{max} \in [0°, 90°]$, a smaller value of θ_{max} corresponds to a higher value of S. For the specific values of $\theta_{max} = 0°$ and $\theta_{max} = 90°$, the values of S are $S = 1$ and $S = 0$, respectively, corresponding to situations with perfect orientational order (S =1) and an isotropic orientational distribution ($S = 0$), as mentioned in 3.1.

At $\chi = 45°$ in the XBI experiment, the angle between the preferred direction (the magnetic field direction) and the horizontal plane (the direction of polarization of the incident X-ray beam) is 45°, and the orientation of the preferred direction is denoted as ($\theta = 45°$, $\varphi = 0°$), referring to Fig. 2.4 (Page 31). As the molecules in the liquid crystal

are oriented within the range of $\pm\theta_{max}$ from the preferred direction, and as the average direction of all the molecules is along the preferred direction, it follows that at χ = 45°, the orientations of all the molecules are in the range of $\theta \in [45° + \theta_{max}, 45° - \theta_{max}]$ and $\varphi \in [-\theta_{max}, +\theta_{max}]$. The range of molecular orientations thus form a circle projection on the *θφ-plane* of the theoretical intensity plot in Fig. 2.6 (Page 33). The radius of the circular projection depends on the value of θ_{max} and the centre of the circle is fixed at (θ = 45°, φ = 0°).

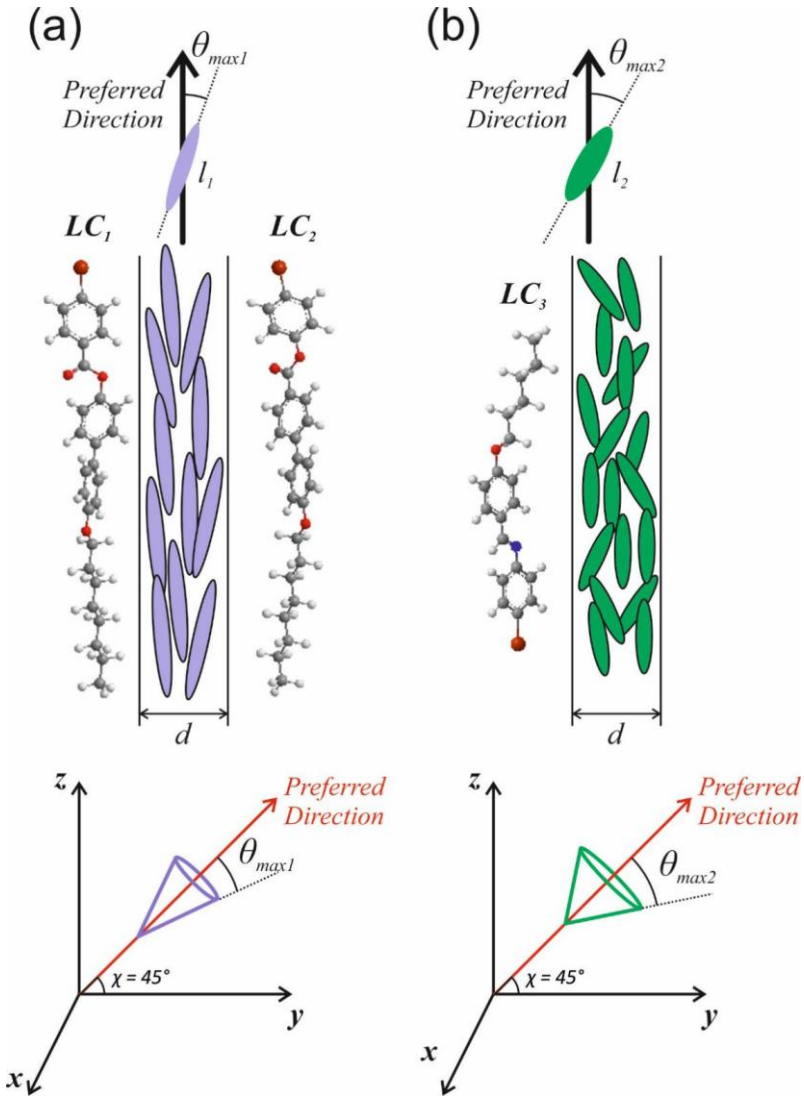

Figure 3.15 *Schematic illustration of molecules of LC_1, LC_2 and LC_3 in a magnetic field: (a) LC_1 and LC_2 have longer molecular length (l_1) and a smaller angular deviation (θ_{max1}); and (b) LC3 has shorter molecular length (l_2) and a larger angular deviation (θ_{max2}). The cone-shaped objects show (schematically) the spatial distribution of the molecular orientations relative to the magnetic field direction (which is also the preferred direction) at χ = 45° in the XBI experiments.*

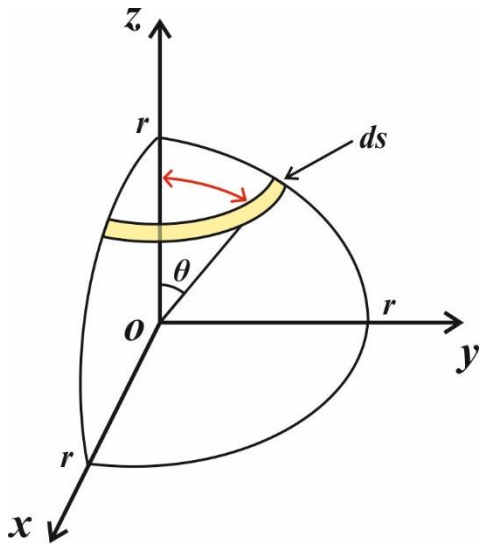

Figure 3.16 *Schematic illustration of the orientational distribution of liquid crystal molecules (red arrows) in spherical polar coordinates (with radius r). The preferred direction is along the z-axis. The angle between the molecule long-axis and the preferred direction is θ. The integral slice is denoted ds, which is a small area as shown on the sphere (yellow).*

$$\left\langle \cos^2\theta \right\rangle = \frac{\int \cos^2\theta \, ds}{\int ds}, \quad ds = \frac{\pi}{2}\cdot r\cdot\sin\theta\cdot r\cdot d\theta$$

$$= \frac{\int_0^{\theta_{\max}} \cos^2\theta\cdot\frac{\pi}{2}\cdot r^2\cdot\sin\theta\cdot d\theta}{\int_0^{\theta_{\max}} \frac{\pi}{2}\cdot r^2\cdot\sin\theta\cdot d\theta}$$

$$= \frac{-\frac{1}{6}\cdot\pi\cdot r^2\cdot\cos^3\theta\Big|_0^{\theta_{\max}}}{-\frac{1}{2}\cdot\pi\cdot r^2\cdot\cos^2\theta\Big|_0^{\theta_{\max}}} \qquad (3.2)$$

$$= \frac{\frac{1}{6}\cdot\pi\cdot r^2 - \frac{1}{6}\cdot\pi\cdot r^2\cdot\cos^3\theta_{\max}}{\frac{1}{2}\cdot\pi\cdot r^2 - \frac{1}{2}\cdot\pi\cdot r^2\cdot\cos\theta_{\max}}$$

$$= \frac{1-\cos^3\theta_{\max}}{3\left(1-\cos\theta_{\max}\right)}$$

$$= \frac{1}{3}\left(\cos^2\theta_{\max} + \cos\theta_{\max} + 1\right)$$

$$S = \frac{3\left\langle \cos^2\theta \right\rangle - 1}{2} = \frac{\cos^2\theta_{\max} + \cos\theta_{\max}}{2} \qquad (3.3)$$

The intensity measured is the average intensity for all the molecules, and the mathematical representation is given in Eq. 3.4. The total number of molecules in the liquid crystal is denoted *N*, with each molecule labelled *i*. According to the equation for the relative XBI intensity introduced in 2.1 (Eq. 2.7, Page 32), the XBI intensity is proportional to a function of θ and φ denoted $f(\theta,\varphi)$ (Eq. 3.5). Thus, Eq. 3.4 can be represented by Eq. 3.6. The XBI intensity of liquid crystals with two different values of θ_{max} is illustrated in Fig. 3.17, and the average intensity in these two cases are represented by Eq. 3.7 and Eq. 3.8 respectively. According to Eq. 3.6, the integral regions in each case are D_1 and D_2, with the total number of molecules given by N_1 and N_2. As region D_2 is composed of region D_1 plus region *S*, Eq. 3.8 can be represented by Eq. 3.9. The region between the two circles is denoted region *S*, and the total number of molecules in this region is N_s. For brevity, the double integral parts are denoted *p* and *q*, as shown in Eq. 3.10, and the values of *p*, *q*, N_1 and N_2 are positive according to their definitions. Thus, the average intensity in each of these two cases are represented by Eq. 3.11 and Eq. 3.12, respectively.

$$\bar{I} = \frac{\sum_{i=1}^{N} I_{3D}}{N} \tag{3.4}$$

$$f(\theta,\varphi) = \sin^2(2\theta)\cdot\sqrt{\frac{1+\tan^2\theta}{1+\tan^2\theta+\tan^2\varphi}} \tag{3.5}$$

$$\bar{I} = \frac{\sum_{i=1}^{N} I_{3D}}{N} = \frac{I_0\cdot K\cdot\iint f(\theta,\varphi)d\theta d\varphi}{N} \tag{3.6}$$

$$\overline{I_1} = \frac{I_0\cdot K\cdot\iint_{D_1} f(\theta,\varphi)d\theta d\varphi}{N_1} \tag{3.7}$$

$$\overline{I_2} = \frac{I_0\cdot K\cdot\iint_{D_2} f(\theta,\varphi)d\theta d\varphi}{N_2} \tag{3.8}$$

$$\overline{I_2} = \frac{I_0 \cdot K \cdot \iint\limits_{D_2} f(\theta,\varphi)\,d\theta d\varphi}{N_2} = \frac{I_0 \cdot K \cdot \iint\limits_{D_1} f(\theta,\varphi)\,d\theta d\varphi + I_0 \cdot K \cdot \iint\limits_{S} f(\theta,\varphi)\,d\theta d\varphi}{N_1 + N_s} \tag{3.9}$$

$$N_1 > 0, \quad N_s > 0$$
$$p = I_0 \cdot K \cdot \iint\limits_{D_1} f(\theta,\varphi)\,d\theta d\varphi > 0 \tag{3.10}$$
$$q = I_0 \cdot K \cdot \iint\limits_{S} f(\theta,\varphi)\,d\theta d\varphi > 0$$

$$\overline{I_1} = \frac{p}{N_1} \tag{3.11}$$

$$\overline{I_2} = \frac{p+q}{N_1 + N_s} \tag{3.12}$$

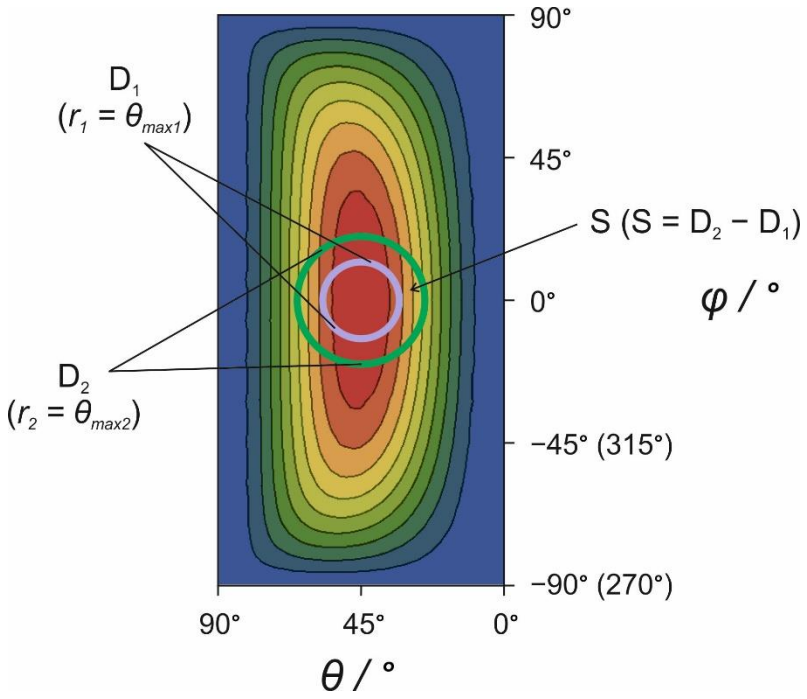

Figure 3.17 *Theoretical XBI intensity plot (calculated from Eq. 2.7, Page 32) for the orientational distributions of liquid crystals with two different values of θ_{max}. The projection of their orientation distributions are represented by two circles (region D_1 and region D_2, as shown in purple and green respectively) on the $\theta\varphi$-plane. The region between the two circles is denoted S. The centre of each circle is fixed at (θ = 45°, φ = 0°). The "angular radii" of the circles are θ_{max1} (for D_1) and θ_{max2} (for D_2), respectively.*

According to Eq. 2.7 (Page 32), the highest intensity in the region defined by $\theta \in [0°, 90°]$ and $\varphi \in [90°, -90°]$ arises at the orientation corresponding to ($\theta = 45°$, $\varphi = 0°$) – i.e., along the preferred direction – and the intensity decreases as the molecular orientation deviates from the preferred direction. As a consequence, the average intensity for the molecules in region D_1 is always higher than the average intensity for the molecules in region S (Eq. 3.13 and Eq. 3.14). Comparing the average intensity of regions D_1 and D_2 (Eq. 3.15), a mathematical relationship (see Eq. 3.16) can be derived to demonstrate that, for liquid crystals, a higher intensity in the XBI measurement corresponds to a smaller range of the orientational distribution, as specified by θ_{max}. As already discussed, a smaller value of θ_{max} corresponds to a higher value of the order parameter (S) (Eq. 3.3, Page 56), and we reach the conclusion that the value of the order parameter (S) for liquid crystal samples can be evaluated, at least qualitatively, from XBI intensity measurements. Thus, higher XBI intensity corresponds to a higher value of the order parameter (S).

$$\frac{p}{N_1} > \frac{q}{N_s} \tag{3.13}$$

$$pN_s > qN_1 \tag{3.14}$$

$$\begin{aligned} \overline{I_1} - \overline{I_2} &= \frac{p}{N_1} - \frac{p+q}{N_1+N_s} \\ &= \frac{pN_1 + pN_s - pN_1 - qN_1}{N_1(N_1+N_s)} \\ &= \frac{pN_s - qN_1}{N_1(N_1+N_s)} > 0 \end{aligned} \tag{3.15}$$

$$\overline{I_1} > \overline{I_2} \tag{3.16}$$

3.4 Conclusions

As liquid crystal phases are not solid and because of the fluidity of the samples, the basic XBI set-up required to be amended to allow liquid samples to be studied. Because it is based on synchrotron radiation, there is much more flexibility and space to modify the accessory parts to fulfil individual types of experiments. The experiments discussed in this chapter have proved that XBI can identify the molecular orientational

properties of liquid crystals, and the corresponding new set-up for liquid samples with temperature control system has also been developed and applied successfully.

For study of liquid crystal samples, the capability of XBI in the following three aspects has been demonstrated: (1) indicating the preferred orientation in each phase; (2) monitoring the real-time process of changing orientational ordering during phase transitions; (3) estimating the order parameter (*S*) of different liquid crystals.

Although POM is now used extensively in characterization of liquid crystals,[58-60] XBI has two obvious advantages compared to POM. Firstly, POM reflects the overall optical properties of the whole sample, while XBI only detects the orientation of the C–Br bonds; for this reason, XBI is more accurate and has a higher sensitivity to identify the orientations of the target molecules. For example, if there are two liquid crystals, both molecules are in a banana-shape and have one C–Br bond at the end, when we consider the whole optical properties in POM, the different curvatures of the banana-shape will have an influence on the overall birefringence. In XBI, however, the situation becomes easier as we only need to consider the C–Br bond orientations. Secondly, XBI is more user-friendly to customize the set-up to suit a particular experiment. In POM, because of the need of optical focus, the sample should be thin and flat. In XBI, however, due to the use of X-rays, there is no need to worry about the optical focus and the shape of the sample is less restricted. A further consideration with regard to optical focus is that the space between the focal plane (sample position) and the front of the lens is fixed in POM, and the space is usually very small (several centimetres, which depends on the magnification). For XBI, on the other hand, the set-up is in a synchrotron hutch, so there is substantially more space (several meters) to add accessories (e.g., temperature control system).

In summary, for research of liquid crystals, XBI is successful to provide the same types of information as POM, but in many aspects XBI performs better.

Chapter 4

X-ray Birefringence Imaging on Bending Crystals

4.1 Introduction

From the traditional view, crystals are solid-state materials with well-ordered arrangements of molecules and they are usually hard and rigid, e.g., table salt, snowflakes and quartz. This phenomenon is understandable if we concentrate on the definition of crystals – a crystal consists of atoms arranged in a pattern that repeats periodically in three dimensions.[34] As a crystal needs to keep such high order at the molecular-level, when some outside mechanical stress is applied, it will disrupt the connections between adjacent molecules or atoms. For example, a crystal of table salt can be broken into two parts because the ionic bonds inside it become broken if an appropriate mechanical stress is applied.

Chemical bonds can be classified into two types, strong bonds and weak bonds,[61] with the above ionic bonds belonging to strong bonds, that is why the breaking of bonds is usually associated with the fracture of the whole crystal. However, if weak bonds between molecules are changed only slightly by application of mechanical stress, some crystals can still retain their macroscopic integrity. The C. Malla Reddy group has found several bending crystals recently and analysed the formation mechanism at the molecular-level.[62-64] Crystals can be bent via the exchange or modulation of weak intermolecular interactions, such as van der Waals (vdW), π-stacking, hydrogen bonding, halogen bonding, and so on.

Furthermore, organic bending crystals can be classified into those that undergo plastic bending and elastic bending.[65, 66] In plastic bending crystals, the existence of slip planes in the crystals is a prerequisite and the strong and weak interactions exist in nearly perpendicular directions, which determines the bending face of the crystal. However, in elastic bending crystals, it is not an essential condition to have slip planes and the crystal can have more than one bending face. Figure 4.1 shows a good example of a material that forms plastic bending crystals – hexachlorobenzene.[67] In the crystal structure of hexachlorobenzene, the bending face is (001). When pressure is applied on the bending

face, sliding layers can be formed by the breaking and reformation of intermolecular Cl···Cl interactions, while it is not possible to bend the (100) face as stronger π···π interactions dominate the packing.[68]

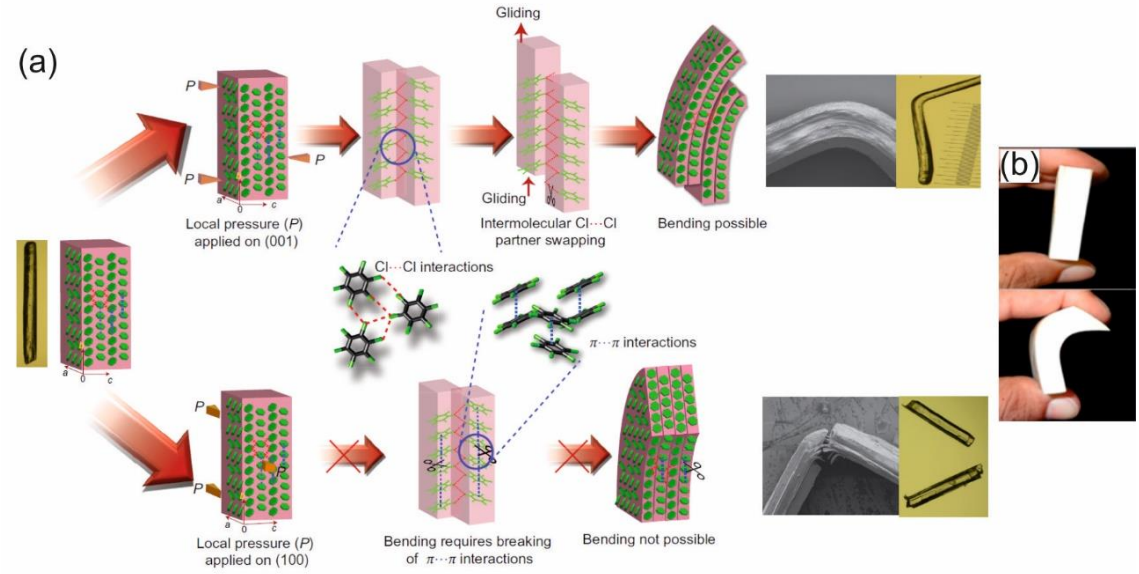

Figure 4.1 *Schematic representation of plastic bending of single crystals of hexachlorobenzene. (a) Top row: a three-point geometry pressure on the (001) face. The layers glide by weakening the Cl···Cl interactions, so bending is possible. Bottom row: the same three-point geometry pressure on the (100) face. Bending requires breaking of π···π interactions and this process is not possible. (b) An analogy of the bending process illustrated by a sticky notes pad. Bending is feasible due to the separation and slip of layers. Each piece of paper is a layer in the bending process, so it can be bent on the direction shown in (b) but can't be bent on the other direction. Reprinted with permission from (1) Panda, M. K.; Ghosh, S.; Yasuda, N.; Moriwaki, T.; Mukherjee, G. D.; Reddy, C. M.; Naumov, P., Spatially Resolved Analysis of Short-Range Structure Perturbations in a Plastically Bent Molecular Crystal. Nat. Chem.* ***2014****, 7, 65-72 (Copyright 2014 Springer Nature); and (2) Krishna, G. R.; Devarapalli, R.; Lal, G.; Reddy, C. M., Mechanically Flexible Organic Crystals Achieved by Introducing Weak Interactions in Structure: Supramolecular Shape Synthons. J. Am. Chem. Soc.* ***2016****, 138, 13561-13567 (Copyright 2016 American Chemical Society).*

From the previous chapters, XBI has proven to be an effective technique in investigating molecular orientations in materials. During the crystal bending process, small domains with slightly different lattice orientations may be generated. Thus, it is

natural to explore the opportunity to apply the XBI to understand the molecular orientations in this kind of novel crystals – organic bending crystals. This chapter will focus on XBI studies of brominated organic materials that undergo crystal bending – focusing on 1,4-dibromo-2,3,5,6-tetramethylbenzene (DBTMB) and 9,10-Dibromoanthracene (DBA).

4.2 Crystal of 1,4-Dibromo-2,3,5,6-tetramethylbenzene

4.2.1 Structural Properties and Phase Transition

Crystals of 1,4-dibromo-2,3,5,6-tetramethylbenzene (DBTMB) (Fig. 4.2) are transparent, long needle-shaped crystals, with rectangular cross-section. DBTMB crystals can be made by a slow-evaporation method from methanol solvent. The size of crystals can be controlled by changing evaporation rate and temperature of crystallization.

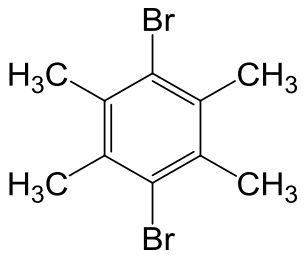

Figure 4.2 *Molecular structure of 1,4-dibromo-2,3,5,6-tetramethylbenzene*

DSC analysis was applied to crystals of DBTMB to investigate their thermal properties (Fig. 4.3) from room temperature to −150 °C. An exothermic peak around −120 °C shows there is a phase transition at low temperature. The corresponding endothermic peak on heating shows that this solid-solid phase transition is reversible. Thus, it is clear there are two solid phases when temperature is changed. In the structure determination process by single-crystal XRD, a room temperature (RT, *ca.* 296 K) study and a lower temperature (LT, 150 K) study were carried out respectively.

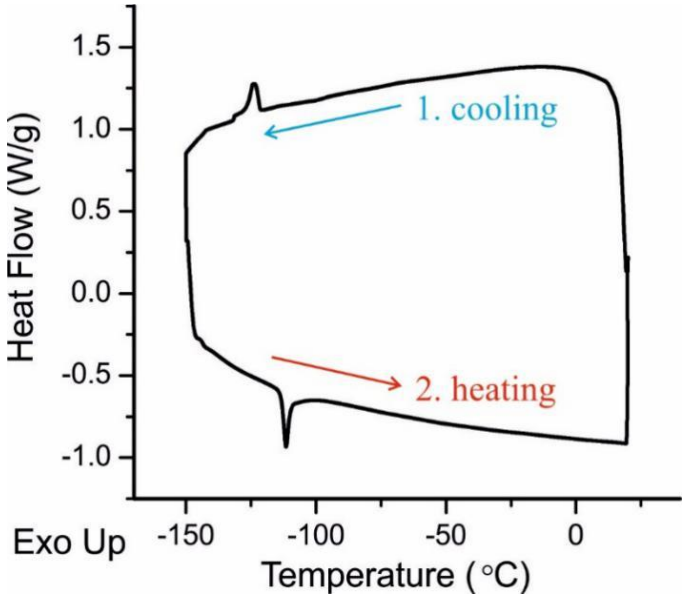

Figure 4.3 *DSC data for DBTMB. Crystals of DBTMB were placed at room temperature, then firstly cooled down to −150 °C and secondly, heated back to room temperature. Both of the rates are 10 °C/min. The phase transitions happen at −121 °C and −113 °C respectively.*

The summaries of the crystal structure (RT and LT) are shown in Table 4.1 (see also Appendix I and Appendix II). Both of them are monoclinic crystals but with different unit cell parameters, which means the structure distorts slightly from RT to LT. The density at RT is lower than at LT because of thermal expansion.

Table 4.1 *Comparison of the crystal structures of the RT and LT phases*

		RT Phase	LT Phase
Formula Sum		$C_{10}H_{12}Br_2$	
Formula Weight		292.02 g/mol	
Crystal System		monoclinic	
Space Group		$P2_1/c$	
Cell Parameters	*a*	8.358 Å	16.556 Å
	b	4.009 Å	11.827 Å
	c	15.404 Å	17.185 Å
	β	91.37°	117.24°

Cell Volume	515.93 Å^3	2991.76 Å^3
Z	2	12
Calculated Density	1.88 g/cm^3	1.94 g/cm^3

Figure 4.4 and Figure 4.5 show the crystal structures of DBTMB in the RT and LT phases. The molecules are not "frozen" in the lattices, instead, in each molecule, methyl groups and bromine atoms undergo exchange, and this phenomenon is represented as different occupancies, which show the probability of a methyl group or a bromine atom occupying a certain substituent position in the crystal structure. So, in the crystal structures shown in Fig. 4.4 and Fig. 4.5, there are fractional occupancies of both a methyl group and a bromine atom on each site. In these two structures, the molecules are packed along the *b-axis* through π-stacking, and the benzene planes are nearly in the *ac-plane*. In crystals prepared by the evaporation method mentioned before, the long-axis of a single crystal is also the *b-axis*.

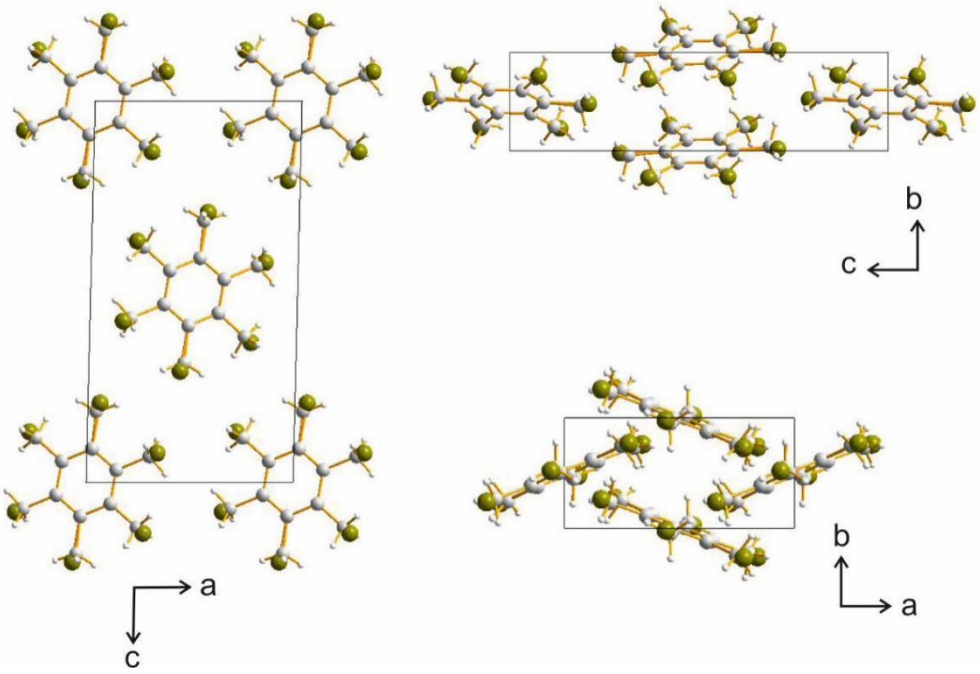

Figure 4.4 *Crystal structure of DBTMB in the RT phase, viewed along different axes.*

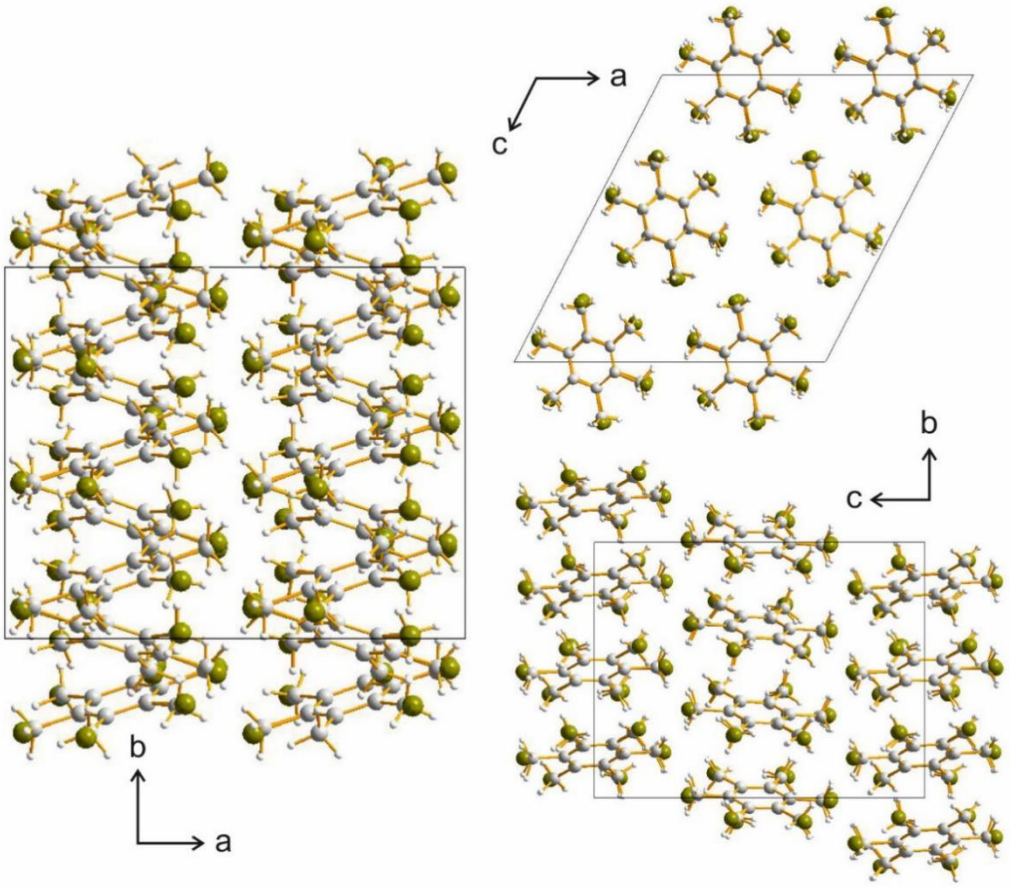

Figure 4.5 *Crystal structure of DBTMB at in the LT phase, viewed along different axes.*

4.2.2 X-ray Birefringence Imaging Studies of 1,4-dibromo-2,3,5,6-tetramethylbenzene

1,4-dibromo-2,3,5,6-tetramethylbenzene (DBTMB) crystals are long needle-shaped crystals, with a rectangular cross-section. In 1.1.3, it is explained in detail how the thickness of a crystal affects the final intensity in birefringence. In order to ensure that the whole crystal has uniform thickness in the XBI studies, we should be careful when we mount the samples. Figure 4.6 shows four examples of mounting strategies. In (a) and (c), the edges of the crystal will be included in the final XBI images, making it hard to distinguish which part has uniform thickness. In (b) and (d), on the other hand, the big face of the single crystal is perpendicular to or parallel to the propagation direction of the incident X-rays, so the images captured on the detector will be uniform, which is convenient for data analysis. In this thesis, DBTMB single crystals are placed in either

mode (b) or (d), which can be achieved by changing the φ value during the sample position adjustment process before XBI measurements.

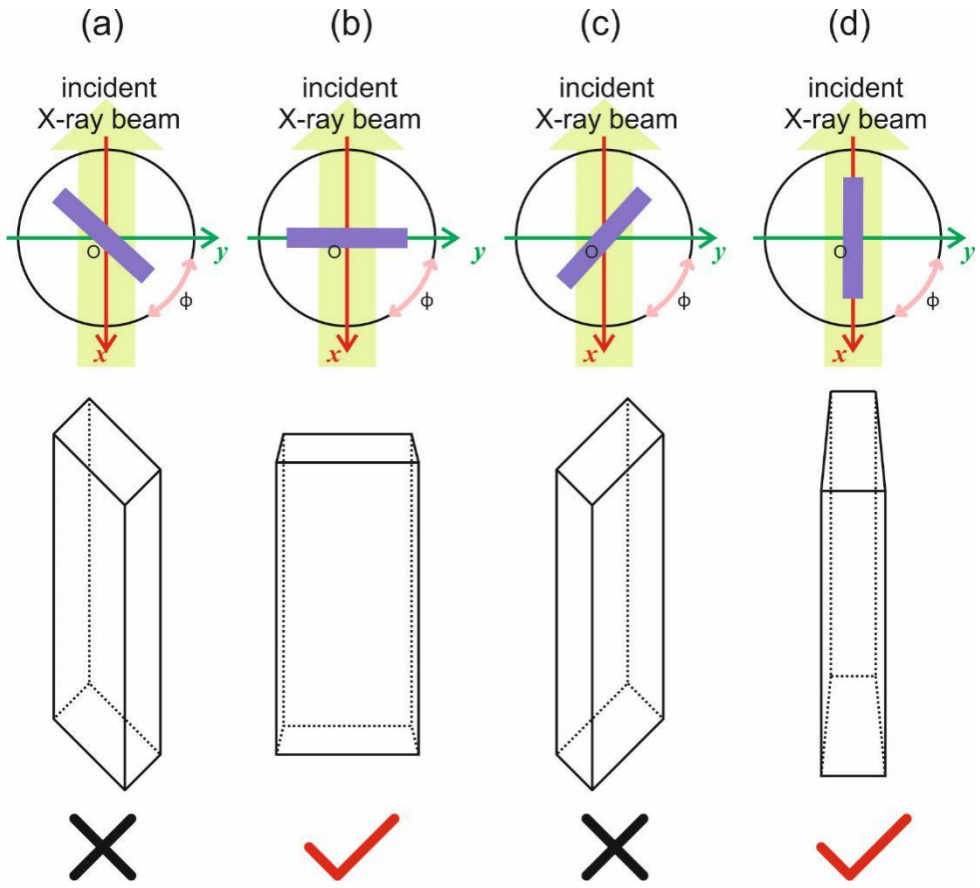

Figure 4.6 *Schematic illustration of DBTMB single crystal mounted in XBI. Only the big face perpendicular [shown in (b)] or parallel [shown in (d)] to the propagation direction of the incident X-rays are suitable.*

Figure 4.7 (Page 69) shows the projection of the DBTMB crystal structure on the *ac-plane* for both the RT and LT phases. In this case, the big face is perpendicular to the propagation direction of the incident X-rays (orange arrow). Face indexing was carried out by single-crystal XRD, and the big face in the RT phase crystal is assigned as (-1 0 1) while in the LT phase it is assigned as (1 0 0). The blue, green and red polygons are three examples of cross-sections of the shape of DBTMB crystals. Even though most of the crystals show needle-shaped crystals with a rectangular cross-section, in practice, we found that it is difficult to index the small face as it is too small for single-crystal XRD. However, we are sure of the identification and assignment of the big face, and the small face can take a range of shapes between the pair of big faces.

Compared with Fig. 4.4 (Page 65) and Fig. 4.5 (Page 66), lines between adjacent molecules in Fig. 4.7 are generated by showing H···Br interactions up to 2.88 Å. The fact that H···Br interactions up to 2.88 Å are observed only parallel to the big face gives evidence that DBTMB molecules are packed closer along the big face than the smaller face. Thus, in the crystal structures of DBTMB, molecular layers parallel with the big face are formed. This layered structure is quite similar to the hexachlorobenzene example in 4.1 (Fig. 4.1, Page 62). Referring to the model of a sticky notes pad (Fig. 4.1.b, Page 62), it is predicted that the bending face of the DBTMB crystal should be the big face.

The parameters of the red parallelogram in the RT and LT structures show the change of crystal structure at the phase transition. The distance between adjacent layers is d and the lengths of each side are l_1 and l_2. When the temperature is cooled to the LT phase, all the values of d and l_1 and l_2 become smaller, which is consistent with the increased density.

Figure 4.8 (Page 70) shows the crystal structure of one layer in both the RT and LT structures, viewed along the propagation direction of the incident X-rays. The long-axis of the crystal is the *b-axis*, and DBTMB molecules are stacked by π···π interactions to form column structures. The orientations of benzene planes in adjacent columns is mirror symmetric.

In order to calculate the theoretical values of relative transmitted intensity in XBI experiments by the method introduced in 2.1, the fractional coordinates need to be transformed into Cartesian coordinates. For a vector of a C–Br bond, its fractional coordinate representation (m, n, l) (Eq. 4.1, Page 70) can be derived directly from the crystal structure (see Appendix I and Appendix II), and the Cartesian coordinate representation (x, y, z) can be determined routinely by the transformation in Eq. 4.2 (Page 70). For mounting mode (b) in Fig. 4.6, it is easier to rotate the Cartesian system to make the coordinates parallel to the standard Cartesian system used in 2.1. Figure 4.9 (Page 71) shows the rotation process, and the rotation angle is ε. The new representation in the rotated Cartesian system is denoted (x', y', z') (Eq. 4.3, Page 70). Thus, the vector of (m, n, l) can be represented as (x', y', z'), and ε is determined by its crystal parameters (Eq. 4.5 and Eq. 4.6, Page 71). For the RT phase, ε is 62.578°, and for the LT phase, ε is −62.763°. The negative sign means the opposite rotation operation.

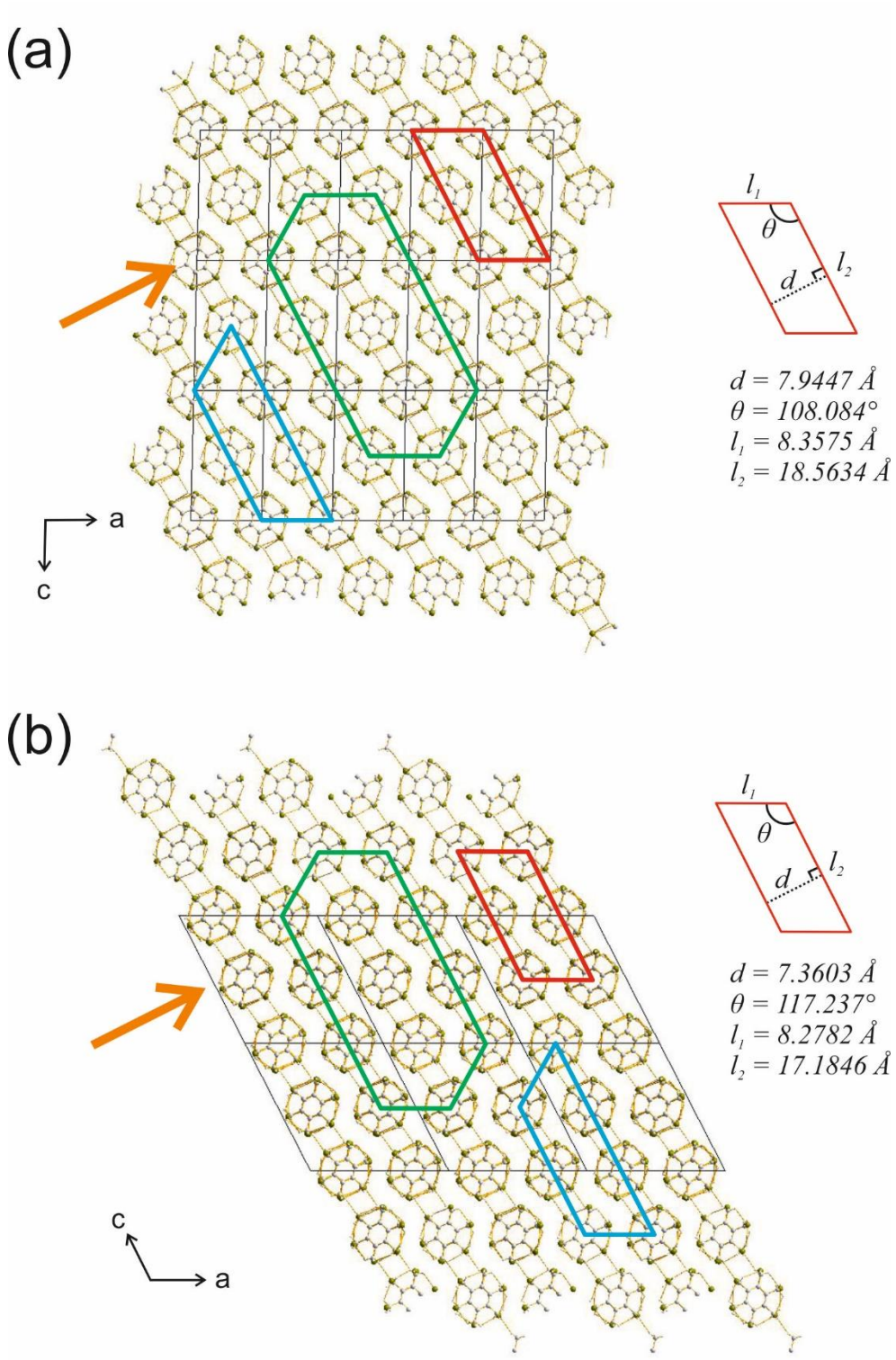

Figure 4.7 *Crystal structures of DBTMB viewed along the b-axis for (a) the RT phase, and (b) the LT phase. The orange arrow is the propagation direction of incident X-rays in the XBI experiment. Green, blue and red polygons are three examples of crystal cross-sections. The details of the red parallelogram are also shown in order to compare the slight change of crystal structures.*

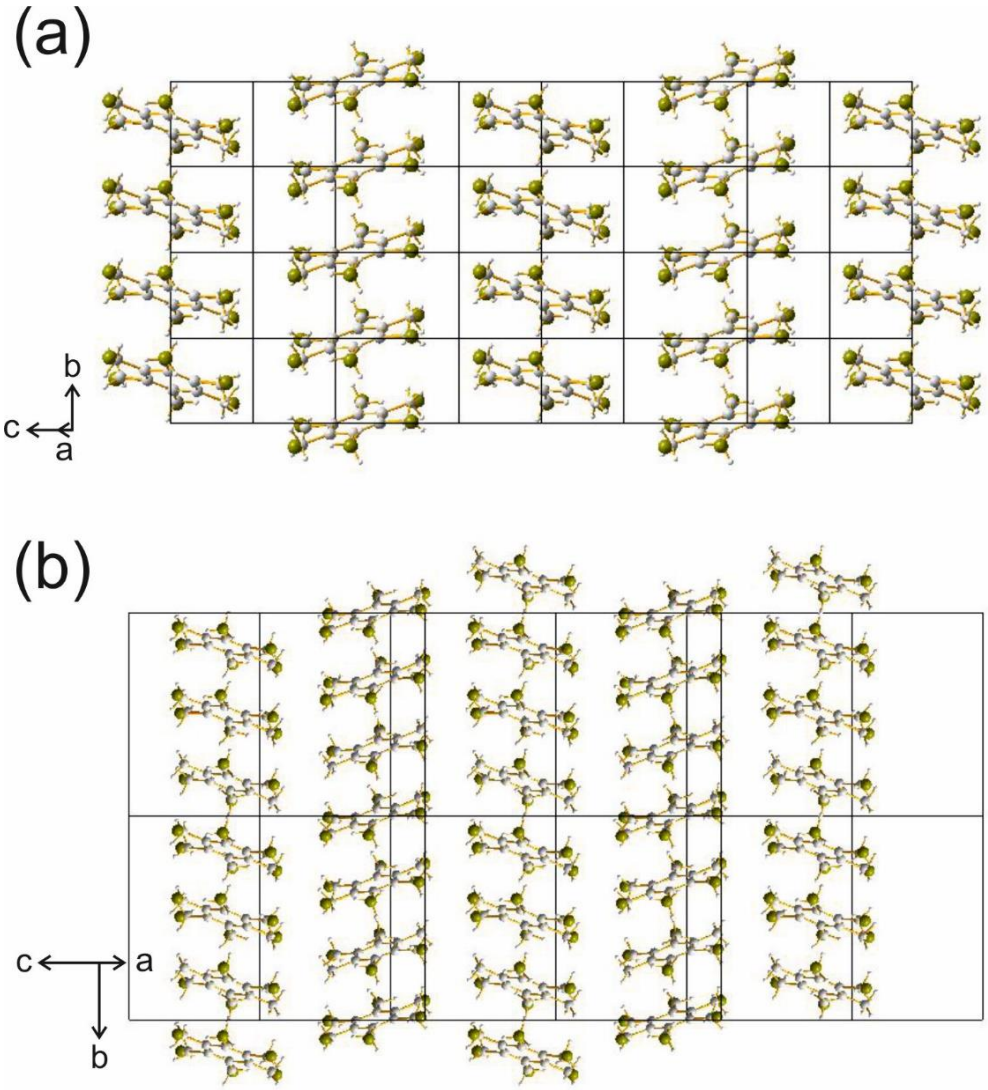

Figure 4.8 *Crystal structures of (a) the RT phase and (b) the LT phase showing one layer of DBTMB molecules viewed perpendicular to the layer plane.*

$$\overrightarrow{C \cdot Br} = (m, n, l) \tag{4.1}$$

$$\begin{bmatrix} x \\ y \\ z \end{bmatrix} = \begin{bmatrix} a & 0 & c \cdot \cos\beta \\ 0 & b & 0 \\ 0 & 0 & c \cdot \sin\beta \end{bmatrix} \cdot \begin{bmatrix} m \\ n \\ l \end{bmatrix} \tag{4.2}$$

$$\begin{bmatrix} x' \\ y' \\ z' \end{bmatrix} = \begin{bmatrix} \cos\varepsilon & 0 & \sin\varepsilon \\ 0 & 1 & 0 \\ -\sin\varepsilon & 0 & \cos\varepsilon \end{bmatrix} \cdot \begin{bmatrix} x \\ y \\ z \end{bmatrix} \tag{4.3}$$

$$\overrightarrow{C \cdot Br} = (x', y', z') \tag{4.4}$$

$$RT: \quad \frac{c}{\sin\varepsilon} = \frac{\sqrt{a^2 + c^2 - 2ac \cdot \cos(180° - \beta)}}{\sin(180° - \beta)} \tag{4.5}$$

$$LT: \quad \varepsilon = \beta - 180° \tag{4.6}$$

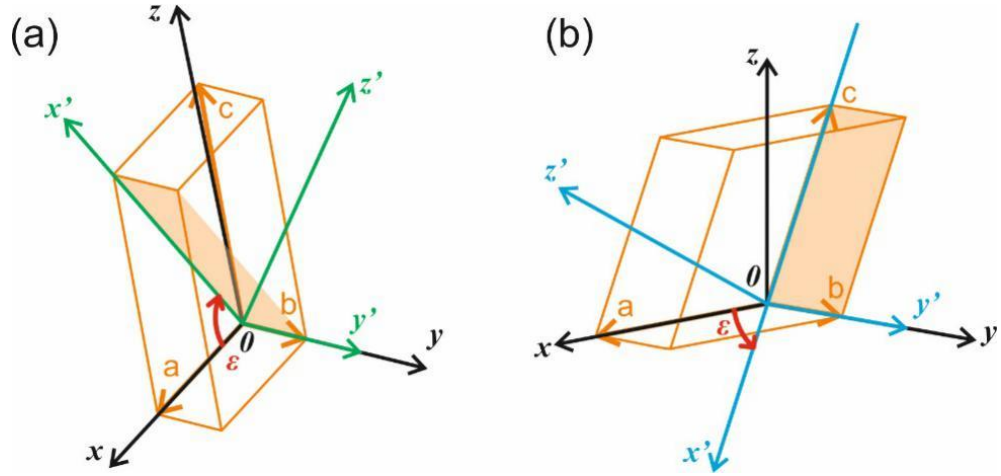

Figure 4.9 *Schematic illustration of rotation of Cartesian system, with the rotation angle denoted ε. Black is the Cartesian system before rotation (i.e., directly derived from the fractional coordinates). (a) Crystal lattice of the RT phase: green is the rotated Cartesian system. (b) Crystal lattice of the LT phase: blue is the rotated Cartesian system.*

Figure 4.10 shows how to get θ and φ for use in the standard Eq. 2.7 (Page 32). As the RT lattice and LT lattice rotate in opposite directions, the situation should be considered separately, and its mathematical derivation is also shown in detail. Thus, once we know the vectors of the C–Br bonds in the fractional coordinate system, their orientations (θ and φ) in the XBI standard Cartesian system can be derived using this methodology.

Table 4.2 (Page 72) and Table 4.3 (Page 73) are the summary of θ and φ values for the C–Br bonds in the RT and LT phases. Because the space group is $P2_1/c$, for a C–Br bond (m, n, l), there is a corresponding (symmetry related) C–Br bond (m, $-n$, l). Thus, for each C–Br bond, two orientations are indicated in the table. As mentioned in 4.2.1, bromine atoms and methyl groups undergo exchange, and for each C–Br bond a weighting factor is introduced according to the occupancy value in the crystal structure.

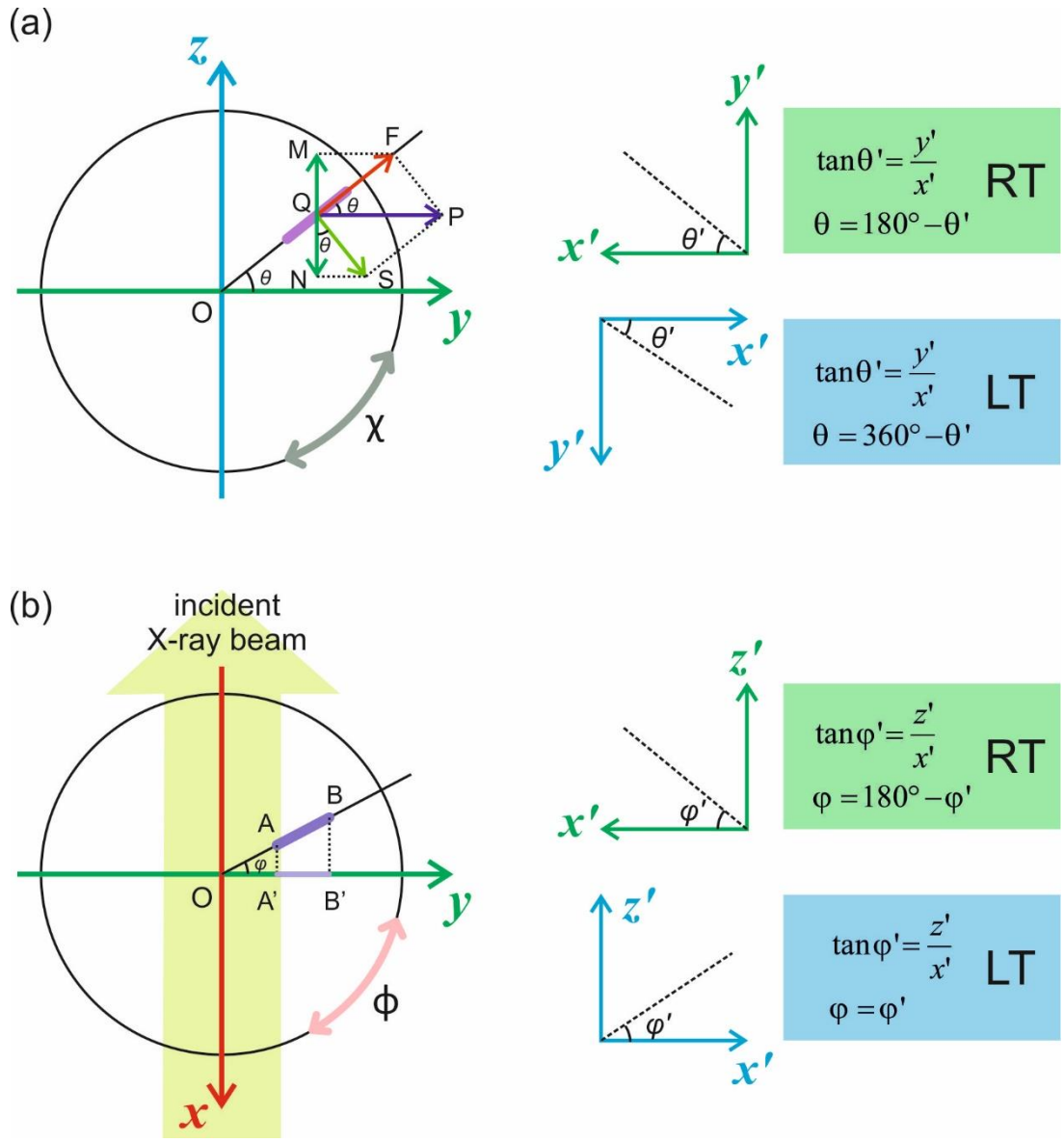

Figure 4.10 *Schematic illustration of the relationship between the crystal Cartesian system derived in Eq. 4.3 (Page 70) and the standard Cartesian system used in Eq. 2.7 (Page 32). The mathematical derivation of (a) θ and (b) φ for both the RT phase (green) and the LT phase (blue) are also shown.*

Table 4.2 *Orientations of C–Br bonds of DBTMB in the RT phase in the standard XBI Cartesian system. The mounting mode corresponds to Fig. 4.6.b (Page 67).*

	C–Br Bond	Weight	θ / °	φ / °
No.1	C(1)–Br(4)	0.328	104.52	265.01
			255.48	265.01
No.2	C(2)–Br(5)	0.364	177.97	142.44

			182.03	142.44
No.3	C(3)–Br(6)	0.308	160.05	200.33
			199.95	200.33

Table 4.3 *Orientations of C–Br bonds of DBTMB in the LT phase in the standard XBI Cartesian system. The mounting mode corresponds to Fig. 4.6.b (Page 67).*

	C–Br Bond	Weight	θ / °	φ / °
No.1	C(1)–Br(1)	0.935	354.85	322.18
			5.15	322.18
No.2	C(2)–Br(7)	0.062	83.59	87.87
			276.41	87.87
No.3	C(4)–Br(2)	0.936	357.37	323.66
			2.63	323.66
No.4	C(5)–Br(9)	0.066	74.24	84.14
			285.76	84.14
No.5	C(11)–Br(3)	0.945	339.48	19.34
			20.52	19.34
No.6	C(12)–Br(17)	0.022	4.74	325.62
			355.26	325.62
No.7	C(13)–Br(18)	0.034	289.23	82.65
			70.77	82.65
No.8	C(14)–Br(4)	0.946	20.85	20.25
			339.15	20.25
No.9	C(15)–Br(19)	0.018	359.87	327.29
			0.13	327.29
No.10	C(16)–Br(20)	0.035	83.99	88.28
			276.01	88.28

No.11	C(21)–Br(5)	0.901	286.56	84.32
			73.44	84.32
No.12	C(22)–Br(27)	0.041	22.95	21.42
			337.05	21.42
No.13	C(23)–Br(28)	0.057	358.08	319.43
			1.92	319.43
No.14	C(24)–Br(6)	0.903	75.88	85.28
			284.12	85.28
No.15	C(25)–Br(29)	0.04	339.64	22.34
			20.36	22.34
No.16	C(26)–Br(30)	0.058	2.64	325.94
			357.36	325.94

In XBI measurements, the χ scan is an important approach to investigate molecular orientations in the material. In order to calculate the intensity at different χ values, it is necessary to get the relationship between the orientation (θ and φ) and the scan angle (χ). Figure 4.11 illustrates how the value of θ and φ change with χ. The red arrow is a C–Br bond, and its orientation relative to the Cartesian system is specified by θ and φ. Assume the C atom is at the origin, and that the original Br position is labelled as P ($-a, b, c$).[*] The blue box is the whole single crystal. In a χ scan, the sample is rotated around the *x-axis* (the propagation direction of the incident X-rays). Figure 4.11.b shows the situation in which the whole single crystal has rotated clockwise around the *x-axis* by angle α. At this moment, the point P becomes P' ($-a, b', c'$), and the new orientation of the C–Br bond is θ' and φ'.

The mathematical relationships between θ, φ, a, b, c, α, θ' and φ' are also shown in Fig. 4.11. The change of θ is quite simple, just subtraction of α. However, the change of φ is not very straightforward. In order to analyse the change of φ, the projection picture of Fig. 4.11.b on the *yz-plane* is introduced (Fig. 4.12, Page 76). P" is the projection point

[*] These a, b and c are positive real numbers defining the C–Br bond vector, and do not represent the crystal lattice parameters.

of P', so its position in Fig. 4.12 is (b', c'). According to the geometrical relationship shown in Fig. 4.12, the following equations (Eq. 4.7 – Eq. 4.10) can be derived.

Thus, b' can be represented by b, c and α (Eq. 4.10). Putting this equation into the equation for tanφ' (Eq. 4.11), the new φ' can be represented in terms of the original orientation (θ and φ) and the rotation angle α. Thus, once we know the original orientation (θ and φ) of the C–Br bond and the rotation angle (α) of the crystal around the *x-axis* (the propagation direction of the incident X-rays), the new orientation (θ' and φ') of the C–Br bond can be calculated through Eq. 4.11 and Eq. 4.12.

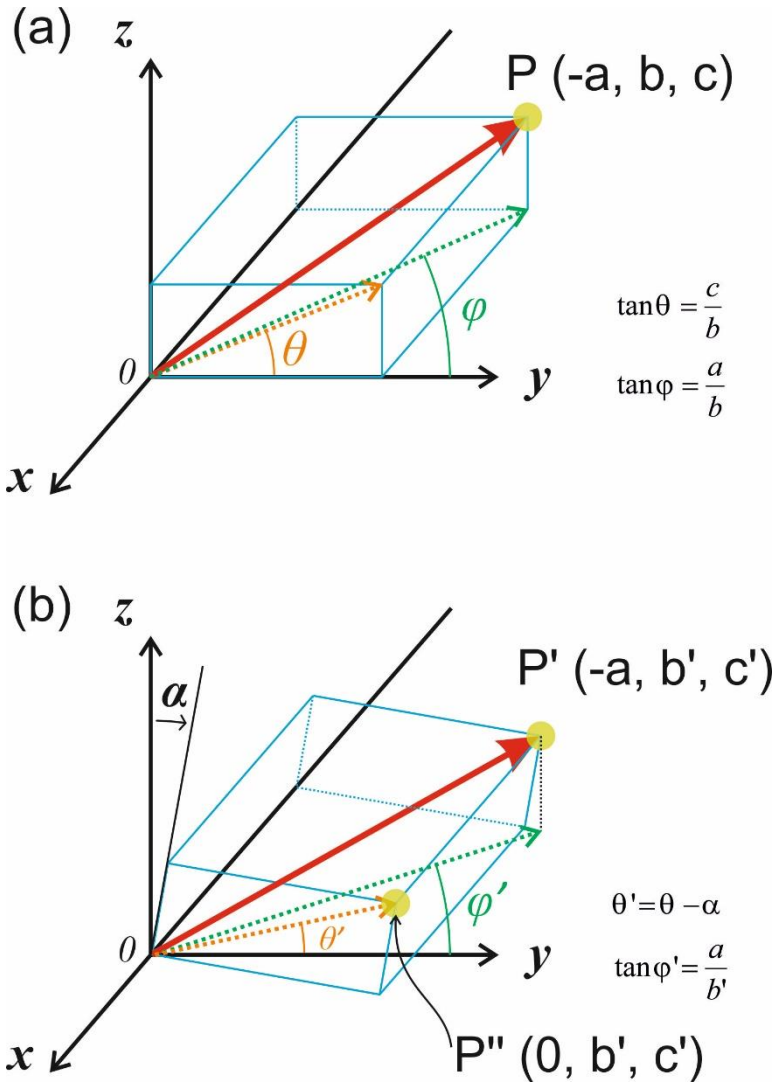

Figure 4.11 *Schematic illustration of the change of θ and φ in the χ scan. (a) The original position of a C–Br bond (red arrow), with orientation specified by θ and φ. (b) The orientation θ' and φ' of the same C–Br bond after clockwise rotation of the crystal by angle α around the x-axis.*

$$MP'' = b,\ MO = c \tag{4.7}$$

$$MN = MO \cdot \tan\alpha = c \cdot \tan\alpha \tag{4.8}$$

$$NP'' = MP'' + MN = b + c \cdot \tan\alpha \tag{4.9}$$

$$b' = QP'' = NP'' \cdot \cos\alpha = (b + c \cdot \tan\alpha) \cdot \cos\alpha \tag{4.10}$$

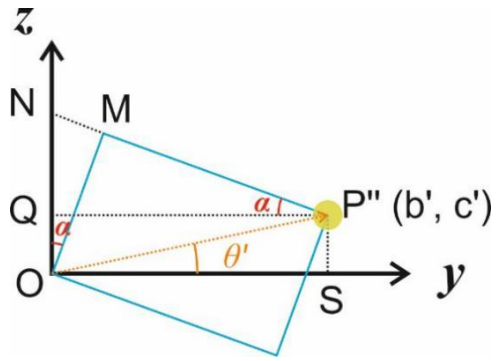

Figure 4.12 *Schematic illustration of the projection of Fig. 4.11.b on the yz-plane.*

$$\begin{aligned}\tan\varphi' &= \frac{a}{b'} \\ &= \frac{a}{(b + c \cdot \tan\alpha) \cdot \cos\alpha} \\ &= \frac{a}{\left(\frac{a}{\tan\varphi} + \frac{a}{\tan\varphi} \cdot \tan\theta \cdot \tan\alpha\right) \cdot \cos\alpha} \\ &= \frac{\tan\varphi}{(1 + \tan\theta \cdot \tan\alpha) \cdot \cos\alpha}\end{aligned} \tag{4.11}$$

$$\theta' = \theta - \alpha \tag{4.12}$$

According to the equation for the relative XBI intensity introduced in 2.1 (Eq. 2.7, Page 32), for a given sample under a stable experimental condition, the XBI intensity is proportional to a function of θ and φ denoted $f(\theta, \varphi)$ (Eq. 4.13). Correspondingly, the XBI intensity after rotation by angle α about the *x-axis* should be represented by the value of $f(\theta', \varphi')$ in Eq. 4.14. By putting Eq. 4.11 and Eq. 4.12 into Eq. 4.14, we obtain the XBI intensity as a function of the rotation angle α denoted $f(\alpha)$ (Eq. 4.15).

$$f(\theta, \varphi) = \sin^2(2\theta) \cdot \sqrt{\frac{1 + \tan^2\theta}{1 + \tan^2\theta + \tan^2\varphi}} \tag{4.13}$$

$$f(\theta', \varphi') = \sin^2(2\theta') \cdot \sqrt{\frac{1 + \tan^2\theta'}{1 + \tan^2\theta' + \tan^2\varphi'}} \tag{4.14}$$

$$f(\alpha) = \sin^2(2\theta') \cdot \sqrt{\frac{1+\tan^2\theta'}{1+\tan^2\theta'+\tan^2\varphi'}}$$
$$= \sin^2(2\theta - 2\alpha) \cdot \sqrt{\frac{1+\tan^2(\theta-\alpha)}{1+\tan^2(\theta-\alpha)+\frac{\tan^2\varphi}{(1+\tan\theta\cdot\tan\alpha)^2\cdot\cos^2\alpha}}} \qquad (4.15)$$

The overall intensity in the XBI measurement of the whole single crystal should consider all the C–Br bonds within the unit cell. Here, a weighted average value is used to describe the overall intensity (Eq. 4.16). The number of different C–Br bond orientations is N, with each orientation labelled *i*. For each C–Br bond orientation *i*, its weight (w_i) and original orientation (θ_i and φ_i) are shown in Table 4.2 (Page 72) and Table 4.3 (Page 73). In the derivations above, α is defined as the angle between the long-axis of the crystal (*b-axis*) and the *z-axis* of the laboratory frame (vertical), but in the actual experiments, the value $\chi = 0°$ was taken as the orientation with the long-axis of the crystal (*b-axis*) parallel to the *y-axis* of the laboratory frame (horizontal), and thus the relationship between χ and α is Eq. 4.17. Thus, the mathematical connection between the overall intensity and χ can be derived (Eq. 4.18), and its corresponding theoretical plot is shown in Fig. 4.13. For each phase, the intensity follows the typical $\sin^2(2\theta)$ dependence, with an interval of 45° between the highest and lowest intensity. However, the amplitude is bigger for the RT phase than the LT phase, which means at the brightest position (e.g., $\chi = 45°$) for the RT phase is brighter than for the LT Phase.

$$Intensity = \frac{\sum_{i=1}^{N} w_i \cdot f_i(\alpha)}{N} \qquad (4.16)$$

$$\chi = 90° - \alpha \qquad (4.17)$$

$$Intensity = \frac{\sum_{i=1}^{N} w_i \cdot f_i(90° - \chi)}{N} \qquad (4.18)$$

In order to compare the experimental results with theoretical results calculated above from the known crystal structures, a cryo system was added to the standard XBI set-up to investigate the influence of temperature on the XBI data for the DBTMB single crystal (Fig. 4.14). The experimental data recorded for the χ scan is shown in Fig. 4.15 (Page 79). In order to analyse the intensity properly and consistently, the intensity of the dark background is set as 0 and the bright background is set as 1, allowing the relative intensity to be measured based on the above scale. The two sets of data recorded at 273

K (black and green) are superposed very well, consistent with the previous conclusion that the phase transition is reversible. The 100 K data (red) has a similar trend to the 273 K in terms of the intensity change as a function of χ; however, at the maxima, the intensity is lower in the 100 K data than the 273 K data. This phenomenon is in a good agreement with the theoretical conclusion shown in Fig. 4.13.

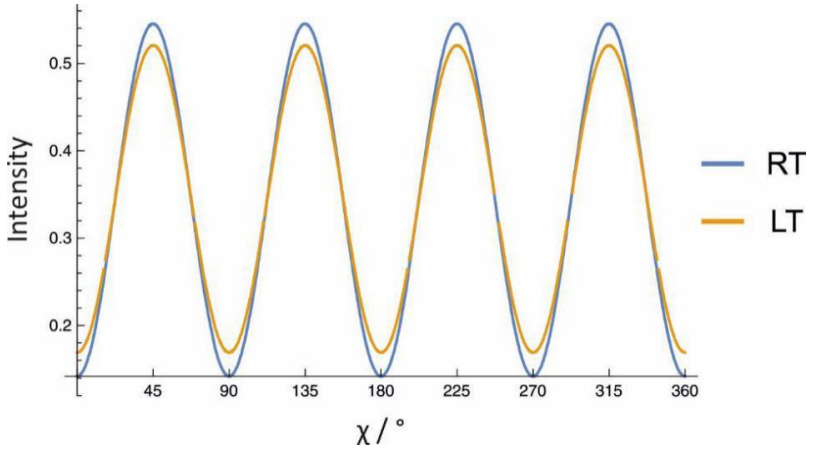

Figure 4.13 *Theoretical calculated data (using Eq. 4.18) for the χ scan in the RT (blue) and LT (orange) phases of DBTMB.*

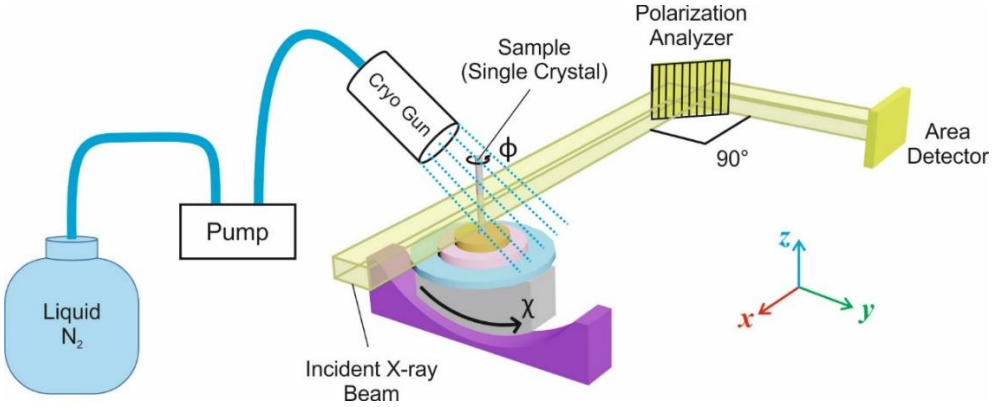

Figure 4.14 *Experimental set-up for XBI with cryo system. The pump is controlled by computer remotely. The sample is placed in the gas streams from the cryo gun.*

There are still some discrepancies between the calculated results and the experimental results. Firstly, in the trough parts, the difference between the data for the RT and LT phases is not as obvious as in the crest parts. According to 1.1.3, the thickness has an effect on the final intensity. As the thickness is fixed in a given experiment, this parameter is usually ascribed to a constant value. However, in this experiment, when the crystal phase changed from LT to RT, the thickness would be increased (Fig. 4.7, Page 69). Thus, considering this factor, the experimental data can move a little down compared

with the calculated data. Secondly, according to the calculated data, the position (χ value) of the crests and the troughs should be the same. However, in the real experimental data, the intensity in the LT data shows a small shift to lower χ. In the theoretical calculation process, it is assumed that, in both phases, the big face of the crystal is exactly perpendicular to the incident X-ray beam. In reality, this assumption may not be strictly valid, as the crystal can exhibit a thermo-mechanically responsive behaviour[69] during the phase transition. Thus, after the phase transition, the angle between the big face and the incident beam may change slightly, which may cause the discrepancy if the big face of the crystal is no longer strictly perpendicular to the incident X-ray beam.

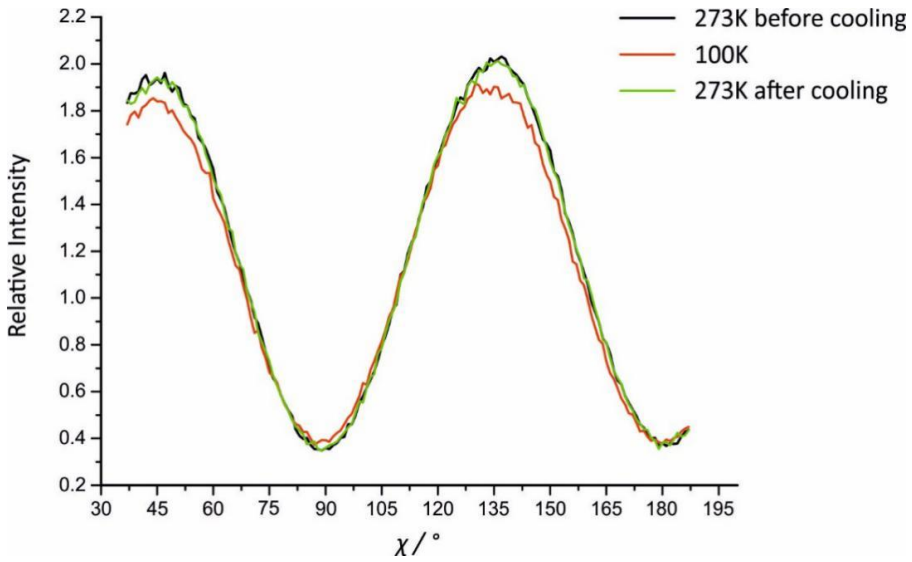

Figure 4.15 *Intensity from an experimental χ scan for a DBTMB single crystal with data recorded at 273 K, then at 100 K, and then at 273 K again.*

Figure 4.16 shows some selective XBI images from the χ scan in Fig. 4.15. Four specific orientations, χ = 45°, 90°, 135° and 180°, are selected. It is obvious that the single crystal is maximally bright at χ = 45° and 135°, and is dark at χ = 90° and 180°. These observations follow from the theoretical analysis above.

Because XBI is sensitive to the change of bond orientations, and phase transitions are often associated with a change in molecular orientations within the material, there is considerable potential to study phase transition phenomena by XBI. Figure 4.17 shows the temperature scan of a DBTMB single crystal at five different orientations: χ = 90°, 100°, 110°, 122.5° and 135°. At each value of χ, both heating and cooling scans were recorded. A change of intensity as a function of temperature is indicative of a phase transition, and the slope of the change shows this is a gradual change not an abrupt

change. The difference in phase transition temperature on cooling and on heating is consistent with the DSC data (Fig. 4.3, Page 64). Because χ = 135° is the brightest orientation, the phase transition exhibits the biggest change of intensity for this orientation of the crystal, and it is the ideal orientation to analyse the phase transition. Thus, this experiment proves that XBI can be an effective technique in characterization of phase transitions.

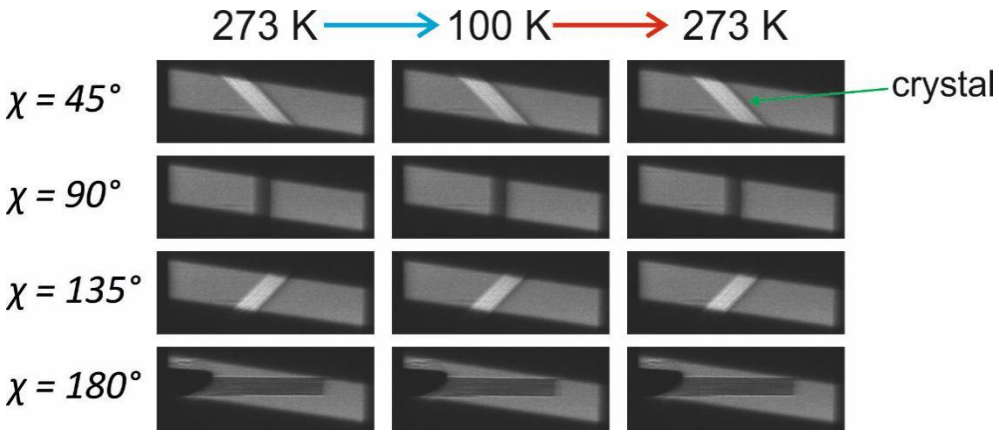

Figure 4.16 *XBI images recorded for χ scans of a DBTMB single crystal with temperature changed from the RT phase (273K) to the LT phase (100K), then back to the RT phase (273K).*

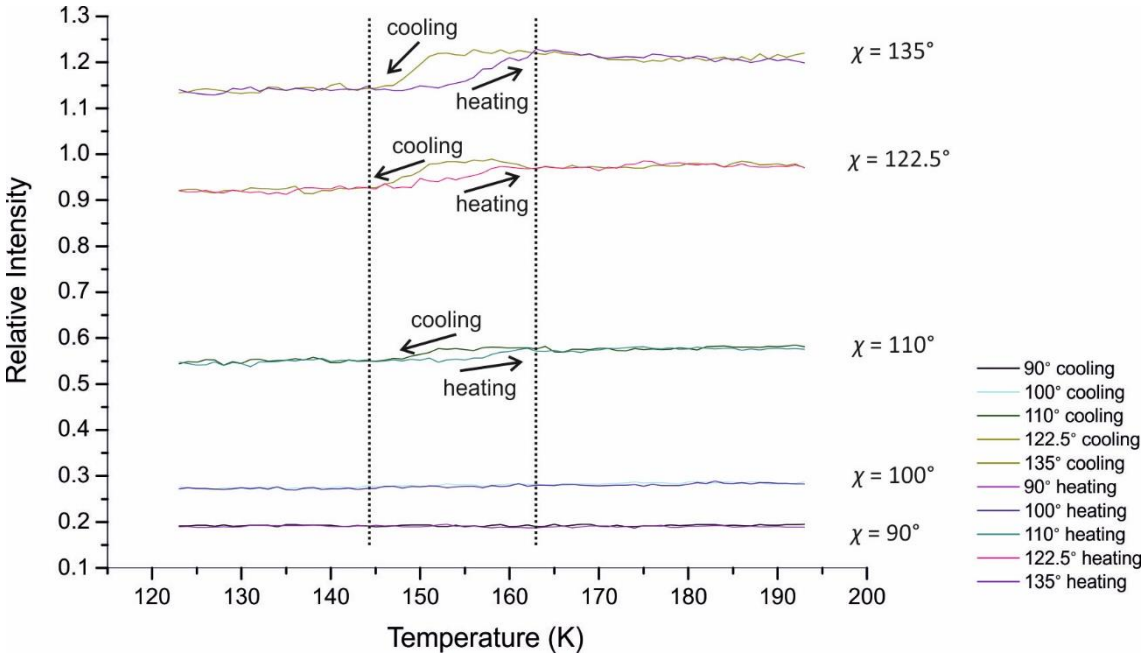

Figure 4.17 *Temperature scan of a DBTMB single crystal oriented at different χ values. Data recorded during both heating and cooling processes are shown.*

4.3 Crystal of 9,10-Dibromoanthracene

4.3.1 Structural Properties

Crystals of 9,10-dibromoanthracene (DBA) (Fig. 4.18) are yellow long needle-shaped crystals. The DBA crystal structure[70] (Fig. 4.19) used in this thesis was taken from the Cambridge Structural Database (CSD) (see Appendix III). The basic information of the crystal structure is summarized in Table 4.4. It is a triclinic crystal with space group $P\bar{1}$. The long-axis of the single crystal morphology is along the *a-axis*, and the DBA molecules are stacked through $\pi\cdots\pi$ interactions to form column structures. In contrast to DBTMB, the cross-section of the DBA crystal is too small to be distinguished by eyes, and the crystals do not have an obvious big face, so the mounting mode in XBI is arbitrary with regard to rotation around the long-axis. Thus, we can only ensure that the long-axis of the DBA single-crystal is perpendicular to the propagation direction of the incident X-rays, and the question of which face is oriented perpendicular to the incident beam is unknown. This issue brings a challenge in the data analysis process.

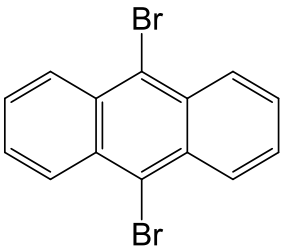

Figure 4.18 *Molecular structure of 9,10-dibromoanthracene*

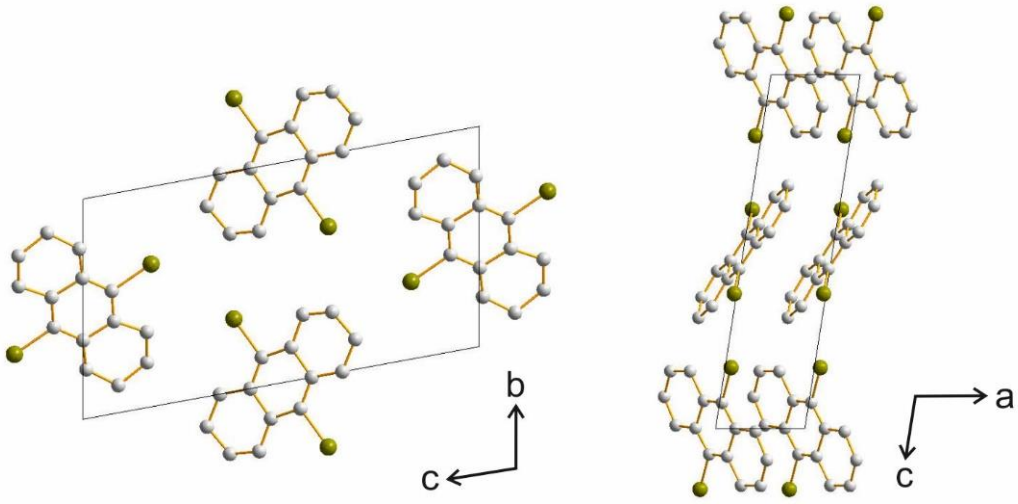

Figure 4.19 *Crystal structure of DBA viewed along different axes.*

Table 4.4 *Crystal structure information for DBA*

Formula Sum		$C_{14}H_8Br_2$
Formula Weight		336.03 g/mol
Crystal System		triclinic
Space Group		$P\bar{1}$
Cell Parameters	*a*	4.06 Å
	b	8.88 Å
	c	16.15 Å
	α	98.83°
	β	97.08°
	γ	100.35°
Cell Volume		559.14 $Å^3$
Z		2
Calculated Density		2.00 g/cm^3

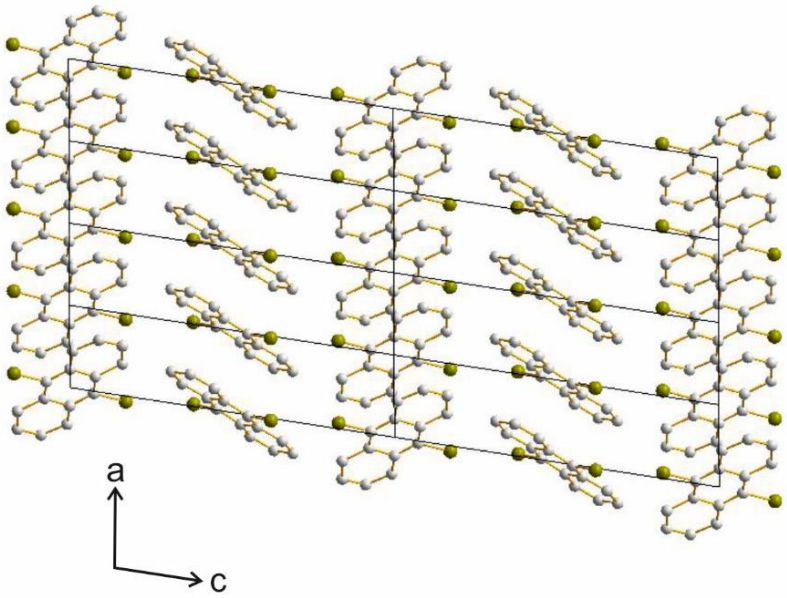

Figure 4.20 *Crystal structure of DBA viewed along b-axis. DBA molecules are stacked by π···π interactions along the a-axis to form column structures.*

4.3.2 X-ray Birefringence Imaging Studies of 9,10-dibromoanthracene

Figure 4.21 shows some selected XBI images from a χ scan for a 9,10-dibromoanthracene (DBA) single crystal. In the previous chapters, all the XBI images show a behaviour with the brightest transmitted intensity at χ = 45°, 135°, 225° and 315° and the darkest transmitted intensity at χ = 0°, 90°, 180° and 270°. However, in Fig. 4.21, the image recorded at χ = 90° is obviously brighter than that recorded at χ = 82°, which means that the maxima and minima in the χ scan of DBA are different from the previous samples. The measured intensity at each value of χ studied is plotted as a function of χ in Fig. 4.22 (red dots). In order to find the values of χ corresponding to the lowest/brightest intensity, a fitting function (Eq. 4.19) was used to fit the experimental data (Fig. 4.22 black line). From this equation, the minima in transmitted intensity are at χ = 80.8°, 170.8°, 260.8° and 350.8° (−9.20°). Compared with the standard intensity equation (Eq. 2.7, Page 32) in which the minima are at χ = 0°, 90°, 180° and 270°, the χ scan for DBA has a left shift for 9.20°.

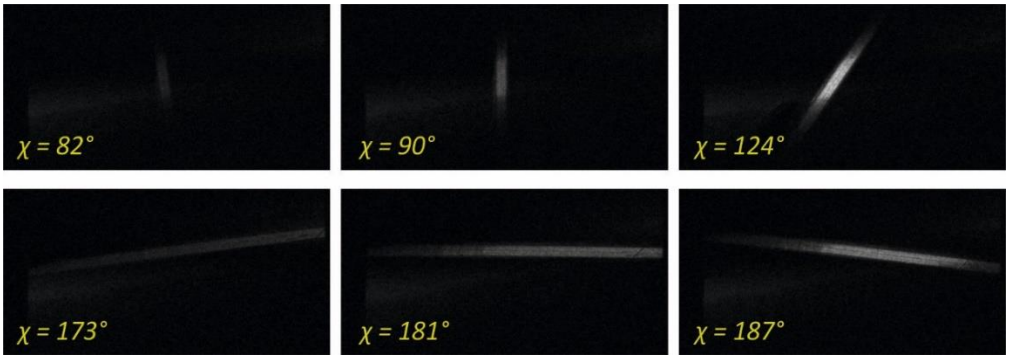

Figure 4.21 *Selected XBI images from a χ scan for a DBA single crystal.*

The process to calculate theoretically the XBI intensity of DBA is similar to the method developed for DBTMB in 4.2.2. As DBA is triclinic, the conversion function (Eq. 4.20) from fractional coordinates to Cartesian coordinates is different from the monoclinic case (Eq. 4.2, Page 70). Because the long-axis of the DBA single crystal is the crystallographic *a-axis*, and this axis lies along the positive direction of the *x-axis* in the Cartesian system, the next stage involving rotation of the Cartesian system (analogous to Eq. 4.3, Page 70, discussed in 4.2.2) requires rotation about the x-axis in this case (see Eq. 4.21). Unlike DBTMB, the shape of a single crystal of DBA is like a human hair, and it does not have an obvious big face. For this reason, the rotation angle (ε) around the long-axis of the crystal is unknown in the experimental set-up. Thus, the C–Br bond can

be represented as Cartesian coordinates (Eq. 4.22). Like the operation described for DBTMB, in order to use the standard XBI intensity equation (Eq. 2.7, Page 32), normalization of θ and φ is still needed (Eq. 4.23 and Eq. 4.24).

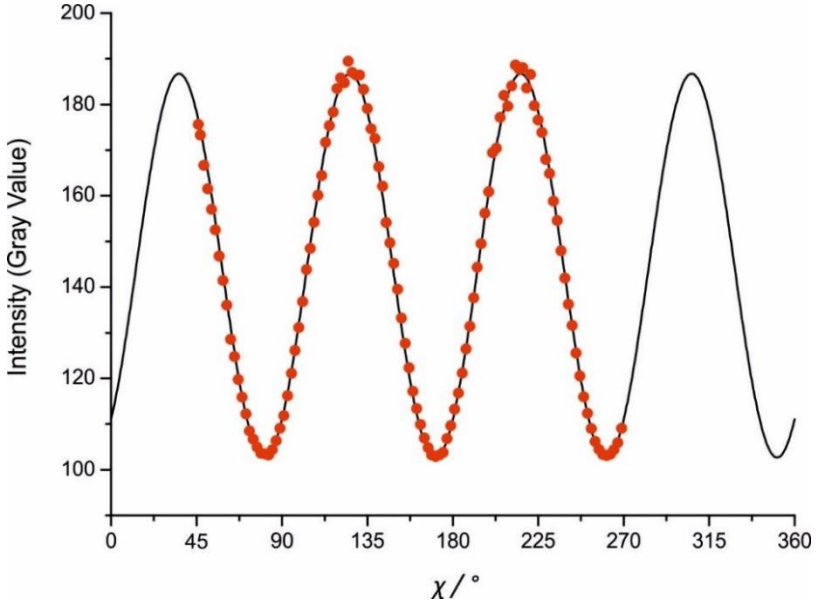

Figure 4.22 *Experimental intensity (red dots) as a function of χ from the χ scan of a DBA single crystal, and the corresponding best-fit equation (black line).*

$$f(x) = 84.07 \times \sin^2\left[2 \times (x + 9.20°)\right] + 102.663 \tag{4.19}$$

$$\begin{bmatrix} x \\ y \\ z \end{bmatrix} = \begin{bmatrix} a & b \cdot \cos\gamma & c \cdot \cos\beta \\ 0 & b \cdot \sin\gamma & c \cdot \dfrac{\cos\alpha - \cos\beta \cdot \cos\gamma}{\sin\gamma} \\ 0 & 0 & \dfrac{\Omega}{ab \cdot \sin\gamma} \end{bmatrix} \cdot \begin{bmatrix} m \\ n \\ l \end{bmatrix} \tag{4.20}$$

$$\text{here, } \Omega = abc\sqrt{1 - \cos^2\alpha - \cos^2\beta - \cos^2\gamma + 2\cos\alpha\cos\beta\cos\gamma}$$

$$\begin{bmatrix} x' \\ y' \\ z' \end{bmatrix} = \begin{bmatrix} 1 & 0 & 0 \\ 0 & \cos\varepsilon & -\sin\varepsilon \\ 0 & \sin\varepsilon & \cos\varepsilon \end{bmatrix} \cdot \begin{bmatrix} x \\ y \\ z \end{bmatrix} \tag{4.21}$$

$$\overrightarrow{C \cdot Br} = (x', y', z') \tag{4.22}$$

$$\tan\theta' = \frac{x'}{z'},\ \theta = \theta' \tag{4.23}$$

$$\tan\varphi' = \frac{y'}{z'},\ \varphi = 360° - \varphi' \tag{4.24}$$

The Crystal rotation angle ε can take any value in the XBI experiment, and each value of ε corresponding to its own orientations of C–Br bonds (θ and φ) in the XBI Cartesian system. Table 4.5 gives three examples with different values of ε. The values of θ and φ are calculated through the above equations. In each unit cell, there are two orientations of C–Br bonds with equal occupancy. As the two C–Br bonds in a given molecule (Fig. 4.18, Page 81) are symmetry related to each other by the crystallographic inversion centre, these two C–Br bonds are strictly anti-parallel, and they give identical XBI behaviour. Once the orientations of the C–Br bonds are known, the theoretical χ scan plots can be calculated for any mounting mode of the crystal (specified by angle ε) using Eq. 4.18 (Page 77) (Fig. 4.23). In the χ range from 0° to 360°, the three plots for ε = 0°, 45° and 81.36° show four crests and four troughs, separated by 45° intervals. However, the positions of the crests and troughs are different for each different value of ε.

Table 4.5 *Orientations of the C–Br bonds in the DBA crystal in the standard XBI Cartesian system. Three mounting modes are shown as examples, i.e., ε = 0°, 45° and 81.36°.*

		C–Br Bond	Weight	θ / °	φ / °
ε = 0°	No.1	C(4)–Br(1)	1	352.13	34.50
	No.2	C(11)–Br(2)	1	335.61	305.90
ε = 45°	No.1	C(4)–Br(1)	1	327.99	79.50
	No.2	C(11)–Br(2)	1	344.93	350.90
ε = 81.36°	No.1	C(4)–Br(1)	1	14.64	295.86
	No.2	C(11)–Br(2)	1	343.34	27.26

Table 4.6 shows the exact positions of the troughs (the minima of intensity) and it is obvious that the differences between them depend on ε. Compared with the conventional XBI χ scan behaviour, all three plots exhibit a left shift in the positions of crests and troughs. For ε = 0°, the shift is 14.82°; for ε = 45°, it is 17.69°; and for ε = 81.36°, the left shift is 9.20°. Looking back at the experimental data in Fig. 4.22, the left shift is also 9.20°. Thus, the mounting mode can be derived, which means that for our experimental χ scan, the initial rotation angle of the crystal around the *a-axis* corresponding to ε = 81.36°.

Through this method, for an unknown mounting mode of the single crystal, the exact position can be analysed by calculating the intensity of the χ scan. Especially for some crystals with very small or poorly defined faces which are difficult to be observed in face-indexing by single-crystal XRD, XBI provides an effective and accurate alternative strategy in the challenge of face-indexing such materials.

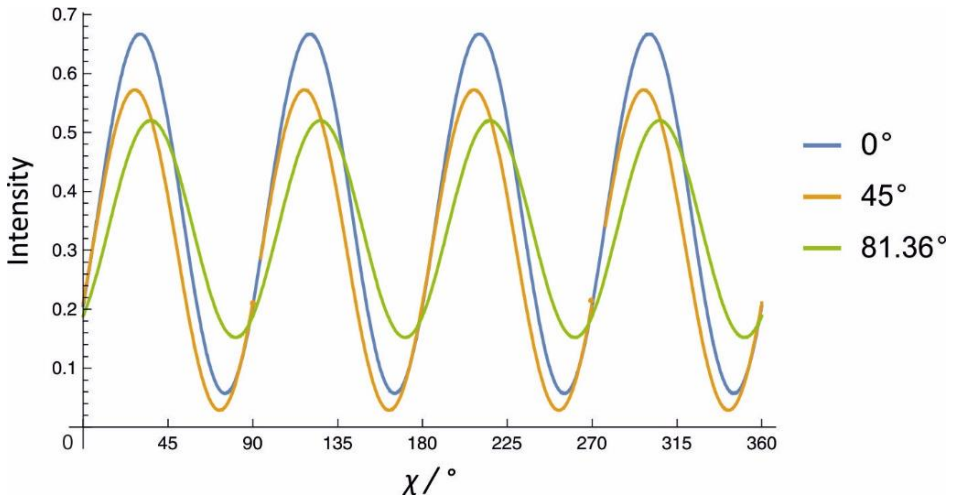

Figure 4.23 *Theoretical plots of the χ scan intensity for three mounting modes corresponding to: (1) ε = 0°, blue line; (2) ε = 45°, orange line; and (3) ε = 81.36°, green line.*

Table 4.6 *Summary of the χ values corresponding to minimum intensity of each plot in Fig. 4.23. The shift is relative to the standard XBI behaviour (i.e., with 90°, 180°, 270° and 360° corresponding to minimum intensity).*

	shift left / °	$\chi_{(1)}$ / °	$\chi_{(2)}$ / °	$\chi_{(3)}$ / °	$\chi_{(4)}$ / °
ε = 0°	14.82	75.18	165.18	255.18	345.18
ε = 45°	17.69	72.31	162.31	252.31	342.31
ε = 81.36°	9.20	80.80	170.80	260.80	350.80

4.4 Static Analysis of Crystal Bending Processes

4.4.1 Crystal Bending Experiments

Three-point bending is a classic test in material science to measure the mechanical strength of materials.[71-73] The “three-point” means that three forces are applied to the test

sample at three aligned points, and the direction of the middle force is opposite to the other two forces. In order to investigate systematically the bent regions of bending crystals by XBI, a small device was designed in this project for the bending process (Fig. 4.24) with the aim of generating bent crystals with a range of uniform and well-defined curvatures. The bending device is composed of a square base and a vertical cylinder. The straight crystal is placed on the base between the cylinder and a pair of tweezers. By pushing the crystal with the tweezers, the cylinder and the tweezers form a three-point bending device, and the cylinder acts as the middle point. Thus, the crystal is bent with a uniform curvature around the cylinder, and this curvature depends on the diameter of the cylinder. The bending devices that were constructed for this work had the following diameters of cylinder: 0.24 mm, 0.99 mm, 1.98 mm, 2.27 mm, 3.18 mm and 6.01 mm. Thus, the curvature of the bent crystal prepared using each of these devices would have approximately the same value of diameter. The samples used in this static analysis of crystal bending were DBTMB single crystals (refer to section introducing DBTMB).

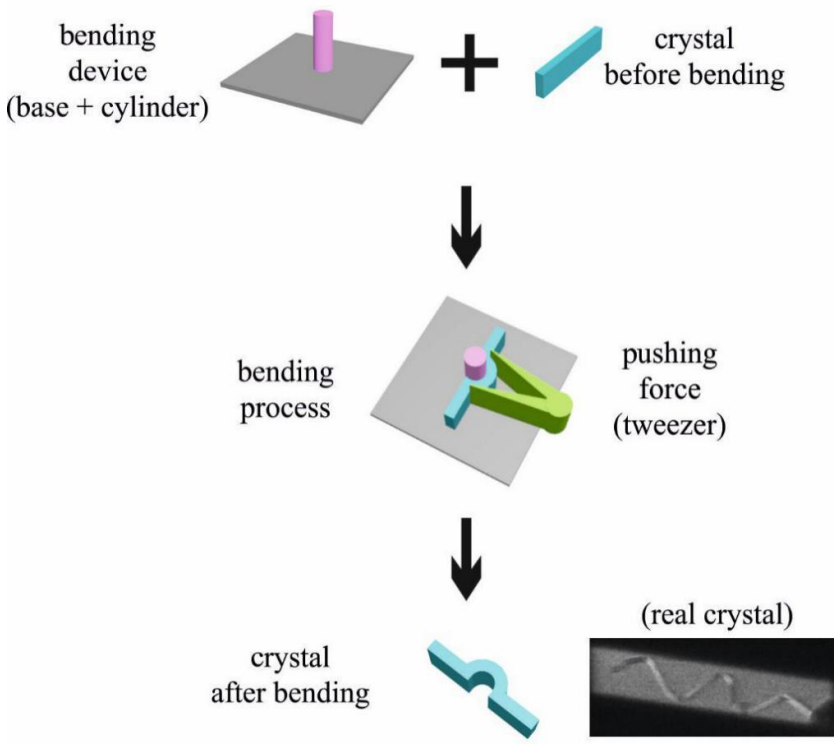

Figure 4.24 *Schematic illustration of the procedure to bend crystals with uniform and well-defined curvature. The last black-and-white image is a XBI image of a bent DBTMB single crystal (with the same crystal bent at five different places).*

Crystal bending processes can also happen during crystal growth. Figure 4.25 is an image from an optical microscope with a computer controlled hot stage. In this experiment, firstly the temperature was increased above the melting point of DBTMB and then decreased. Single crystals are generated randomly on decreasing the temperature. If a crystal exists at a three-point confined geometric position incidentally, the growth of the crystal is influenced by the outside forces and its final morphology may be bent. In Fig. 4.25, there is a bent crystal as an example to demonstrate this phenomenon.

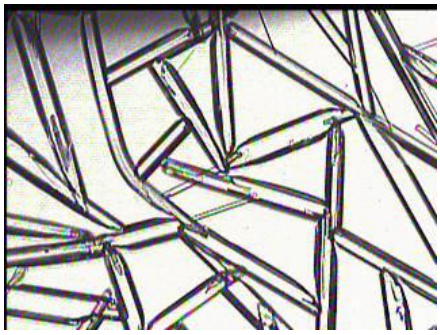

Figure 4.25 *DBTMB single crystals formed from the molten state in an optical microscope. In the middle-left part of the image, a bent crystal is observed to have formed during the crystallization process.*

4.4.2 X-ray Birefringence Imaging Studies of Bent Crystals of Different Curvatures

By using the bending device described in 4.4.1, six bent crystals of DBTMB with different uniform curvatures were prepared. Here, our experiments also prove that the bending face is the big face of a single crystal, which is consistent with the theoretical prediction in 4.2.2.

In our XBI studies, a previously bent crystal was mounted in the standard XBI set up (Fig. 2.1, Page 29) with the bending face parallel to the propagation direction of the incident X-rays and also parallel to the axis of bending. Figure 4.26 shows XBI images for the six crystals of different curvature. For each crystal, the intensity changes gradually along the crystal, and the crystal is always dark (minimum transmitted intensity) on the top region in the image. A quantitative measurement of the intensity was carried out, as now discussed. The yellow lines show the measurement positions and green sectors show the circle centres of curvature for each crystal and the χ range encompassed by the yellow lines. The orientation of the line (shown in red in Fig. 4.26) between circle centre and the

measurement point is χ. The radius of each sector depends on the radius of the cylinder on the bending device used to bend the crystal. As the beam area in the XBI images is limited and fixed, for crystals bent using cylinders with large radius (i.e., low curvature), only partial regions of the crystal are recorded in XBI. However for sample No.1, as the radius is very small, the whole bent (in this case, circular) crystal can be recorded completely.

Figure 4.27 shows the intensity measurement along the yellow lines of Fig. 4.26. The results for all six samples follow the typical XBI intensity change of χ scan, showing a sinusoidal variation of intensity, with the lowest intensity around χ = 90°. Especially for crystal No.1, additional minima of intensity are observed around χ = 180° and χ = 270° as expected. The beginning part (from *ca.* 55° to *ca.* 90°) of crystal No.1 does not show a perfect intensity change in Fig. 4.27 because of the irregular shape of the bent crystal in this region (see Fig. 4.26 top-left image). Another feature is that the intensity variation for crystal No.1 has a smaller amplitude compared with the others. This discrepancy is a consequence of the thickness of the crystal, which can influence the amplitude of the observed intensity (see 1.1.3). From Fig. 4.26, it is obvious crystal No.1 has a rather smaller size than the others.

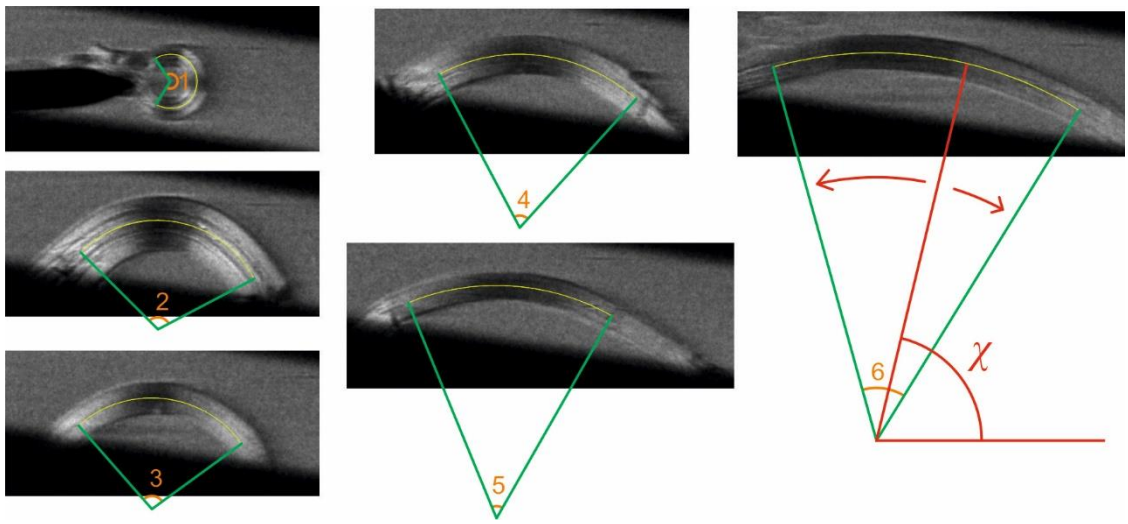

Figure 4.26 *XBI images of six DBTMB bent crystals with different curvatures. Yellow lines indicate the contours along the crystal used for intensity measurements. Red lines indicate the orientation of the line between the circle centre and the measurement point is χ. Green sectors show the circle centres of the curvature and the χ range encompassed by the yellow lines.*

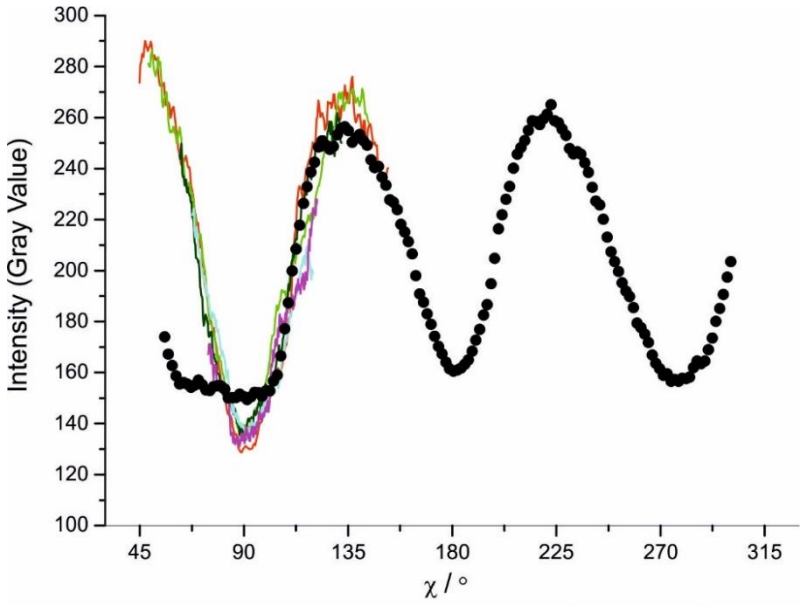

	range of χ	diameter of bent crystals
● ∠1	from 55.8° to 300.5°	d_1 = 0.24 mm
— ∠2	from 44.8° to 152.3°	d_2 = 0.99 mm
— ∠3	from 48.7° to 143.9°	d_3 = 1.98 mm
— ∠4	from 62.1° to 132.2°	d_4 = 2.27 mm
— ∠5	from 67.7° to 119.8°	d_5 = 3.18 mm
— ∠6	from 74.5° to 121.7°	d_6 = 6.01 mm

Figure 4.27 *Measured intensity as a function of position along the crystal for the XBI data for six bent crystals of DBTMB in Fig. 4.26. The position along the crystal is expressed in terms of* χ.

In bending crystals, small domains with slightly different orientations may be generated during the bending process. The experimental results in Fig. 4.27 show that the intensity of each small domain is related to its χ value. Thus, the bent crystals of DBTMB may be described, in principle, as lots of small crystal lattices with a gradual change of orientations. These small domains may be as small as individual unit cells, and are certainly smaller than the resolution of the XBI measurements (given that the results in Fig. 4.27 are essentially continuous sinusoidal curves). The orientation of the *b-axis* of each small domain is parallel to the tangent line of the point at which the domain exists on the whole curve. This change of orientations is quite similar to the model in Fig. 1.18 (Page 20), so the theoretical calculated results can be built by simulating an intensity

change of χ scan. The procedures are the same as in 4.2.2. At this moment, as the bending face is parallel to the incident beam, the mounting mode is now the type of Fig. 4.6.d (Page 67). The beginning orientations of the C–Br bonds, therefore, need to be calculated again, and the results are summarized in Table 4.7.

Table 4.7 *Orientations of C–Br bonds in a single crystal of DBTMB in the RT phase relative to the XBI standard Cartesian system. The mounting mode of the sample corresponds to Fig. 4.6.d (Page 67).*

	C–Br Bond	Weight	θ / °	φ / °
No.1	C(1)–Br(4)	0.328	198.64	175.01
			161.36	175.01
No.2	C(2)–Br(5)	0.364	177.36	232.44
			182.64	232.44
No.3	C(3)–Br(6)	0.308	224.40	110.33
			135.60	110.33

The calculated χ scan is shown in Fig. 4.28. It has a conventional sinusoidal variation of intensity as a function of χ, with the brightest regions at χ = 45°, 135°, 225° and 315° and the darkest regions at χ = 0°, 90°, 180° and 270°. The calculated results are in a good agreement with the experimental results (see Fig. 4.27), which proves the hypothesis in terms of the distribution of molecular orientations in the bent crystals.

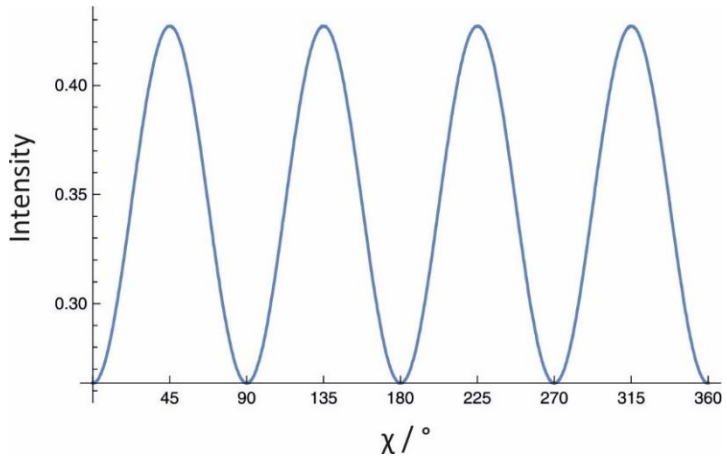

Figure 4.28 *Theoretical calculated χ scan for a single crystal of DBTMB in the RT phase with the mounting mode of the crystal as shown in Fig. 4.6.d (Page 67).*

As the intensity of the bent crystals in the XBI images depends on the orientation of the tangent lines, if regions have the same tangent lines, the intensity should be the same. A movie of a χ scan of crystal No.1 is a good example, as the whole circular shape of this crystal can be recorded. Figure 4.29 shows four images at different χ position during this χ scan. It is clear that the black and white regions remain at the same relative positions during the χ scan, with the bright and dark parts forming the classical Maltese cross pattern shown in Fig. 1.12 (Page 12) and Fig. 1.18 (Page 20).

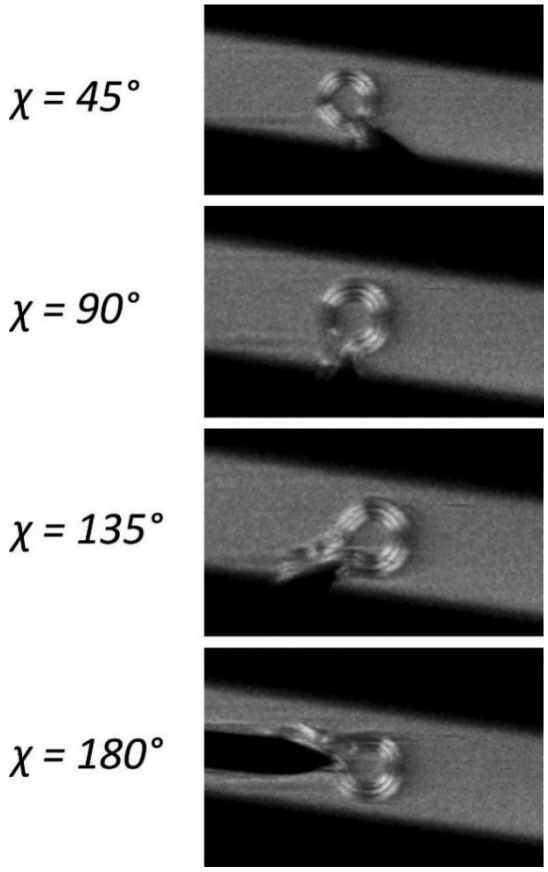

Figure 4.29 *XBI images of the whole circle bent DBTMB single crystal (crystal No.1) recorded at four different orientations (defined by angle χ). The positions of the bright and dark regions do not change with χ.*

4.4.3 Energy Change Test

In the XBI studies reported in this thesis, the X-ray energy was fixed at the Br K-edge to make sure the birefringence is only sensitive to the orientational characteristics of the C–Br bonds rather than the whole crystals (as in POM). This specificity is the

biggest advantage of XBI, as it can evaluate the target element selectively, with no interference from the other elements.[21]

In order to check the specificity, an energy change test was carried out using, as the test sample, the bent DBTMB single crystal prepared using the 0.24 mm bending device. The X-ray energy used to record the XBI images of this bent crystal (e.g., Fig. 4.29) was 13676.7 eV. XBI images were then recorded on changing the energy by +10 eV and −10 eV respectively for the same sample. The results are shown in Fig. 4.30. The middle XBI image has the typical Maltese cross pattern with alternatively bright and dark regions as observed in the earlier XBI studies of the same crystal. However, for both the higher or lower energy, the crystal ring shows a uniform dark intensity without evidence for any significant birefringence. This experiment proves that the optimal selection of the incident X-ray energy is critical for observing the phenomenon of X-ray birefringence.

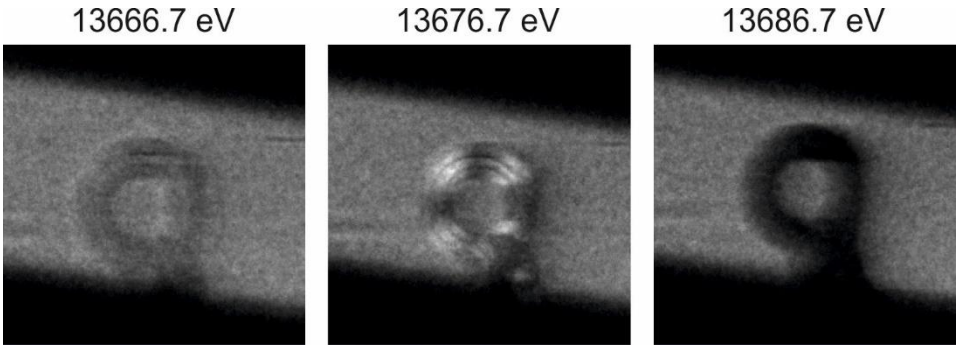

Figure 4.30 *XBI images of a bent DBTMB single crystal recorded for three different incident X-ray energies. X-ray birefringence is observed only for the data recorded with E = 13676.7 eV.*

4.5 Dynamic Analysis of Crystal Bending Processes

4.5.1 Experiments

In 4.4, it has been shown that XBI is an effective technique for investigating the orientational distributions of molecules in bent crystals. However, the analysis described is a "static analysis", as only the final bent crystals were studied. In order to investigate the bending process itself, a new experimental set-up was designed to carry out dynamic analysis, allowing detailed information during the bending process can be captured by *in-situ* XBI measurements of crystal bending.

Figure 4.31 shows the new set-up for dynamic analysis of bending processes. This new set-up involves an additional accessory part in the standard XBI set-up, with the accessory placed at the position of the single crystal in Fig. 2.1 (Page 29). The support base and the loading anvil in Fig. 4.31 form a three-point bending geometric construction. Thus, the sample single crystal is placed on the support base and it will bend when the loading anvil is moved down (under automated control).

There are two types of bending crystals: plastic and elastic.[66] Here, these two types are investigated separately in 4.5.2 and 4.5.3. Because plastic bending crystals only have one pair of bending faces, care should be taken when placing the original straight crystal on the support base to make sure that the bending face is perpendicular to the loading anvil. In this work, the sample of plastic bending crystal studied is DBTMB and the sample of elastic bending crystal studied is DBA. The crystal structures of DBTMB and DBA have been discussed fully in 4.2 and 4.3.

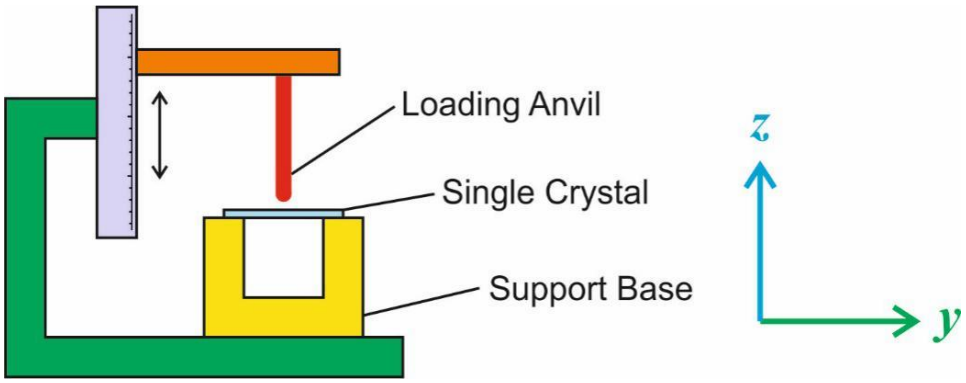

Figure 4.31 *Experimental set-up for dynamic analysis of crystal bending processes by in-situ XBI. The loading anvil can be controlled by computer remotely. The axes show the relative position of this set-up in the context of the standard XBI set-up in Fig. 2.1 (Page 29). The propagation direction of the incident beam is perpendicular to the yz-plane, and is polarized along the y-axis.*

4.5.2 Plastic Bending Process

A single crystal of DBTMB (before bending) was placed horizontally with the bending face perpendicular to the loading anvil. The long-axis of the crystal is along the direction corresponding to $\chi = 0°$ (180°). According to the results in 4.4.2, the transmitted X-ray intensity in this orientation should be very low. Figure 4.32.a shows the XBI image

of the crystal before bending, and the uniform dark appearance is consistent with the low intensity corresponding to $\chi = 0°$ (180°). When the loading anvil is moved down, bending of the crystal at the point of contact with the loading anvil generates two different orientations of the remaining straight regions of the crystal – a straight region at the left hand side (with χ changing from 0° → 90° as the loading anvil is moved down) and a straight region at the right hand side (with χ changing from 180° → 90° as the loading anvil is moved down). The XBI images in (b) – (f) record this bending process as the loading anvil is progressively moved down. With the pushing of the loading anvil, the transmitted intensities of the left and right parts increase observably; while, the middle (bent) part of the crystal still keeps relatively dark as its orientation does not change substantially.

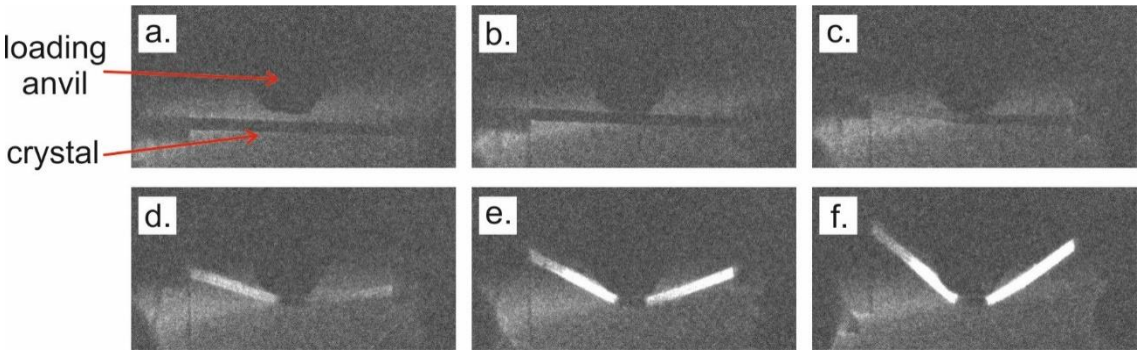

Figure 4.32 *XBI images of a DBTMB single crystal recorded as the loading anvil is progressively moved down. The sequence from (a) to (f) is in chronologic order.*

One way to identify plasticity is to check if the sample returns to the original shape after the applied force is removed.[74] Figure 4.33 shows the situation when the loading anvil is moved up. From the XBI images in (a) to (c), even though the anvil becomes progressively separated from the bent crystal, the deformation of the crystal does not change. The image in (d) is the normal X-ray image taken by the camera without the analyzer mentioned in Fig. 2.3 (Page 31). In this image, it is clear that the loading anvil is no longer in contact with the sample; and the bent single crystal keeps the maximally deformed shape resulting from the plastic bending process. Another feature to note is that (c) and (d) are mirror images to each other. As explained in 2.1, the images with and without the analyzer are left-to-right reversed; in (c), the anvil is closer to the left part of crystal, but in (d) it is closer to the right part.

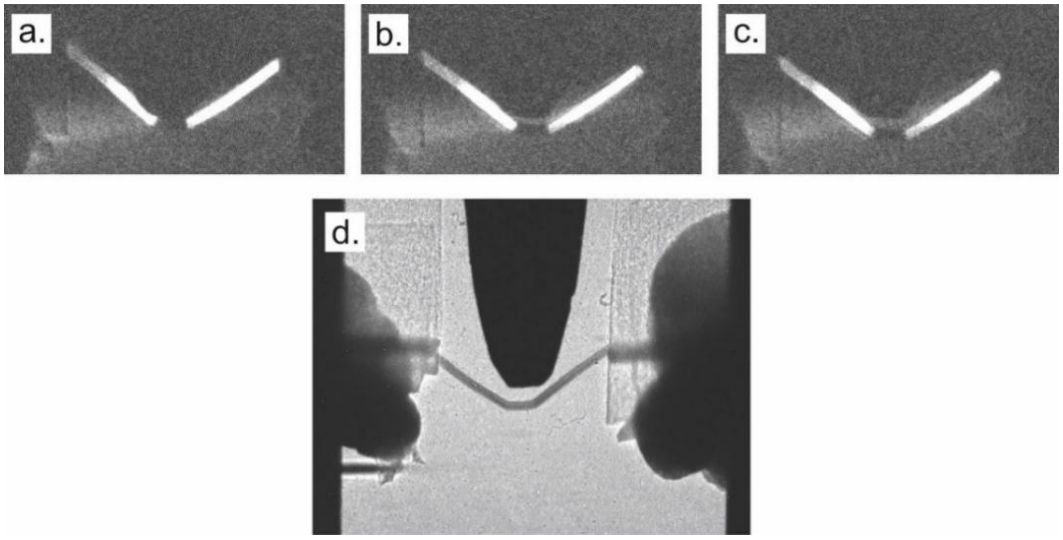

Figure 4.33 *XBI images recorded following bending of the DBTMB single crystal in Fig. 4.32, with the XBI images in (a), (b) and (c) recorded on progressively moving the anvil upwards, away from the crystal. The sequence from (a) to (c) is in chronologic order. In (d), the normal X-ray image is shown of the same sample as in (c).*

4.5.3 Elastic Bending Process

To explore elastic bending by *in-situ* XBI studies, a single crystal of DBA was chosen as the test sample. Because the sample has no obvious big face, in contrast to DBTMB in 4.5.2, the placement of the crystal of DBA in the experimental set-up for dynamic bending (Fig. 4.31, Page 94) is done without any knowledge of the orientation of the crystal with respect to rotation around the long-axis. Thus, the front face in the captured image is unknown. Also, from 4.3, it is known that, in most circumstances, the orientation $\chi = 0°$ (180°) is not the lowest intensity orientation for this material.

Figure 4.34 shows the deformation of a DBA single crystal with the loading anvil moving down and up. The XBI image before bending is shown in (a). In contrast to the dark sample in Fig. 4.32.a, the single crystal in Fig. 4.34.a shows a uniform grey colour meaning it is not in the orientation of lowest intensity. As described for DBTMB in 4.5.2, on moving the loading anvil down, the crystal of DBA (Fig. 4.34) becomes bent at the point of contact with the loading anvil, generating two different orientations for the remaining straight regions of the crystal at the left side and right side of the loading anvil. However, in contrast to the change observed for DBTMB, the intensity of the left part of the DBA crystal decreases, while the intensity of the right part increases (see Fig. 4.34.b

and Fig. 4.34.c). When the loading anvil is moved back (see Fig. 4.34.d and Fig. 4.34.e), the intensities and the deformation of the left and right parts both show a reversible behaviour. When the loading anvil separates from the crystal completely (see Fig. 4.34.f), the crystal has returned to its original straight shape (horizontal), and the intensity of the crystal goes has returned to a uniform intensity across the whole crystal.

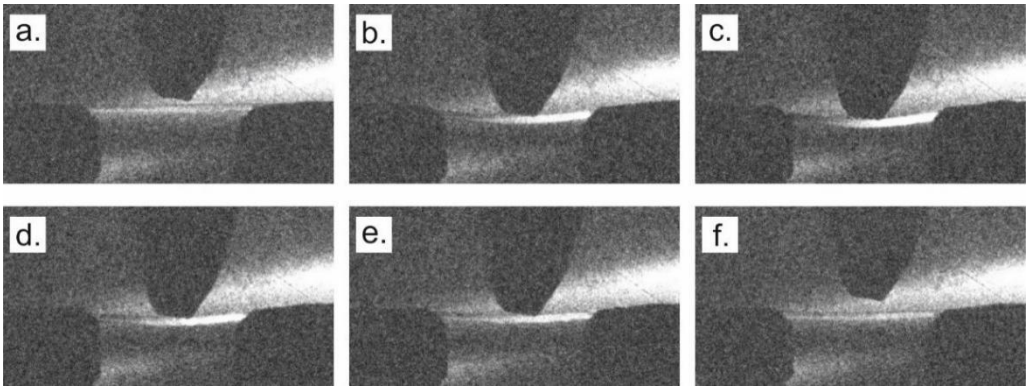

Figure 4.34 *XBI images of a DBA single crystal recorded in-situ during crystal bending. In (a – c), the loading anvil is moved down. In (d – f), the loading anvil is moved up. The sequence from (a) to (f) is in chronologic order.*

This phenomenon can be explained using the theoretical intensity plot for a χ scan of DBA in Fig. 4.35. The orange dot represents the intensity for the initial state of the crystal before bending ($\chi = 180°$). As the front face is unknown, the orange dot can be at any position on the plot and its horizontal ordinate is $\chi = 180°$. In the three point bending process, the left and right parts of the crystal will show an equal but opposite change in orientation point of contact of the loading anvil. A green dot and a red dot are used to represent the resultant orientations of the left and right parts of the bent crystal. As the loading anvil is moved down, the orientations of the left and right parts will change at the same rate but in opposite directions. The green and red arrows indicate the opposite directions. Thus, the green dot and the red dot move along the plot in opposite ways as the degree of bending increases, which means that the intensity of one part increases and the other part decreases. This theory can also explain the results of DBTMB. In the DBTMB case, the initial horizontal position of the crystal ($\chi = 0°$) corresponds to lowest intensity (the orange dot is at the trough). As the bending process proceeds, the green dot (left part of crystal) and red dot (right part of crystal) will move away from the trough at the same rate but in opposite directions, so the two parts of the crystal exhibit the same increase of intensity as the degree of bending increases.

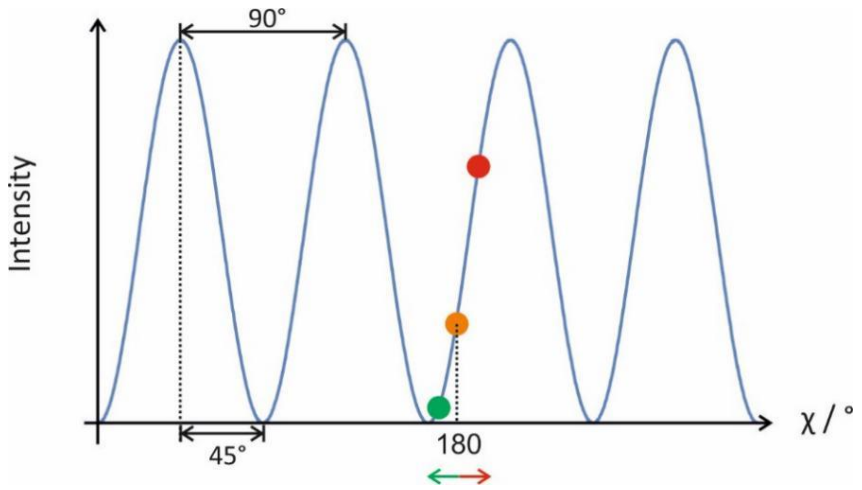

Figure 4.35 *Schematic illustration of the intensity change observed in the XBI images of the dynamic bending of a DBA single crystal (Fig. 4.34). Orange is the single crystal before bending with χ = 0° (180°). Green and red are the left and right parts generated during the three-point bending process.*

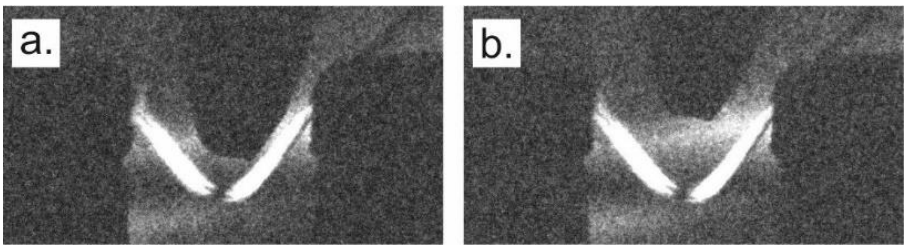

Figure 4.36 *XBI images of a DBA single crystal recorded on moving the loading anvil up after undergoing elastic bending several times, resulting in a plastic state.*

The mechanical properties of an elastic bending crystal reflect the behaviour of conventional elastic materials, e.g., natural rubber. Figure 4.36 shows the consequence of material fatigue in the DBA sample. The XBI data were recorded after the single crystal had been bent several times resulting in loss of its elasticity. When the loading anvil is moved back up in this case, the crystal does not return to its original straight shape, but instead remains bent as a plastic deformation. Another cause of plastic formation is to go across the yield point of the stress-strain curve.[75] If the pressure is too high, the deformation can be permanent, i.e., changing into plastic state. A similar mechanical phenomenon has also been reported recently for copper (II) acetylacetonate,[74] which is also an elastic bending crystal.

4.6 Conclusions

Experiments reported in this chapter provide evidence that the bent crystal is composed of numerous small lattices (certainly smaller than the resolution of the XBI measurements) with slightly changed orientations. With the accessory of a three-point bending device in the XBI set-up, we have shown that *in-situ* XBI studies can unveil the process of bending on both plastic and elastic materials to give real-time information on changes of crystal and molecular orientations. As the deformation is accompanied by a change in molecular orientation and hence by a change of intensity in the XBI images, some small deformations can be detected by XBI that may be not obvious in other tests.

Although the samples studies in this chapter are all bending crystals, XBI also shows two applications in universal studies of materials. Firstly, with the accessory of a temperature control system, XBI can be used in phase transition research. It does not only provide the temperature point of phase transition like in DSC, but also shows the changes in orientational distributions of the molecules resulting from the phase transitions. Furthermore, the contrast can be adjusted by changing the sample orientations (χ angle). Secondly, XBI can be used in face-indexing of single crystals. For some crystals, if the sample is not feasible to do face-indexing by traditional single-crystal XRD, XBI provides an alternative way. The basic principle is to find the matched angle of the χ scan plot.

The additional energy change test described in this chapter verifies further that the X-ray birefringence phenomena depend critically on matching the incident X-ray energy to the absorption edge of a target element. Thus, all the intensity changes observed in the XBI data arise from the orientations of the target elements, and do not result from optical birefringence (or other optical phenomena, which are small enough to be ignored compared with XBI).

This chapter has proven that XBI is an effective and versatile technique for the study of both bending crystals and other materials. Especially for the study of molecular orientations in small domains, it has remarkable advantages.

Chapter 5

X-ray Birefringence Imaging on Composite Organic Materials

5.1 Introduction

The previous chapters have shown that XBI images are only sensitive to the orientational properties of the X-ray absorbing element (in this thesis, we focus on bromine as the X-ray absorber). This unique exclusiveness eliminates the optical phenomena from the other elements. In order to demonstrate this advantage remarkably, composite organic materials are investigated in this chapter. In these materials, only some regions of the material contain the Br atoms, while the whole crystal has the same structure and the same optical properties.

Urea inclusion compounds[76, 77] are ideal samples for this purpose, in which the urea molecules form a hexagonal tunnel-containing host structure, and suitable guest molecules are packed along the one-dimensional tunnels (diameter *ca.* 5.5 Å) formed by the urea molecules (Fig. 5.1.a, Page 102). The host molecules are always urea, but the guest molecules can vary. In some circumstances, more than one type of guest molecule can be included within a given crystal of a urea inclusion compound.[78, 79]

Figure 5.1 (Page 102) shows an example of a single crystal of a urea inclusion compound containing two different types of guest molecule, forming a core-shell crystal structure where the core is pentadecane (PD) and the shell is 1,8-dibromooctane (DBO). This type of composite crystal structure is prepared by the transfer method – firstly, a single crystal of the PD/urea inclusion compound is grown in the normal way, and secondly, the single crystal is transferred into a solution of DBO and urea; then, the crystal growth continues with the DBO/urea inclusion compound growing on the original PD/urea crystal to form the "shell" (Fig. 5.1.c, Page 102). It is important to note that this two-stage growth process occurs with retention of the single crystal character of the urea host structure. The molecular spatial distributions of the two types of guest within the single crystal may be mapped quantitatively by confocal Raman microspectrometry (Fig. 5.1.e, Page 102), which conforms the hexagonal core-shell structure.[79]

For urea inclusion compounds, different types of guest molecules have different relative affinities for inclusion within the urea host structures. Generally, long-chain unbranched guest molecules are energetically more favourable.[80] Because the molecular length of PD is longer than DBO, the PD/urea inclusion compound is more thermodynamically stable than the DBO/urea inclusion compound.

Experiments involving molecular transport through a single crystal of the DBO/urea inclusion compound has also been demonstrated, by means of a designed set-up (Fig. 5.2.a, Page 103).[81-84] The DBO/urea single crystal is inserted into a reservoir containing liquid PD. As PD/urea is more favourable than DBO/urea, there is a thermodynamic driving force for PD molecules to enter at the end of the tunnel in contact with liquid PD, and the DBO molecules are expelled at the other end of the crystal. Confocal Raman microspectrometry is again used to record the transport process as a function of time.[83] As expected, the PD molecules push the DBO molecules from left to right in Fig. 5.2.a (Page 103), while the urea host structure does not change.

Figure 5.3 (Page 104) is another case of a molecular transport process. In this one, both ends of a DBO/urea single crystal are attached to reservoirs containing liquid PD. It has been concluded that in this case, the transport process occurs in both directions through the crystal.[85] The mechanism for this bi-directional transport process requires that the PD molecules are able to move into the adjacent tunnels because of crystal defects.

The above composite samples have been investigated previously by confocal Raman microspectrometry.[78, 79, 81-85] In this chapter, we investigate these samples by XBI, to explore the capability of XBI to qualify the spatial distributions of the two types of guest molecule in these materials. In addition, the decomposition of DBO/urea inclusion compounds by heat is also investigated.

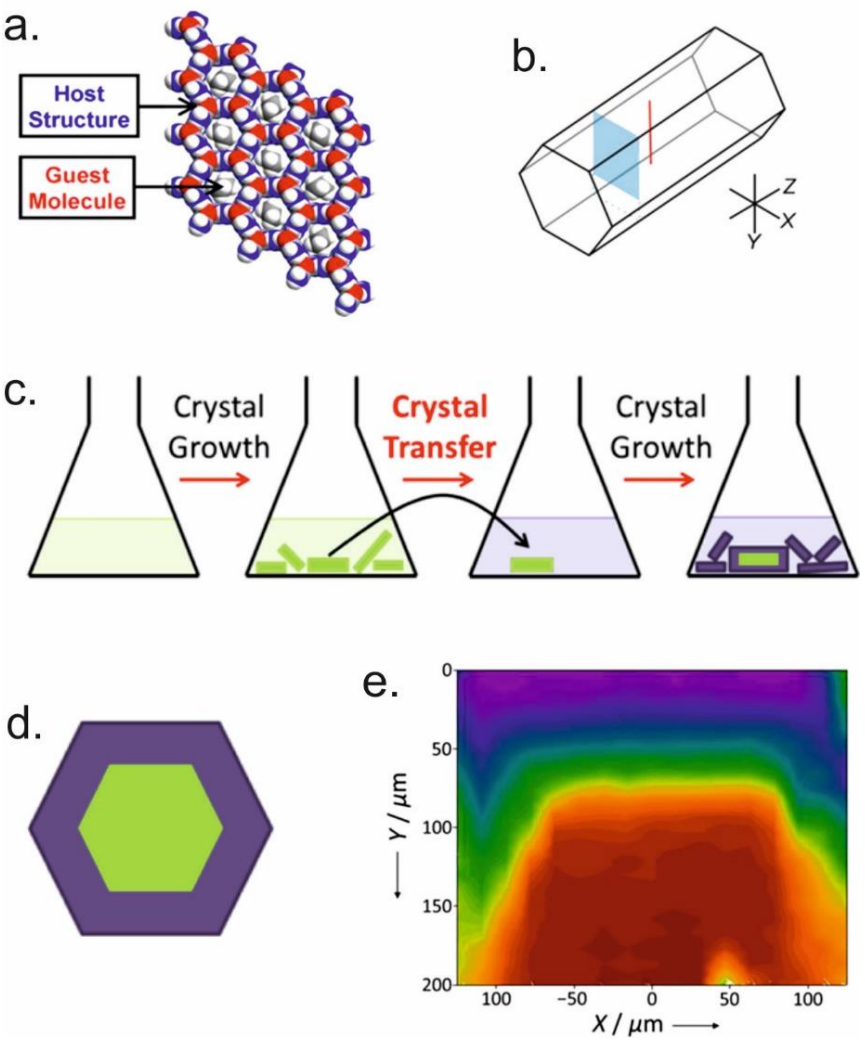

Figure 5.1 *(a) Crystal structure of a urea inclusion compound viewed along the tunnel axis, which is also the long-axis of the single crystal morphology. (b) Schematic illustration of mapped region (blue) by confocal Raman microspectrometry. (c) Crystal growth method to prepare core-shell urea inclusion compounds by the transfer method. The "core" is a PD/urea inclusion compound (green); and the "shell" is a DBO/urea inclusion compound (purple). (d) A schematic drawing of the theoretical molecular spatial distribution in cross-section (perpendicular to the tunnel axis). (e) Experimental scan results of the cross-section by confocal Raman microspectrometry. The color scale indicates the ratio of PD and DBO. The well-defined hexagonal spatial distributions are consistent with the theoretical drawing in (d). Reprinted with permission from Palmer, B. A.; Le Comte, A.; Harris, K. D. M.; Guillaume, F., Controlling Spatial Distributions of Molecules in Multicomponent Organic Crystals, with Quantitative Mapping by Confocal Raman Microspectrometry. J. Am. Chem. Soc.* ***2013****, 135, 14512-14515. Copyright 2013 American Chemical Society.*

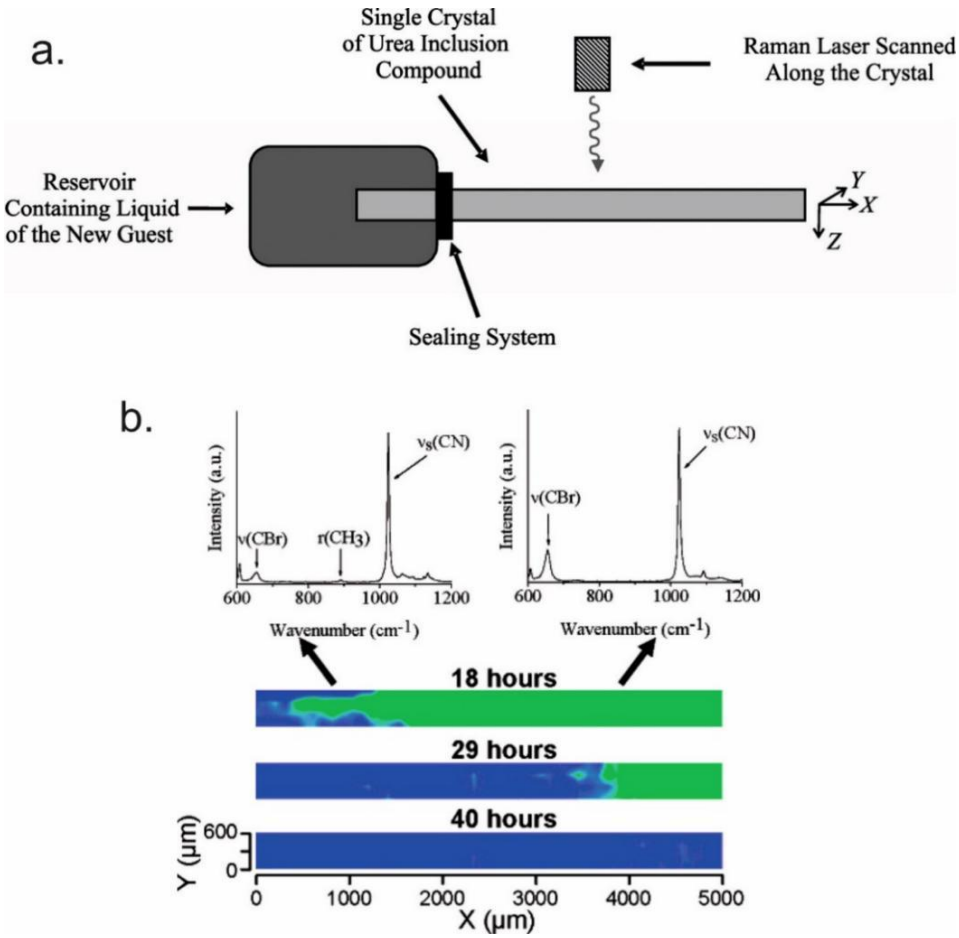

Figure 5.2 *(a) Schematic illustration of the experimental set-up for the molecular transport experiment. A single crystal of the DBO/urea inclusion compounds is attached horizontally on the right side of a reservoir containing liquid PD. The confocal Raman microspectrometry scans the whole crystal from left to right repeatedly during the molecular transport process, allowing the spatial distribution of the DBO and PD guest molecules within the crystal to be determined as a function of time. (b) Raman spectroscopy results of the single crystal at 18 hours, 29 hours and 40 hours. Blue is the PD-rich region, and green is the DBO-rich region. The two Raman spectra show the change of peaks between the DBO-rich region (right) and the region containing both DBO and PD (left). Reprinted with permission from (1) Martí-Rujas, J.; Harris, K. D. M.; Desmedt, A., In-situ Monitoring of Alkane-Alkane Guest Exchange in Urea Inclusion Compounds Using Confocal Raman Microspectrometry. Mol. Cryst. Liq. Cryst.* ***2006****, 456, 139-147 (Copyright 2006 American Chemical Society); and (2) Martí-Rujas, J.; Desmedt, A.; Harris, K. D. M.; Guillaume, F., Direct Time-Resolved and Spatially Resolved Monitoring of Molecular Transport in a Crystalline Nanochannel System. J. Am. Chem. Soc.* ***2004****, 126, 11124-11125 (Copyright 2004 American Chemical Society).*

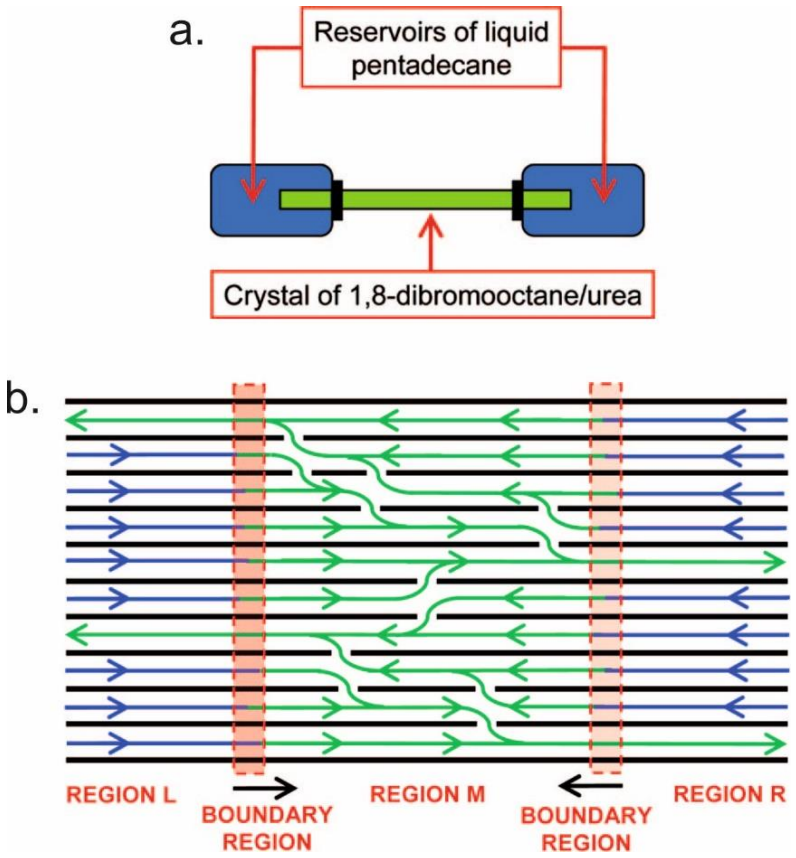

Figure 5.3 *(a) Schematic illustration of the experimental set-up for the bi-directional molecular transport experiment. A single crystal of the DBO/urea inclusion compound is attached horizontally between two reservoirs containing liquid PD. (b) Schematic illustration of the bi-directional molecular transport process, showing an intermediate stage in which PD guest molecules have penetrated both ends of the crystal (region L and region R), while the central region of the crystal contains only DBO guest molecules. Green is the DBO molecules; blue is the PD molecules; and black lines show the urea tunnels. Reprinted with permission from Martí-Rujas, J.; Desmedt, A.; Harris, K. D. M.; Guillaume, F., Bi-directional Transport of Guest Molecules through the Nanoporous Tunnel Structure of a Solid Inclusion Compound. J. Phys. Chem. C* ***2009****, 113, 736-743. Copyright 2009 American Chemical Society.*

5.2 X-ray Birefringence Imaging and X-ray Tomography Studies of Core-Shell Crystal

Core-shell single crystals were prepared by the transfer method, with the PD/urea inclusion compound as the "core" and the DBO/urea inclusion compound as the "shell".

The cross-section of the single crystal is shown in an X-ray tomography image, which was recorded under pink beam at the I13 beamline of Diamond Light Source (different from B16 of XBI). The hexagonal cross-section is quite clear, which is the overall shape of the crystal. The outside bright parts represent the DBO/urea inclusion compound, and the inner dark region represents the PD/urea inclusion compound.

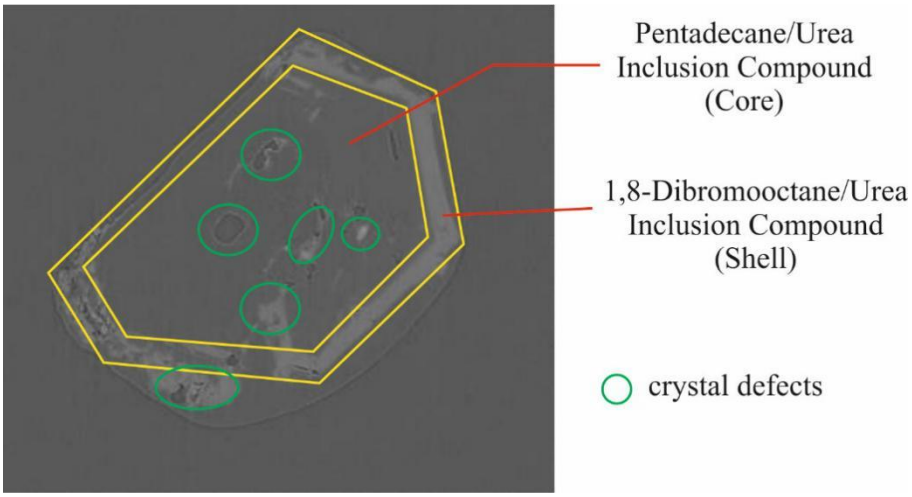

Figure 5.4 *An X-ray tomography image of the cross-section of a core-shell single crystal under pink beam. The outside bright regions are the "shell" part comprising the DBO/urea inclusion compounds. The imperfections are from crystal defects.*

Single crystals of the DBO/urea inclusion compound have been proved to be birefringent in XBI with the effective X-ray optic axis parallel to the tunnel axis (i.e., the long-axis of the crystal morphology).[24] As PD/urea does not have Br atoms, XBI data recorded with X-ray energy of Br K-edge would not exhibit the birefringence phenomenon. Thus, for composite crystals containing regions of both DBO/urea and PD/urea, the XBI images would be expected to show birefringence only for those regions of the crystal containing DBO guest molecules.

Figure 5.5 (Page 107) illustrates the spatial distributions of DBO and PD guest molecules within a core-shell crystal of a urea inclusion compound. As PD is more favorable than DBO to form urea inclusion compounds,[80] the "core" part – a single crystal of the PD/urea inclusion compound – is prepared firstly. Then, the DBO/urea inclusion compound forms the "shell" part surrounding the PD/urea. In the final completed core-shell single crystal, the tunnels of the urea host structure are along the long-axis of the single crystal, so the long-chains of both PD and DBO guest molecules are also parallel with the long-axis of the single crystal. This means that in the core-shell two-component

crystals, the orientations of the PD and DBO guest molecules are the same as in the corresponding single-component crystals of PD/urea and DBO/urea respectively.

The previous study[24] has demonstrated that, for a single crystal of the DBO/urea inclusion compound with the long-axis (tunnel axis) perpendicular to the direction of propagation of the incident X-rays, the highest transmitted intensity arises for $\chi = 45°$ and $\chi = 135°$, and the lowest transmitted intensity arises at $\chi = 90°$. In the core-shell single crystal, if the single crystal is also mounted in the *yz-plane*, the projected image on the detector should be a rectangle. As the "shell" region of the crystal is DBO/urea, the rectangle can be divided into three parts: the middle part contains regions of both PD/urea and DBO/urea within the path of the beam, while the two side parts are pure DBO/urea. Because only the regions of the crystal containing DBO give birefringence phenomenon for the selected X-ray energy (i.e., Br K-edge), the regions of pure DBO/urea should exhibit a bigger contrast in the XBI images, which is shown in the "XBI Predicted Images" part of Fig. 5.5. The actual experimental images (bottom of Fig. 5.5) verify that this assumption is correct. It is clear that, at $\chi = 45°$ and $\chi = 135°$, there are two bright edges in the single crystal, and these two bright edges become dark at $\chi = 90°$. The middle part of the crystal also exhibits birefringence; however, the change in intensity as a function of crystal orientation is much lower than that for the two edge, reflecting the fact that, for this region of the crystal, only a fraction of the material in the path of the beam contains DBO guest molecules.

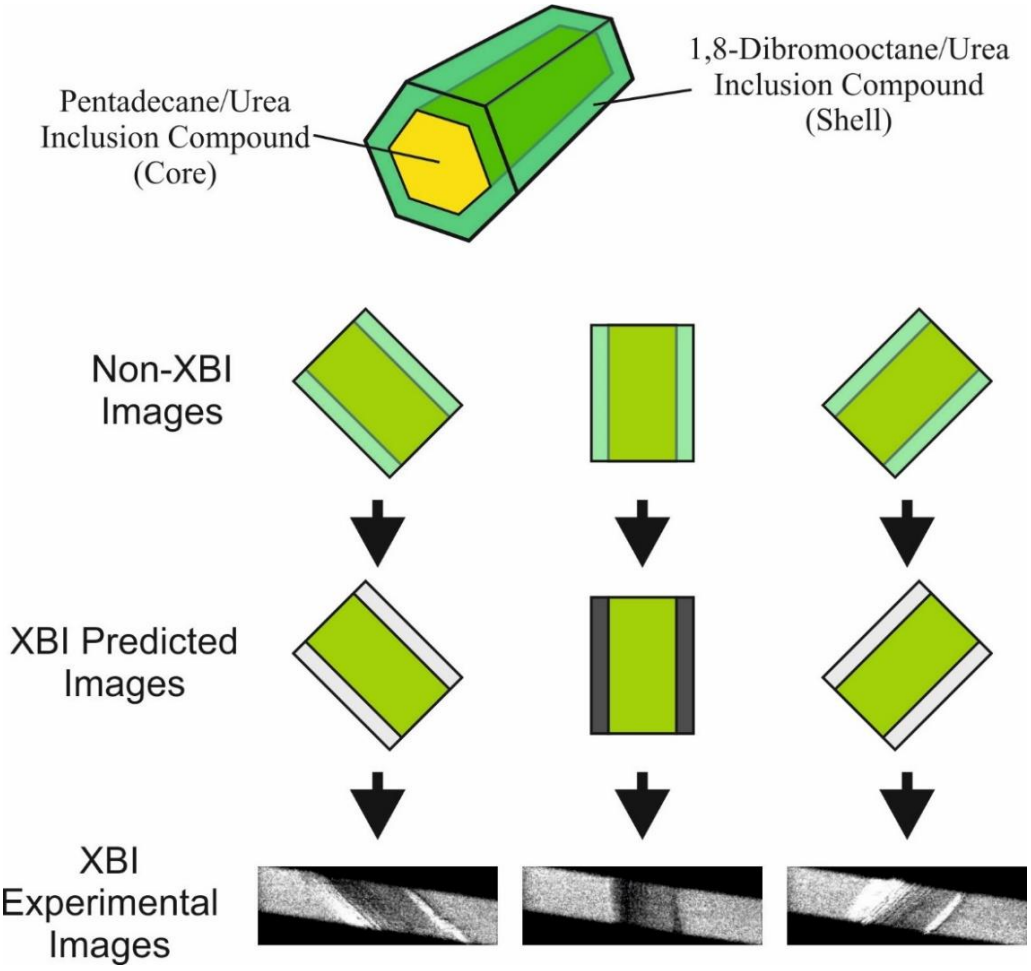

Figure 5.5 *XBI images of a core-shell single crystal. The yellow parts are the PD/urea inclusion compound and the green parts are the DBO/urea inclusion compound. Viewing from the side of the single crystal, the middle part comprises region of both PD/urea and DBO/urea; while, the side parts comprise only DBO/urea.*

5.3 X-ray Birefringence Imaging Studies of Molecular Transport Process

In *in-situ* confocal Raman microspectrometry experiments, both one-directional and bi-directional transport processes have been investigated.[81-85] Similarly, the two types of transport process are investigated separately in our XBI measurements.

In order to get the biggest contrast in the XBI images between regions of the crystal containing DBO and regions containing PD, all the DBO/urea single crystals were oriented with a 45° tilt angle relative to the plane of incident X-ray polarization

(horizontal). For one-directional transport experiment, a sample cell with a 45° tilt metal tube on the lid was designed (Fig. 5.6.a). The liquid PD was first put into the cell, and then the DBO/urea single crystal was inserted into the cell through the tilt metal tube. Thus, the bottom end of the DBO/urea single crystal is immersed in the liquid PD and the whole crystal is oriented at the 45° tilt orientation. For the bi-directional transport experiment, the DBO/urea single crystal was fixed at 45° tilt orientation with the help of a glass tube and a plastic tube (Fig. 5.7.a). As glass and plastic are transparent to X-rays, this set-up provides a suitable opportunity to observe the transport process by XBI. Strictly speaking, the set-up in Fig. 5.7.a is a totally immersed design, different from the previous model with only two ends of the crystal immersed in the liquid PD (Fig. 5.3, Page 104). This means that, if there are defects on the crystal surface, the transport may also start from the surface, but the main pathway for molecular transport should be still along the urea tunnels.

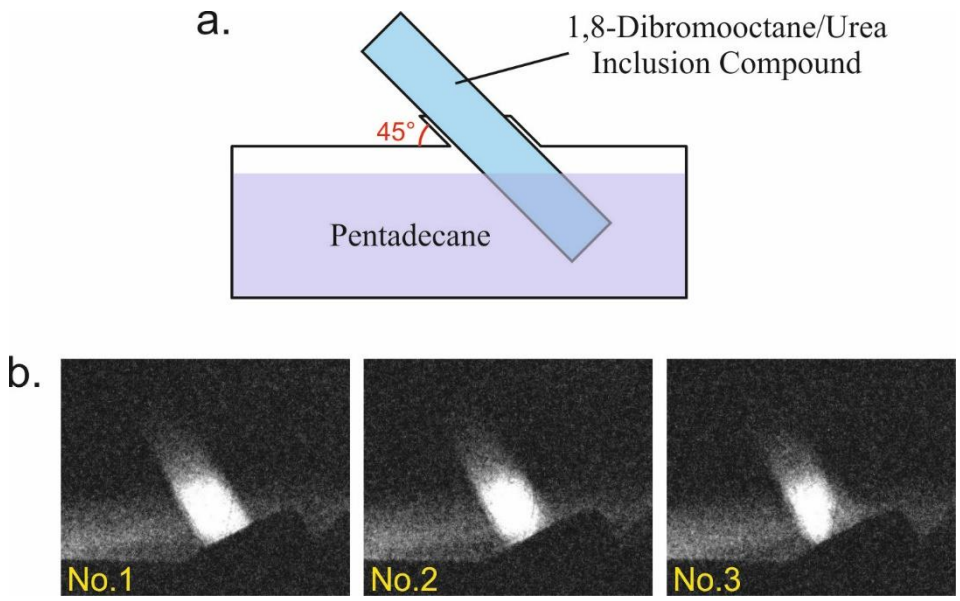

Figure 5.6 *One-directional molecular transport experiment. (a) Schematic illustration of the experimental set-up. Liquid PD is located in a cell with a metal tube on the lid tilted at 45°. A single crystal of the DBO/urea inclusion compound is placed into the metal tube, and the end of the crystal is immersed in the liquid PD. (b) XBI images of the single crystal as a function of time. The black edge on the right-bottom is the metal tube. No.1 is the XBI image of DBO/urea which has been immersed in liquid PD for ca. 14 hours. No.2 is the XBI image of the same sample recorded ca. 1.5 hours later after No.1. No.3 is the XBI image of the same sample recorded ca. 4 hours later after No.2.*

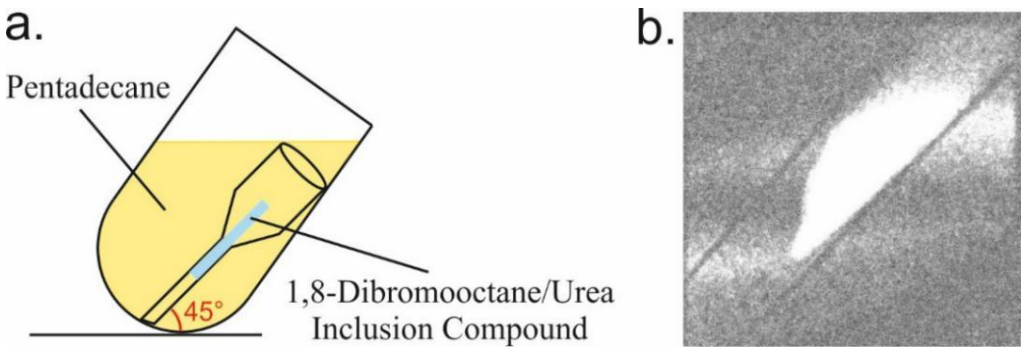

Figure 5.7 *Experimental set-up for XBI study of bi-directional molecular transport. (a) Schematic illustration of experimental set-up. A single crystal of the DBO/urea inclusion compound is stuck in a glass funnel-shaped tube. This glass tube is placed into a plastic test tube. The angle between the long-axis of the single crystal and the horizontal plane is 45°. Enough liquid PD is added to the plastic test tube to make sure all the DBO/urea single crystal is totally immersed in the liquid PD. (b) XBI image of the single crystal after ca. 24 hours.*

Figure 5.6.b and Figure 5.7.b show XBI images recorded during the one-directional and bi-directional transport experiments respectively. At the beginning, the DBO/urea single crystal shows the conventional birefringence, and is maximally bright in the χ = 45° orientation shown. As the transport progresses, the PD molecules will enter the crystal and displace the DBO molecules along the urea tunnels. Thus, after enough time, some dark regions are generated at the end of the single crystal, which is indicative of the regions of the crystal occupied by PD guest molecules.

Interestingly, in contrast to the results from the study of the transport by confocal Raman microspectrometry, in the XBI results, the boundary between the PD and the DBO regions of the crystal is not perpendicular to the urea tunnels. In both types of transport process, the boundary is tilted by nearly 45° compared to the urea tunnel direction. This phenomenon is still unknown and required to be investigated further.

5.4 X-ray Birefringence Imaging Studies of Thermal Decomposition of Urea Inclusion Compounds

Thermal decomposition of urea inclusion compounds has been investigated for over 50 years.[86-88] The decomposition process is endothermal and happens below the

melting point of urea.[88, 89] It is accompanied by loss of guest molecules, and the temperature at which decomposition begins to occur depends on the molecular length of the guest molecules.[86] Here, we use the DBO/urea inclusion compound as an example to explore the opportunity to apply XBI measurements in a time resolved manner to explore this kind of thermal decomposition process.

The traditional methodology to investigate thermal changes is DSC. In order to understand more about the thermal decomposition of the DBO/urea inclusion compound before XBI measurements, a DSC test was first carried out (Fig. 5.8). A small broad endothermal peak around 90 °C represents the decomposition of the inclusion compound. It cannot represent any other physical change of DBO, because the melting point of pure DBO is 12 – 16 °C and the DBO boiling point is 270 – 272 °C. After decomposition of the DBO/urea inclusion compound, the DBO released from the crystal is likely to vaporize, leaving pure crystalline urea in the DSC pan. The endothermal peak at 133 °C represents the subsequent melting of the pure urea. The cooling curve does not have any exothermal peak, showing this kind of decomposition is irreversible.

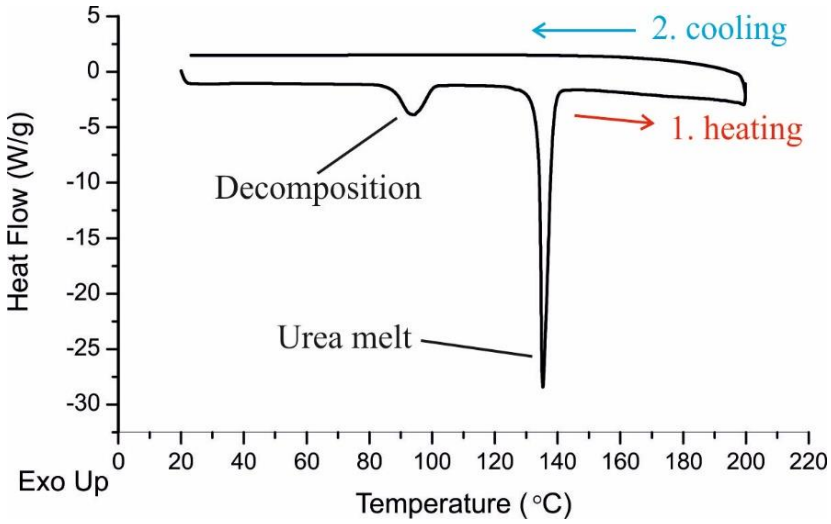

Figure 5.8 *DSC data for single crystals of the DBO/urea inclusion compound. Crystals were placed at room temperature and heated to 200 °C. The sample was then cooled back to room temperature. The rates of heating and cooling were 10 °C/min. The small broad peak is from the thermal decomposition of DBO/urea. The big sharp peak is from the melting of pure crystalline urea.*

Figure 5.9 illustrates the molecular change in the thermal decomposition process. The outside light pink cages are the urea tunnels and each tunnel has hexagonal cross-

section. The DBO molecules (dark pink cylinders) are packed into the urea tunnels with the molecular chains parallel with the tunnels. This well-ordered DBO arrangement is the reason that birefringence is observed in XBI. However, with the loss of DBO guest molecules upon decomposition and the collapse of the urea host structures, the previous ordered arrangement is progressively lost. As the birefringence is generated by Br in the DBO, the loss of DBO will weaken the birefringence signal. Figure 5.10 shows the XBI experimental images of a single crystal of the DBO/urea inclusion compound (a) before, (b) during and (c) after the heat treatment. To give better contrast, the crystal was oriented at $\chi = 45°$. It is obvious that, after thermal decomposition, the XBI image becomes darker, which is consistent with the theoretical prediction due to loss of the DBO guest molecules. This *in-situ* experiment also shows that the thermal decomposition is generated from outside, and the DBO molecules in the outside part lose their order firstly (Fig. 5.10.b).

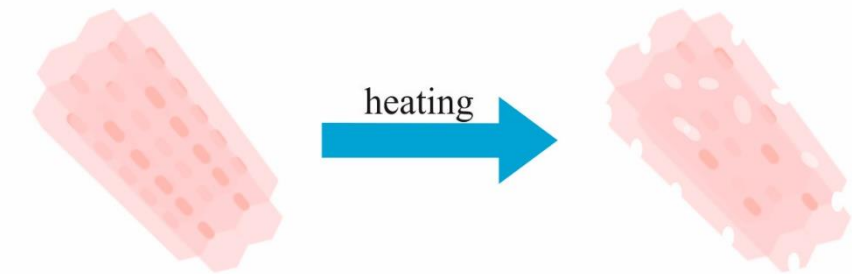

Figure 5.9 *Schematic illustration of thermal decomposition of a single crystal of the DBO/urea inclusion compound. The outside hexagonal tunnels are the urea "host" structure. The inside small cylinders are DBO "guest" molecules.*

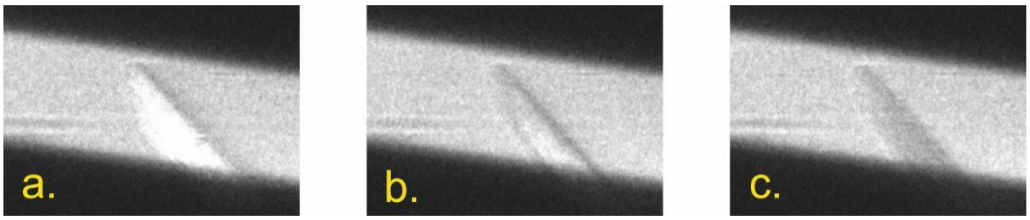

Figure 5.10 *XBI images of a DBO/urea inclusion compound single crystal at $\chi = 45°$ captured (a) before, (b) during and (c) after the thermal decomposition. The temperature is kept at 85 °C.*

In order to evaluate the decomposition rate at different temperatures, three individual DBO/urea inclusion compounds single crystals were studied at 79 °C, 82 °C and 85 °C respectively. In each case, the single crystal was fixed at $\chi = 45°$, and XBI images were recorded every 3.6 seconds. The intensity is normalized by consideration of

the strongest intensity (at the beginning of the process) and the lowest intensity (at the end of the process). The change in intensity as a function of time is shown in Fig. 5.11. The transmitted X-ray intensity at χ = 45° is interpreted to be proportional to the amount of DBO guest molecules present in tunnels of the urea host structure oriented at χ = 45°, and hence correlates with the amount of "un-decomposed" DBO/urea crystal that remains as a function of time. After enough time, no more DBO molecules are present and the intensity remains at the final low value. As thermal decomposition of urea inclusion compounds is an activated process, higher temperature is expected to speed up the decomposition process. The trend of the slope of these three curves is green (85 °C) > red (82 °C) > black (79 °C), which proves that increasing temperature increases the rate of thermal decomposition of urea inclusion compounds.

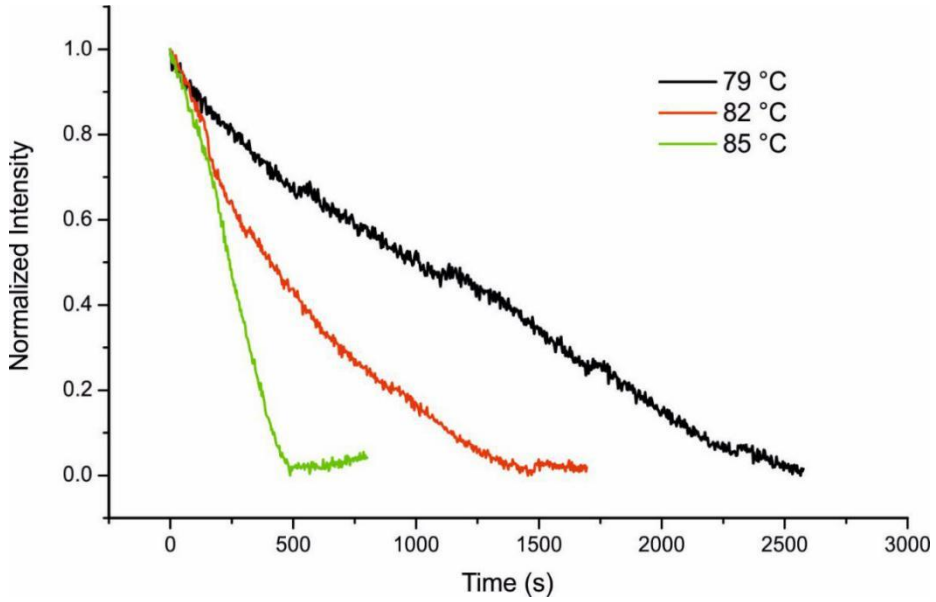

Figure 5.11 *The XBI intensity as a function of time at different temperatures, for the thermal decomposition of DBO/urea single crystals. Green, 85 °C; red, 82 °C; and black, 79 °C.*

The activation energy (*Ea*) for this decomposition process can be calculated by the Arrhenius Equation[90] (Eq. 5.1):

$$\ln k = \ln A - \frac{Ea}{RT} \qquad (5.1)$$

where k is the rate constant, A is the pre-exponential factor, T is the absolute temperature (in Kelvin) and R is the universal gas constant (8.314 J mol^{-1} K^{-1}).

Figure 5.12 shows the relationship between the rate constant (k) and temperature (T) for the three experimental data sets (79 °C, 82 °C and 85 °C) in Fig. 5.11. The three data points form a linear Arrhenius plot (blue dashed line in Fig. 5.12), and the best-fit straight line is given in Eq. 5.2, with a fitting coefficient (R^2) of 0.9505. Then, the activation energy (Ea) is determined (Eq. 5.3) to be 316 kJ mol^{-1}.

$$\ln k = 109.26 - \frac{38051}{T} \tag{5.2}$$

$$Ea = 38051 \times R = 316 \text{ kJ mol}^{-1} \tag{5.3}$$

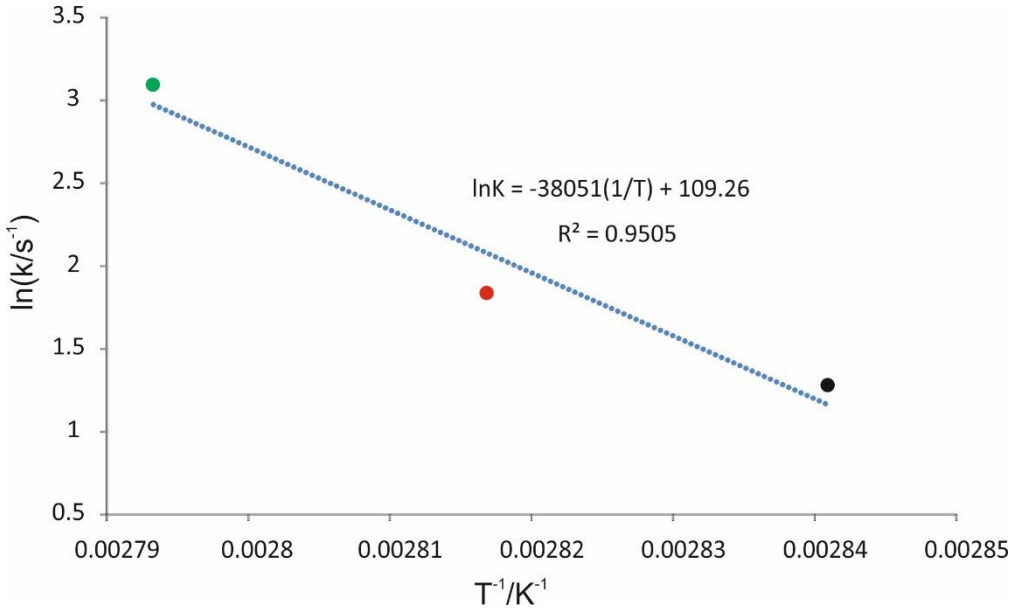

Figure 5.12 *Plot of ln(k/s^{-1}) versus T^{-1}/K^{-1} for the three experimental data sets (at 79 °C, 82 °C and 85 °C) in Fig. 5.11. The rate constant (k) at each temperature is determined from a linear fit to the data in Fig. 5.11. The best-fit straight line (dashed line) and the equation for this line are also shown.*

5.5 Conclusions

In this chapter, through the study of three types of crystals and processes, XBI has demonstrated the capability to characterize the spatial distribution of molecules in composite organic materials and to study the time-dependence of processes in which the spatial distribution changes with time.

For core-shell crystals of PD/urea and DBO/urea, XBI is successful to give the information on the distribution of the DBO molecules within the crystals. Compared with

confocal Raman microspectrometry, XBI not only shows the molecular spatial distributions, but also detects the orientations of the target molecules. For example, if the "core" and "shell" both contained C–Br bonds but with different orientations, this difference could be distinguished in XBI but not in confocal Raman microspectrometry.

For molecular transport experiments, apart from the spatial distribution, a significant feature in the XBI results is the tilt of the boundary line between the original and new guest molecules. This phenomenon was not observed in the previous study by confocal Raman microspectrometry, perhaps because the sample is placed non-horizontally in the XBI study. As synchrotron beam time is always limited and the transport experiment usually takes long time (~ several days), only a few samples (less than 5) could be tested in the present work. For rigorous consideration, some more tests are required to investigate the above observations.

For the thermal decomposition experiments, with the addition of the temperature control system, XBI can take be exploited to express thermal behaviour of materials – e.g., to identify phase transitions. Furthermore, in the present study of thermal decomposition, as the XBI intensity is related to the amount of the DBO "guest" molecules aligned within regions of un-decomposed DBO/urea inclusion compound crystals, the decomposition rate of the DBO/urea inclusion compound can be evaluated by XBI, and then the corresponding activation energy can be derived.

Before the development of XBI, the birefringence phenomenon was used almost exclusively in optical analyses,[91] especially by Polarizing Optical Microscopy (POM). For the composite organic materials, for example in the urea inclusion compounds studied here, the POM results would be identical for DBO/urea and PD/urea, as the optical birefringence is dictated by the overall crystal symmetry (hexagonal), which is the same for the DBO/urea and PD/urea regions of the composite crystals. Thus, POM could not be used to characterize the spatial distribution of PD and DBO guest molecules within the composite materials. However, for XBI, the X-ray birefringence selectively observes the target Br atoms, which allows accurate characterization of the spatial distributions of the two different types of guest molecule within the composite urea inclusion compounds.

Chapter 6

X-ray Birefringence Imaging on Pairs of Crystals with Independent Orientations

6.1 Introduction

The previous XBI experiments described in this thesis are all based on the situation with a single sample in the beam (either a single crystal or a liquid crystalline phase). As the research moves further, an interesting question is what the XBI behaviour will be like when two single crystals are present in the beam with different orientations. In this chapter, some preliminary researches about this question are described.

Figure 6.1 gives a schematic illustration of the XBI set-up for such experiments involving pairs of crystals with independent orientations. A rotation stage was added into the standard XBI set-up for mounting the second single crystal. The first single crystal is mounted on the same goniometer used to orient the sample in the earlier studies. Both the goniometer and the rotation stage can be controlled independently, thus, different combinations of the orientations of the two crystals can be achieved with this experimental set-up.

In previous research, single crystals of the 1-bromoadmantane/thiourea inclusion compound (1-BA/thiourea) were demonstrated to behave as a dichroic filter for X-ray polarization analysis.[92, 93] The crystal structure of the 1-BA/thiourea inclusion compound single crystal was introduced previously in Fig. 1.20 (Page 22), in which the thiourea molecules construct hexagonal-shaped host tunnels and the 1-BA guest molecules are aligned inside these tunnels, with the C–Br bonds of all guest molecules parallel to the tunnel axis (the long-axis of the single crystal). Figure 6.2 (Page 117) shows that this material exhibits a strong dichroic resonance close to the Br K-edge, and the transmittance of linearly polarized X-rays as a function of the orientation of the crystal is also shown. When the C–Br bonds are parallel to the plane of the incident polarized X-rays (tuned to the Br K-edge), the lowest transmittance is observed; when the C–Br bonds are perpendicular to this plane, the highest transmittance is observed. This demonstrates that

the single crystal of 1-BA/thiourea can attenuate the linearly polarized X-ray photons along one preferable direction, and thus behaves as an X-ray dichroic filter.

The 1-BA/thiourea dichroic filter for X-ray analysis was reported in 2003 (about 15 years ago).[93] However, at that time, no strategy had been developed for producing large flat-plate crystals of this material, thus inhibiting its practical applications as a transmission-based polarization analyzer. In this chapter, we report a strategy that enables flat-plate single crystals of 1-BA/thiourea to be prepared successfully, based on an epitaxial crystal growth method. Analogous to the Polaroid sheet in Polarizing Optical Microscopy (POM), the flat-plate single crystal of 1-BA/thiourea is also a new XBI set-up using, for the first time, a transmission-based X-ray polarization analyzer.

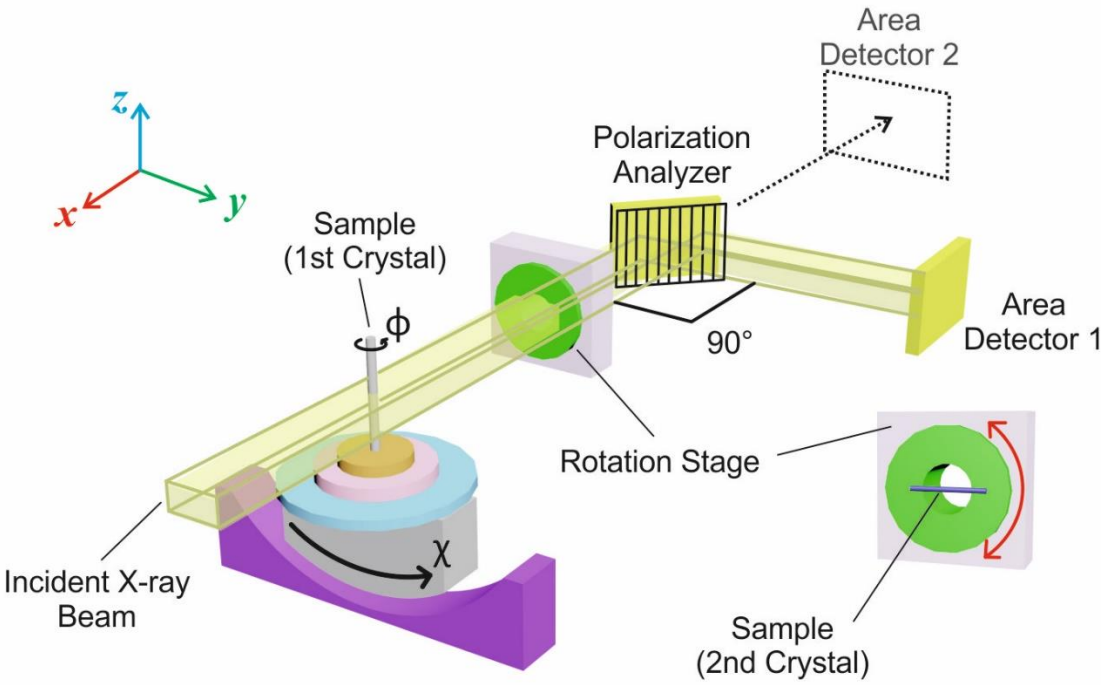

Figure 6.1 *Experimental set-up for XBI studies of two independently oriented crystals. An additional rotation stage is placed between the goniometer and the analyzer. The rotation stage can rotate by 360°. There is a small hole in the middle of the rotation stage to allow the X-rays pass through. The first crystal is mounted as usual on the goniometer. The second crystal is mounted on the rotation stage, with X-ray optic axis (C–Br bond direction) aligned perpendicular to the x-axis.*

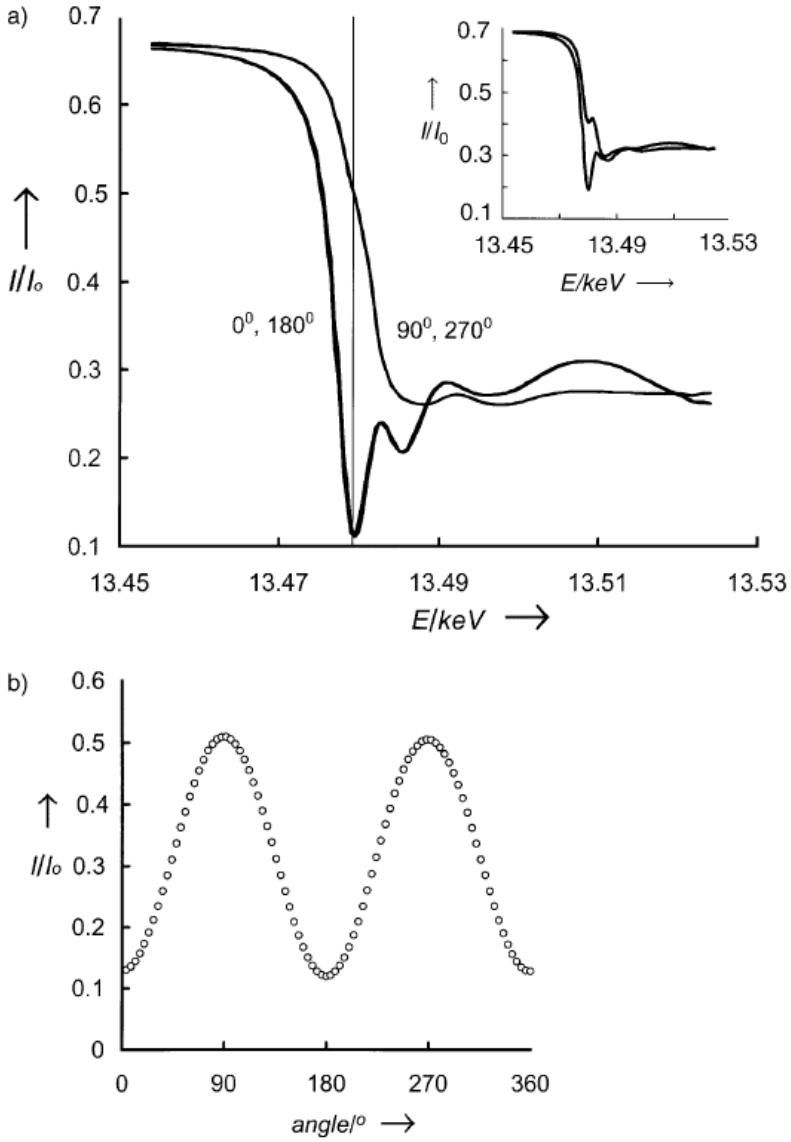

Figure 6.2 *(a) X-ray transmittance (I/I_0) through a single crystal of 1-BA/thiourea as a function of energy (E) close to the Br K-edge, with the X-ray polarization parallel (0° and 180°) and perpendicular (90° and 270°) to the long-axis of the crystal (parallel to the C–Br bonds). (b) X-ray transmittance (I/I_0) as a function of the orientation of a single crystal of the 1-BA/thiourea inclusion compound (the angle is defined between the long-axis of the crystal and the direction of polarization of the incident polarized X-rays) at the Br K-edge energy. Reprinted with permission from Chao, M. H.; Kariuki, B. M.; Harris, K. D. M.; Collins, S. P.; Laundy, D., Design of a Solid Inclusion Compound with Optimal Properties as a Linear Dichroic Filter for X-ray Polarization Analysis. Angew. Chem.* ***2003****, 42, 2982-2985. Copyright 2003 John Wiley and Sons.*

6.2 XBI Studies of Two Independently Oriented Single Crystals

In Chapter 4, the intensity change in XBI images of 1,4-dibromo-2,3,5,6-tetramethylbenzene (DBTMB) was discussed in depth. For a single crystal at room temperature (RT) with the big face perpendicular to the incident beam, the brightest orientations were at χ = 45°, 135°, 225° and 315°, and the darkest orientations were at χ = 0° (360°), 90°, 180° and 270°. If two single crystals aligned at the brightest or darkest orientations are now present in the X-ray beam, what will be the observed behaviour? For example, if the first crystal is at χ = 45° (the brightest orientation) and the second crystal is at χ = 135° (the brightest orientation), would the common area (i.e., the region in which the X-ray beam passes through both crystals) be brighter than for an individual crystal? If the second crystal is instead at χ = 90° (the darkest orientation), would the behaviour of the two crystals cancel each other out? In order to answer the above questions and to understand the X-ray birefringence observed for two independently oriented crystals, we now report XBI experiments with two individual single crystals.

The first experiment is based on DBTMB single crystals. Two crystals were glued to the rotation stage, either at an angle of 45° or 90° with respect to each other, and then placed on the rotation stage. In this experiment, there is no sample on the goniometer (so the set-up is different from Fig. 6.1, Page 116).

Figure 6.3 shows the XBI images for the case of two crystals glued at 90°. As the angle between the two crystals is fixed at 90°, when one crystal is at the brightest (or darkest) position, the other crystal must also be at another brightest (or darkest) position. The common area of the two single crystals is a rectangle. From the XBI images in Fig. 6.3, the common rectangle is dark for all orientations of the two-crystal sample, irrespective of whether the two crystals are at brightest positions or darkest positions. Especially when the two crystals are at brightest positions (the 2^{nd}, 4^{th}, 6^{th} and 8^{th} images), it is clear that the common rectangle is dark, while the non-overlaid parts of each crystal still show the conventional brightness. Thus, for such two-layer crystals in XBI, bright plus bright, does not produce brighter.

Figure 6.4 (Page 120) shows the XBI images for two crystal glued at 45°. As the angle between the two crystals is fixed as 45°, when one crystal is at the brightest orientation, the other crystal must be at the darkest orientation, and *vice versa*. The common area is a rhombus and its intensity changes as the pair of crystals is rotated.

However, the intensity of the common area is not simply represented by the addition of the intensities of the two individual single crystals.

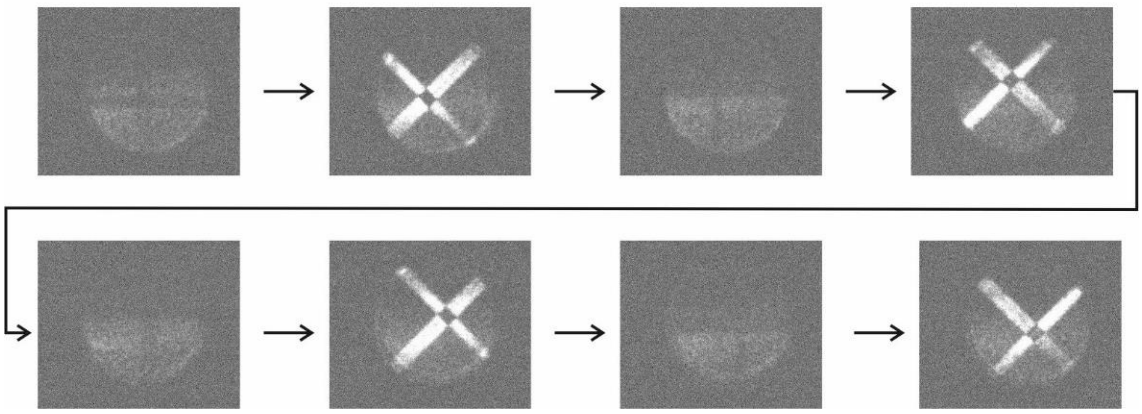

Figure 6.3 *XBI images of two overlaid single crystals of DBTMB at RT. The two single crystals were glued on the rotation stage with the (-1 0 1) faces of both crystals perpendicular to the propagation direction of the incident X-ray beam. The angle between the long-axes of the two crystals is fixed at 90°. The rotation direction of the stage is clockwise.*

From the above experimental results, the XBI behaviour of the two-layer crystals seems more complicated than we expected at the beginning. In order to understand the observed phenomena, a detailed analysis is needed. In Chapter 1, we already discussed that, when a plane wave passes through a birefringent sample, it is split into two orthogonal plane waves with a phase discrepancy (Fig. 1.10, Page 9). This is the situation that exists for the X-rays after passing through the first single crystal. Thus, the nature of the X-rays incident on the second crystal is different from the X-rays that were incident on the first crystal. As all the previous calculations of XBI intensity were based on the assumption that the incident rays are a polarized plane wave, if the incident X-rays for the second crystal are different, then the previous types of analysis of XBI behaviour cannot necessarily be applied to rationalize the XBI behaviour of the two-layer crystals.

When two orthogonal plane waves propagating in the same direction are combined, they can form three types of polarized light: linear, circular and elliptical. Figure 6.5 (Page 121) shows the interference phenomena in each case. Green arrows show the propagation direction. The area detector is perpendicular to the propagation direction. The phase difference between the two plane waves is ε. The amplitudes of each plane wave are A_1 and A_2. If ε is 0 or π, the projection on the detector is a line, corresponding

to linearly polarized light. If the phase difference is ±½ π and the amplitudes are equal, the projection is a circle, corresponding to circularly polarized light. In the other cases, the projection is an ellipse, corresponding to elliptically polarized light. The left or right polarization is defined as viewed from the detector to the light source. Thus, if the rotation of the combined electric vectors is anti-clockwise, it is described as right polarization and *vice versa*. Actually, both linear polarization and circular polarization can be regarded as special cases of elliptical polarization.

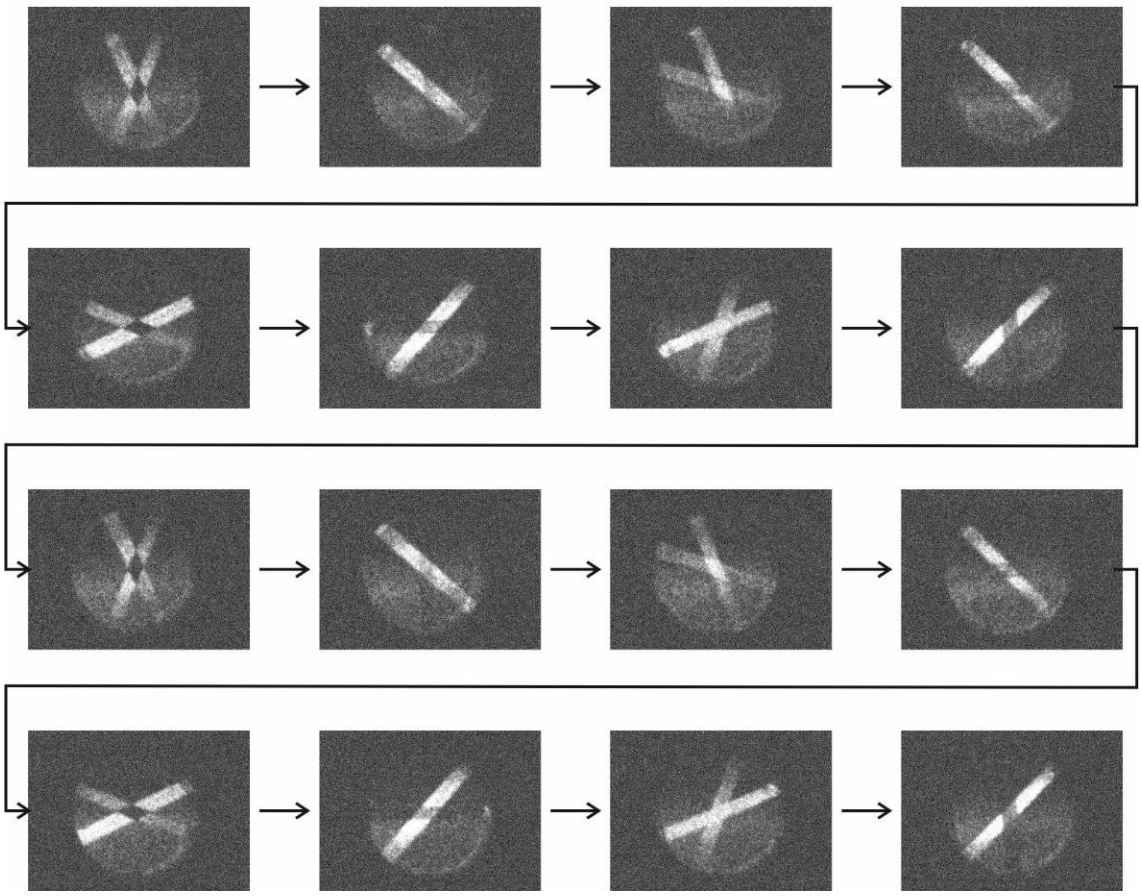

Figure 6.4 *XBI images of two overlaid single crystals of DBTMB at RT. The two single crystals were glued on the rotation stage with the (-1 0 1) faces of both crystals perpendicular to the propagation direction of the incident X-ray beam. The angle between the long-axes of the two crystals is fixed at 45°. The rotation direction of the stage is anti-clockwise.*

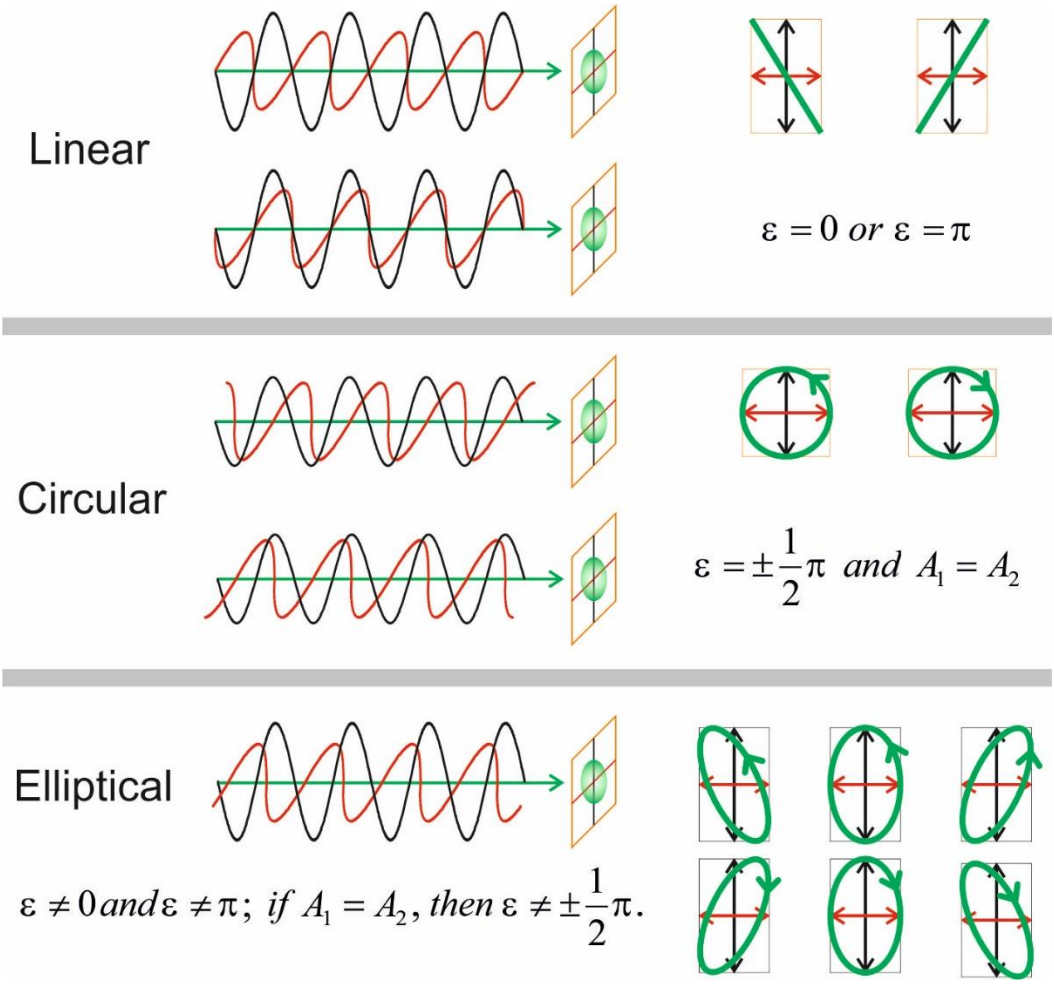

Figure 6.5 *Schematic illustration of three types of polarized light generated by a pair of orthogonal plane waves: linear, circular and elliptical. The phase difference is ε, and the amplitudes of the two plane waves are A_1 and A_2.*

From Fig. 6.5, it is clear that the incident X-rays for the second crystal could represent any one of the above three cases, depending on the phase difference (ε) and the amplitude of each plane wave (A_1 and A_2) emerging from the first crystal. From Eq. 1.13 (Page 10) and Eq. 1.16 (Page 10), the phase difference (ε) is determined by the sample thickness (d) and the refractive indices of the slow-ray and the fast-ray (n_s and n_f). Until now, we do not know the refractive index for the materials under the conditions of our XBI measurements, and therefore the type of the incident X-rays for the second crystal in the experiments described above cannot be established. The following theoretical analysis is based on the assumption of elliptically polarized light, because in most circumstances, the general case in which the incident X-rays for the second crystal are elliptically polarized may be expected.

Figure 6.6 is a general mathematical representation of an ellipse. The distance between the centre and the point (R) on the ellipse is r. The angle between the vector $\overrightarrow{OR}$ and the *x-axis* is α. As the projection of the polarized light is elliptical, the value of r represents the resultant amplitude of the two plane waves. Thus, the amplitude of the elliptically polarized light is different for different orientations. The position of R can be represented by Eq. 6.1. After several deductive processes (Eq. 6.2 and Eq. 6.3), the value of r can be represented by a, b and α (Eq. 6.4). In Chapter 1, we established the XBI intensity representation, which is proportional to $\sin^2(2\theta)$ (Eq. 6.5). As the light intensity is proportional to the square of the amplitude, in the two-layer crystals case, the intensity should be proportional to $r^2\sin^2(2\theta)$ (Eq. 6.6). Substituting the expression for r (Eq. 6.4) into this expression for intensity, we can derive an equation that describes intensity as a function of θ and α (Eq. 6.7).

When the χ value of the first crystal is changed, the direction of the X-ray optic axis in space is also changed. Thus, the corresponding elliptical projection of the transmitted X-rays will also change orientation (Fig. 6.7). Considering this phenomenon, a further function $f(\theta_1, \theta_2)$ is derived (Eq. 6.8), in which θ_1 and θ_2 correspond to the χ values of the first crystal and the second crystal respectively. Figure 6.8 (Page 124) shows a 3D plot of this function. In order to compare the function $f(\theta_1, \theta_2)$ with our experimental data, the ranges of θ_1 and θ_2 in Fig. 6.8 (Page 124) are taken as [45°, 270°] and [0°, 360°] respectively (the same ranges as our experimental data).

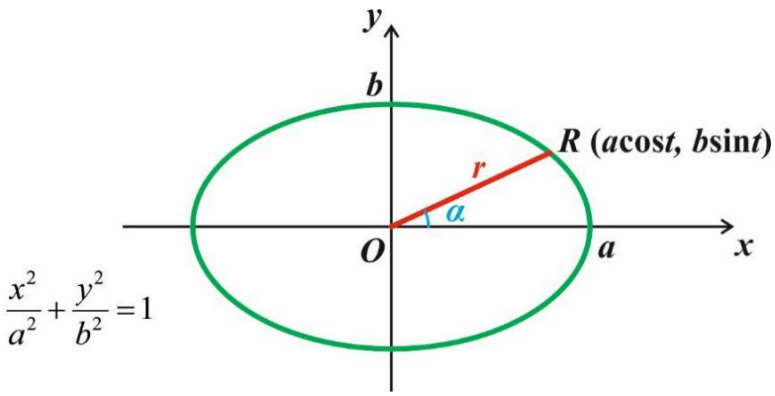

Figure 6.6 *An ellipse with the major axis along the x-axis and the minor axis along the y-axis. R is a point on the ellipse. The distance between the point R and the centre of the ellipse is r. The angle between the vector* $\overrightarrow{OR}$ *and the x-axis is α.*

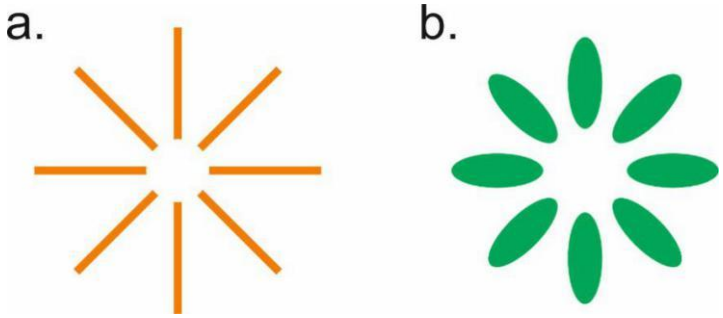

Figure 6.7 *Schematic illustration of (a) different orientations of the X-ray optic axis of the crystal and (b) the corresponding elliptically polarized transmitted radiation.*

$$x = a\cos t,\ y = b\sin t \tag{6.1}$$

$$\begin{aligned}
&\because \frac{y}{x} = \tan\alpha = \frac{b}{a}\tan t \\
&\therefore \frac{a^2}{b^2}\times\tan^2\alpha = \tan^2 t \\
&\therefore \frac{a^2}{b^2}\times\tan^2\alpha + 1 = \frac{1}{\cos^2 t} \\
&\therefore \frac{a^2}{b^2}\times\tan^2\alpha\times\cos^2\alpha + \cos^2\alpha = \frac{\cos^2\alpha}{\cos^2 t} \\
&\therefore \frac{a^2}{b^2}\times\sin^2\alpha + \cos^2\alpha = \frac{\cos^2\alpha}{\cos^2 t}
\end{aligned} \tag{6.2}$$

$$\begin{aligned}
r^2 &= x^2 + y^2 \\
&= a^2\cos^2 t + b^2\sin^2 t \\
&= \cos^2 t\times\left(a^2 + b^2\tan^2 t\right) \\
&= \cos^2 t\times\left(a^2 + a^2\tan^2\alpha\right) \\
&= \cos^2 t\times a^2\times\left(1+\tan^2\alpha\right) \\
&= \cos^2 t\times a^2\times\frac{1}{\cos^2\alpha}
\end{aligned} \tag{6.3}$$

$$r = \sqrt{\frac{a^2b^2}{a^2\sin^2\alpha + b^2\cos^2\alpha}} \tag{6.4}$$

$$I \propto \sin^2(2\theta) \tag{6.5}$$

$$I_{two} \propto r^2\sin^2(2\theta) \tag{6.6}$$

$$f(\theta,\alpha) = \sin^2(2\theta)\times\frac{a^2b^2}{a^2\sin^2\alpha + b^2\cos^2\alpha} \tag{6.7}$$

$$f(\theta_1,\theta_2)=\sin^2(2\theta_2)\times\frac{a^2b^2}{a^2\sin^2(\theta_2-\theta_1)+b^2\cos^2(\theta_2-\theta_1)} \qquad (6.8)$$

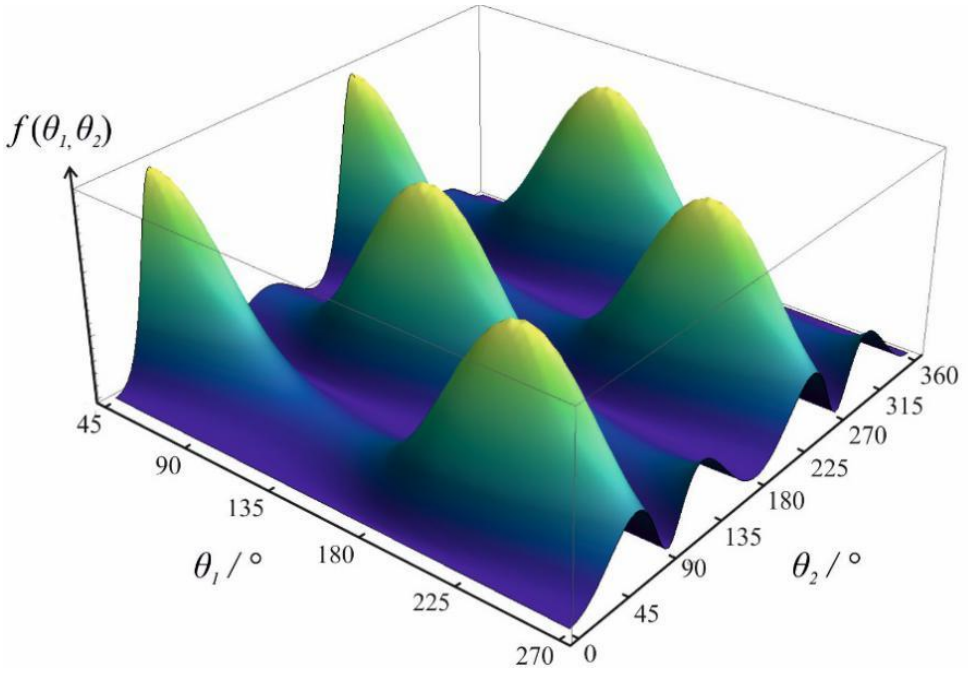

Figure 6.8 *Theoretical 3D plot of the function of f* (θ_1, θ_2) in *Eq. 6.8, where* θ_1 *and* θ_2 *correspond to the* χ *values of the first crystal and the second crystal respectively.*

Figure 6.9 shows the experimental XBI results recorded for the pair of single crystals of the 1-bromoadmantane/thiourea inclusion compound (1-BA/thiourea), specifically as a plot of transmitted X-ray intensity as a function of the orientations (θ_1 and θ_2) of the two crystals. The C–Br bonds in 1-BA/thiourea are all parallel to the long-axis of the crystal and the XBI behaviour for a single crystal is the simplest case, as we discussed before. The first crystal is mounted on the goniometer with the long-axis perpendicular to the propagation direction of the incident beam, and a χ scan of this crystal was carried out with step size of 5° in range from 45° to 135° and with step size of 15° in range from 135° to 270°. The second crystal was mounted on the rotation stage and the χ value for this crystal was varied from 0° to 360° with step size of 1°. In the range of θ_1 and θ_2 studied, the highest intensity arises for (θ_1, θ_2) values of (45°, 45°), (225°, 45°), (135°, 135°), (45°, 225°), (225°, 225°) and (135°, 315°). Compared with the calculated plot in Fig. 6.8, the highest intensity also happens at the same positions and the theoretical 3D plot is very similar to the experimental plot in Fig. 6.9.

We now return back to the experimental data in Fig. 6.3 (Page 119) and Fig. 6.4 (Page 120) for the case of two crystals with fixed angle between them. As the angle

between the two crystals were fixed at 90° and 45°, respectively, each image during the rotation can be represented as a point in the 3D plot in Fig. 6.8. Figure 6.10 is a contour plot representation of Eq. 6.8 in the range of 0° to 360° for both θ_1 and θ_2. Line (1) represents the case with the angle between the two crystals fixed at 90° (i.e., $\theta_2 - \theta_1 = 90°$). Clearly, the intensity varies along this line (i.e., as the pair of crystals are rotated), but at all orientations the intensity along the line in Fig. 6.10 remains low. This is consistent with the phenomenon observed in Fig. 6.3 (Page 119) that the common area of the two crystals remained dark in all orientations. Line (2) is the case with $\theta_2 - \theta_1 = 45°$, the intensity fluctuates over a bigger range than line (1). Line (3) represents the situation in which the two crystals have the same orientation (i.e., $\theta_2 - \theta_1 = 0°$). In this case, the pair of crystals can be regarded as one crystal, and the highest intensities are at $\chi = 45°$, 135°, 225° and 315°, as is known to be the XBI behaviour of a single crystal of 1-BA/thiourea (see Fig. 1.21.a, Page 23).

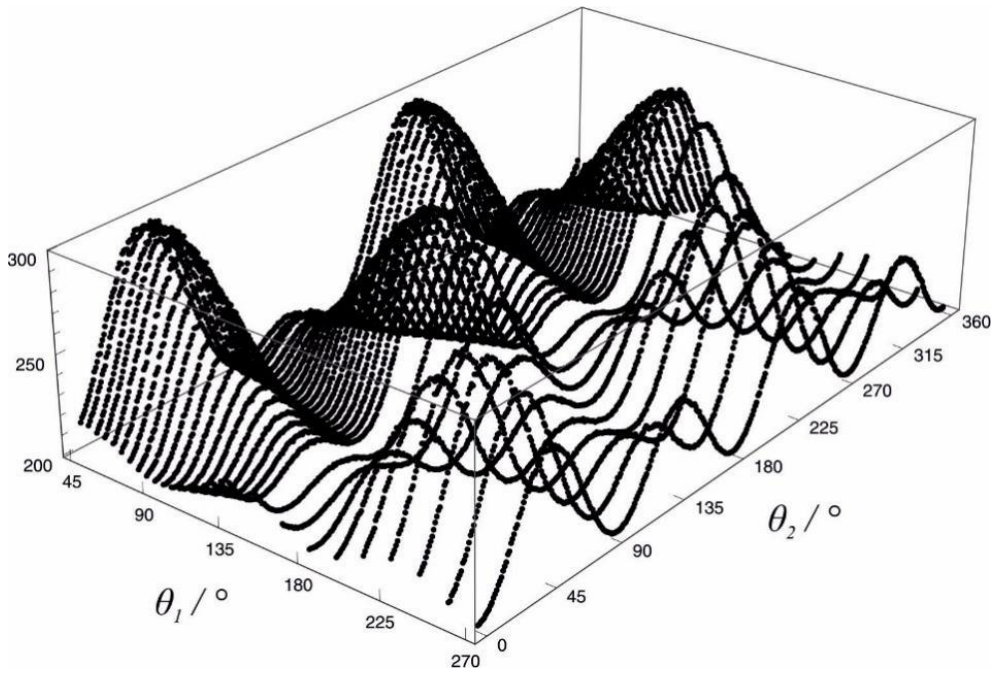

Figure 6.9 *Experimental XBI data for two single crystals of the 1-BA/thiourea inclusion compound representing the integrated intensity measured for the common area of the two crystals in the XBI images (i.e., the region in which the X-ray beam passes through both crystals). The χ range of the first crystal on the goniometer is from θ_1 = 45° to 270°. The χ range of the second crystal on the rotation stage is from θ_2 = 0° to 360°.*

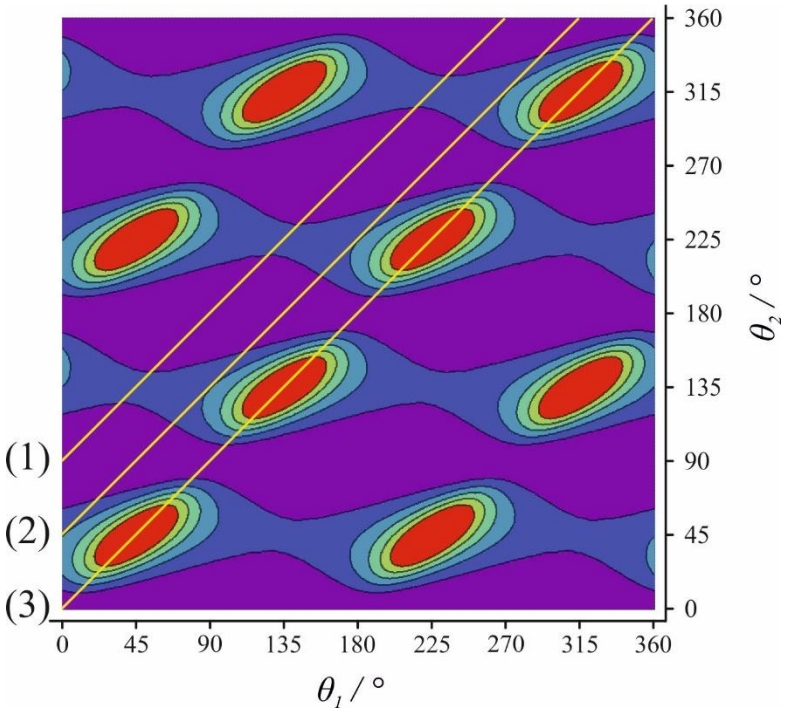

Figure 6.10 *Contour plot representation of Eq. 6.8 (Page 124). Yellow lines (1), (2) and (3) correspond to cases in which the relative orientations of the two crystals are fixed at* $\theta_2 - \theta_1 = 90°$, *45° and 0° respectively.*

6.3 X-ray Birefringence Imaging Using a Transmission-Based Polarization Analyzer

Analogous to Polarizing Optical Microscopy (POM), we can also envisage an experimental set-up for XBI in which the analyzer is an X-ray dichroic filter material (operating at the Br K-edge), instead of the diffraction-based analyzer used in the set-up described previously. Single crystals of the 1-BA/thiourea inclusion compound have been demonstrated as an ideal dichroic material in X-ray polarization analysis at the Br K-edge, but the inability to prepare single crystals of this material of suitable size and shape inhibits such practical applications. Here, flat-plate crystals satisfying the requirement that the X-ray optic axis (C–Br bond direction) is parallel to the plate have been prepared by an epitaxial crystal growth method and are applied in a new XBI set-up as a transmission-based polarization analyzer. The original XBI set-up by using the Bragg Diffraction crystal (Fig. 2.1, Page 29) as the analyzer should be classified as “reflected mode” XBI and the new set-up may be described as “transmitted mode” XBI.

Figure 6.11 shows the set-up for "transmitted mode" XBI. A flat-plate single crystal of 1-BA/thiourea is glued on the rotation stage with the C–Br bonds parallel to the *y-axis*. As the incident polarized X-rays are linearly polarized along the *y-axis*, the requirement for a "crossed polar" configuration (as in POM) is that the transmission-based analyzer should transmit X-rays polarized along the *z-axis*. Thus the direction of maximum absorption for the analyzer should be along the *y-axis* (corresponding to the C–Br bond direction). The sample is still mounted on the goniometer, which can be moved agilely in three dimensions. The area detector is now positioned along the x-axis (i.e., parallel to the direction of propagation of the incident X-ray beam), in the new "transmitted mode" XBI set-up.

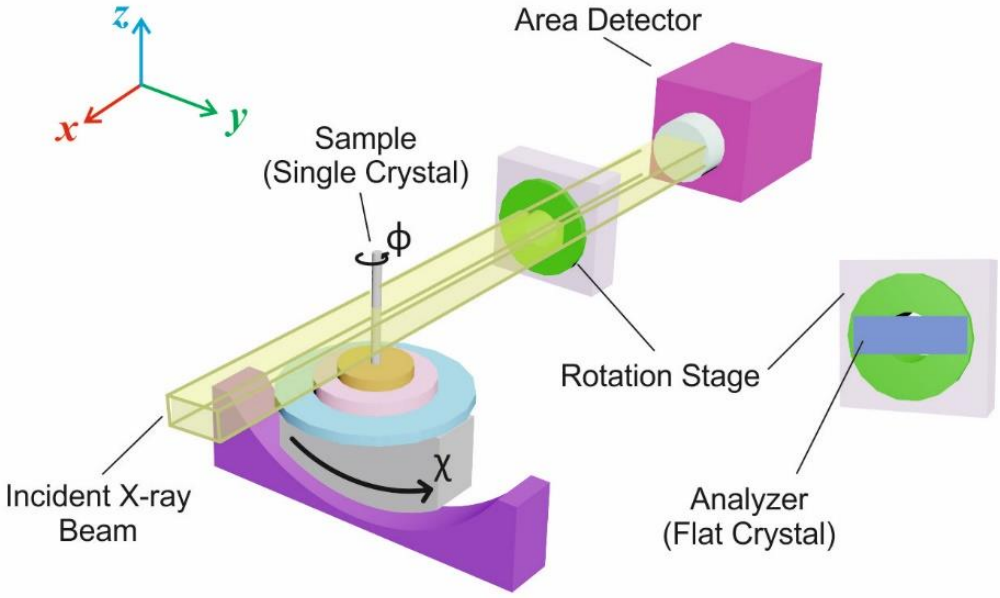

Figure 6.11 *Schematic illustration of the "transmitted mode" XBI set-up. The polarization analyzer is a flat-plate single crystal of 1-BA/thiourea fixed on the rotation stage, oriented with the C–Br bonds parallel to the y-axis. The area detector is down-stream of the incident beam (along the x-axis).*

The conventional crystal growth method for 1-BA/thiourea is slow evaporation: the compounds are dissolved in the solvent in a container (e.g., a small vial) and the crystals are grown through solvent evaporation (Fig. 6.12.a). For 1-BA/thiourea, the crystals formed by this method are needle-shaped crystals with regular hexagon cross-section and these crystals are randomly oriented in the vial. Crystallization was also attempted by placing a cover glass (*ca.* 20 mm diameter) at the bottom of the vial (*ca.* 20 mm diameter), with the same evaporation treatment. After solvent evaporation, some flat-

plate crystals (elongated along one direction) were found to be formed on the cover glass and further study identified that the cross-section is a flat hexagon (Fig. 6.12.b). Crystallization of the 1,8-dibromooctane/urea inclusion compound (DBO/urea) was also tested by the new method, which formed the flat-plate crystal morphology as well. The only difference between the two methods shown in Fig. 6.12 is the presence of the cover glass. Apparently, the cover glass has an influence on the morphology of the final crystals and this kind of substrate-induced crystal growth is called "epitaxy".

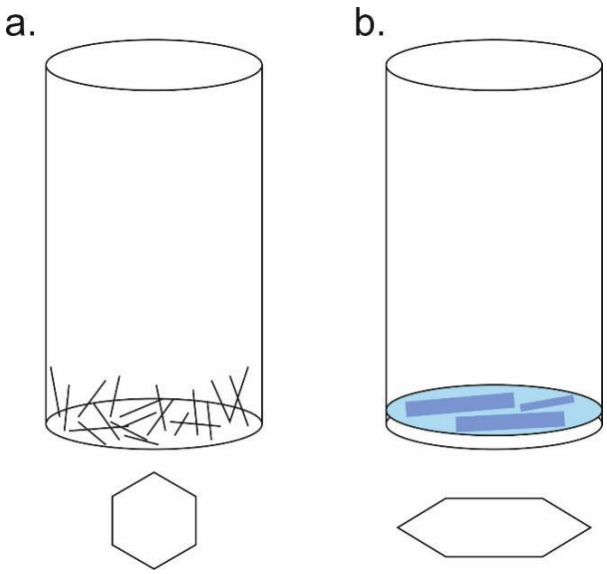

Figure 6.12 *Schematic illustration of crystal growth of urea and thiourea inclusion compounds by slow evaporation method. (a) The conventional growth: needle-shaped single crystals grow in random orientations in the vial during solvent evaporation. The cross-section of the single crystal is a hexagon. (b) The epitaxial growth: a piece of cover glass is placed at the bottom of the vial, and the final single crystals are flat-plate crystals with the rectangular big face on the cover glass. The cross-section of the singe crystal is an elongated hexagon.*

For a regular hexagon (i.e., the tunnels of the urea and thiourea host structures), there are two "special" directions: one is from the middle point of one side to the middle point of the opposite side (line "a" of the orange hexagon in Fig. 6.13); and another is from one vertex to the opposite vertex (line "b" of the orange hexagon in Fig. 6.13). Face-indexing of the flat-plate crystals by single-crystal XRD determines that the big face on the glass is along the "a" direction relative to the hexagonal tunnels of the host structure.

Figure 6.13 illustrates a possible model for the inter-molecular interactions between the cover glass and the thiourea or urea inclusion compounds. As there are many

of hydroxyl groups on the surface of the glass,[94] the N–H bonds of the urea or thiourea molecules that are oriented perpendicular to the big face of the flat crystals can be connected to the hydroxyl groups on the cover glass by N–H···O(H) hydrogen bonds. Thus, during the crystal growth, the affinities between the surface of the glass and the urea or thiourea molecules may induce the crystal to grow in a preferred orientation and result in the elongated hexagonal cross-section. The epitaxial crystal growth method only changes the crystal morphology not the crystal structure, so the "guest" molecules are still packed inside the "host" molecular tunnels,[95, 96] i.e., the C–Br bonds of the 1-BA molecules are still parallel to the thiourea tunnels, and thus in the flat-plate crystal morphology, the C–Br bonds are parallel to the plane of the flat plate.

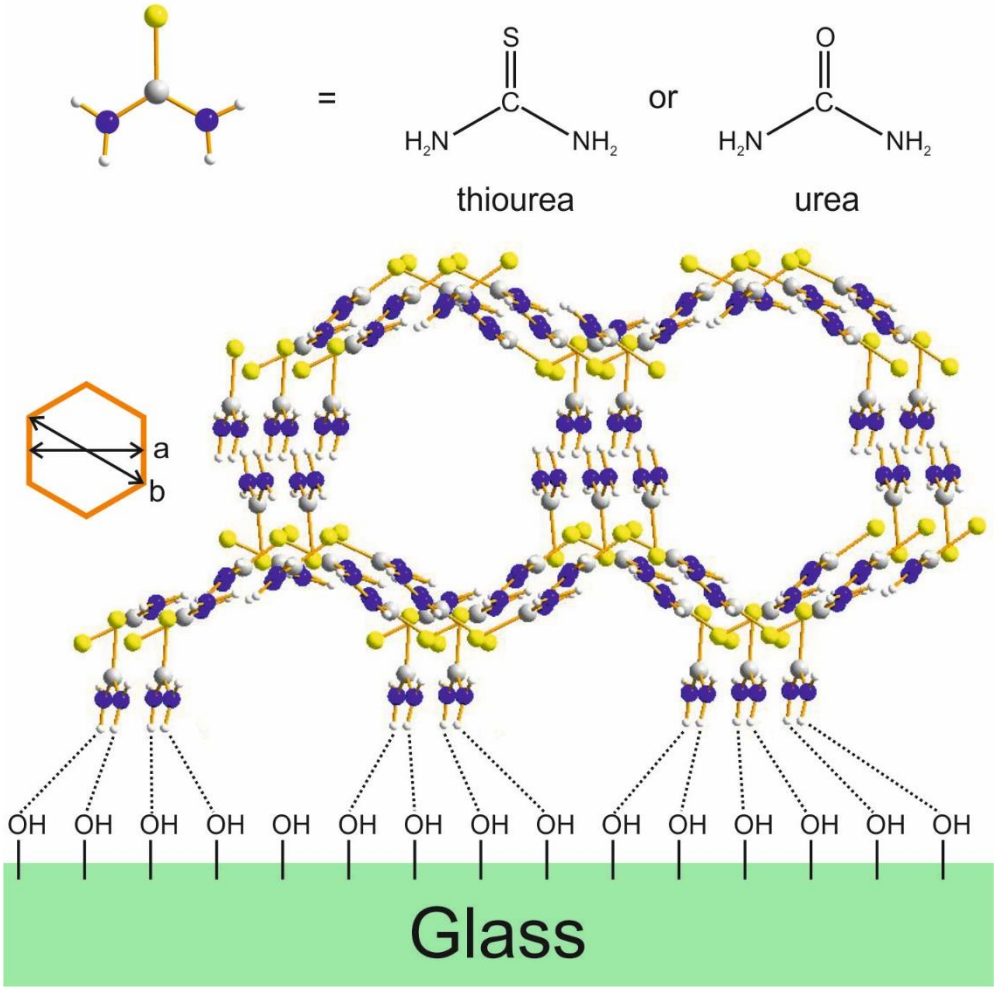

Figure 6.13 *Schematic illustration of inter-molecular interactions between the cover glass and the thiourea or urea molecules. Hydrogen bonds N–H···O(H) are formed between the single crystal and the glass surface. The crystal face on the glass is along the "a" direction of the hexagonal tunnels.*

Figure 6.14 shows X-ray images of a flat-plate single crystal of 1-BA/thiourea on the rotation stage for two different orientations (χ = 0° and χ = 90°). Because the electric vector of the incident polarized beam is horizontal (see 1.2.1), at the energy of Br K-edge, when the C–Br bonds are also horizontal (χ = 0°), the single crystal exhibits high absorption of the X-rays and the image looks darker (Fig. 6.14.a). At the orientation with χ = 90°, the C–Br bonds are perpendicular to the electric vector of the incident polarized beam, and the crystal exhibits low absorption of X-rays. Thus, at χ = 90°, more X-rays photons are transmitted and the image is brighter (Fig. 6.14.b). To further check this dichroic[97] property, a χ scan of the flat-plate crystal was carried out, and the transmitted intensity is shown as a function of χ in Fig. 6.15, which is in a good agreement with the data in Fig. 6.2.b (Page 117). These results indicate that the flat-plate single crystal of 1-BA/thiourea prepared by the epitaxial growth method shows excellent performance as an X-ray dichroic filter material.

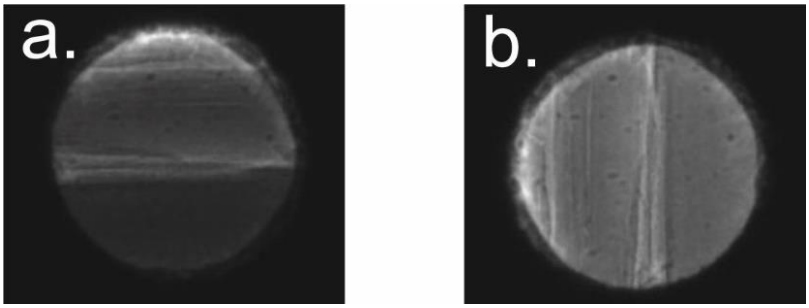

Figure 6.14 *X-ray images of a flat-plate single crystal of 1-BA/thiourea on the rotation stage at the orientations (a) χ = 0° and (b) χ = 90°.*

Now that a suitable X-ray dichroic filter with the optical crystal morphology has been found, the following work is to explore its application in XBI, which is the first practical application of 1-BA/thiourea as a transmission-based X-ray polarization analyzer. A single crystal of 2-bromobenzoic acid (BBA) was used as the test sample mounted on the goniometer as the normal way. The flat-plate single crystal of 1-BA/thiourea is used as the analyzer mounted on the rotation stage with χ = 0°. Thus, the C–Br bond direction is horizontal in the experimental set-up for "transmitted mode" XBI shown in Fig. 6.11 (Page 127). If the test sample exhibits X-ray birefringence, the sample will show different intensity at different χ values. Figure 6.16 shows the "transmitted mode" XBI images of BBA at χ = 0°, χ = 45° and χ = 90°. It is clear that at χ = 45°, the single crystal of BBA is brighter than at χ = 0° and χ = 90°. The same BBA sample was also tested in the original "reflected mode" XBI set-up (Fig. 6.17, Page 132); and the

images at χ = 45° is obviously brighter than at χ = 180° and χ = 90°, consistent with the results in Fig. 6.16. These experimental results demonstrate that the "transmitted mode" XBI can be established through this new experimental set-up and the dichroic filter works well as a polarization analyzer in this application.

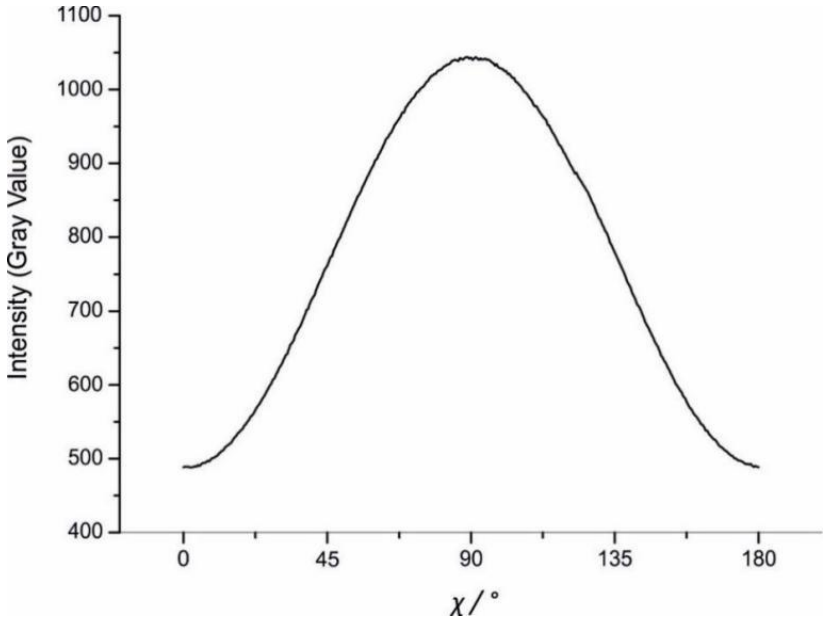

Figure 6.15 *Intensity of transmitted X-rays as a function of orientation (χ) for a flat-plate single crystal of 1-BA/thiourea. At the vertical position (χ = 90°), the image has the highest intensity; and at the horizontal position (χ = 0° and χ = 180°), the image has the lowest intensity.*

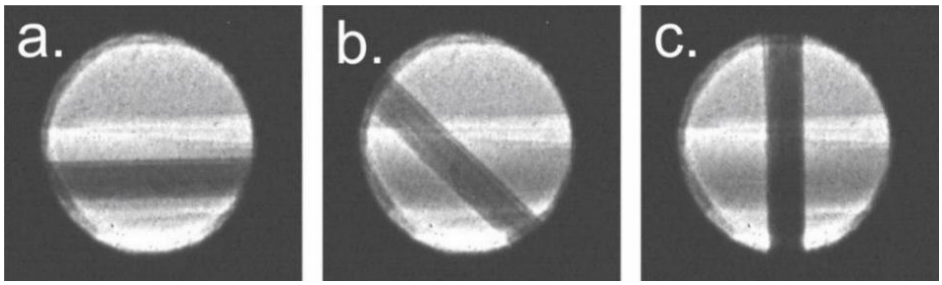

Figure 6.16 *"Transmitted mode" XBI images of a 2-bromobenzoic acid single crystal at three different orientations: (a) χ = 0°, (b) χ = 45° and (c) χ = 90°. The analyzer crystal is a flat-plate single crystal of 1-BA/thiourea.*

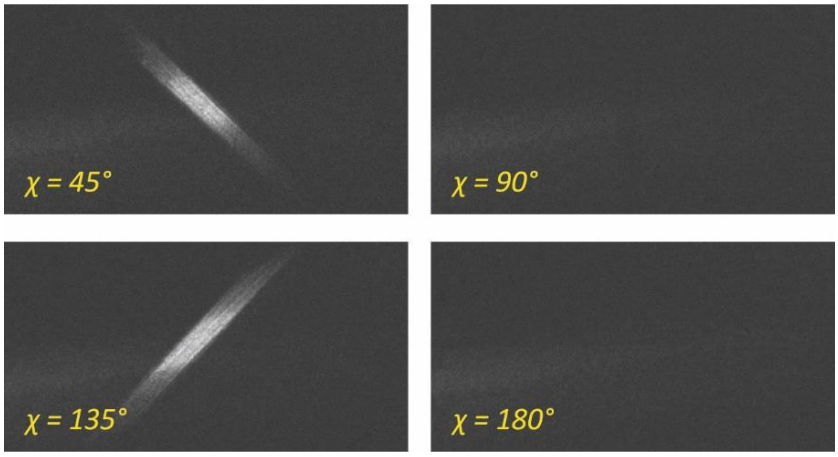

Figure 6.17 *"Reflected mode" XBI (the conventional XBI set-up) images of a 2-bromobenzoic acid single crystal at χ = 45°, χ = 90°, χ = 135° and χ = 180°.*

6.4 Conclusions

The works in this chapter are the last part of XBI research in my PhD study, in which we tried experiments that were innovative and unprecedented. However, due to the limited amount of beam time, the results in this chapter are quite preliminary and require further study in the future.

XBI images of pairs of single crystals with independent orientations are more complicated than the studies of single crystals in the previous chapters (from Chapter 3 to Chapter 5). Even though some information are lacking (e.g., the relative thickness of the two crystals and the refractive indices of the material in different directions), an approximate mathematical model has been derived, which gives a reasonable understanding of the results obtained in this case. Actually, once a more accurate mathematical description is developed, one unknown parameter (d, ε, n_s, n_f …) can be deduced retrospectively from the other known parameters, which may be a useful application of XBI.

The work to develop a set-up for "transmitted mode" XBI was inspired by the above study of XBI involving two types of crystal in the X-ray beam. Here, the second crystal is used as the polarization analyzer crystal and the first crystal is the test sample. The successful attempt to make flat-plate crystals by epitaxial growth has made it possible to get a suitable analyzer crystal to record XBI images. Compared to the original "reflected mode" XBI, the image contrast in "transmitted mode" XBI is lower, but this

does not detract from the significance of reporting the first “transmitted mode” XBI study. The low contrast can be improved by adjusting the thickness of the analyzer crystal or by choosing a material that exhibits stronger X-ray dichroism.

In 2.1, it was explained that for conventional “reflected mode” XBI, finding a suitable analyzer crystal is crucial. For different elements, it is necessary to find the element-matched analyzer crystal (giving a Bragg angle close to 45° for the X-ray energy dictated by the element under study), and usually this screening process is not easy (including consideration of the practical crystal size and the commercial price), which limits the applications of this technique on other elements. However, the crystal analyzer of “transmitted mode” XBI does not require strict mathematical matching (Bragg equation, crystal inter-planar spacing equation and the Planck’s equation), which may expand the opportunities to apply XBI (in “transmitted mode”) to a wider range of elements.

Chapter 7

Crystal Structure Determination from Powder X-ray Diffraction Data

7.1 Introduction

This chapter is focused on structure determination of two types of crystal. One type comprises two different urea co-crystals and the other type is a poly-aromatic compound. These three crystal structures are all determined directly from the powder XRD data by the method introduced in 1.3 and 2.4.

Urea molecules can form two distinct types of solid-state assembly when crystallized with other molecules: (i) inclusion compounds,[77, 92, 96, 98-107] in which the urea molecules form a hexagonal "host" tunnel structure, with another type of molecule included into the tunnels as "guest" molecules (this kind of urea inclusion compounds has been encountered in Chapter 5); (ii) co-crystals,[108-121] in which the urea molecules and another type of molecule are connected by hydrogen bonding with each other in the crystal structure. The first two structures determined in this chapter belong to the second type – co-crystals formed between urea and α,ω-dihydroxyalkane.

The structural diversity in a homologous co-crystal family of even-chain α,ω-dihydroxyalkanes [$HO(CH_2)_nOH$ with n = 4, 6, 8, 10, 12, 14, 16] and urea (in 1:2 molar ratio) has been investigated previously.[122, 123] All these structures have two characteristic features: (i) the urea molecules are aggregated by hydrogen bonds to form double-stranded ribbons, and these two strands can be parallel (P) or antiparallel (A-P); (ii) the angle between the positive direction of the urea strand and the molecular chain of α,ω-dihydroxyalkanes can be either acute (A) or obtuse (O). Table 7.1 summarizes the different structure types in this family categorized according to whether the urea ribbon is P or A-P, and whether the angle between the urea ribbon and the α,ω-dihydroxyalkane is A or O. We use **n**/urea to refer to the co-crystal of $HO(CH_2)_nOH$-$(urea)_2$. The two new polymorphs found in this chapter are A-P/O structures of **6**/urea and **8**/urea. So far, there is no P/O structure found in this family.

Figure 7.1 shows the known crystal structures of **6**/urea, **8**/urea and **10**/urea, which are A-P/A, P/A and A-P/O respectively. The structures of **12**/urea, **14**/urea and **16**/urea are not shown as they all have the same A-P/O structure type as **10**/urea. One NH_2 group and the oxygen atom of each urea molecules form the edge of the urea ribbon, and the positive direction is defined from the nitrogen to oxygen. The adjacent urea molecules within the ribbon are connected through N–H···O hydrogen bonds. Between the urea ribbons, the α,ω-dihydroxyalkane molecules are aligned parallel to each other with a ladder-like arrangement. The α,ω-dihydroxyalkane molecules and the urea molecules are connected together through N–H···O hydrogen bonds by bonding the N–H bond in urea and oxygen of α,ω-dihydroxyalkane.

Table 7.1 *Polymorphs in a family of α,ω-dihydroxyalkane/urea co-crystals (tick marks, the known structures prior to the present work; dash lines, structures that have not yet been found)*

	6/urea	**8**/urea	**10**/urea	**12**/urea	**14**/urea	**16**/urea
A-P/A	✓	-	-	-	-	-
P/A	-	✓	-	-	-	-
A-P/O	New	New	✓	✓	✓	✓

Mechanochemistry can transfer energy from mechanical force to drive chemical or structural transformations.[124-131] A remarkable merit of Mechanochemistry is to enable chemical reactions to occur under environmentally friendly and essentially solvent-free conditions.[126] Solid-state molecular syntheses by Mechanochemistry requires only rather simple equipment, such as a shaker-type ball mill, in which it has been reported that an archetypal metal-organic framework $Cu_3(BTC)_2$ can be prepared by grinding $Cu(OAc)_2•H_2O$ and H_3BTC for 15 minutes without any solvent.[132, 133] Figure 7.2 (Page 137) shows the mechanochemical milling process: different solid starting materials are ground together by a mill ball with the whole jar shaken at a specific frequency.

As the new materials prepared by milling are microcrystalline powders, the crystal structure cannot be determined by conventional single-crystal XRD, and powder XRD must be used instead. In this chapter, another sample that we have studied is a poly-aromatic compound synthesized by a collaborating organic chemistry research group,

which also required structure determination from powder XRD data because the size of the crystals is too small for single-crystal XRD.

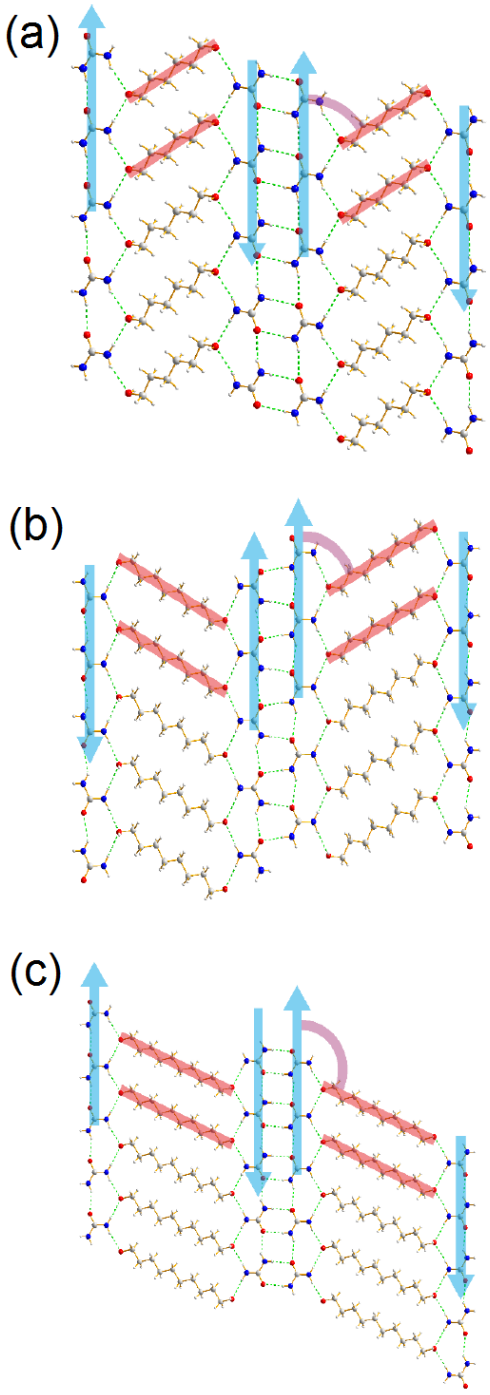

Figure 7.1 *Crystal structures of (a)* ***6****/urea, (b)* ***8****/urea and (c)* ***10****/urea determined previously. Blue arrows indicate the positive direction of the urea ribbon strand (from nitrogen to oxygen on the same urea molecule). Red bars indicate the molecular chain of the α,ω-dihydroxyalkane. Magenta arcs indicate the angle between the positive direction of the urea ribbon strand and the molecular chain of the α,ω-dihydroxyalkane.*

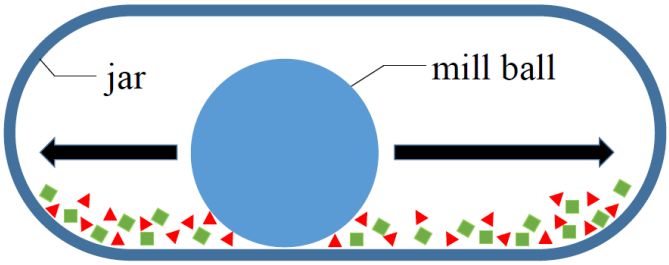

Figure 7.2 *Schematic illustration of mechanochemical milling process. Two different materials (red triangles and green rectangles) and one metal ball are sealed into a metal jar. The materials are milled by shaking the whole jar.*

This material of interest is from a series of O-doped poly-aromatic hydrocarbons (Table 7.2) in which two polycyclic aromatic hydrocarbon subunits are bridged through one or two oxygen atoms. These compounds have tunable spectroscopic properties, which is achieved by fine tuning both the π extension of the carbon scaffold and the oxygen linkages,[134] and Fig. 7.3 shows their colours in the solution state under visible light. Figure 7.4 – 7.6 show the crystal structures (determined previously from single-crystal XRD) of compound **2**, compound **6** and compound **7**, respectively. It is clear that the molecules in these three structures are organized in π···π stacking, with a similar average inter-planar spacing of about 3.6 Å in each case. The crystal structure determined from powder XRD data in this chapter is compound **9**, which is dark blue under visible light.

Table 7.2 *IUPAC names of the nine compounds in a series of O-doped poly-aromatic hydrocarbons.*

	IUPAC Name
Compound **1**	dinaphtho[2,1-b:1',2'-d]furan
Compound **2**	naphtho[2,1-b]phenanthro[9,10-d]furan
Compound **3**	xantheno[2,1,9,8-klmna]xanthene
Compound **4**	benzo[c]xantheno[2,1,9,8-klmna]xanthene
Compound **5**	5,5',8,8',11,11'-hexa-tert-butyl-[3,3'-biperylene]-2,2'-diol

Compound **6**	10,13,16-tri-tert-butylnaphtho[2,1-b]peryleno[3,2-d]furan
Compound **7**	2,5,8,14,17,20-hexa-tert-butyldiperyleno[2,3-b:3',2'-d]furan
Compound **8**	9,12,15-tri-tert-butylbenzo[1,8]isochromeno[5,4,3-cde]benzo[5,10]anthra[9,1,2-hij]isochromene
Compound **9**	2,5,9,12,15,19-hexa-tert-butylbenzo[5',10']anthra[9',1',2':7,8,1]isochromeno[5,4,3-cde]benzo[5,10]anthra[9,1,2-hij]isochromene

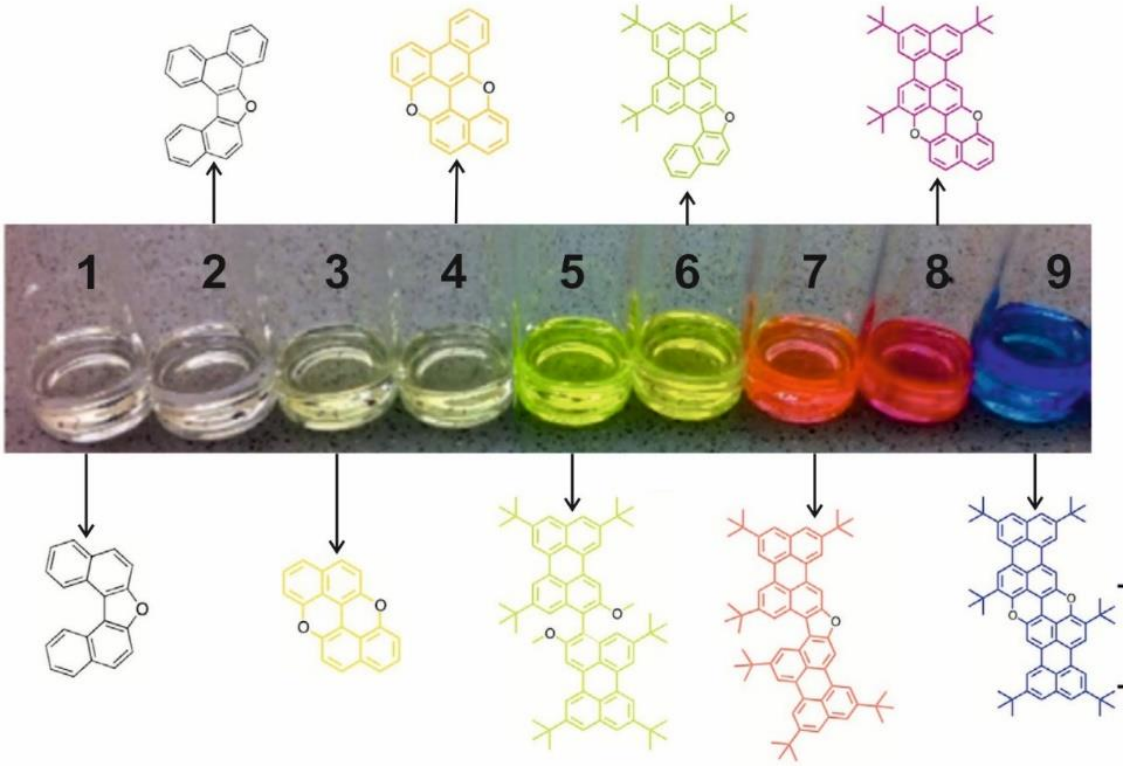

Figure 7.3 *Images of compounds formed on dissolving compounds* ***1*** *–* ***9*** *in 1,2-dichlorobenzene. The corresponding molecular structures are also shown. Reprinted with permission from Miletić, T.; Fermi, A.; Orfanos, I.; Avramopoulos, A.; De Leo, F.; Demitri, N.; Bergamini, G.; Ceroni, P.; Papadopoulos, M. G.; Couris, S., Tailoring Colors by O Annulation of Polycyclic Aromatic Hydrocarbons. Chem. Eur. J.* ***2017****, 23, 2363-2378. Copyright 2017 John Wiley and Sons.*

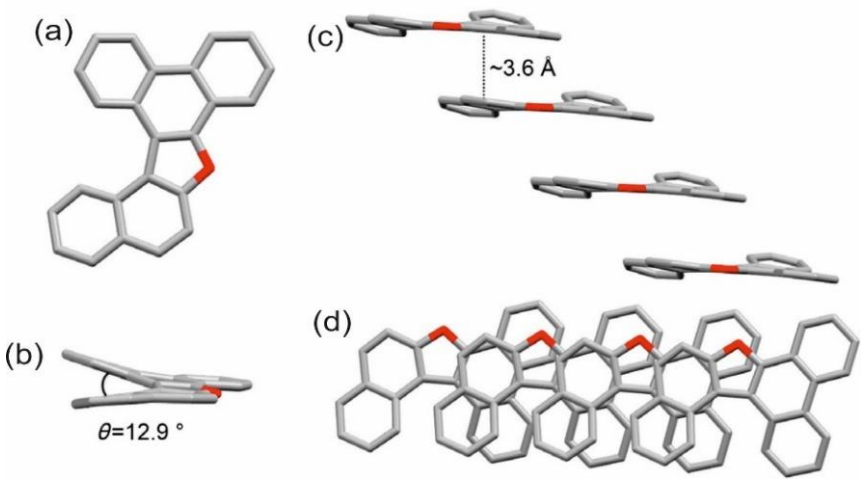

Figure 7.4 *(a,d) Top views, and (b,c) side views of the crystal structure and π···π stacking arrangement of compound* ***2****. Reprinted with permission from Miletić, T.; Fermi, A.; Orfanos, I.; Avramopoulos, A.; De Leo, F.; Demitri, N.; Bergamini, G.; Ceroni, P.; Papadopoulos, M. G.; Couris, S., Tailoring Colors by O Annulation of Polycyclic Aromatic Hydrocarbons. Chem. Eur. J.* ***2017****, 23, 2363-2378. Copyright 2017 John Wiley and Sons.*

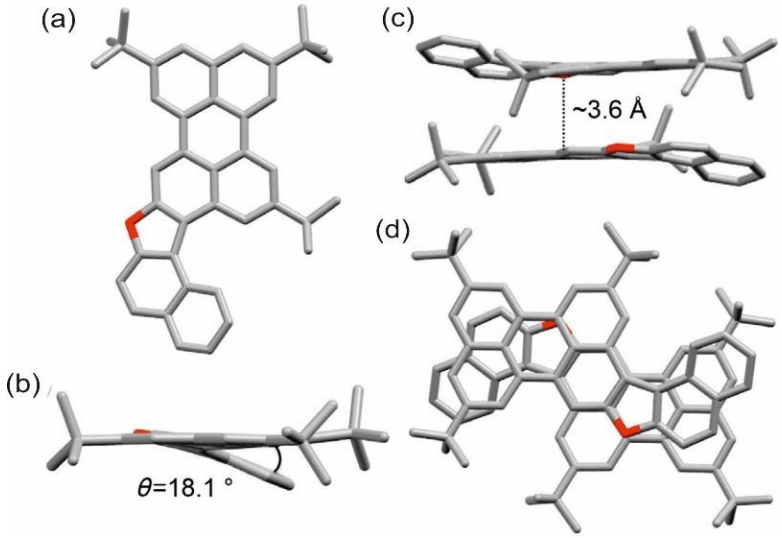

Figure 7.5 *(a,d) Top views, and (b,c) side views of the crystal structure and π···π stacking arrangement of compound* ***6****. Reprinted with permission from Miletić, T.; Fermi, A.; Orfanos, I.; Avramopoulos, A.; De Leo, F.; Demitri, N.; Bergamini, G.; Ceroni, P.; Papadopoulos, M. G.; Couris, S., Tailoring Colors by O Annulation of Polycyclic Aromatic Hydrocarbons. Chem. Eur. J.* ***2017****, 23, 2363-2378. Copyright 2017 John Wiley and Sons.*

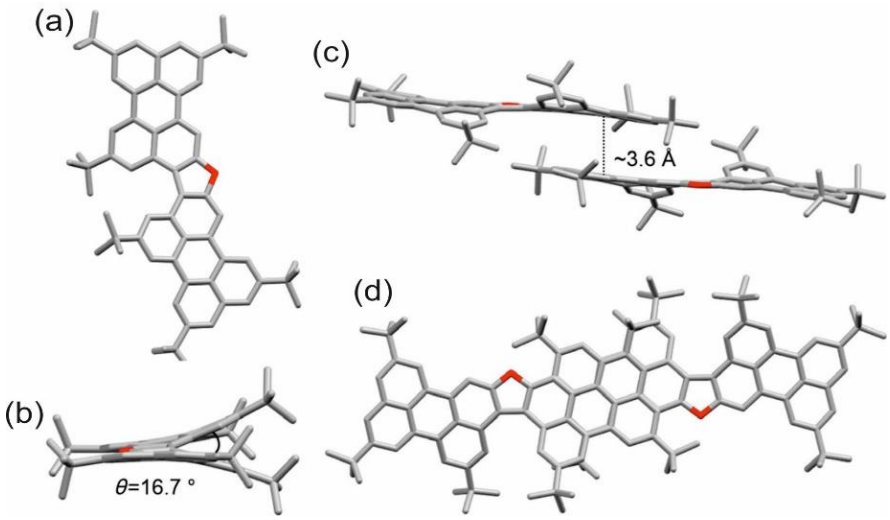

Figure 7.6 *(a,d) Top views, and (b,c) side views of the crystal structure and π···π stacking arrangement of compound **7**. Reprinted with permission from Miletić, T.; Fermi, A.; Orfanos, I.; Avramopoulos, A.; De Leo, F.; Demitri, N.; Bergamini, G.; Ceroni, P.; Papadopoulos, M. G.; Couris, S., Tailoring Colors by O Annulation of Polycyclic Aromatic Hydrocarbons. Chem. Eur. J.* ***2017****, 23, 2363-2378. Copyright 2017 John Wiley and Sons.*

7.2 Two New Polymorphs of α,ω-Dihydroxyalkane/Urea Co-crystals

7.2.1 Experiments

Powders of urea and an α,ω-dihydroxyalkane (in 2:1 molar ratio) were put into a Retsch shaker-type ball mill. The **6**/urea sample was milled at 25 Hz for 20 min, and **8**/urea was milled at 25 Hz for 40 min. The samples obtained were characterized immediately by powder XRD, and powder XRD data for the same samples were also recorded periodically over the following days. Part of the **6**/urea powder obtained from ball-milling was stored in a refrigerator (*ca*. 4 °C).

The samples of both **6**/urea and **8**/urea were studied by powder XRD immediately, and were left at room temperature. For **6**/urea, the same sample was also studied by powder XRD after 8 and 20 days later. For **8**/urea, the same sample was studied by powder XRD after 6, 11 and 18 days later. The part of the **6**/urea sample that was stored in the refrigerator immediately after milling and was studied by powder XRD after 8 days.

This sample was then left at ambient temperature and the powder XRD data were recorded again on the following day.

All powder XRD data were recorded on a Bruker D8 instrument (Ge-monochromated CuKα_1 radiation) operating in transmission mode. For phase identification, a foil sample holder was used, and the data were recorded over the 2θ range of 4° – 40°, with typical data collection time *ca*. 20 – 40 min. To record high-quality data for structure determination, the powder sample was packed into two capillaries, which were flame sealed and attached to the disc sample holder of the powder XRD instrument. The data for **6**/urea and **8**/urea were both recorded over a 2θ range of 4° – 70° (step size 0.017°) with a total time of 15 hr 44 min in each case.

DFT calculations were carried out on the structures determined from powder XRD data using the program CASTEP[135] (Academic Release version 7.02). Calculations were performed with a basis set cut-off energy of 700 eV, ultrasoft pseudopotentials, PBE functional, semiempirical dispersion corrections (TS correction scheme), fixed unit cell, preserved space group symmetry and periodic boundary conditions.

7.2.2 Results and Discussions

A monophasic sample of a new polymorph of **6**/urea was obtained after mechanical milling. A sample containing a new polymorph of **8**/urea was also obtained, although this material also contained a small amount of the known P/A phase and pure urea. In the following crystal structure determination, these impurities will be considered.

For **6**/urea, the powder XRD pattern was indexed using the program TREOR[136] within CRYSFIRE,[137] giving the following unit cell with triclinic metric symmetry: a = 5.17 Å, b = 7.43 Å, c = 8.57 Å, α = 81.5°, β = 86.4°, γ = 78.2° (V = 318.3 Å^3). For **8**/urea, the following unit cell[†] was found to give a good fit to the peak positions for the new polymorph: a = 5.18 Å, b = 7.40 Å, c = 10.39 Å, α = 70.8°, β = 80.5°, γ = 78.7° (V = 366.6 Å^3). Profile fitting using the Le Bail method[138] in the GSAS program[139] gave a good quality of fit for both **6**/urea (R_{wp} = 3.16%, R_p = 2.33%; Fig. 7.7.a, Page 144) and

[†] For **8**/urea, the presence of additional crystalline phases in the sample rendered indexing from the measured peak positions unreliable. Instead, an initial trial unit cell was determined from the average of the unit cell parameters of the known (A-P/O) form of **10**/urea and the new (A-P/O) polymorph of **6**/urea. This unit cell was found to be an acceptable starting point for the Le Bail fitting procedure.

8/urea (R_{wp} = 2.67%, R_p = 2.02%; Fig. 7.7.b, Page 144). The refined unit cells and profile parameters obtained in the Le Bail fitting procedure were used in the subsequent structure solution calculations.

Structure solution was carried out using the direct-space genetic algorithm (GA) technique[30, 31, 140-148] incorporated in the program EAGER.[140, 146, 149-153] Given the volume of the unit cells and consideration of density, the unit cell contents for both **6**/urea and **8**/urea were assigned as one molecule of **6** or **8** and two molecules of urea. In each case, structure solution was carried out using space group $P\bar{1}$ (with the intention to consider space group *P*1 if satisfactory structures were not obtained for $P\bar{1}$).For space group $P\bar{1}$, the contents of the asymmetric unit correspond to one half molecule of **6** or **8** and one molecule of urea.

In the GA structure solution calculation for **6**/urea, the half-molecule of 1,6-dihydroxyhexane in the asymmetric unit was defined by a total of 7 structural variables[‡] (3 positional variables, 3 orientational variables and 1 torsional variable). For **8**/urea, the half-molecule of 1,8-dihydroxyoctane was defined by 8 structural variables (3 positional variables, 3 orientational variables and 2 torsional variables). In each case, the urea molecule was defined by 6 structural variables (3 positional variables and 3 orientational variables). Each GA structure solution calculation involved the evolution of 100 generations for a population of 100 structures, with 10 mating operations and 50 mutation operations carried out per generation. In total, 16 independent GA calculations were carried out for **6**/urea and for **8**/urea.

The best structure solution (i.e., the trial structure with lowest R_{wp} obtained in the GA calculations) was used as the initial structural model for Rietveld refinement,[154, 155] which was carried out using the GSAS program. Standard restraints were applied to bond lengths and bond angles.[§] For **8**/urea, the known structure of the P/A form of **8**/urea was

[‡] In this work, the half-molecule of **6** or **8** was allowed to translate freely in the unit cell, with the requirement that, in the best structure solution, the position of the $HO(CH_2)_3$ or $HO(CH_2)_4$ half-molecule should be located at an appropriate position and orientation relative to a crystallographic inversion centre such that the complete molecule of **6** or **8** is generated with sensible geometry. Clearly, any mirror discrepancies in the geometry of the complete molecule generated in this way may be readily corrected with the subsequent Rietveld refinement process.

[§] Standard bond-length and bond-angle restraints were obtained from the mean values for similar structures deposited in the Cambridge Structural Database, as determined using the program Mogul (version 1.7) for bonds between non-hydrogen atoms. Bond-length restraints for bonds involving hydrogen atoms were taken from Allen, F. H.; Kennard, O.; Watson, D. G.; Brammer, L.; Orpen, A. G.; Taylor, R. *J. Chem. Soc. Perkin Trans. 2* **1987**, S1-S19.

included as a second phase in the Rietveld refinement to account for the presence of a small amount of this phase in the powder sample. In the final Rietveld refinements, a good quality of fit was obtained for the powder XRD patterns of both **6**/urea (R_{wp} = 3.59%, R_p = 2.57%; Fig. 7.8.a, Page 145) and **8**/urea (R_{wp} = 3.33%, R_p = 2.40%; Fig. 7.8.b, Page 145), with the following refined parameters: **6**/urea, a = 5.1601(5) Å, b = 7.4276(5) Å, c = 8.5686(7) Å, α = 81.465(4)°, β = 86.299(6)°, γ = 78.209(5)°; V = 317.72(6) Å^3 (2θ range, 4° – 70°; 3868 profile points; 79 refined variables); **8**/urea, a = 5.1707(5) Å, b = 7.3963(5) Å, c = 10.3805(10) Å, α = 70.786(4)°, β = 80.442(7)°, γ = 78.634(6)°; V = 365.32(6) Å^3 (2θ range, 4° – 70°; 3868 profile points; 93 refined variables).

The crystal structures after Rietveld refinement are shown in Fig. 7.9 (Page 146) (**6**/urea) and Fig. 7.10 (Page 147) (**8**/urea). Both new phases have the typical sheet-like molecular layers and in each sheet the urea and α,ω-dihydroxyalkane molecules form the new A-P/O crystal structures. Thus, it has proved that the new solid-state co-crystal phase can be prepared by mechanochemical milling.

Figure 7.11 (Page 148) shows the powder XRD patterns of the previous known phases (A-P/A for **6**/urea and P/A for **8**/urea) and the new A-P/O phases. DFT calculations were carried out to assess the energy of each phase. The calculation results show that the A-P/O phases of both **6**/urea and **8**/urea have a higher energy than the previously known phases of **6**/urea (A-P/A) and **8**/urea (P/A), respectively. We therefore conclude that the new A-P/A phases obtained from mechanical milling are meta-stable and have the potential to transform into the more stable known phases.

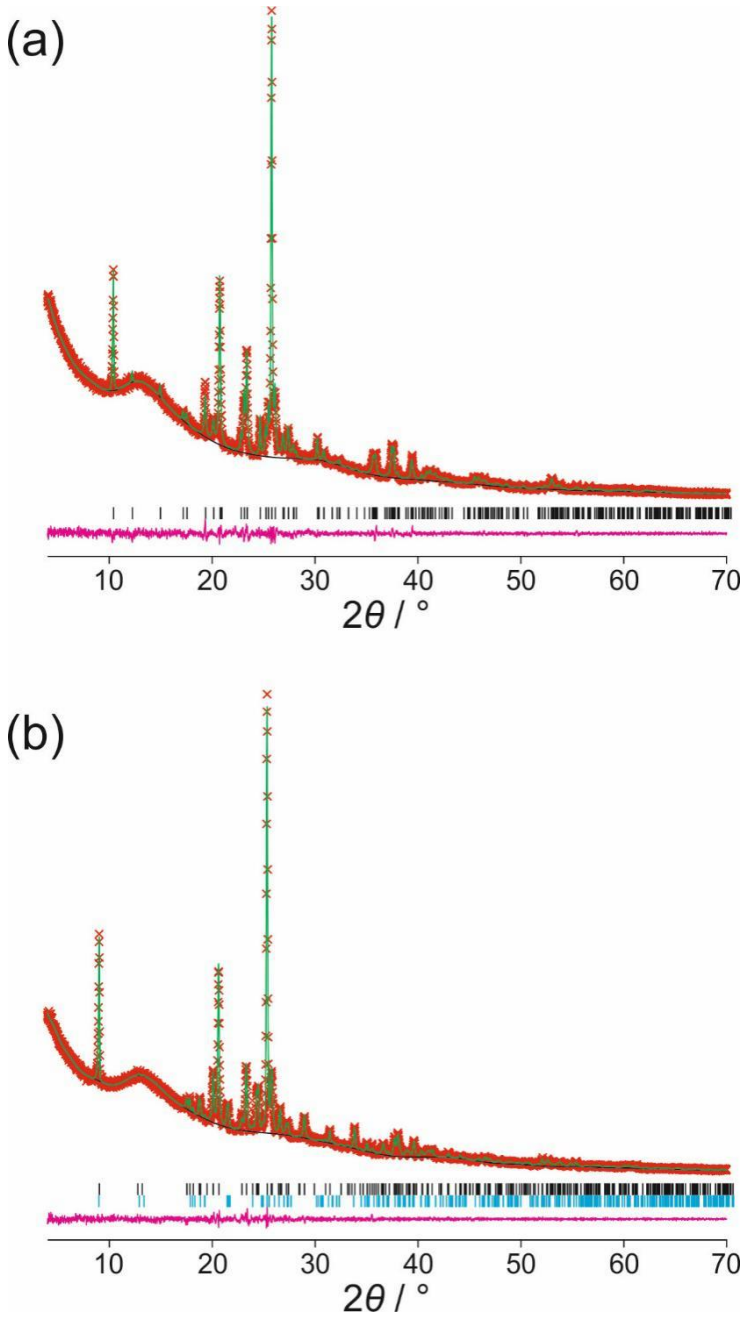

Figure 7.7 *Le Bail fitting of the powder XRD data for the new polymorphs of (a)* ***6****/urea and (b)* ***8****/urea (red crosses, experimental data; green line, calculated data; black line, background; tick marks, peak positions; magenta line, difference plot). In (b), black tick marks represent peak positions for the new A-P/O polymorph and cyan tick marks represent those for the known P/A polymorph (which was included as a second phase in the fitting).*

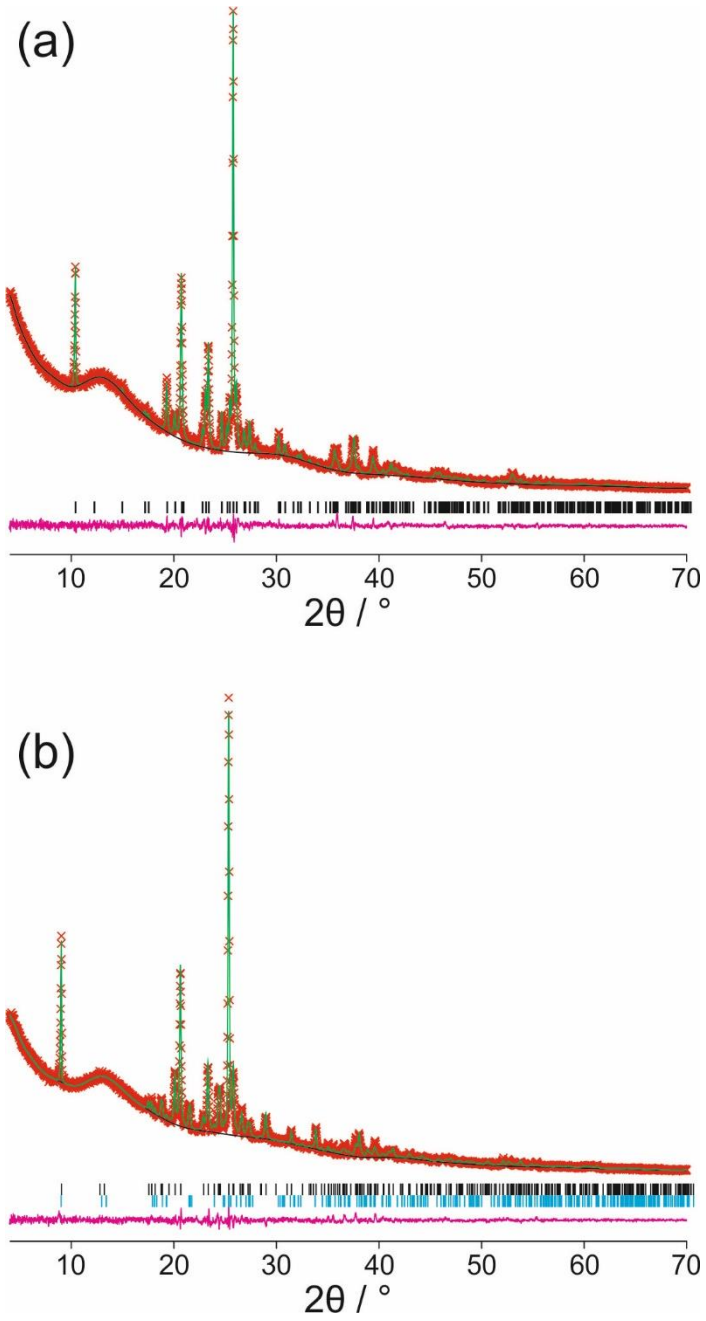

Figure 7.8 *Final Rietveld refinements for the new polymorphs of (a)* ***6****/urea and (b)* ***8****/urea (red crosses, experimental data; green line, calculated data; black line, background; tick marks, peak positions; magenta line, difference plot). In (b), black tick marks represent peak positions for the new A-P/O polymorph and cyan tick marks represent those for the known P/A polymorph (which was included as a second phase in the refinement).*

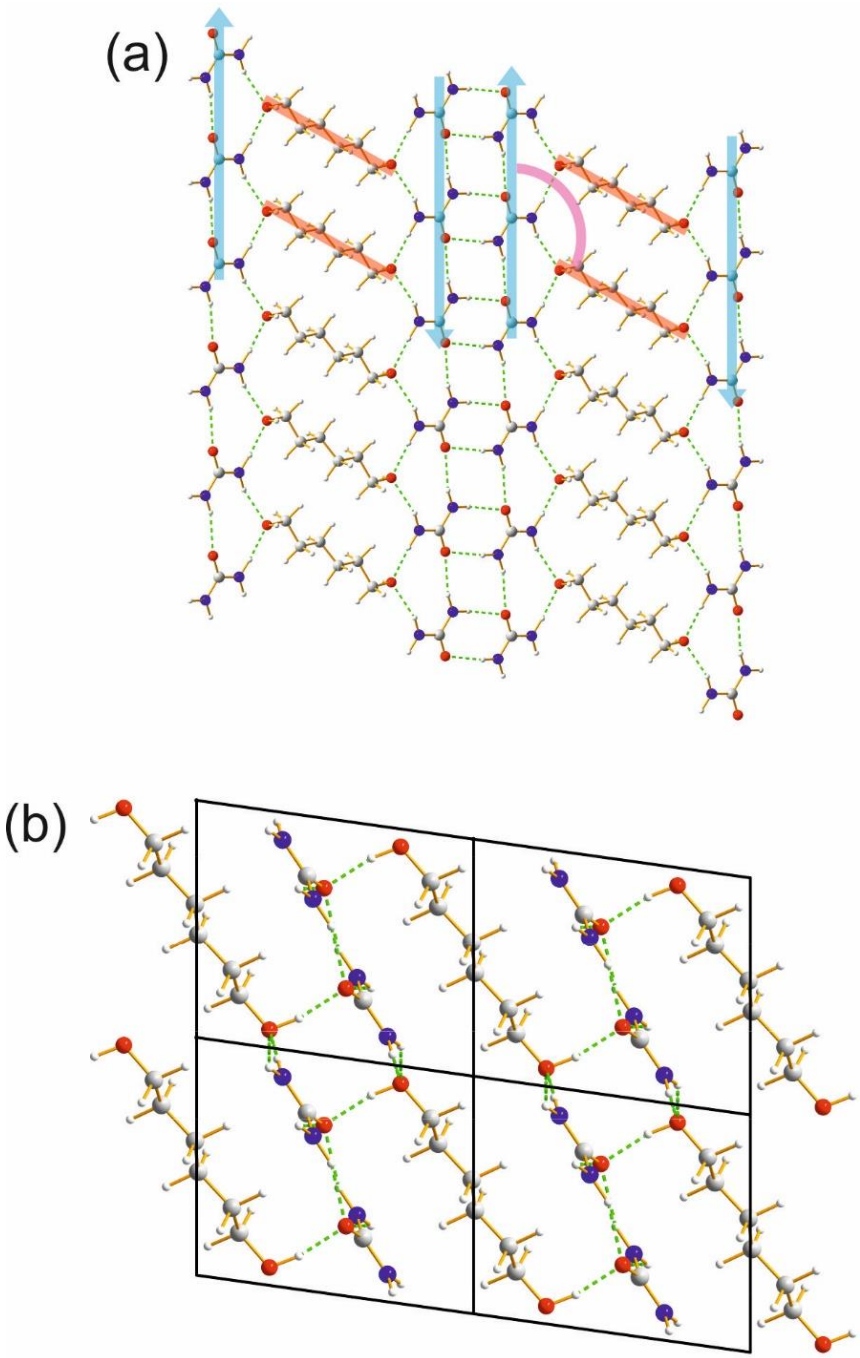

Figure 7.9 *(a) One sheet in the crystal structure of the new A-P/O polymorph of* ***6****/urea prepared by mechanochemical milling (blue arrows, direction of each strand within the urea ribbon; red bars, axis of the 1,6-dihydroxyhexane molecule; magenta arc, angle between the positive direction of the urea ribbon and the axis of the 1,6-dihydroxyhexane molecule). (b) Stacking of sheets in the new polymorph of* ***6****/urea (green dashed lines indicate hydrogen bonds).*

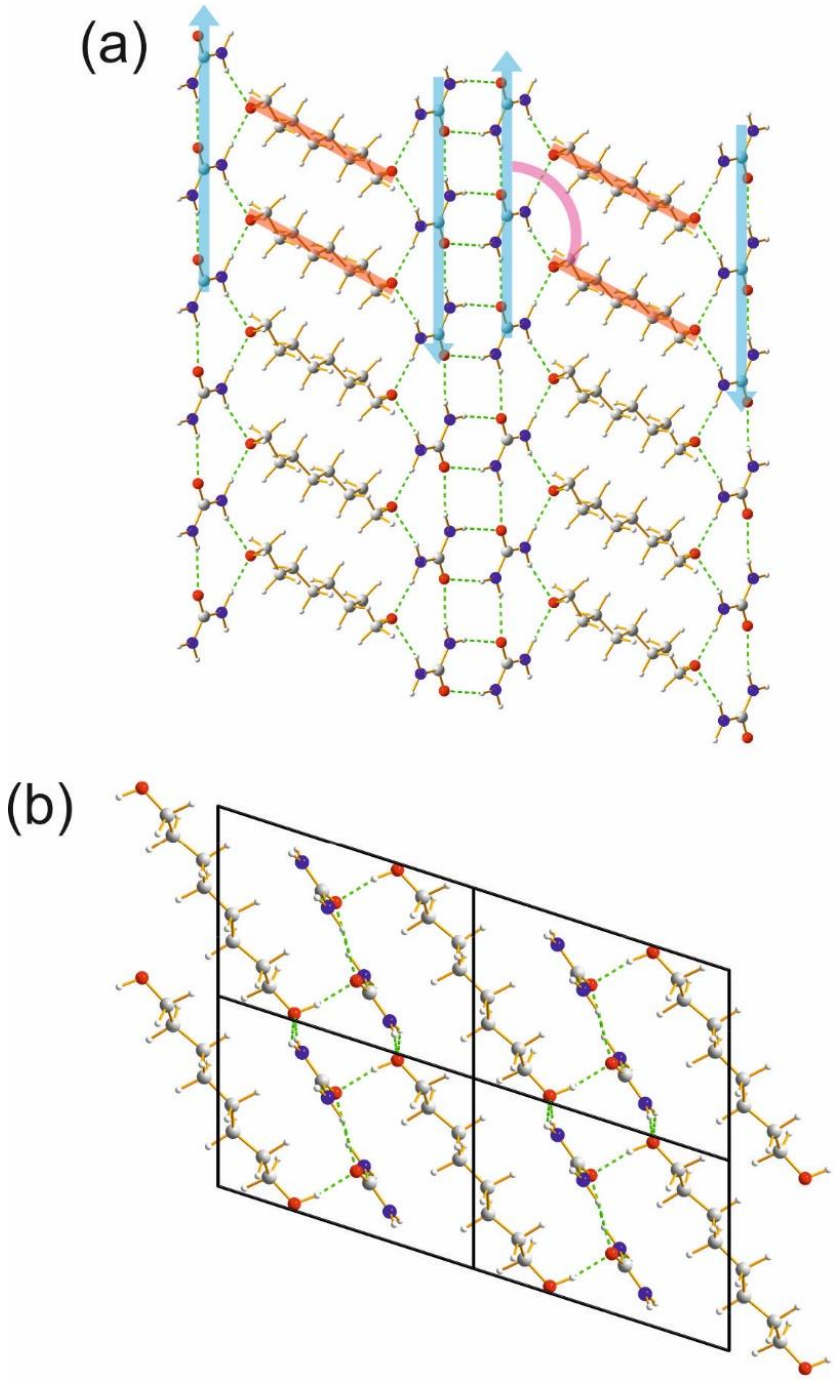

Figure 7.10 *(a) One sheet in the crystal structure of the new A-P/O polymorph of* ***8****/urea prepared by mechanochemical milling (blue arrows, direction of each strand within the urea ribbon; red bars, axis of the 1,8-dihydroxyoctane molecule; magenta arc, angle between the positive direction of the urea ribbon and the axis of the 1,8-dihydroxyoctane molecule). (b) Stacking of sheets in the new polymorph of* ***8****/urea (green dashed lines indicate hydrogen bonds).*

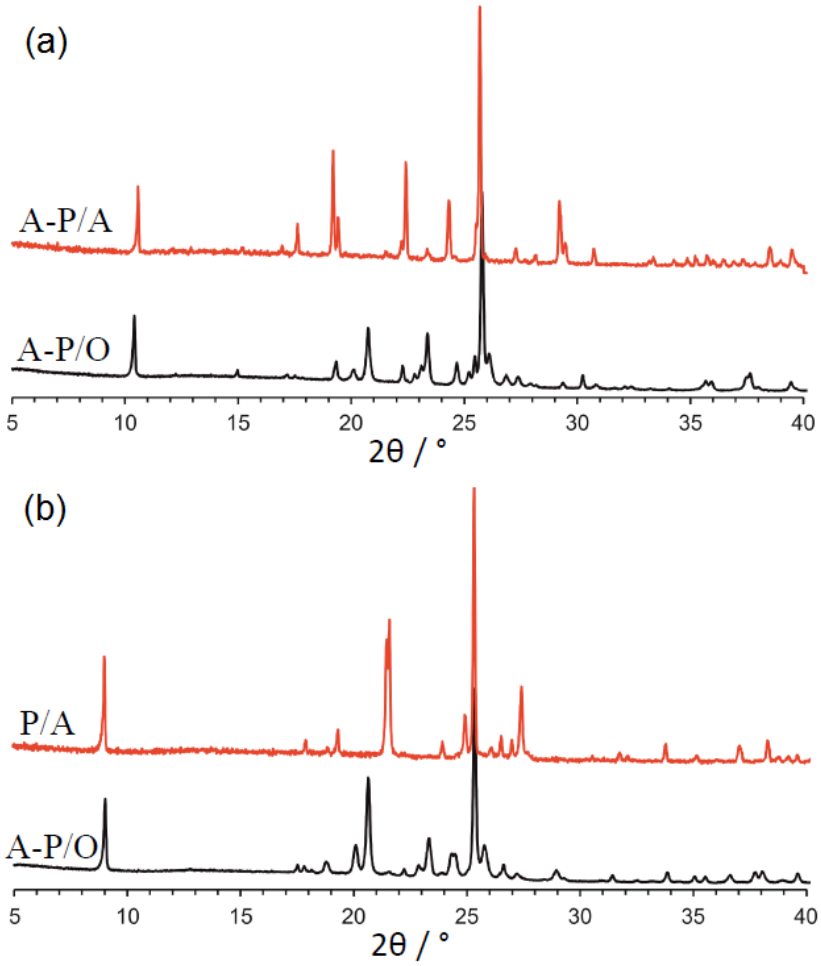

Figure 7.11 *Powder XRD patterns of the polymorphs of (a)* ***6****/urea and (b)* ***8****/urea. Red lines, the known phases (obtained by crystallization from solution); back lines, the new phases by mechanical grinding.*

Some preliminary studies demonstrate the occurrence of phase transition phenomena from the new A-P/O phases to the known phases. The powder samples obtained by grinding were checked periodically over time by powder XRD to assess whether the meta-stable phases transform into the more stable phases. For **6**/urea, after 8 days the new meta-stable A-P/O phase transforms to the known A-P/A phase and remains as this more stable phase for the remainder of our investigation (Fig. 7.12.a). For **8**/urea, the new A-P/O phase shows greater kinetic stability, with no evidence for a phase transition after 18 days (Fig. 7.12.b). For this different behaviour between **6**/urea and **8**/urea, one possible explanation is that the transformation from A-P/O to A-P/A (**6**/urea case) is kinetically more facile than from A-P/O to P/A (**8**/urea case). The change of the angle between the α,ω-dihydroxyalkanes and the urea ribbon can be achieved by molecular gliding, which is easier than flipping one urea strand within the urea ribbon (to

convert from A-P to P). For **6**/urea, only the angle needs to change from O to A, while the urea ribbon remains as A-P. For **8**/urea, the urea ribbon must change from A-P to P. Another experiment shows that low temperature can inhibit the phase transition (Fig. 7.13). The A-P/O phase of **6**/urea placed in refrigerator still keeps the new meta-stable phase, but it changes into the known A-P/A phase within just one day under ambient conditions.

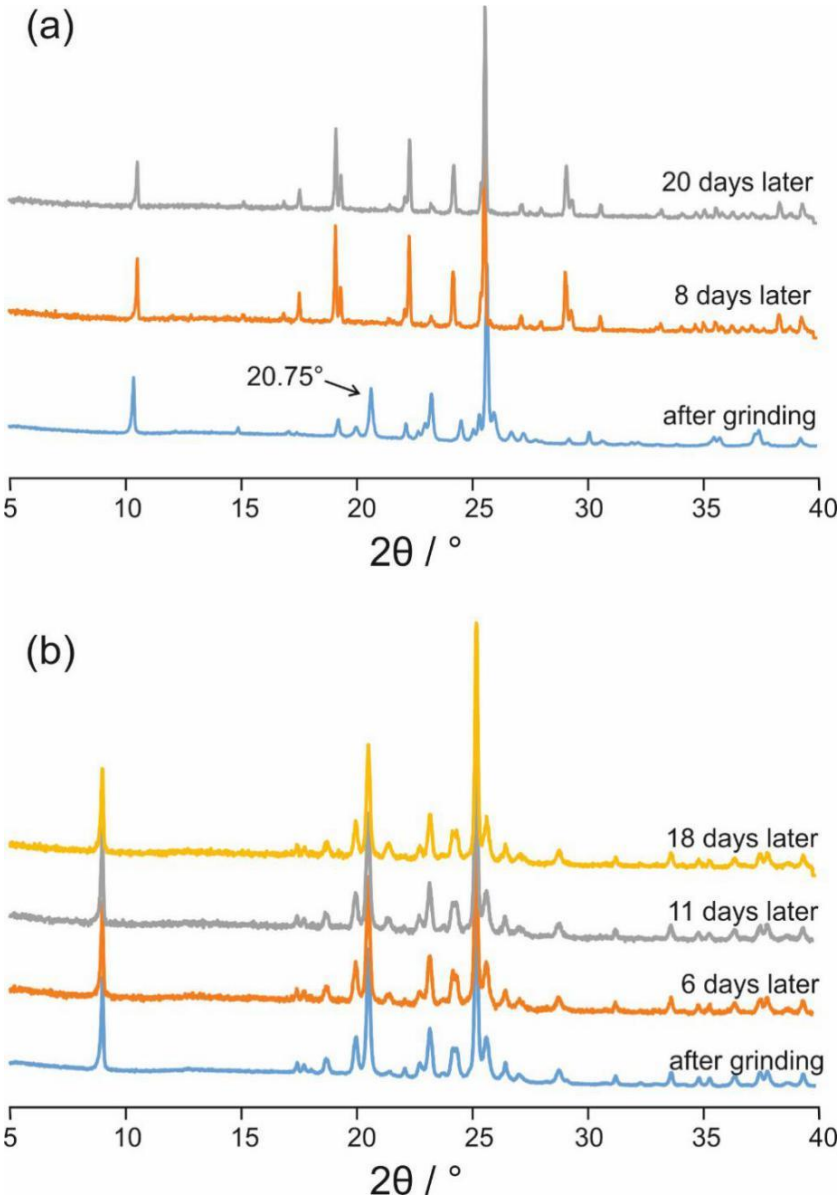

Figure 7.12 *Powder XRD data of the new A-P/O polymorphs tracked immediately after grinding and several days later: (a)* ***6****/urea, was not stable and the characteristic peak at 20.75° disappeared after 8 days; and (b)* ***8****/urea, exhibits greater kinetic stability without change within 18 days.*

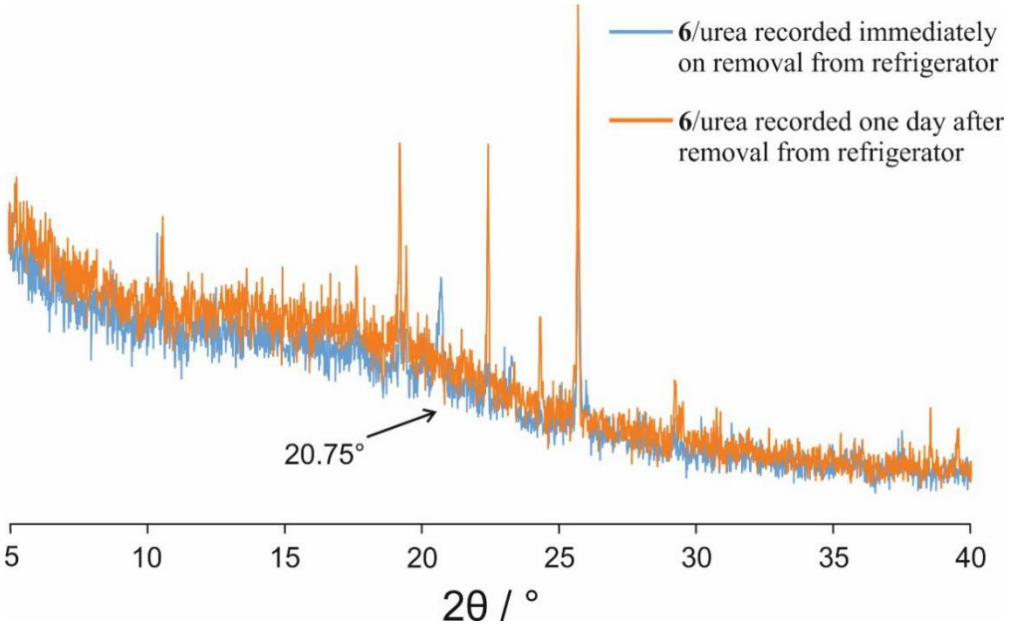

Figure 7.13 *Powder XRD pattern of the new A-P/O polymorph of* ***6****/urea recorded immediately on removal from the refrigerator (already stored for 8 days) (blue) and recorded again the next day after storing under ambient conditions (orange). The peak at 2θ = 20.75°, characteristic of the A-P/O polymorph, is clearly absent after being at ambient temperature for one day following removal from the refrigerator.*

7.3 A Poly-aromatic Compound

A polycrystalline sample called 2,5,9,12,15,19-hexa-tert-butylbenzo[5',10']anthra[9',1',2':7,8,1]isochromeno[5,4,3-cde]benzo[5,10]anthra[9,1,2-hij]isochromene (compound **9**) (Table 7.2, Page 137, and Fig. 7.14) was prepared by sublimation. Due to the challenge of crystallizing suitable crystals for single-crystal XRD, structure determination from powder XRD was essential for determination of the crystal structure.

Powder XRD data were recorded on a Bruker D8 instrument (Ge-monochromated CuKα1 radiation) operating in transmission mode. In order to record high-quality data for structure determination, the powder sample was packed into two capillaries (to minimize the effects of preferred orientation). The powder XRD data were recorded over the 2θ range 4° – 70° (step size 0.017°) with a total data collection time of 64 hours 4 minutes.

The two-dimensional powder XRD pattern of one capillary containing the sample powder was recorded using a two-dimensional detector on a single-crystal X-ray

diffractometer (Fig. 7.15). The overall intensity statistic of the data recorded on this instrument is very high compared with the powder XRD data, but the resolution is significantly poorer (Fig. 7.16). The good agreement of the two powder XRD patterns identifies that the sample does not contain obvious preferred orientation.

The powder XRD pattern of compound **9** was indexed using the program DICVOL[156] within the CRYSFIRE[137] suite of indexing programs, giving the following unit cell with monoclinic metric symmetry: a = 13.505 Å, b = 5.976 Å, c = 29.774 Å, β = 94.67° (V = 2394.8 Å^3). In the indexing process, two peaks were removed as they were identified as originating from impurity crystalline phases. The impurity peaks are recognized through incompatible peaks by recrystallization from different solvents.

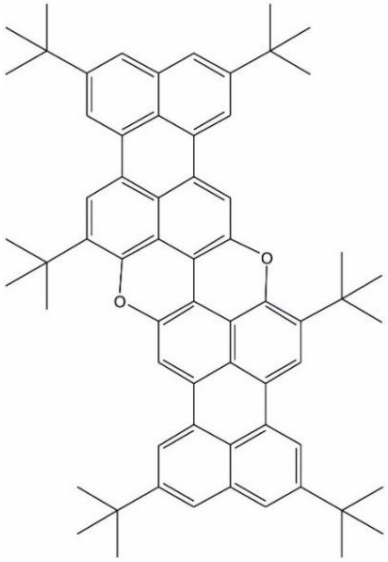

Figure 7.14 *Molecular structure of compound* ***9*** *(chemical formula is* $C_{64}O_2H_{66}$*).*

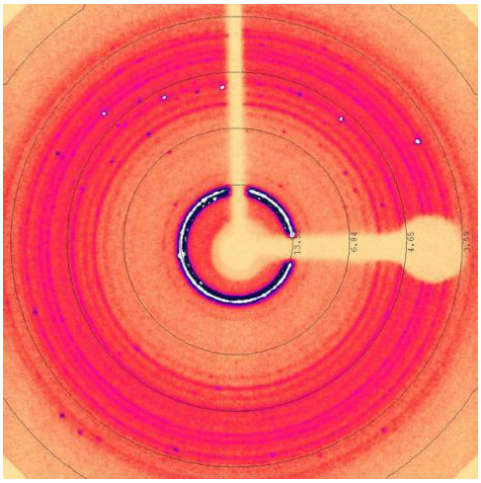

Figure 7.15 *The two-dimensional powder XRD pattern of compound* ***9*** *packed in a capillary.*

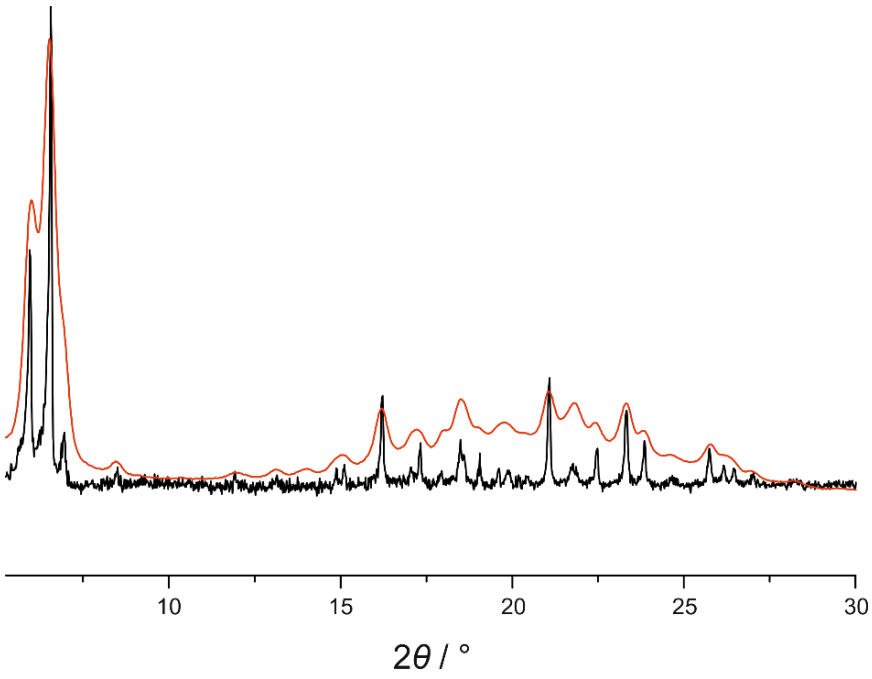

Figure 7.16 *The agreement of the powder XRD data recorded on the single-crystal XRD instrument (red) and the powder XRD instrument (black). Impurity phases are included.*

Given the volume of this unit cell and consideration of density, the number of formula units in the unit cell was assigned as $Z = 2$. As the compound **9** molecule has an inversion centre, Z = 2 can be divided into three types: 2 × 1, 1 × 2, and ½ × 4 corresponding to 2, 1 or ½ molecules in the asymmetric unit, respectively, and space group multiplicity of 1, 2 or 4, respectively. Solid state ^{13}C NMR using the non-quaternary suppression (NQS) technique was used to identify the multiplicity. Figure 7.17 shows the solid-state ^{13}C NMR spectra in the aromatic region and 6 peaks are suppressed in NQS compared with the non-NQS spectrum. As the whole compound **9** molecule has 12 non-quaternary carbons on the aromatic rings (Fig. 7.18), the number of molecules of compound **9** in the asymmetric unit is $Z' = ½$ and the multiplicity should be 4. From systematic absences, the space group was assigned as $P2_1/c$. Profile fitting using the Le Bail method[138] gave a good quality of fit (R_{wp} = 2.03%, R_p = 1.51%; Fig. 7.19). The refined unit cell and profile parameters obtained from the Le Bail fitting procedure were then used in the subsequent structure-solution calculations.

Structure solution was carried out using the direct-space genetic algorithm (GA) technique[30, 31, 142, 143] incorporated in the program EAGER.[140, 146, 149-153] As $Z' = ½$ (see above), the centrosymmetric compound **9** molecule was fixed at a crystallographic inversion centre, and thus the asymmetric unit corresponds to half the compound **9**

molecule. In the GA structure solution calculation, trial crystal structures were defined by a total of six structural variables – three orientational variables and three torsion angle variables (specified in Fig. 7.20). Each GA structure solution calculation involved the evolution of 100 generations for a population of 100 structures, with 10 mating operations and 50 mutation operations carried out per generation. In total, 16 independent GA calculations were carried out, with the same good-quality structure solution obtained in 9 cases.

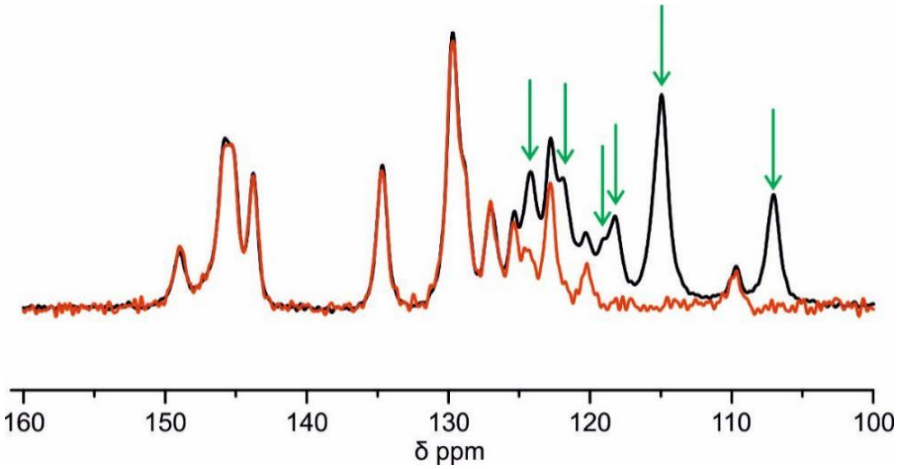

Figure 7.17 *Solid-state ^{13}C NMR spectra of compound* ***9*** *in the aromatic region: NQS (red) and non-NQS (black). Green arrows indicate the difference between the two spectra, identifying the signals due to ^{13}C nuclei that are directly bonded to ^{1}H nuclei (and non-mobile).*

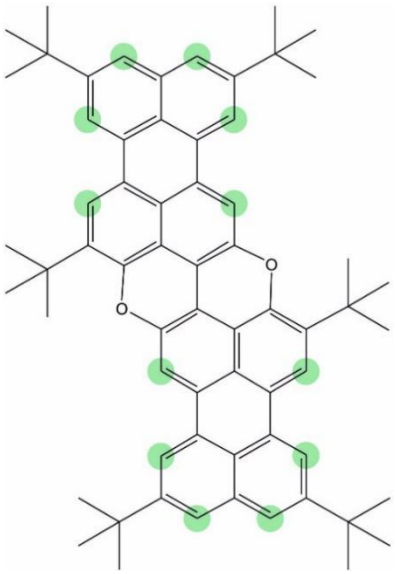

Figure 7.18 *Non-quaternary carbons (12 green dots) on the aromatic rings of the compound* ***9*** *molecule.*

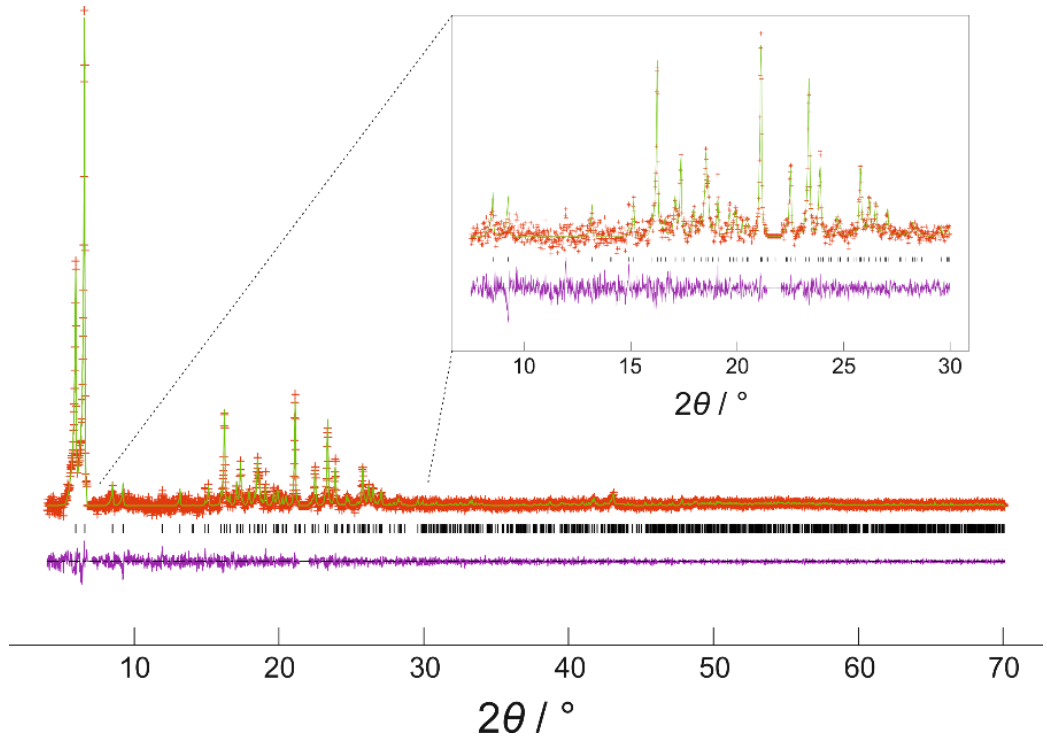

Figure 7.19 *Le Bail fitting of the powder XRD data for compound* ***9*** *(red crosses, experimental data; green line, calculated data; black tick marks, peak positions; magenta line, difference plot). The inset shows an expanded region of the powder XRD data in the range 2θ = 7.5° – 30°. The excluded regions (6.753° – 7.112° and 21.391° – 22.058°) correspond to the positions of two peaks from impurity phases.*

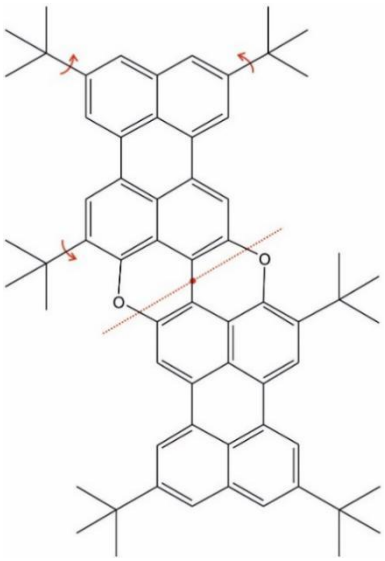

Figure 7.20 *The compound* ***9*** *molecule, indicating the three variable torsion angles in the half-molecule (red dot, inversion centre; red arrows, torsion angles; red dashed line, C_2 rotation axis perpendicular to the molecular plane).*

The best structure solution (the trial structure with lowest R_{wp} obtained in the GA calculations) was used as the initial structural model for a geometry optimization calculation using periodic Density Functional Theory (DFT) carried out using the CASTEP program.[135] The crystal structure obtained following DFT optimization was used as the initial structural model for Rietveld refinement,[154, 155] which was carried out using the GSAS program.[139] Standard restraints were applied to bond lengths (97 restraints) and bond angles (101 restraints), and planar restraints were applied to the aromatic system (5 restraints). The values of these geometric restraints were obtained from the DFT calculation. The final Rietveld refinement gave a good fit to the powder XRD data (R_{wp} = 2.13%, R_p = 1.56%; Fig. 7.21), with the following refined parameters: a = 13.4779(16) Å, b = 5.9653(4) Å, c = 29.7019(27) Å, β = 94.631(12)°; V = 2380.23(50) Å^3 (2θ range, 4° – 70°; 3868 profile points; 218 refined variables).

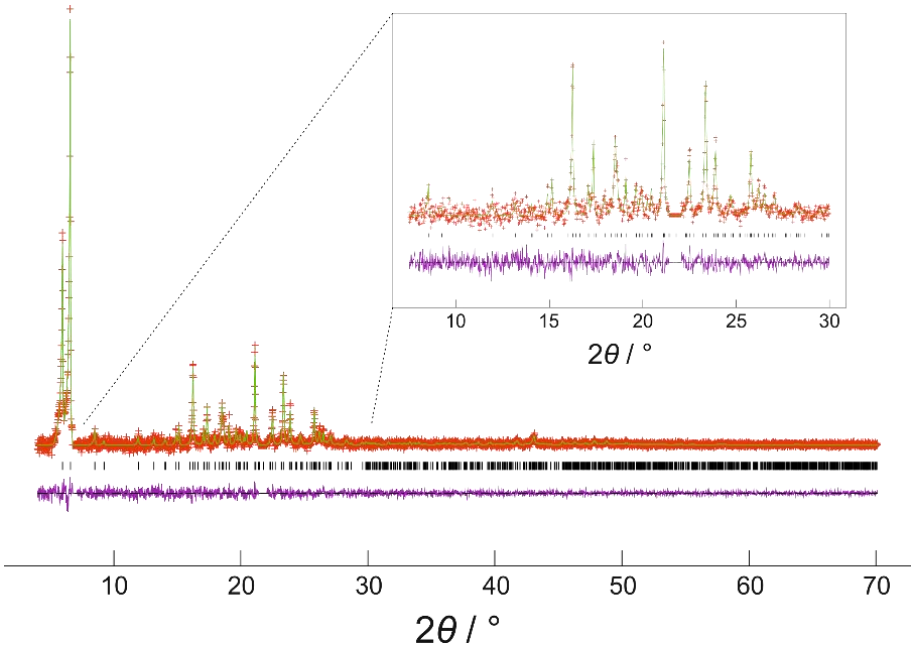

Figure 7.21 *Final Rietveld refinement of the powder XRD data for compound* ***9*** *(red crosses, experimental data; green line, calculated data; black tick marks, peak positions; magenta line, difference plot). The inset shows an expanded region of the powder XRD data in the range 2θ = 7.5° – 30°. The excluded regions (6.753° – 7.112° and 21.391° – 22.058°) correspond to the positions of two peaks from impurity phases.*

A further periodic DFT geometry optimization calculation was carried out on the structure obtained in the final Rietveld refinement. The geometry optimization led to only very minor structural changes, confirming that the final refined structure is structurally reasonable and energetically stable. The final crystal structure of compound **9** is shown

in Fig. 7.22 and Fig. 7.23 (see also Appendix VI). In this structure, the molecules aggregate through π···π stacking in a zigzag fashion along the [010] direction. The inter-planar distance of the molecules in the crystal structure of compound **9** molecules is also about 3.6 Å, which is consistent with the corresponding distance observed for compound **2**, compound **6** and compound **7** in the series of O-doped poly-aromatic hydrocarbons. The crystal structures of these four compounds are summarized in Table 7.3.

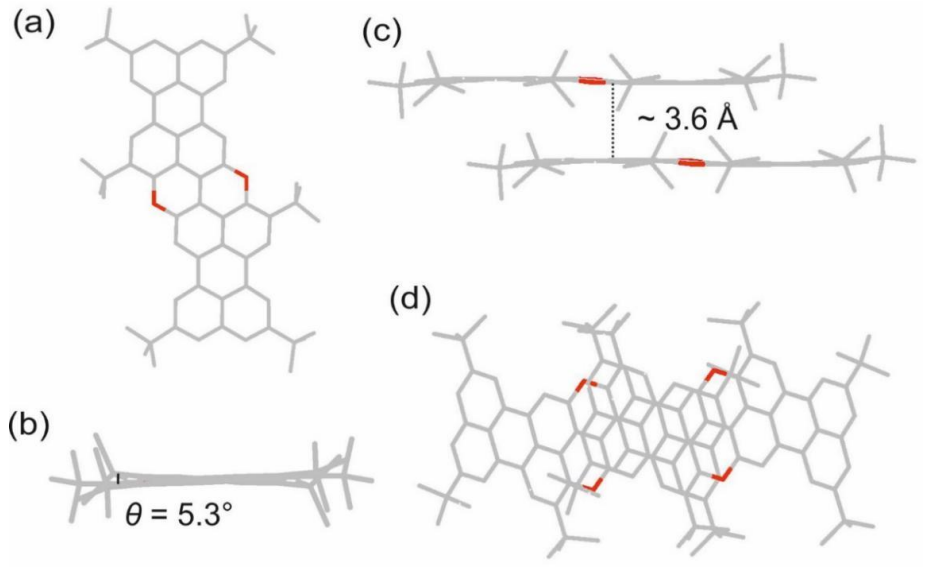

Figure 7.22 *(a,d) Top views, and (b,c) side views of the crystal structure and π···π stacking arrangement in the crystal structure of compound* ***9****, determined in this thesis from powder XRD data.*

Table 7.3 *Crystal structure data for compound* ***2****,* ***6****,* ***7*** *and* ***9*** *in the series of O-doped poly-aromatic hydrocarbons in Table 7.2.*

		Compound **2**	Compound **6**	Compound **7**	Compound **9**
Crystal System		orthorhombic	monoclinic	monoclinic	monoclinic
Space Group		$P2_12_12_1$	$P2_1/c$	$P2/c$	$P2_1/c$
Cell Parameters	*a* / Å	5.633(1)	11.049(5)	10.730(2)	13.4779(16)
	b / Å	14.558(3)	11.024(1)	12.406(3)	5.9653(4)
	c / Å	18.397(4)	25.124(4)	22.974(5)	29.7019(27)
	β / °	-	93.41(5)	102.10(3)	94.631(12)
Cell Volume / Å^3		1508.65(53)	3054.79(150)	2990.27(117)	2380.23(50)

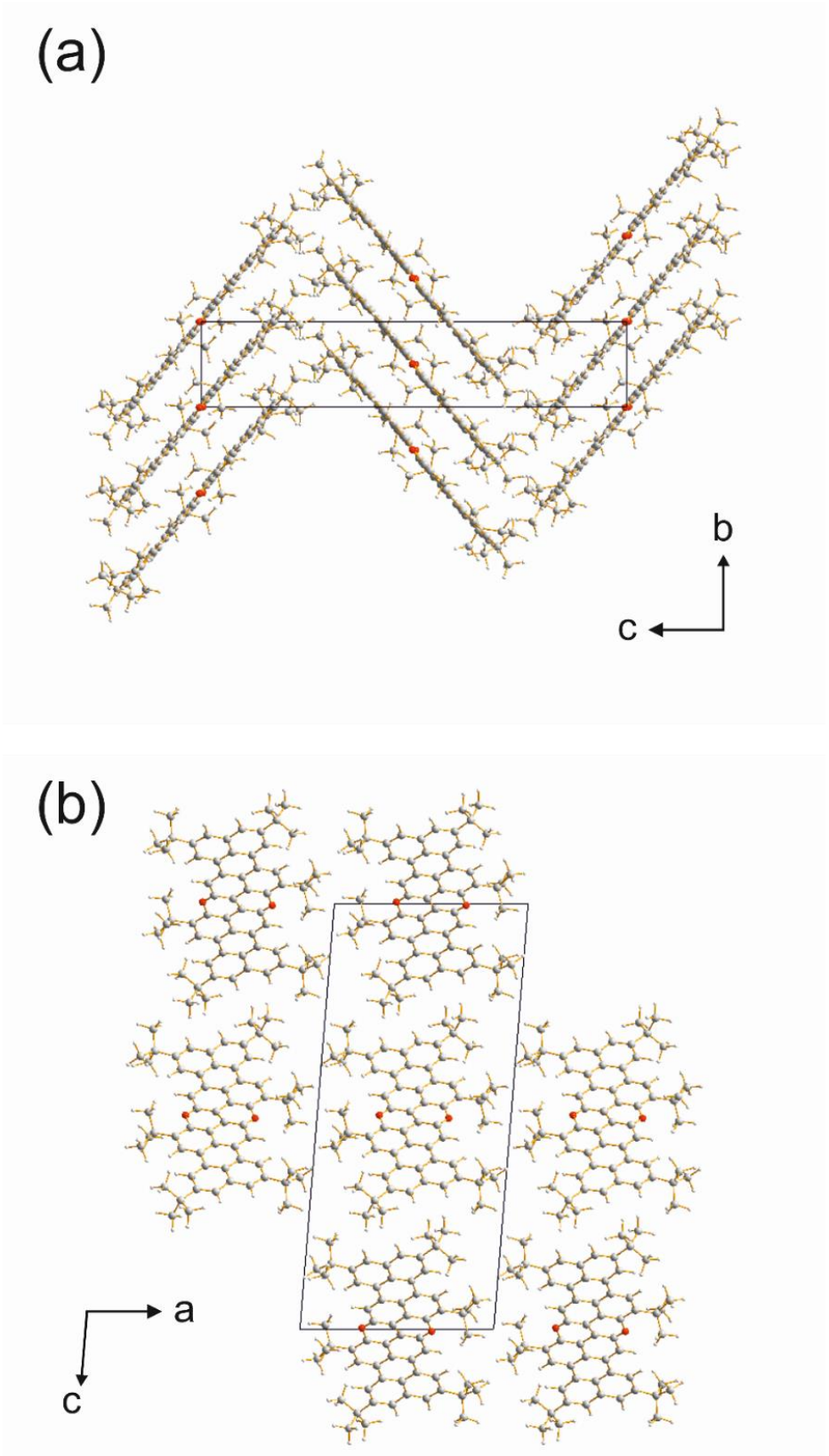

Figure 7.23 *Crystal structure of compound* ***9****: (a) viewed along the a-axis; (b) viewed along the b-axis.*

7.4 Conclusions

The three samples in this chapter have proven again that the direct-space Genetic Algorithm (GA) technique is an effective technique in solving crystal structures of organic materials from powder XRD data. For an isotropic good quality powder sample, structure determination can be now carried out routinely by following the flow chart in Fig. 1.24.

The new polymorphs found for **6**/urea and **8**/urea have demonstrated that mechanochemical milling can produce crystalline phases that are quite different from those obtained by traditional crystal growth methods. Thus, in the family of co-crystal of even chain α,ω-dihydroxyalkanes and urea, the A-P/O phases of all materials from **6**/urea to **16**/urea are now discovered (see Table 7.1). The phase transition experiments show that the new polymorphs of **6**/urea and **8**/urea are meta-stable, transforming to the more stable A-P/A and P/A polymorphs respectively, particularly at higher temperature.

The crystal structure of compound **9** in the series of O-doped poly-aromatic hydrocarbons show a similar π···π stacking structures and *ca.* 3.6 Å inter-planar spacing.

Chapter 8

Conclusions and Future Work

8.1 Conclusions

X-ray Birefringence Imaging (XBI) is a new technique (first reported in 2014) to investigate molecular orientational distributions in materials. The aim of this thesis was to advance the fundamentals and applications of this technique. Here, beyond model single crystals, new types of materials have been tested: liquid crystals (Chapter 3), bending crystals (Chapter 4), composite organic materials (Chapter 5) and situations with two crystals in the X-ray beam (Chapter 6). Correspondingly, customized accessories have been designed and constructed to suit different experimental requirements: a sample cell for liquid crystals (Fig. 3.3, Page 43), temperature control system (Fig. 4.14, Page 78), *ex-situ* and *in-situ* bending devices (Fig. 4.24, Page 87, and Fig. 4.31, Page 94), molecular transportation devices (Fig. 5.6, Page 108, and Fig. 5.7, Page 109) and a rotation stage for the studies of multiple crystals (Fig. 6.1, Page 116). As the XBI apparatus is assembled in a synchrotron beamline hutch (Fig. 8.1), there is enough space to fulfil many kinds of experiments.

Based on the experiments in this thesis, XBI has been demonstrated to have general applications in the following three aspects. (I) Investigation of phase transitions: phase transitions are usually accompanied by rearrangements of molecules, and XBI can detect such transitions by analysing the changes in orientations of the molecules (see 3.2 and 4.2). (II) Investigation of *in-situ* processes: molecular change can be monitored by recording XBI images during the process (see 3.2, 4.2, 4.5, 5.3 and 5.4). (III) Investigation of spatial distributions of molecules in complex materials: due to the element specific nature of XBI, the distributions of different molecular components in a composite sample can be characterized by XBI images (see 4.4, 5.2 and 5.3).

XBI also shows special applications for different types of samples. For liquid crystals, XBI can identify the order parameters and changes in order parameters under different conditions (e.g., temperature) (see 3.3). For single crystals, XBI can be used to

enable the face-indexing of small crystal faces (see 4.3). For bending crystals, XBI can detect even slight deformations (see 4.5).

Some preliminary studies of involving two independently oriented crystals in the XBI experiment further expand the applications of XBI to more complicated cases and a preliminary model is also provided to explain this phenomenon (see 6.2). Furthermore, an experimental set-up for "transmitted mode" XBI has been demonstrated by using a flat-plate single crystal as a transmission-based X-ray polarization analyzer (see 6.3).

Figure 8.1 *The synchrotron experimental hutch of beamline B16 in Diamond Light Source (Didcot, Oxfordshire), where all the XBI experiments reported in this thesis were carried out. The green equipment in the middle of the hutch is the Huber diffractometer.*

During the intervals between synchrotron beam time for XBI and analysis of XBI results, some work involving crystal structure determination from powder XRD data has also been carried out in my PhD study. Three crystal structures were determined from powder XRD data (see 7.2 and 7.3).

8.2 Future Work

In this thesis, all the XBI experiments reported were based on the Br K-edge. In order to apply this technique to a wider range of different materials, it is necessary to find other matched single crystals as the analyzer for XBI studies of different elements. A

recent experiment has shown the adaptability of XBI in studies of copper (II) acetylacetonate at an X-ray energy of 8979.005 eV (Cu K-edge) using a Si (2 2 0) crystal as a diffraction-based polarization analyzer.

The synchrotron hutch provides enough space to add experimental accessories to further expand the scope of XBI experiments. The sample cell developed to study liquid crystals (see Fig. 3.3, Page 43) has shown the successful application to liquid-state samples. In future experiments, it is worth designing sample holders or containers for gas samples. As there have been some reports of molecular orientation in the gas phase,[157-161] XBI could be another effective analysis tool to study this phenomenon. Thus, solid, liquid and gas, or any state with anisotropic molecular orientations could all be investigated in XBI. For the already used sample cell for liquids, further experiments can be carried out by changing the concentration of the liquid or the thickness of the cell to study the influential factors on the final intensity.

As an imaging technique, investigation of spatial distributions in complex materials is a significant application of XBI. In Chapter 4, XBI has shown advantages in the study of bending crystals. As hexabromobenzene is reported as non-bending at ambient temperature while the isostructural hexachlorobenzene is a prototypical example of a bending crystal,[63] composite crystals formed by these two chemicals with different ratios may be expected to show a critical point at which bending occurs, and the spatial distribution of the two types of molecule would be revealed in XBI images. In Chapter 5, the composite materials studies were made of one brominated component and another non-brominated component. In the future, it would be interesting to find other composite samples both containing brominated organic molecules but having different C–Br bond orientations.

Because of the limited beam time available for synchrotron experiments, some experiments reported in this thesis are still at a preliminary stage and also need further investigation. It would be interesting to study further the unknown “black-band” phenomenon in 3.2 and the “tilted boundary” phenomenon in 5.3. In 6.2, more information is required to build an accurate mathematical model for the general case of two independent crystals in the X-ray beam. In 6.3, the image contrast of “transmitted mode” XBI can be improved by some adjustment of the set-up and investigation of other transmission-based polarization analyzers.

X-ray Birefringence Imaging (XBI) is a new technique which is analogous to Polarizing Optical Microscopy (POM). However, its element selective nature makes XBI more accurate and effective in analysing selective element environments. POM has been used in many different areas of science since its invention in the 19th century.[58, 60, 91, 162] With further development and research, this new 21st Century technique – XBI – is fully expected to be demonstrated as a powerful technique in more versatile applications in the future.

References

1. Khurana, A. K., *Theory and Practice of Optics and Refraction*. Elsevier India: UP, India, 2008.
2. Riedl, M. J., *Optical Design Fundamentals for Infrared Systems*. SPIE Optical Engineering Press: Washington, USA, 1995.
3. Hecht, E., *Optics*. Pearson: London, UK, 2016.
4. Glazer, A. M., *Crystallography: A Very Short Introduction*. Oxford University Press: New York, USA, 2016.
5. Gribble, C. D.; Hall, A. J., *Optical Mineralogy: Principles & Practice*. Routledge: London, UK, 2003.
6. Ackermann, G. K.; Eichler, J., *Holography*. Wiley-VCH Verlag GmbH: Weinheim, Germany, 2007.
7. Murphy, D. B.; Davidson, M. W., *Fundamentals of Light Microscopy and Electronic Imaging*. Wiley-Blackwell: Hoboken, NJ, USA, 2013.
8. Group, C. P., *The Theory of Birefringence*. Cambridge Polymer Group, Inc.: Boston, Massachusetts, 2004.
9. Woolfson, M. M., *An Introduction to X-ray Crystallography*. Cambridge University Press: Cambridge, UK, 1997.
10. Brümmer, O.; Eisenschmidt, C.; Höche, H. R., Polarization Phenomena of X-rays in the Bragg Case. *Acta Cryst. A* **1984**, *40*, 394-398.
11. Materlik, G.; Suortti, P., Measurement of the Polarization of X-rays from a Synchrontron Source. *J. Appl. Cryst.* **1984**, *17*, 7-12.
12. Buerger, M. J.; Klein, G. E., Correction of X-ray Diffraction Intensities for Lorentz and Polarization Factors. *J. Appl. Phys.* **1945**, *16*, 408-418.
13. Sherwood, D.; Cooper, J., *Crystals, X-rays, and Proteins: Comprehensive Protein Crystallography*. Oxford University Press: New York, USA, 2011.
14. Cole, H.; Chambers, F. W.; Wood, C. G., X-ray Polarizer. *J. Appl. Phys.* **1961**, *32*, 1942-1945.
15. Hasegawa, Y.; Ueji, Y.; Okitsu, K.; Ablett, J. M.; Siddons, D. P.; Amemiya, Y., Transmission-Type X-ray Linear Polarizer with Perfect Crystals. *J. Synchrotron Rad.* **1998**, *5*, 738-740.
16. Marx, B.; Schulze, K. S.; Uschmann, I.; Kämpfer, T.; Wehrhan, O.; Wille, H. C.; Schlage, K.; Röhlsberger, R.; Weckert, E.; Förster, E.; Stöhlker, T.; Paulus, G. G., High Precision Measurement of Undulator Polarization in the Regime of Hard X-rays. *Appl. Phys. Lett.* **2014**, *105*, 1-4.
17. Paolasini, L., In *Resonant and Magnetic X-ray Diffraction by Polarized Synchrotron Radiation*, Conference on Neutrons and Magnetism, Seignosse,

France, May 18-24, 2012; Ecole Thematique de la Societe Francaise de la Neutronique, 2014.

18. Siddons, D. P.; Hart, M.; Amemiya, Y.; Hastings, J. B., X-ray Optical Activity and the Faraday Effect in Cobalt and Its Compounds. *Phys. Rev. Lett.* **1990**, *64*, 1967-1970.

19. Dirac, P. A. M., *The Principles of Quantum Mechanics*. Snowball Publishing: New York, USA, 2013.

20. Volobuev, A. N.; Tolstonogov, A. P., Malus' Law for X-ray Radiation. *J. Surf. Invest.: X-ray, Synchrotron Neutron Tech.* **2013**, *7*, 762-773.

21. Palmer, B. A.; Edwards-Gau, G. R.; Kariuki, B. M.; Harris, K. D. M.; Dolbnya, I. P.; Collins, S. P., X-ray Birefringence Imaging. *Science* **2014**, *344*, 1013-1016.

22. Palmer, B. A.; Morte-Ródenas, A.; Kariuki, B. M.; Harris, K. D. M.; Collins, S. P., X-ray Birefringence from a Model Anisotropic Crystal. *J. Phys. Chem. Lett.* **2011**, *2*, 2346-2351.

23. Palmer, B. A.; Edwards-Gau, G. R.; Morte-Ródenas, A.; Kariuki, B. M.; Lim, G. K.; Harris, K. D. M.; Dolbnya, I. P.; Collins, S. P., X-ray Birefringence: A New Strategy for Determining Molecular Orientation in Materials. *J. Phys. Chem. Lett.* **2012**, *3*, 3216-3222.

24. Palmer, B. A.; Edwards-Gau, G. R.; Kariuki, B. M.; Harris, K. D. M.; Dolbnya, I. P.; Collins, S. P.; Sutter, J. P., X-ray Birefringence Imaging of Materials with Anisotropic Molecular Dynamics. *J. Phys. Chem. Lett.* **2015**, *6*, 561-567.

25. Sutter, J. P.; Dolbnya, I. P.; Collins, S. P.; Harris, K. D. M.; Edwards-Gau, G. R.; Kariuki, B. M.; Palmer, B. A. In *Novel Technique for Spatially Resolved Imaging of Molecular Bond Orientations Using X-ray Birefringence*, 12th International Conference on Synchrotron Radiation Instrumentation (SRI), New York, USA, Jul 06-10, 2015; AIP Conference Proceedings, 2016.

26. Warren, B. E., *X-ray Diffraction*. Dover Publications: New York, USA, 2014.

27. Harris, K. D. M.; Cheung, E. Y., How to Determine Structures when Single Crystals Cannot be Grown: Opportunities for Structure Determination of Molecular Materials Using Powder Diffraction Data. *Chem. Soc. Rev.* **2004**, *33*, 526-538.

28. Harris, K. D. M.; Tremayne, M., Crystal Structure Determination from Powder Diffraction Data. *Chem. Mat.* **1996**, *8*, 2554-2570.

29. Zhou, Z. F.; Harris, K. D. M., Multiple-Fragment Representations of Molecular Geometry in Direct-Space Structure Solution from Powder X-ray Diffraction Data Using Genetic Algorithms. *Comput. Mater. Sci.* **2009**, *45*, 118-121.

30. Kariuki, B. M.; Serrano-González, H.; Johnston, R. L.; Harris, K. D. M., The Application of a Genetic Algorithm for Solving Crystal Structures from Powder Diffraction Data. *Chem. Phys. Lett.* **1997**, *280*, 189-195.

31. Habershon, S.; Harris, K. D. M.; Johnston, R. L., Development of a Multipopulation Parallel Genetic Algorithm for Structure Solution from Powder Diffraction Data. *J. Comput. Chem.* **2003**, *24*, 1766-1774.

32. Segall, M. D.; Lindan, P. J. D.; Probert, M. J.; Pickard, C. J.; Hasnip, P. J.; Clark, S. J.; Payne, M. C., First-Principles Simulation: Ideas, Illustrations and the CASTEP Code. *J. Phys.: Condens. Matter* **2002**, *14*, 2717-2744.

33. Myers, R. L., *The Basics of Physics*. Greenwood Press: London, UK, 2006.

34. Sands, D. E., *Introduction to Crystallography*. Dover Publications: New York, USA, 2012.

35. Sutter, J. P.; Dolbnya, I. P.; Collins, S. P.; Harris, K. D. M.; Edwards-Gau, G. R.; Palmer, B. A., Theoretical Analysis of the Background Intensity Distribution in X-ray Birefringence Imaging Using Synchrotron Bending-Magnet Radiation. *J. Appl. Phys.* **2015**, *117*, 10.

36. He, B. B.; Preckwinkel, U.; Smith, K. L., Comparison between Conventional and Two-Dimensional XRD. *Adv. X-ray Anal.* **2003**, *46*, 37-42.

37. Schawe, J. E. K.; Höhne, G. W. H., Modulated Temperature DSC Measurements Relating to the Cold Crystallization Process of Poly(ethylene terephtalate). *J. Thermal Anal.* **1996**, *46*, 893-903.

38. Tanaka, M.; Motomura, T.; Ishii, N.; Shimura, K.; Onishi, M.; Mochizuki, A.; Hatakeyama, T., Cold Crystallization of Water in Hydrated Poly(2-methoxyethyl acrylate)(PMEA). *Polym. Int.* **2000**, *49*, 1709-1713.

39. Mano, J. F.; Wang, Y.; Viana, J. C.; Denchev, Z.; Oliveira, M. J., Cold Crystallization of PLLA Studied by Simultaneous SAXS and WAXS. *Macromol. Mater. Eng.* **2004**, *289*, 910-915.

40. Naumann, C.; Brumm, T.; Bayerl, T. M., Phase Transition Behavior of Single Phosphatidylcholine Bilayers on a Solid Spherical Support Studied by DSC, NMR and FT-IR. *Biophys. J.* **1992**, *63*, 1314-1319.

41. Yasuniwa, M.; Sakamo, K.; Ono, Y.; Kawahara, W., Melting Behavior of Poly (l-lactic acid): X-ray and DSC Analyses of the Melting Process. *Polymer* **2008**, *49*, 1943-1951.

42. Sakurai, K.; Maegawa, T.; Takahashi, T., Glass Transition Temperature of Chitosan and Miscibility of Chitosan/Poly (N-vinyl pyrrolidone) Blends. *Polymer* **2000**, *41*, 7051-7056.

43. Yukimitu, K.; Oliveira, R. C.; Araújo, E. B.; Moraes, J. C. S.; Avanci, L. H., DSC Studies on Crystallization Mechanisms of Tellurite Glasses. *Thermochim. Acta* **2005**, *426*, 157-161.

44. Gabbott, P., *Principles and Applications of Thermal Analysis*. Blackwell Publishing: Oxford, UK, 2008.

45. Chambers, L., *The Practical Handbook of Genetic Algorithms: Applications*. CRC Press LLC: Florida, USA, 2001.

46. Singh, S.; Dunmur, D. A., *Liquid Crystals: Fundamentals*. World Scientific: New Jersey, USA, 2002.

47. Boamfa, M. I.; Lazarenko, S. V.; Vermolen, E. C. M.; Kirilyuk, A.; Rasing, T., Magnetic Field Alignment of Liquid Crystals for Fast Display Applications. *Adv. Mater.* **2005**, *17*, 610-614.

48. Gleeson, H.; Southern, C.; Brimicombe, P.; Goodby, J.; Görtz, V., Optical Measurements of Orientational Order in Uniaxial and Biaxial Nematic Liquid Crystals. *Liq. Cryst.* **2010**, *37*, 949-959.

49. Vorobiev, A. K.; Yankova, T. S.; Chumakova, N. A., Orientation Distribution Function and Order Parameters of Oriented Spin Probe as Determined by EPR Spectroscopy. *Chem. Phys.* **2012**, *409*, 61-73.

50. Robinson, B. H.; Johnson, L. E.; Eichinger, B. E., Relation of System Dimensionality and Order Parameters. *J. Phys. Chem. B* **2015**, *119*, 3205-3212.

51. Jenz, F.; Osipov, M. A.; Jagiella, S.; Giesselmann, F., Orientational Distribution Functions and Order Parameters in "de Vries"-Type Smectics: A Simulation Study. *J. Chem. Phys.* **2016**, *145*, 1-5.

52. Vollmer, A.; Feng, X. L.; Wang, X.; Zhi, L. J.; Müllen, K.; Koch, N.; Rabe, J. P., Electronic and Structural Properties of Graphene-based Transparent and Conductive Thin Film Electrodes. *Appl. Phys. A* **2009**, *94*, 1-4.

53. Fielden, M. L.; Hayes, R. A.; Ralston, J., Surface and Capillary Forces Affecting Air Bubble − Particle Interactions in Aqueous Electrolyte. *Langmuir* **1996**, *12*, 3721-3727.

54. Nalwa, H. S., *Handbook of Advanced Electronic and Photonic Materials and Devices*. Academic Press: New York, USA, 2001.

55. Cagnon, M.; Durand, G., Mechanical Shear of Layers in Smectic-A and Smectic-B Liquid Crystal. *Phys. Rev. Lett.* **1980**, *45*, 1418.

56. Pindak, R.; Moncton, D. E.; Davey, S. C.; Goodby, J. W., X-ray Observation of a Stacked Hexatic Liquid-Crystal B Phase. *Phys. Rev. Lett.* **1981**, *46*, 1135-1138.

57. Lagerwall, S. T.; Rudquist, P.; Giesselmann, F., The Orientational Order in So-Called de Vries Materials. *Mol. Cryst. Liq. Cryst.* **2009**, *510*, 148-157.

58. In, I.; Jun, Y. W.; Kim, Y. J.; Kim, S. Y., Spontaneous One Dimensional Arrangement of Spherical Au Nanoparticles with Liquid Crystal Ligands. *Chem. Commun.* **2005**, 800-801.

59. Goto, H.; Akagi, K., Preparation of Poly (3,4-ethylenedioxythiophene) in a Chiral Nematic Liquid – Crystal Field. *Macromol. Rapid Commun.* **2004**, *25*, 1482-1486.

60. Bisoyi, H. K.; Kumar, S., Liquid-Crystal Nanoscience: An Emerging Avenue of Soft Self-Assembly. *Chem. Soc. Rev.* **2011**, *40*, 306-319.

61. Soboyejo, W., *Mechanical Properties of Engineered Materials*. Dekker: New York, USA, 2003.

62. Reddy, C. M.; Krishna, G. R.; Ghosh, S., Mechanical Properties of Molecular Crystals – Applications to Crystal Engineering. *CrystEngComm* **2010**, *12*, 2296-2314.

63. Reddy, C. M.; Gundakaram, R. C.; Basavoju, S.; Kirchner, M. T.; Padmanabhan, K. A.; Desiraju, G. R., Structural Basis for Bending of Organic Crystals. *Chem. Commun.* **2005**, 3945-3947.

64. Reddy, C. M.; Padmanabhan, K. A.; Desiraju, G. R., Structure-Property Correlations in Bending and Brittle Organic Crystals. *Cryst. Growth Des.* **2006**, *6*, 2720-2731.

65. Takamizawa, S.; Miyamoto, Y., Superelastic Organic Crystals. *Angew. Chem.* **2014**, *53*, 6970-6973.

66. Ghosh, S.; Reddy, C. M., Elastic and Bendable Caffeine Cocrystals: Implications for the Design of Flexible Organic Materials. *Angew. Chem. Int. Ed.* **2012**, *51*, 10319-10323.

67. Panda, M. K.; Ghosh, S.; Yasuda, N.; Moriwaki, T.; Mukherjee, G. D.; Reddy, C. M.; Naumov, P., Spatially Resolved Analysis of Short-Range Structure Perturbations in a Plastically Bent Molecular Crystal. *Nat. Chem.* **2015**, *7*, 65-72.

68. Krishna, G. R.; Devarapalli, R.; Lal, G.; Reddy, C. M., Mechanically Flexible Organic Crystals Achieved by Introducing Weak Interactions in Structure: Supramolecular Shape Synthons. *J. Am. Chem. Soc.* **2016**, *138*, 13561-13567.

69. Dharmarwardana, M.; Welch, R. P.; Kwon, S.; Nguyen, V. K.; McCandless, G. T.; Omary, M. A.; Gassensmith, J. J., Thermo-Mechanically Responsive Crystalline Organic Cantilever. *Chem. Commun.* **2017**, *53*, 9890-9893.

70. Trotter, J., The Crystal Structures of Some Anthracene Derivatives. II. 9:10-Dibromoanthracene. *Acta Cryst.* **1958**, *11*, 803-807.

71. Mannocci, F.; Sherriff, M.; Watson, T. F., Three-Point Bending Test of Fiber Posts. *J. Endodont.* **2001**, *27*, 758-761.

72. Arnautov, A. K., The Method of Three-Point Bending in Testing Thin High-Strength Reinforced Plastics at Large Deflections. *Mech. Compos. Mater.* **2005**, *41*, 467-476.

73. Kourtis, L. C.; Carter, D. R.; Beaupre, G. S., Improving the Estimate of the Effective Elastic Modulus Derived from Three-Point Bending Tests of Long Bones. *Ann. Biomed. Eng.* **2014**, *42*, 1773-1780.

74. Worthy, A.; Grosjean, A.; Pfrunder, M. C.; Xu, Y.; Yan, C.; Edwards, G.; Clegg, J. K.; McMurtrie, J. C., Atomic Resolution of Structural Changes in Elastic Crystals of Copper(II) Acetylacetonate. *Nat. Chem.* **2018**, *10*, 65-69.

75. Bertram, A., *Elasticity and Plasticity of Large Deformations: An Introduction*. Springer-Verlag: Berlin, Germany, 2005.

76. Hollingsworth, M. D.; Brown, M. E.; Hillier, A. C.; Santarsiero, B. D.; Chaney, J. D., Superstructure Control in the Crystal Growth and Ordering of Urea Inclusion Compounds. *Science* **1996**, *273*, 1355-1359.

77. Schmicker, D.; van Smaalen, S.; de Boer, J. L.; Haas, C.; Harris, K. D. M., Obervation of the Sliding Mode in Incommensurate Intergrowth Compounds: Brillouin Scattering from the Inclusion Compound of Urea and Heptadecane. *Phys. Rev. Lett.* **1995**, *74*, 734-737.

78. Palmer, B. A.; Harris, K. D. M.; Guillaume, F., A Strategy for Retrospectively Mapping the Growth History of a Crystal. *Angew. Chem.* **2010**, *49*, 5096-5100.

79. Palmer, B. A.; Le Comte, A.; Harris, K. D. M.; Guillaume, F., Controlling Spatial Distributions of Molecules in Multicomponent Organic Crystals, with Quantitative Mapping by Confocal Raman Microspectrometry. *J. Am. Chem. Soc.* **2013**, *135*, 14512-14515.

80. Khan, A. A.; Bramwell, S. T.; Harris, K. D. M.; Kariuki, B. M.; Truter, M. R., The Design of a Molecularly Selective Capillary Based on an Incommensurate Intergrowth Structure. *Chem. Phys. Lett.* **1999**, *307*, 320-326.

81. Martí-Rujas, J.; Desmedt, A.; Harris, K. D. M.; Guillaume, F., Kinetics of Molecular Transport in a Nanoporous Crystal Studied by Confocal Raman Microspectrometry: Single-File Diffusion in a Densely Filled Tunnel. *J. Phys. Chem. B* **2007**, *111*, 12339-12344.

82. Martí-Rujas, J.; Harris, K. D. M.; Desmedt, A.; Guillaume, F., Significant Conformational Changes Associated with Molecular Transport in a Crystalline Solid. *J. Phys. Chem. B* **2006**, *110*, 10708-10713.

83. Martí-Rujas, J.; Harris, K. D. M.; Desmedt, A.; Guillaume, F., In-situ Monitoring of Alkane-Alkane Guest Exchange in Urea Inclusion Compounds Using Confocal Raman Microspectrometry. *Mol. Cryst. Liq. Cryst.* **2006**, *456*, 139-147.

84. Marti-Rujas, J.; Desmedt, A.; Harris, K. D. M.; Guillaume, F., Direct Time-Resolved and Spatially Resolved Monitoring of Molecular Transport in a Crystalline Nanochannel System. *J. Am. Chem. Soc.* **2004**, *126*, 11124-11125.

85. Martí-Rujas, J.; Desmedt, A.; Harris, K. D. M.; Guillaume, F., Bidirectional Transport of Guest Molecules through the Nanoporous Tunnel Structure of a Solid Inclusion Compound. *J. Phys. Chem. C* **2009**, *113*, 736-743.

86. Nakaoki, T.; Nagano, H.; Yanagida, T., Molecular Mobility Depending on Chain Length and Thermally Induced Molecular Motion of n-Alkane/Urea Inclusion Compounds. *J. Mol. Struct.* **2004**, *699*, 1-7.

87. McAdie, H. G., Thermal Decomposition of Molecular Complexes I. Urea-n-Paraffin Inclusion Compounds. *Can. J. Chem.* **1962**, *40*, 2195-2203.

88. McAdie, H. G., Thermal Decomposition of Molecular Complexes III. Urea Inclusion Compounds of Monosubstituted Aliphatic Series. *Can. J. Chem.* **1963**, *41*, 2144-2153.

89. Thakral, S.; Madan, A. K., Topological Models for Prediction of Heat of Decomposition of Urea Inclusion Compounds Containing Aliphatic Endocytes. *J. Incl. Phenom. Macrocycl. Chem.* **2008**, *60*, 187-192.

90. Reger, D. L.; Goode, S. R.; Ball, D. W., *Chemistry: Principles and Practice*. Brooks/Cole, Cengage Learning: Belmont, CA, USA, 2010.

91. Singfield, K. L.; Chisholm, R. A.; King, T. L., A Physical Chemistry Experiment in Polymer Crystallization Kinetics. *J. Chem. Educ.* **2012**, *89*, 159-162.

92. Harris, K. D. M., Fundamental and Applied Aspects of Urea and Thiourea Inclusion Compounds. *Supramol. Chem.* **2007**, *19*, 47-53.

93. Chao, M. H.; Kariuki, B. M.; Harris, K. D. M.; Collins, S. P.; Laundy, D., Design of a Solid Inclusion Compound with Optimal Properties as a Linear Dichroic Filter for X-ray Polarization Analysis. *Angew. Chem.* **2003**, *42*, 2982-2985.

94. Nawrocki, J., The Silanol Group and Its Role in Liquid Chromatography. *J. Chromatogr. A* **1997**, *779*, 29-71.

95. Harris, K. D. M.; Thomas, J. M., Structural Aspects of the Chlorocyclohexane/Thiourea Inclusion System. *J. Chem. Soc. Faraday Trans.* **1990**, *86*, 1095-1101.

96. George, A. R.; Harris, K. D. M., Representing and Understanding Geometric Features of One-Dimensional Tunnel Structures in Solid Inclusion Compounds. *J. Mol. Graphics* **1995**, *13*, 138-141.

97. Savenkov, S. N.; Sydoruk, O. I.; Muttiah, R. S., Conditions for Polarization Elements to be Dichroic and Birefringent. *J. Opt. Soc. Am. A* **2005**, *22*, 1447-1452.

98. Harris, K. D. M.; Thomas, J. M., Structural Aspects of Urea Inclusion Compounds and their Investigation by X-ray Diffraction: A General Discussion. *J. Chem. Soc. Faraday Trans.* **1990**, *86*, 2985-2996.

99. Lefort, R.; Toudic, B.; Etrillard, J.; Guillaume, F.; Bourges, P.; Currat, R.; Breczewski, T., Dynamical Molecular Disorder and Diffuse Scattering in an Alkane/Urea Incommensurate Inclusion Compound. *Eur. Phys. J. B* **2001**, *24*, 51-57.

100. Harris, K. D. M., Investigating the Structure and Dynamics of a Family of Organic Solids: The Alakne/Urea Inclusion Compounds. *J. Solid State Chem.* **1993**, *106*, 83-98.

101. Harris, K. D. M., Structural and Dynamic Properties of Urea and Thiourea Inclusion Compounds. *J. Mol. Struct.* **1996**, *374*, 241-250.

102. Harris, K. D. M., Meldola Lecture: Understanding the Properties of Urea and Thiourea Inclusion Compounds. *Chem. Soc. Rev.* **1997**, *26*, 279-289.

103. Hollingsworth, M. D., Crystal Engineering: from Structure to Function. *Science* **2002**, *295*, 2410-2413.

104. Rennie, A. J. O.; Harris, K. D. M., A Mathematical Model of One-Dimensional Inclusion Compounds: a New Approach Towards Understanding Commensurate and Incommensurate Behaviour. *Proc. R. Soc. lond. A* **1990**, *430*, 615-640.

105. Smith, A. E., The Crystal Structure of the Urea-Hydrocarbon Complexes. *Acta Cryst.* **1952**, *5*, 224-235.

106. Toudic, B.; Garcia, P.; Odin, C.; Rabiller, P.; Ecolivet, C.; Collet, E.; Bourges, P.; McIntyre, G. J.; Hollingsworth, M. D.; Breczewski, T., Hidden Degrees of Freedom in Aperiodic Materials. *Science* **2008**, *319*, 69-71.

107. Toudic, B.; Lefort, R.; Ecolivet, C.; Guérin, L.; Currat, R.; Bourges, P.; Breczewski, T., Mixed Acoustic Phonons and Phase Modes in an Aperiodic Composite Crystal. *Phys. Rev. Lett.* **2011**, *107*, 205502.

108. Chadwick, K.; Davey, R.; Sadiq, G.; Cross, W.; Pritchard, R., The Utility of a Ternary Phase Diagram in the Discovery of New Co-crystal Forms. *CrystEngComm* **2009**, *11*, 412-414.

109. Deutsch, Z.; Bernstein, J., Cocrystal of Urea and Imidazolidone: Formation of an Unexpected 1-D Substructure in a Plausibly Predictable Cocrystal. *Cryst. Growth Des.* **2008**, *8*, 3537-3542.

110. Cruz-Cabeza, A. J.; Day, G. M.; Jones, W., Towards Prediction of Stoichiometry in Crystalline Multicomponent Complexes. *Chem. Eur. J.* **2008**, *14*, 8830-8836.

111. Aliev, A. E.; Harris, K. D. M.; Champkin, P. H., Structural and Dynamic Aspects of Hydrogen-Bonded Complexes and Inclusion Compounds Containing α,ω-Dicyanoalkanes and Urea, Investigated by Solid-State ^{13}C and ^{2}H NMR Techniques. *J. Phys. Chem. B* **2005**, *109*, 23342-23350.

112. Hollingsworth, M. D.; Brown, M. E.; Santarsiero, B. D.; Huffman, J. C.; Goss, C. R., Template-Directed Synthesis of 1:1 Layered Complexes of α,ω-Dinitriles and Urea: Packing Efficiency versus Specific Functional Group Interactions. *Chem. Mat.* **1994**, *6*, 1227-1244.

113. Hollingworth, M. D.; Santarsiero, B. D.; Oumarmahamat, H.; Nichols, C. J., New Series of 1:1 Layered Complexes of α,ω-Dinitriles and Urea. *Chem. Mat.* **1991**, *3*, 23-25.

114. Harkema, S.; Ter brake, J. H. M.; Helmholdt, R. B., Structure of Urea-Oxalic Acid (1/1), $CH_4N_2O.C_2H_2O_4$, Determined by Neutron Diffraction. *Acta Cryst. C* **1984**, *40*, 1733-1734.

115. Pickering, M.; Small, R. W. H., Structure of the 1:1 Complex of Resorcinol and Urea. *Acta Cryst. B* **1982**, *38*, 3161-3163.

116. Fábry, J.; Podlahová, J.; Loub, J.; Langer, V., Structure of the 1:1 Adduct of Orthoperiodic Acid and Urea. *Acta Cryst. B* **1982**, *38*, 1048-1050.

117. Itai, A.; Yamada, H.; Okamoto, T.; Iitaka, Y., The Structure of the Crystalline Complex of Purine and Urea (2:1). *Acta Cryst. B* **1977**, *33*, 1816-1820.

118. Mahmoud, M. M.; Wallwork, S. C., The Crystal Structure of the 1:1 Complex between Quinol and Urea. *Acta Cryst. B* **1975**, *31*, 338-342.

119. Duax, W. L., The Structure of the Crystalline Complex Estradiol.Urea (1:1). *Acta Cryst. B* **1972**, *28*, 1864-1871.

120. Snyder, R. L.; Rosenstein, R. D., The Crystal and Molecular Structure of the 1:1 Hydrogen Bond Complex between α-D-Glucose and Urea. *Acta Cryst. B* **1971**, *27*, 1969-1975.

121. Colman, P. M.; Medlin, E. H., The Crystal Structure of Urea Parabanic Acid. *Acta Cryst. B* **1970**, *26*, 1547-1553.

122. Lee, S. O.; Kariuki, B. M.; Harris, K. D. M., Hydrogen-Bonded Chains of α,ω-Diaminoalkane and α,ω-Dihydroxyalkane Guest Molecules Lead to Disrupted Tunnel Structures in Urea Inclusion Compounds. *New J. Chem.* **2005**, *29*, 1266-1271.

123. Martí-Rujas, J.; Kariuki, B. M.; Hughes, C. E.; Mórte-Rodenas, A.; Guo, F.; Glavcheva-Laleva, Z.; Taştemür, K.; Ooi, L.; Yeo, L.; Harris, K. D. M., Structural Diversity, but no Polymorphism, in a Homologous Family of Co-crystals of Urea and α,ω-Dihydroxyalkanes. *New J. Chem.* **2011**, *35*, 1515-1521.

124. Bučar, D. K.; Filip, S.; Arhangelskis, M.; Lloyd, G. O.; Jones, W., Advantages of Mechanochemical Cocrystallisation in the Solid-State Chemistry of Pigments: Colour-Tuned Fluorescein Cocrystals. *CrystEngComm* **2013**, *15*, 6289-6291.

125. Käldström, M.; Meine, N.; Farès, C.; Schüth, F.; Rinaldi, R., Deciphering 'Water-Soluble Lignocellulose' Obtained by Mechanocatalysis: New Insights into the Chemical Processes Leading to Deep Depolymerization. *Green Chem.* **2014**, *16*, 3528-3538.

126. Baláž, P.; Achimovičová, M.; Baláž, M.; Billik, P.; Cherkezova-Zheleva, Z.; Criado, J. M.; Delogu, F.; Dutková, E.; Gaffet, E.; Gotor, F. J.; Kumar, R.; Mitov, I.; Rojac, T.; Senna, M.; Streletskii, A.; Wieczorek-Ciurowa, K., Hallmarks of Mechanochemistry: from Nanoparticles to Technology. *Chem. Soc. Rev.* **2013**, *42*, 7571-7637.

127. Ventura, B.; Bertocco, A.; Braga, D.; Catalano, L.; d'Agostino, S.; Grepioni, F.; Taddei, P., Luminescence Properties of 1,8-Naphthalimide Derivatives in Solution, in Their Crystals, and in Co-crystals: Toward Room-Temperature Phosphorescence from Organic Materials. *J. Phys. Chem. C* **2014**, *118*, 18646-18658.

128. Braga, D.; Maini, L.; Grepioni, F., Mechanochemical Preparation of Co-crystals. *Chem. Soc. Rev.* **2013**, *42*, 7638-7648.

129. Boldyreva, E., Mechanochemistry of Inorganic and Organic Systems: What is Similar, What is Different? *Chem. Soc. Rev.* **2013**, *42*, 7719-7738.

130. James, S. L.; Adams, C. J.; Bolm, C.; Braga, D.; Collier, P.; Friščić, T.; Grepioni, F.; Harris, K. D. M.; Hyett, G.; Jones, W.; Krebs, A.; Mack, J.; Maini, L.; Orpen, A. G.; Parkin, I. P.; Shearouse, W. C.; Steed, J. W.; Waddell, D. C., Mechanochemistry: Opportunities for New and Cleaner Synthesis. *Chem. Soc. Rev.* **2012**, *41*, 413-447.

131. Yoshida, J.; Nishikiori, S.; Kuroda, R.; Yuge, H., Three Polymorphic Cd^{II} Coordination Polymers Obtained from the Solution and Mechanochemical Reactions of 3-Cyanopentane-2,4-dione with Cd^{II} Acetate. *Chem. Eur. J.* **2013**, *19*, 3451-3457.

132. Kaupp, G., Solid-State Molecular Syntheses: Complete Reactions Without Auxiliaries Based on the New Solid-State Mechanism. *CrystEngComm* **2003**, *5*, 117-133.

133. Yuan, W.; Garay, A. L.; Pichon, A.; Clowes, R.; Wood, C. D.; Cooper, A. I.; James, S. L., Study of the Mechanochemical Formation and Resulting Properties of An Archetypal MOF: $Cu_3(BTC)_2$ (BTC=1,3,5-benzenetricarboxylate). *CrystEngComm* **2010**, *12*, 4063-4065.

134. Miletić, T.; Fermi, A.; Orfanos, I.; Avramopoulos, A.; De Leo, F.; Demitri, N.; Bergamini, G.; Ceroni, P.; Papadopoulos, M. G.; Couris, S.; Bonifazi, D.,

Tailoring Colors by O Annulation of Polycyclic Aromatic Hydrocarbons. *Chem. Eur. J.* **2017**, *23*, 2363-2378.

135. Clark, S. J.; Segall, M. D.; Pickard, C. J.; Hasnip, P. J.; Probert, M. J.; Refson, K.; Payne, M. C., First Principles Methods Using CASTEP. *Z. Kristallogr.* **2005**, *220*, 567-570.

136. Werner, P. E.; Eriksson, L.; Westdahl, M., TREOR, A Semi-Exhaustive Trial-and-Error Powder Indexing Program for All Symmetries. *J. Appl. Cryst.* **1985**, *18*, 367-370.

137. Shirley, R., *The CRYSFIRE System for Automatic Powder Indexing: User's Manual*. The Lattice Press: Guildford, U.K., 1999.

138. Le Bail, A.; Duroy, H.; Fourquet, J. L., Ab-initio Structure Determination of $LiSbWO_6$ by X-ray Powder Diffraction. *Mater. Res. Bull.* **1988**, *23*, 447-452.

139. Larson, A. C.; Von Dreele, R. B., GSAS. *Report LAUR* **1994**, 86-748.

140. Tedesco, E.; Turner, G. W.; Harris, K. D. M.; Johnston, R. L.; Kariuki, B. M., Structure Determination of an Oligopeptide Directly from Powder Diffraction Data. *Angew. Chem. Int. Ed.* **2000**, *39*, 4488-4491.

141. Kariuki, B. M.; Psallidas, K.; Harris, K. D. M.; Johnston, R. L.; Lancaster, R. W.; Staniforth, S. E.; Cooper, S. M., Structure Determination of a Steroid Directly from Powder Diffraction Data. *Chem. Commun.* **1999**, 1677-1678.

142. Turner, G. W.; Tedesco, E.; Harris, K. D. M.; Johnston, R. L.; Kariuki, B. M., Implementation of Lamarckian Concepts in a Genetic Algorithm for Structure Solution from Powder Diffraction Data. *Chem. Phys. Lett.* **2000**, *321*, 183-190.

143. Harris, K. D. M.; Johnston, R. L.; Kariuki, B. M., The Genetic Algorithm: Foundations and Apllications in Structure Solution from Powder Diffraction Data. *Acta Cryst. A* **1998**, *54*, 632-645.

144. Kariuki, B. M.; Calcagno, P.; Harris, K. D. M.; Philp, D.; Johnston, R. L., Evolving Opportunities in Structure Solution from Powder Diffraction Data – Crystal Structure Determination of a Molecular System with Twelve Variable Torsion Angles. *Angew. Chem. Int. Ed.* **1999**, *38*, 831-835.

145. Cheung, E. Y.; Kitchin, S. J.; Harris, K. D. M.; Imai, Y.; Tajima, N.; Kuroda, R., Direct Structure Determination of a Multicomponent Molecular Crystal Prepared by a Solid-State Grinding Procedure. *J. Am. Chem. Soc.* **2003**, *125*, 14658-14659.

146. Albesa-Jové, D.; Kariuki, B. M.; Kitchin, S. J.; Grice, L.; Cheung, E. Y.; Harris, K. D. M., Challenges in Direct-Space Structure Determination from Powder Diffraction Data: A Molecular Material with Four Independent Molecules in the Asymmetric Unit. *ChemPhysChem* **2004**, *5*, 414-418.

147. Cheung, E. Y.; McCabe, E. E.; Harris, K. D. M.; Johnston, R. L.; Tedesco, E.; Raja, K. M. P.; Balaram, P., C−H···O Hydrogen Bond Mediated Chain Reversal in a Peptide Containing a γ-Amino Acid Residue, Determined Directly from Powder X-ray Diffraction Data. *Angew. Chem. Int. Ed.* **2002**, *41*, 494-496.

148. Tedesco, E.; Harris, K. D. M.; Johnston, R. L.; Turner, G. W.; Raja, K. M. P.; Balaram, P., Ab initio Structure Determination of a Peptide β-Turn from Powder X-ray Diffraction Data. *Chem. Commun.* **2001**, 1460-1461.

149. Fujii, K.; Young, M. T.; Harris, K. D. M., Exploiting Powder X-ray Diffraction for Direct Structure Determination in Structural Biology: the P2X4 Receptor Trafficking Motif YEQGL. *J. Struct. Biol.* **2011**, *174*, 461-467.

150. Guo, F.; Harris, K. D. M., Structural Understanding of a Molecular Material that is Accessed Only by a Solid-State Desolvation Process: the Scope of Modern Powder X-ray Diffraction Techniques. *J. Am. Chem. Soc.* **2005**, *127*, 7314-7315.

151. Guo, F.; Martí-Rujas, J.; Pan, Z.; Hughes, C. E.; Harris, K. D. M., Direct Structural Understanding of a Topochemical Solid State Photopolymerization Reaction. *J. Phys. Chem. C* **2008**, *112*, 19793-19796.

152. Martí-Rujas, J.; Meazza, L.; Lim, G. K.; Terraneo, G.; Pilati, T.; Harris, K. D. M.; Metrangolo, P.; Resnati, G., An Adaptable and Dynamically Porous Organic Salt Traps Unique Tetrahalide Dianions. *Angew. Chem. Int. Ed.* **2013**, *52*, 13444-13448.

153. Pan, Z.; Xu, M.; Cheung, E. Y.; Harris, K. D. M.; Constable, E. C.; Housecroft, C. E., Understanding the Structural Properties of a Dendrimeric Material Directly from Powder X-ray Diffraction Data. *J. Phys. Chem. B* **2006**, *110*, 11620-11623.

154. McCusker, L. B.; Von Dreele, R. B.; Cox, D. E.; Louër, D.; Scardi, P., Rietveld Refinement Guidelines. *J. Appl. Cryst.* **1999**, *32*, 36-50.

155. Rietveld, H. M., A Profile Refinement Method for Nuclear and Magnetic Structures. *J. Appl. Cryst.* **1969**, *2*, 65-71.

156. Boultif, A.; Louër, D., Indexing of Powder Diffraction Patterns for Low-Symmetry Lattices by the Successive Dichotomy Method. *J. Appl. Cryst.* **1991**, *24*, 987-993.

157. Seideman, T., Rotational Excitation and Molecular Alignment in Intense Laser Fields. *J. Chem. Phys.* **1995**, *103*, 7887-7896.

158. Minemoto, S.; Sakai, H., Measuring Polarizability Anisotropies of Rare Gas Diatomic Molecules by Laser-Induced Molecular Alignment Technique. *J. Chem. Phys.* **2011**, *134*, 214305.

159. Minemoto, S.; Tanji, H.; Sakai, H., Polarizability Anisotropies of Rare Gas van der Waals Dimers Studied by Laser-Induced Molecular Alignment. *J. Chem. Phys.* **2003**, *119*, 7737-7740.

160. Pinkham, D.; Vogt, T.; Jones, R. R., Extracting the Polarizability Anisotropy from the Transient Alignment of HBr. *J. Chem. Phys.* **2008**, *129*, 064307.

161. Poterya, V.; Votava, O.; Fárník, M.; Ončák, M.; Slavíček, P.; Buck, U.; Friedrich, B., Generation and Orientation of Organoxenon Molecule H-Xe-CCH in the Gas Phase. *J. Chem. Phys.* **2008**, *128*, 104313.

162. Kaminsky, W.; Claborn, K.; Kahr, B., Polarimetric Imaging of Crystals. *Chem. Soc. Rev.* **2004**, *33*, 514-525.

Appendices

Appendix I: Crystal Structure of 1,4-Dibromo-2,3,5,6-tetramethylbenzene at 296 K

This crystal structure is determined by conventional single-crystal XRD method at 296 K. It has a monoclinic space group as $P2_1/c$, with the following cell parameters: a = 8.3575(7) Å, b = 4.0087(4) Å, c = 15.4040(16) Å, β = 91.367(9)°, V = 515.93(9) Å^3. The atomic fractional coordinates and the corresponding occupancies are shown in the following table:

Atom	Occupancy	x / *a*	y / *b*	z / *c*
C(1)	1	0.8561(3)	0.3875(8)	0.03276(19)
C(2)	1	0.9753(3)	0.5074(7)	0.08867(19)
C(3)	1	1.1198(3)	0.6213(8)	0.05596(19)
C(4)	0.672	0.6975(15)	0.265(6)	0.0687(14)
H(4)A	0.672	0.71290	0.05050	0.09530
H(4)B	0.672	0.61940	0.24700	0.02220
H(4)C	0.672	0.66060	0.42060	0.11120
C(5)	0.636	0.960(2)	0.545(6)	0.1868(6)
H(5)A	0.636	0.86030	0.45030	0.20430
H(5)B	0.636	0.96320	0.77710	0.20200
H(5)C	0.636	1.04700	0.43070	0.21580
C(6)	0.692	1.249(2)	0.752(5)	0.1177(12)
H(6)A	0.692	1.20070	0.85970	0.16610
H(6)B	0.692	1.31470	0.90990	0.08780
H(6)C	0.692	1.31450	0.57000	0.13810
Br(4)	0.328	0.6610(4)	0.2382(13)	0.0769(3)

Br(5)	0.364	0.9412(4)	0.5205(9)	0.20819(18)
Br(6)	0.308	1.2795(5)	0.7711(12)	0.1330(3)

Appendix II: Crystal Structure of 1,4-Dibromo-2,3,5,6-tetramethylbenzene at 150 K

This crystal structure is determined by conventional single-crystal XRD method at 150 K. It has a monoclinic space group as $P2_1/c$, with the following cell parameters: a = 16.5563(6) Å, b = 11.8267(3) Å, c = 17.1846(6) Å, β = 117.237(4)°, V = 2991.76(19) Å^3. The atomic fractional coordinates and the corresponding occupancies are shown in the following table:

Atom	Occupancy	x / *a*	y / *b*	z / *c*
C(1)	1	0.1939(2)	0.1712(3)	-0.0825(2)
C(2)	1	0.1592(2)	0.1272(3)	-0.0291(2)
C(3)	1	0.2165(2)	0.1206(3)	0.0610(2)
C(4)	1	0.3055(2)	0.1603(3)	0.0917(2)
C(5)	1	0.3404(2)	0.2029(3)	0.0381(2)
C(6)	1	0.2831(2)	0.2094(3)	-0.0522(2)
C(7)	0.938	0.0610(5)	0.0882(12)	-0.0688(8)
H(7)A	0.938	0.02430	0.12850	-0.12160
H(7)B	0.938	0.03760	0.10430	-0.02480
H(7)C	0.938	0.05770	0.00670	-0.07810
C(8)	1	0.1820(3)	0.0736(3)	0.1237(3)
H(8)A	1	0.22670	0.02030	0.16450
H(8)B	1	0.12410	0.03450	0.09000
H(8)C	1	0.17320	0.13600	0.15660

C(9)	0.934	0.4393(5)	0.2410(11)	0.0754(9)
H(9)A	0934	0.44470	0.31910	0.09620
H(9)B	0.934	0.45900	0.23660	0.02970
H(9)C	0.934	0.47760	0.19170	0.12430
C(10)	1	0.3172(3)	0.2558(3)	-0.1157(3)
H(10)A	1	0.32020	0.19410	-0.15230
H(10)B	1	0.37780	0.28870	-0.08220
H(10)C	1	0.27520	0.31400	-0.15300
Br(7)	0.062	0.0382(8)	0.0773(19)	-0.0786(14)
Br(9)	0.066	0.4602(8)	0.2571(18)	0.0804(14)
C(11)	1	0.2195(2)	0.4601(3)	0.0541(2)
C(12)	1	0.3097(2)	0.4969(3)	0.0892(2)
C(13)	1	0.3399(2)	0.5393(3)	0.0307(2)
C(14)	1	0.2787(2)	0.5420(3)	-0.0578(2)
C(15)	1	0.1887(2)	0.5057(3)	-0.0928(2)
C(16)	1	0.1588(2)	0.4618(3)	-0.0340(2)
C(17)	0.978	0.3742(5)	0.4898(6)	0.1871(3)
H(17)A	0.978	0.35420	0.54250	0.21880
H(17)B	0.978	0.43580	0.50970	0.19750
H(17)C	0.978	0.37400	0.41260	0.20770
C(18)	0.966	0.4388(4)	0.5782(7)	0.0654(6)
H(18)A	0.966	0.45370	0.58500	0.01660
H(18)B	0.966	0.47920	0.52260	0.10760
H(18)C	0.966	0.44660	0.65170	0.09430
C(19)	0.982	0.1235(4)	0.5130(5)	-0.1907(3)
H(19)A	0.982	0.14460	0.57170	-0.21750

H(19)B	0.982	0.06250	0.53210	-0.19900
H(19)C	0.982	0.12180	0.44000	-0.21840
C(20)	0.965	0.0611(4)	0.4198(7)	-0.0679(5)
H(20)A	0.965	0.05110	0.39550	-0.01850
H(20)B	0.965	0.05070	0.35590	-0.10770
H(20)C	0.965	0.01890	0.48110	-0.09930
Br(17)	0.022	0.382(2)	0.486(3)	0.2116(7)
Br(18)	0.034	0.4588(11)	0.594(3)	0.070(2)
Br(19)	0.018	0.119(2)	0.506(4)	-0.2165(7)
Br(20)	0.035	0.0355(8)	0.418(2)	-0.0852(16)
C(21)	1	0.1633(2)	0.7964(3)	-0.0305(2)
C(22)	1	0.2192(2)	0.7893(3)	0.0594(2)
C(23)	1	0.3092(2)	0.8260(3)	0.0918(2)
C(24)	1	0.3374(2)	0.8694(3)	0.0325(2)
C(25)	1	0.2817(2)	0.8771(3)	-0.0570(2)
C(26)	1	0.1915(2)	0.8389(3)	-0.0898(2)
C(27)	0.959	0.1838(4)	0.7451(6)	0.1219(4)
H(27)A	0.959	0.18240	0.80700	0.15920
H(27)B	0.959	0.22390	0.68500	0.15860
H(27)C	0.959	0.12230	0.71490	0.08790
C(28)	0.943	0.3739(7)	0.8165(11)	0.1893(4)
H(28)A	0.943	0.43200	0.78520	0.19740
H(28)B	0.943	0.34730	0.76650	0.21700
H(28)C	0.943	0.38380	0.89160	0.21620
C(29)	0.96	0.3145(6)	0.9252(8)	-0.1206(6)
H(29)A	0.96	0.37180	0.96590	-0.08760

H(29)B	0.96	0.26870	0.97720	-0.16150
H(29)C	0.96	0.32400	0.86310	-0.15340
C(30)	0.942	0.1266(7)	0.8462(11)	-0.1876(4)
H(30)A	0.942	0.06690	0.81720	-0.19860
H(30)B	0.942	015050	0.80080	-0.22020
H(30)C	0.942	0.12090	0.92510	-0.20660
Br(27)	0.041	0.1761(12)	0.7314(16)	0.1345(10)
Br(28)	0.057	0.3914(13)	0.822(2)	0.2103(7)
Br(29)	0.04	0.3279(17)	0.929(2)	-0.1329(15)
Br(30)	0.058	0.1196(13)	0.845(2)	-0.2126(6)
Br(1)	0.935	0.11442(3)	0.18269(6)	-0.20526(3)
Br(2)	0.936	0.38242(3)	0.15432(6)	0.21518(3)
Br(3)	0.945	0.17882(3)	0.40612(5)	0.13544(3)
Br(4)	0.946	0.32106(3)	0.59642(5)	-0.13748(3)
Br(5)	0.901	0.04066(3)	0.74532(5)	-0.07413(3)
Br(6)	0.903	0.46035(3)	0.91965(6)	0.07802(3)
C(1)A	0.065	0.130(2)	0.181(10)	-0.1821(12)
H(1)A(1)	0.065	0.12150	0.10620	-0.20930
H(1)A(2)	0.065	0.15610	0.23270	-0.20880
H(1)A(3)	0.065	0.07050	0.21010	-0.19130
C(2)A	0.064	0.369(3)	0.155(10)	0.1916(10)
H(2)A(1)	0.064	0.43170	0.14400	0.20230
H(2)A(2)	0.064	0.35060	0.09090	0.21670
H(2)A(3)	0.064	0.36380	0.22510	0.21910
C(3)A	0.055	0.187(3)	0.411(10)	0.1188(13)
H(3)A(1)	0.055	0.19130	0.46950	0.16100

H(3)A(2)	0.055	0.22520	0.34660	0.15010
H(3)A(3)	0.055	0.12370	0.38610	0.08620
C(4)A	0.054	0.313(3)	0.585(11)	-0.1227(12)
H(4)A(1)	0.054	0.37580	0.61220	-0.08980
H(4)A(2)	0.054	0.27430	0.64670	-0.15800
H(4)A(3)	0.054	0.31160	0.52280	-0.16120
C(5)A	0.099	0.0635(15)	0.756(6)	-0.0666(11)
H(5)A(1)	0.099	0.04780	0.74900	-0.01830
H(5)A(2)	0.099	0.05670	0.68230	-0.09510
H(5)A(3)	0.099	0.02310	0.81100	-0.10930
C(6)A	0.097	0.4358(17)	0.915(6)	0.0699(11)
H(6)A(1)	0.097	0.45710	0.90910	0.02540
H(6)A(2)	0.097	0.47570	0.87150	0.12160
H(6)A(3)	0.097	0.43690	0.99500	0.08630

Appendix III: Crystal Structure of 9,10-Dibromoanthracene

This crystal structure is downloaded from the Cambridge Structural Database (CSD) with the code as DBANTH01. It was determined by J Trotter in 1958.[70] It has a triclinic space group as $P\bar{1}$, with the following cell parameters: a = 4.06(1) Å, b = 8.88(2) Å, c = 16.15(4) Å, α = 98.83(17)°, β = 97.08(17)°, γ = 100.35(17)°, V = 559.14(239) Å^3. The atomic fractional coordinates and the corresponding occupancies are shown in the following table:

Atom	Occupancy	x / *a*	y / *b*	z / *c*
Br(1)	1	-0.06710	0.35170	0.17220
C(1)	1	-0.63050	0.12430	-0.08960
C(2)	1	-0.45080	0.22350	-0.00890

C(3)	1	-0.22420	0.35860	-0.00070
C(4)	1	-0.02700	0.44200	0.07300
C(5)	1	0.17910	0.58050	0.07860
C(6)	1	0.38630	0.65700	0.16140
C(7)	1	-0.60500	0.20490	-0.16210
Br(2)	1	0.02680	0.67000	0.38110
C(8)	1	0.38500	1.13650	0.31300
C(9)	1	0.25670	1.00090	0.34570
C(10)	1	0.12830	1.00050	0.42270
C(11)	1	0.01550	0.86760	0.45110
C(12)	1	-0.12830	0.84680	0.52570
C(13)	1	-0.25670	0.70780	0.55520
C(14)	1	0.38500	1.27960	0.37110
C(5)A	1	-0.17910	0.41950	-0.07860
C(3)A	1	0.22420	0.64140	0.00070
C(7)A	1	0.60500	0.79510	0.16210
C(6)A	1	-0.38630	0.34300	-0.16140
C(4)A	1	0.02700	0.55800	-0.07300
C(2)A	1	0.45080	0.77650	0.00890
C(1)A	1	0.63050	0.87570	0.08960
Br(1)A	1	0.06710	0.64830	-0.17220
C(12)A	1	0.12830	1.15320	0.47430
C(10)A	1	-0.12830	0.99950	0.57730
C(14)A	1	-0.38500	0.72040	0.62890
C(13)A	1	0.25670	1.29220	0.44480
C(11)A	1	-0.01550	1.13240	0.54890

C(9)A	1	-0.25670	0.99910	0.65430
C(8)A	1	-0.38500	0.86350	0.68700
Br(2)A	1	-0.02680	1.33000	0.61890

Appendix IV: Crystal Structure of A-P/O Phase of 6/Urea

This crystal structure is determined by powder XRD method. It has a triclinic space group as $P\bar{1}$, with the following cell parameters: a = 5.1601(5) Å, b = 7.4276(5) Å, c = 8.5685(7) Å, α = 81.465(4)°, β = 86.299(6)°, γ = 78.209(5)°, V = 317.72(6) Å^3. The atomic fractional coordinates and the isotropic displacement parameters are shown in the following table:

Atom	x / a	y / b	z / c	Uiso / Å^2
C(1)	0.0647(11)	0.2532(6)	0.3989(5)	0.0440(15)
O(2)	0.2566(14)	0.2940(9)	0.4604(6)	0.0440(15)
N(3)	0.1039(16)	0.1157(7)	0.3106(5)	0.0440(15)
H(4)	0.2887(20)	0.0434(8)	0.2925(9)	0.0529(18)
H(5)	-0.0511(24)	0.0842(14)	0.2619(6)	0.0529(18)
N(6)	-0.1823(12)	0.3459(9)	0.4204(8)	0.0440(15)
H(7)	-0.2182(23)	0.4505(8)	0.4865(10)	0.0529(18)
H(8)	-0.3336(15)	0.3114(16)	0.3702(11)	0.0529(18)
C(9)	0.7311(12)	0.7962(13)	0.1537(12)	0.0440(15)
H(10)	0.9034(22)	0.694(2)	0.1979(34)	0.0529(18)
H(11)	0.785(4)	0.871(4)	0.0408(11)	0.0529(18)
O(12)	0.6543(18)	0.9248(9)	0.2628(7)	0.0440(15)
H(13)	0.670(12)	0.8596(13)	0.3692(11)	0.0529(18)
C(14)	0.5167(14)	0.6952(12)	0.1273(11)	0.0440(15)

H(15)	0.3424(21)	0.7978(20)	0.0865(32)	0.0529(18)
H(16)	0.468(5)	0.6158(32)	0.2391(10)	0.0529(18)
C(17)	0.5950(15)	0.5635(13)	0.006(1)	0.0440(15)
H(18)	0.612(6)	0.6458(35)	-0.1095(8)	0.0529(18)
H(19)	0.7878(12)	0.4771(29)	0.036(4)	0.0529(18)

Appendix V: Crystal Structure of A-P/O Phase of 8/Urea

This crystal structure is determined by powder XRD method. It has a triclinic space group as $P\bar{1}$, with the following cell parameters: a = 5.1707(5) Å, b = 7.3963(5) Å, c = 10.3805(10) Å, α = 70.786(4)°, β = 80.442(7)°, γ = 78.634(6)°, V = 365.32(6) Å^3. The atomic fractional coordinates and the isotropic displacement parameters are shown in the following table:

Atom	x / a	y / b	z / c	Uiso / Å^2
C(1)	0.0779(12)	0.2735(4)	0.4070(5)	0.0418(14)
O(2)	0.2560(16)	0.3120(7)	0.4589(7)	0.0418(14)
N(3)	-0.1754(12)	0.3495(7)	0.4294(8)	0.0418(14)
H(4)	-0.2254(23)	0.4384(6)	0.4883(9)	0.0501(17)
H(5)	-0.3169(19)	0.3180(13)	0.3875(13)	0.0501(17)
N(6)	0.1365(20)	0.1564(5)	0.3286(5)	0.0418(14)
H(7)	0.3264(24)	0.0969(5)	0.3098(9)	0.0501(17)
H(8)	-0.0089(32)	0.1274(10)	0.2880(8)	0.0501(17)
C(9)	0.4404(15)	0.2300(15)	0.8231(8)	0.0418(14)
H(10)	0.6191(16)	0.1225(28)	0.8422(27)	0.0501(17)
H(11)	0.481(4)	0.3485(34)	0.7300(8)	0.0501(17)
C(12)	0.2282(15)	0.1347(18)	0.8002(7)	0.0418(14)

H(13)	0.0603(20)	0.2462(31)	0.7648(24)	0.0501(17)
H(14)	0.164(4)	0.032(4)	0.8976(7)	0.0501(17)
O(15)	0.3159(17)	0.0346(10)	0.7020(9)	0.0418(14)
H(16)	0.277(12)	0.1205(21)	0.6122(16)	0.0501(17)
C(17)	0.3689(21)	0.3117(17)	0.9422(8)	0.0418(14)
H(18)	0.1657(14)	0.388(4)	0.9372(26)	0.0501(17)
H(19)	0.380(6)	0.1908(34)	1.0371(10)	0.0501(17)
C(20)	0.5455(15)	0.4501(15)	0.9454(9)	0.0418(14)
H(21)	0.7439(13)	0.3690(33)	0.9626(35)	0.0501(17)
H(22)	0.554(6)	0.562(4)	0.8456(5)	0.0501(17)

Appendix VI: Crystal Structure of the Poly-aromatic Compound

This crystal structure is determined by powder XRD method. It has a monoclinic space group as $P2_1/c$, with the following cell parameters: a = 13.4779(16) Å, b = 5.9653(4) Å, c = 29.7019(27) Å, β = 94.631(12)°, V = 2380.23(50) Å^3. The atomic fractional coordinates and the isotropic displacement parameters are shown in the following table:

Atom	x / a	y / b	z / c	Uiso / Å^2
C(1)	0.75158	1.34932	0.64131	0.0311
C(2)	0.67971	1.47347	0.66116	0.0311
H(3)	0.70092	1.60772	0.68496	0.0373
C(4)	0.57709	1.43214	0.65187	0.0311
C(5)	0.50707	1.54907	0.67610	0.0311
H(6)	0.53567	1.67849	0.69949	0.0373
C(7)	0.40658	1.50107	0.67078	0.0311

C(8)	0.37538	1.32965	0.63994	0.0311
H(9)	0.29621	1.29041	0.63546	0.0373
C(10)	0.44059	1.21011	0.61477	0.0311
C(11)	0.54476	1.25786	0.62114	0.0311
C(12)	0.61789	1.12942	0.60018	0.0311
C(13)	0.71876	1.17807	0.61101	0.0311
H(14)	0.77441	1.08000	0.59526	0.0373
C(15)	0.40783	1.02830	0.58407	0.0311
C(16)	0.48001	0.90481	0.56206	0.0311
C(17)	0.58480	0.94677	0.56953	0.0311
C(18)	0.65130	0.81116	0.54791	0.0311
H(19)	0.73120	0.83769	0.55304	0.0373
C(20)	0.61694(5)	0.6337(6)	0.52030(15)	0.002(9)
C(21)	0.51608(4)	0.5904(5)	0.51278(12)	0.002(9)
C(22)	0.44632(4)	0.7265(4)	0.53300(11)	0.002(9)
C(23)	0.34393(5)	0.6751(5)	0.52499(12)	0.023(9)
C(24)	0.27218	0.79542	0.54647	0.0311
C(25)	0.30821	0.96793	0.57569	0.0311
H(26)	0.25338	1.06149	0.59289	0.0373
O(27)	0.31308(14)	0.4993(7)	0.49673(18)	0.023(9)
C(28)	0.86213	1.40409	0.65356	0.0311
C(29)	0.88911	1.61869	0.62850	0.0311
H(30)	0.87265	1.76858	0.64815	0.0373
H(31)	0.96887	1.62133	0.62305	0.0373
H(32)	0.84725	1.63083	0.59531	0.0373
C(33)	0.87875	1.44419	0.70504	0.0311

H(34)	0.83877	1.31697	0.72343	0.0373
H(35)	0.85084	1.60996	0.71409	0.0373
H(36)	0.95788	1.43525	0.71716	0.0373
C(37)	0.93352	1.21791	0.64124	0.0311
H(38)	0.99757	1.28362	0.62499	0.0373
H(39)	0.96279	1.13041	0.67210	0.0373
H(40)	0.89660	1.09209	0.61880	0.0373
C(41)	0.33077	1.62564	0.69760	0.0311
C(42)	0.29246	1.46088	0.73245	0.0311
H(43)	0.30523	1.52934	0.76682	0.0373
H(44)	0.21247	1.42700	0.72577	0.0373
H(45)	0.33168	1.30001	0.73152	0.0373
C(46)	0.37760	1.82802	0.72327	0.0311
H(47)	0.38320	1.79354	0.75967	0.0373
H(48)	0.33261	1.98040	0.71733	0.0373
H(49)	0.45345	1.86234	0.71413	0.0373
C(50)	0.24196	1.71018	0.66643	0.0311
H(51)	0.26107	1.71413	0.63126	0.0373
H(52)	0.17605	1.60316	0.66800	0.0373
H(53)	0.22104	1.88045	0.67627	0.0373
C(54)	0.16051	0.74332	0.53984	0.0311
C(55)	0.14027	0.49400	0.54929	0.0311
H(56)	0.08805	0.42630	0.52235	0.0373
H(57)	0.20847	0.39354	0.55098	0.0373
H(58)	0.10617	0.47401	0.58136	0.0373
C(59)	0.09905	0.88122	0.57127	0.0311

H(60)	0.02769	0.79630	0.57428	0.0373
H(61)	0.08212	1.04968	0.55806	0.0373
H(62)	0.13557	0.89788	0.60547	0.0373
C(63)	0.12206	0.79943	0.49094	0.0311
H(64)	0.14414	0.67116	0.46729	0.0373
H(65)	0.04051	0.81165	0.48820	0.0373
H(66)	0.15162	0.96177	0.48073	0.0373